

**Faculty of Science and Engineering  
Department of Petroleum Engineering**

**Simulation of Hydraulic Fracture Propagation Interacted with  
Natural Fractures**

**Hassan Fatahi**

**This thesis is presented for the Degree of  
Doctor of Philosophy  
of  
Curtin University**

**November 2016**

# Declaration

To the best of my knowledge and belief this thesis contains no material previously published by any other person except where due acknowledgment has been made.

This thesis contains no material which has been accepted for the award of any other degree or diploma in any university.

Name:

**Hassan Fatahi**

Signature:

Date:

12 November 2016

# Abstract

Increased demands for energy and the decline of production from conventional sources of oil and gas have pushed industry to develop unconventional oil and gas resources such as coal seam gas, shale gas and shale oil reservoirs. These reservoirs are now new conventional reservoirs, thanks to the application of horizontal drilling technology and massive multistage hydraulic fracturing advancements.

Rocks have been created during geological eras and subjected to tectonic forces, which have caused natural fractures. Because the direction of tectonic forces has changed over and over again, different sets of natural fractures with different orientations and properties have been created in the rocks. The presence of natural fractures can affect the propagation of hydraulic fractures.

This study focuses on advancing the understanding of the mechanisms of hydraulic fracture initiation, propagation, and its interaction with natural fractures, and investigates the effect of natural fractures on the propagation of hydraulic fractures through distinct element-based numerical simulation and laboratory experiments. The thesis describes different steps in the development of numerical simulation modelling and experimental validation. The study begins with the development of rock samples with the desired mechanical properties, and then validates fluid flow through the created rock samples. Created rock samples with desired fluid flow properties are hydraulically fractured to investigate the initiation and breakdown pressure as well as the propagation path. In the next stage, simulation is used to investigate the interaction mechanism between hydraulic fractures and natural fractures through extensive sensitivity studies. For each step of the simulation development, the results are compared against analytical or experimental results to validate their accuracy. In the last step, the validated simulation model is used to perform extensive sensitivity analysis to investigate the effect of different parameters and their influence on the natural and hydraulic fracture interaction mechanism. The effect of parameters such as natural fractures' permeability, their orientation with respect to the direction of principal stresses, their size, their distance from the borehole, and the magnitude of principal stresses are investigated. It was found from the simulation results that the permeability of natural fractures is the most important

parameter that affects the interaction of natural and hydraulic fractures. It was observed that the interaction of hydraulic and natural fractures can mostly cause fracture re-initiation from the tip of natural fractures when their permeability is very high. The second most important parameter was found to be the orientation of natural fractures with respect to the direction of principal stresses. Low angles between the natural fracture plane and minimum horizontal stress direction encourage the crossing of induced hydraulic fractures. At high angles, hydraulic fractures re-initiate at the tip of natural fractures. The simulation results as well as the experimental results also demonstrate that hydraulic fractures predominantly progress in the direction of maximum horizontal stress. However, the presence of natural fractures can cause offsetting of hydraulic fractures. The net effect is that a fracture not only moves away from the wellbore in the maximum horizontal stress direction, but it also shifts in the direction of minimum horizontal stress direction. This phenomenon can explain the reason that micro seismic events reveal a cloud of data when hydraulic fracturing is performed in formations with natural fractures in the formation. In these formations, instead of having a bi-wing smooth hydraulic fracture in the direction of maximum horizontal stress, a branch-out fracture can be created.

# Acknowledgements

I appreciate the support of all those people who have helped, inspired and encouraged me during my PhD study.

First, I would like to express my heartfelt appreciation to my supervisor, Dr Md Mofazzal Hossain: for his continuous guidance, support and sharing of his invaluable knowledge of hydraulic fracturing; for his support to help me to attend national and international conferences; for his advice on publishing papers in journals; and for his generous time and dedication to reviewing and editing my thesis. It is an honour for me to graduate as a PhD student under his supervision.

My sincere appreciation goes to my co-supervisor, Professor Brian Evans, for his support and guidance, without which this study could not have matured.

Special gratitude is extended to Professor Reza Rezaee, the chairman of my PhD candidacy committee, for his leadership, patience and support.

I thank Dr Christina Houen of Perfect Words Editing for her thorough work on final editing of the thesis according to the guidelines of the Institute of Professional Editors (IPEd).

I would like to thank Dr Seyed Hassan Fallahzadeh for helping me with experimental tests, and Dr Mohammad Sarmadivaleh for his suggestions during Numerical Code development, and providing further experimental data for code validation.

I further wish to express appreciation to Dr Ali Saeedi for his support, and the opportunities that he provided for me to work safely and efficiently in Curtin University laboratories.

I would like to express my gratitude to Curtin University Research and Scholarship department for providing me with a generous Australian Postgraduate Award (APA) Scholarship and Curtin Research Scholarship.

I would like to express my appreciation to the Australian and Western Australian Governments and The North West Shelf joint Venture Partners, as well as the

Western Australian Energy Research Alliance (WA:ERA) for providing me with a scholarship top-up fund.

Dedicated To:

My wife Somaya Khateri

and

My Parents;

For their love, patience, encouragement and support.

# Contents

Declaration .....	i
Abstract .....	ii
Acknowledgements .....	iv
List of Figures .....	ix
List of Tables .....	xvi
Nomenclature .....	xvii
Publications related to this thesis .....	xx
Chapter 1 Introduction .....	1
1.1. Objective of the study.....	5
1.2. Significance of this research.....	6
1.3. Outline of Thesis .....	7
Chapter 2 Mechanics of Hydraulic Fracture Initiation, Propagation and Interaction with Natural Fracture .....	1
2.1. Initiation and Breakdown Pressure.....	2
2.2. Interaction Mechanism of Hydraulic and Natural Fracture.....	20
Chapter 3 Simulation of Rock's Mechanical Properties.....	33
3.1. Introduction to Discrete Element Method, Distinct Element Method (DEM) and PFC2D .....	33
3.2. Simulating Rocks in PFC2D .....	37
Chapter 4 Simulation of Fluid Flow using DEM.....	42
4.1. Distinct Element Method Fluid Flow .....	43
4.2. Analytical Methods .....	53
4.2.1. Linear Fluid Flow Condition.....	53
4.2.2. Radial fluid flow .....	60
4.3. Comparison of Numerical and Analytical Models.....	68
4.3.1. Linear Fluid Flow with Constant Boundary Pressures .....	68
4.3.2. Radial Fluid Flow.....	73

Chapter 5	Hydraulic Fracture Initiation Pressure, Breakdown Pressure and Propagation Path .....	80
5.1.	Simulated Samples: Mechanical and Fluid Flow Properties.....	80
5.2.	Simulation of Hydraulic Fracturing.....	83
5.3.	Laboratory Experiments .....	86
5.4.	Comparison between Numerical Simulation and Experimental Studies.....	94
Chapter 6	Numerical and Experimental Investigation of the Interaction of Natural and Propagated Hydraulic Fracture.....	101
6.1.	Simulation of the Interaction of Hydraulic and Natural Fractures .....	102
6.2.	Experimental Studies.....	104
6.3.	Results and discussion.....	108
Chapter 7	Sensitivity Analysis.....	119
7.1.	Isotropic Stress State .....	120
7.2.	Hydraulic Fracture Propagation in Presence of Natural Fractures.....	124
7.3.	Hydraulic Fracturing in Presence of Abundant Natural Fractures .....	138
Chapter 8	Conclusion and Recommendations .....	145
8.1.	Conclusions .....	145
8.2.	Recommendations .....	148
References	.....	150
Copyright Permissions	.....	156

# List of Figures

Figure 1-1: World population growth, (U.S. Census Bureau, 2015) .....	3
Figure 1-2: Total world energy consumption by energy source, 1990–2040 (Quadrillion Btu), (EIA, 2016) .....	3
Figure 1-3: Resource Triangle, (Chan et al, 2012) .....	4
Figure 1-4: Increase in calculation per second per \$1000 based on Moore’s Law (Seth, 2016) .....	5
Figure 2-1: Pressure/flow rate versus time since the beginning of flow injection to create a hydraulic fracture, propagate, close and re-open it. ....	2
Figure 2-2: Fluid pressure variation during fracturing of layered samples. After (Daneshy, 1978) .....	6
Figure 2-3: Circular borehole drilled in an intact infinite medium with a bi-wing crack of half-length $l$ in the direction of $\sigma_H$ . After (Rummel, 1987) .....	7
Figure 2-4: Spherical (left) and cylindrical (right) holes in the sample (Medlin & Masse, 1979) .....	8
Figure 2-5: Breakdown pressure as a function of horizontal stress ratio for minimum horizontal stresses of 6.9 and 13.8 MPa. Dashed lines show expected decline in breakdown pressure for elastic rock. After (Boyce et al, 1984) .....	10
Figure 2-6: Effect of borehole size on $P_{c0}$ . a) Lac du Bonnet Granite, b) Indiana limestone. After (Haimson & Zhao, 1991) .....	10
Figure 2-7: Effect of pressurisation rate on $P_{c0}$ . a) Ldb granite, b) Indiana limestone. After (Haimson & Zhao, 1991) .....	11
Figure 2-8: Wellbore pressure versus normalised fracture length for three cases of 1) isotropic far field stress, 2) non-isotropic far field stress, and 3) reopening test. (a) Slow pressurisation (b) Fast pressurisation. After (Detournay & Carbonell, 1997) .....	14
Figure 2-9: Dimensionless wellbore pressure ( $\Pi$ ) and dimensionless fracture length ( $\mathcal{L}$ ) versus dimensionless time $\tau$ for $M=0.1$ and $C=0.4$ . After (Lakirouhani et al., 2008) .....	16
Figure 2-10: Dimensionless breakdown and initiation pressure difference versus dimensionless viscosity. After (Lakirouhani et al., 2008) .....	16
Figure 2-11: Wellbore with an initial flaw. After (Zhang et al., 2010) .....	17
Figure 2-12: Fracture trajectory for different sets of injection rate and fluid viscosity. After (Zhang et al., 2010) .....	18
Figure 2-13: Extension of hydraulic fracture near a-large open flaw, b-large closed flaw. (Daneshy, 1974) .....	21
Figure 2-14: Effect of natural interfaces on hydraulic fracture propagation. (Hanson et al., 1981) .....	22
Figure 2-15: Schematic view of the tests on left and a sample tested on the right for $60^\circ$ and $30^\circ$ interaction angles. (Blanton, 1982) .....	23
Figure 2-16: Opening criteria, from left to right $\gamma = 0.2, 0.4$ and $0.6$ <i>psi. in</i> , (Blanton, 1982) .....	24
Figure 2-17: Arresting criteria for a- $\mu = 0.75$ and $\gamma = 0.2, 0.4$ and $0.6$ <i>psi. in</i> , b- $\gamma = 0.4$ <i>psi. in</i> and $\mu = 1.0, 0.75$ and $0.5$ from left to right, (Blanton, 1982) .....	25

Figure 2-18: Hydraulic fracture intersecting natural fracture.....	26
Figure 2-19: Interaction criteria versus experimental results comparison, (Blanton, 1986) .....	26
Figure 2-20: Comparison of analytical and experimental results for hydraulic fracture interacting with natural interface in Colton sandstone. (Gu et al, 2011).....	31
Figure 3-1: A sample that has been simulated by: a- Finite Element Method, b- Discrete Element Method. (Tavarez & Plesha, 2007).....	35
Figure 3-2: Characteristics of Discrete Element Method classes as well as Limit Equilibrium Limit Analysis. After (Cundall & Hart, 1992) .....	36
Figure 3-3: Algorithm used in PFC2D for force, velocity and displacement calculation. (Itasca, 2008).....	36
Figure 3-4: Particle-particle interaction analogy and concept in PFC2D. After (Huynh, 2014) .....	37
Figure 3-5: a- Direct tension test of Lean shale; b- Uniaxial compression test of Lean shale; c- Direct tension test of Rich shale; d- Uniaxial compression test of Rich shale. (Fatahi, 2014) .....	40
Figure 3-6: Confined compression test of Lean shale (10 MPa confinement stress); b- Confined compression test of Rich shale (10 MPa confinement stress); c- Confined compression test of Lean shale (20 MPa confinement stress); d- Confined compression test of Rich shale (20 MPa confinement stress). (Fatahi, 2014) .....	40
Figure 4-1: Particles and Domains. (Fatahi & Hossain, 2016) .....	43
Figure 4-2: A sample composed of grey particles. Black circles are centres of domains and their size is based on size of domain volume. Black lines connect each domain to its neighbouring domains. Red lines show boundaries of each domain. (Fatahi & Hossain, 2016).....	43
Figure 4-3: a- Parallelepiped connecting two domains. Parallelepiped is shown in red. b- Parallelepiped with length $LP$ , width $w$ , and depth 1. (Fatahi & Hossain, 2016) .....	44
Figure 4-4: Sample with principle stresses acting on its sides. (Fatahi & Hossain, 2016) .....	47
Figure 4-5: a) Domain with pressure $P$ ; b) Pressure applied to part of particle 1 that is exposed to domain 1 and generated force $F$ because of pressure $P$ . (Fatahi & Hossain, 2016) .....	47
Figure 4-6: $\Theta$ is greater than $\pi$ . The value of $\Theta$ should be replaced by $\beta$ in (4-6). (Fatahi & Hossain, 2016) .....	48
Figure 4-7: Algorithm of fluid flow calculation. Calculations are explicit in time. (Fatahi & Hossain, 2016) .....	52
Figure 4-8: Sample with two sets of natural fractures. (Fatahi & Hossain, 2016).....	52
Figure 4-9: a) Sample. Each yellow circle shows a particle; b) Sample after setting pore pressure. Each brown circle shows the domain pore pressure. (Fatahi & Hossain, 2016) .....	69
Figure 4-10: Simulation results at four different times; a:t=67 seconds, b:t=267 seconds, c:t=667 seconds and d:t=15067 seconds. (Fatahi & Hossain, 2016).....	70
Figure 4-11: Simulation results. Pressure of domains against linear distance from left hand side of sample at different times. As time increases, domain pressures decrease until a steady state condition is established. (Fatahi & Hossain, 2016) .....	70

Figure 4-12: Simulated versus analytical results. Vertical axis shows dimensionless pressure and horizontal axis shows dimensionless position. On each curve coloured dots are simulation results and black dots are analytical results. (Fatahi & Hossain, 2016) .....	73
Figure 4-13: a) Reservoir with wellbore at centre; b) Reservoir with boundary pressure of 7 MPa. Brown circles show domain pressure. (Fatahi & Hossain, 2016) .....	73
Figure 4-14: Reservoir with initial pore pressure set to 7 MPa. (Fatahi & Hossain, 2016) .....	74
Figure 4-15: Simulation results at four different times; a: t=120.03 seconds; b: t=420.03; c: t=1420.03 and d: t=24086.70 seconds (Fatahi & Hossain, 2016) .....	75
Figure 4-16: Simulation results of pressure vs. radius. (Fatahi & Hossain, 2016) .....	76
Figure 4-17: $[Y1\lambda J0\lambda RDe - J1\lambda Y0\lambda RDe]$ vs. $\lambda$ . The function approaches zero very quickly as the value of $\lambda$ increases. (Fatahi & Hossain, 2016) .....	78
Figure 4-18: Simulated dimensionless pressure and analytical dimensionless pressure vs. dimensionless radius. (Fatahi & Hossain, 2016) .....	79
Figure 5-1: a-Sample with wellbore in the middle and four plates around it for stress installation. Horizontal maximum and minimum stresses are applied on the sample. b- Sample with vertical crack on left and zoomed in view at right. This represents the initial crack in the direction of maximum horizontal stress in Sandstone 1.1. C- Beginning of fluid injection into the wellbore. Blue circles show normalised fluid pressure with the biggest circle showing the highest pressure. The vertical axis shows the wellbore pressure and the horizontal axis shows time elapsed since the beginning of fluid injection. The black diagonal line shows pressure versus time. d- Onset of fracture initiation. The red line shows created fracture. The pressure profile starts to deviate from a linear trend with the creation of the first fracture. e- Fracture propagation. Bonds between particles break one after the other. f- Fracture breakdown pressure is the maximum pressure that the wellbore experiences. g- Fracture arriving at top boundary (left), arriving at bottom boundary (right), and zoomed-in view of fracture with pressure profile rotated 90° clockwise. (Fatahi et al, 2016) .....	85
Figure 5-2: Stabilised flow through the fracture after the fracture arrived at the top and bottom boundaries. Pressure decline rate is high at the beginning when the fracture arrived at the boundaries. It gradually levelled off and got a constant value. The stabilised pressure value is equal to the pressure that is required to keep the fracture open, plus the frictional pressure drop inside the fracture. The bottom part of the figure shows the pressure profile inside the fracture. Bottom picture is rotated 90° clockwise. (Fatahi et al, 2016) .....	86
Figure 5-3: Schematic view of the sample showing the wellbore, top plug, bottom injection tubing and notch along the wellbore. (Sarmadivaleh & Rasouli, 2014) .....	87
Figure 5-4: Laboratory picture of True Triaxial Stress Cell. The top view shows the whole apparatus. The bottom picture shows a 10 cm sample in the centre. Four spacers are placed	

between the sample and the loading plates. The loading plates are connected to loading rams. After (Sarmadivaleh, 2012) .....	88
Figure 5-5: Schematic view of True Tri-axial Stress Cell. Top view of the apparatus is shown on the top. Side view of the apparatus is shown at the bottom. (Sarmadivaleh, 2012).....	89
Figure 5-6: Hydraulic fracturing pressure profile. In the laboratory two pressure gauges are installed near the borehole with a chock between them. The blue curve shows the pressure from the gauge closest to the borehole. The red curve shows the pressure before the chock. Before fracture initiation, both curves fall on each other. During this time, the pressurisation rate is constant. After initiation, the pressurisation rate drops and the two red and blue curves separate. Breakdown pressure is the maximum pressure that the borehole experiences. (Fatahi et al, 2016).....	91
Figure 5-7: Sandstone 2.7. a) Prismatic sample; b) sample with hole drilled through and vertical notch; c) injection tubing glued to the sample; d, e, f) sample after hydraulic fracturing test. Figures b and c show the direction of principal stresses. The hydraulic fracture was created and propagated in the direction of maximum horizontal stress. (Fatahi et al, 2016) .....	93
Figure 5-8: a- Sandstone 1.1; b- Sandstone 1.2; C- Sandstone 2.5; d- mortar sample. b and d show the hydraulic fracture aligned itself very well in the direction of $\sigma_H$ . For Sandstone 1.1, one wing of the hydraulic fracture deviated away from $\sigma_H$ direction. Sample 2.5 had no horizontal stresses. (Fatahi et al, 2016) .....	94
Figure 5-9: a- Experimental pressure vs time for hydraulic fracturing Sandstone 1.1; b- Simulated pressure vs time for hydraulic fracturing Sandstone 1.1; c- Experimental pressure vs time for hydraulic fracturing Sandstone 1.2; d- Simulated Pressure vs time for hydraulic fracturing Sandstone 1.2. For each sample, simulated and experimental breakdown pressure values are very close. In the experimental plots green curves show principal stresses. The blue curve shows borehole pressure. (Fatahi et al, 2016) .....	97
Figure 5-10: a- Experimental pressure vs time for hydraulic fracturing of mortar sample. After Sarmadivaleh (Sarmadivaleh, 2012); b- Simulated pressure vs time for hydraulic fracturing of mortar sample. Experimental and simulated initiation and breakdown pressures are very close. (Fatahi et al, 2016).....	98
Figure 5-11: Pressure-time curve of hydraulic fracturing. a- Experimental pressure profile of Sandstone 2.5; b- Simulated pressure profile of Sandstone 2.5 c- Experimental pressure profile of Sandstone 2.7; d- Simulated pressure profile of Sandstone 2.7. In experimental plots, red and blue curves show pressure reading from Inj1 and Inj2 pressure transducers respectively. Green curves show principal stresses. Cyan curve shows pressurisation rate calculated from Inj2 pressure transducer readings. (Fatahi et al, 2016) .....	98
Figure 6-1: Geometry of a hydraulic and natural fracture interaction. a: Sample dimension; b: Natural fracture distance from centre of the wellbore; R: wellbore diameter; l: natural fracture	

size; $\alpha$ : natural fracture angle; $\sigma_H$ : Maximum horizontal stress; and $\sigma_h$ : Minimum horizontal stress.....	103
Figure 6-2: a) Sample in yellow colour. The natural fracture is shown as black dashed lines. The induced hydraulic fracture is shown as red dashed lines. The wellbore is shown as a white circle in the middle of the sample. b) Pressure is shown as blue circles. The larger the size of the circles the higher the pressure. The hydraulic fracture has not reached the natural fracture yet. c) The lower wing of the hydraulic fracture arrived at the natural fracture. d) Both wings of the hydraulic fracture have crossed the natural fractures. The hydraulic fracture propagated in the direction of maximum horizontal stress.....	104
Figure 6-3: Two 10 cm samples with 90° (left) and 60° (middle and right) natural fractures with respect to the anticipated hydraulic fracture direction. (Sarmadivaleh & Rasouli, 2015) .....	106
Figure 6-4: a) schematic view of the aluminium plates epoxied together (Technology, 2016); b) Simulated sample for aluminium lap shear strength test.....	107
Figure 6-5: a) Schematic view of the sample and plot of Force versus Time. (Technology, 2016). b) Simulated sample under tension and its Force-Time relationship. At failure the tensile force will drop suddenly to zero value. The value of tensile force at failure is divided by the epoxied section's area to calculate the shear strength of the epoxy.....	108
Figure 6-6: Brown glue as natural fracture filling material. a) Top view of the sample. The hydraulic fracture arrived at the natural fracture at 90°. The hydraulic fracture is arrested at the natural fracture. b) Simulated sample. It shows that the hydraulic fracture is arrested at the natural fracture. c) Sample opened to show the created hydraulic fracture. Slab A shows mainly arresting of the hydraulic fracture with minor opening. Slab B shows complete arresting of the hydraulic fracture. The slab was broken while trying to detach it from the main section C. Section C shows a bi-wing hydraulic fracture with the fracture surface shown in dark grey colour, as the fracturing fluid caused wetting of the fracture surface. Modified from (Sarmadivaleh, 2012) .....	109
Figure 6-7: White glue as the natural fracture filling material. a) Experimental result for the natural fracture at 30° with respect to the hydraulic fracture. No interaction between hydraulic fracture and natural fracture occurred. b) Simulated fracturing test for the natural fracture at 30° with respect to the hydraulic fracture. No interaction between hydraulic fracture and natural fracture occurred. c) Experimental result for natural interface at 60° with respect to hydraulic fracture. Hydraulic fracture crossed natural fracture with small offset at right wing. d) Simulated fracturing test for the natural fracture at 60° with respect to hydraulic fracture. The hydraulic fracture crossed the natural fracture with a small offset at the left wing. ....	111
Figure 6-8: Cement as natural fracture filling material. a) Experimental result for the natural fracture at 0° with respect to the hydraulic fracture. No interaction between the hydraulic	

fracture and the natural fractures occurred. b) Simulated fracturing test for the natural fracture at  $0^\circ$  with respect to the hydraulic fracture. No interaction between the hydraulic fracture and the natural fractures occurred. c) Experimental result for the natural fracture at  $90^\circ$  with respect to the hydraulic fracture. The top wing arrested at the intersection point. The bottom wing crossed the natural fracture. d) Simulated result for the natural fracture at  $90^\circ$  with respect to the hydraulic fracture. Both wings crossed the natural fractures. .... 113

Figure 6-9: Cement as natural fracture filling material. a) Experimental result for natural fracture at  $60^\circ$  with respect to hydraulic fracture. Left wing of hydraulic fracture arrested at intersection point and right wing crossed natural fracture. b) Simulated fracturing test for the natural fracture at  $60^\circ$  with respect to the hydraulic fracture. Both wings crossed the natural fractures with small offsetting. Offset is larger at the left wing. c) Experimental result for natural fractures at anticipated  $30^\circ$  with respect to the hydraulic fracture. The hydraulic fracture didn't propagate in the desired direction. Both wings were arrested by natural fractures. d) Simulated result for anticipated natural fracture at  $30^\circ$  with respect to the hydraulic fracture. Both wings arrested at natural fractures. Shear slippage occurred at some intervals over natural fracture surfaces. e) Two natural fractures at  $30^\circ$  and a third one in the direction of experimental hydraulic fracture. f) Shear slippage at natural fracture surfaces. .... 115

Figure 7-1: Geometry of a hydraulic and natural fracture interaction. a: sample dimension b: Natural fracture distance from centre of the wellbore; R: wellbore diameter; l: natural fracture size;  $\alpha$ : natural fracture angle;  $\sigma_H$ : Maximum horizontal stress; and  $\sigma_h$ : Minimum horizontal stress. .... 120

Figure 7-2: Isotropic stress state hydraulic fracturing. (a)- Zero horizontal stresses. Wellbore notches are created at  $0^\circ$  and  $90^\circ$ . (b)- Zero horizontal stresses. Wellbore notches are created at  $+45^\circ$  and  $-45^\circ$ . (c)- 6.89 MPa horizontal stresses. Wellbore notches are created at  $0^\circ$  and  $90^\circ$ . (d)- 6.89 MPa horizontal stresses. Wellbore notches are created at  $+45^\circ$  and  $-45^\circ$ . (e)- 13.79 MPa horizontal stresses. Wellbore notches are created at  $0^\circ$  and  $90^\circ$ . (f)- 13.79 MPa horizontal stresses. Wellbore notches are created at  $+45^\circ$  and  $-45^\circ$ . Dashed lines in (b), (d) and (f) connect the edges of sample and show the  $45^\circ$  angle direction. .... 122

Figure 7-3: Breakdown pressure versus isotropic stress for two cases of  $90^\circ$  and  $45^\circ$  fracture propagation. The intercept shows hydraulic fracturing tensile strength. .... 123

Figure 7-4: Test result images. Sample is shown in yellow. Hydraulic fracture is in red. Blue circles show pressure with bigger circles showing higher pressures. Black dashed lines show natural fractures. Plot shows wellbore pressure versus time. Vertical axis shows pressure in (Pa) and horizontal axis shows time in (sec). For all plots, maximum value for pressure axis is 31 MPa and maximum value for time axis is 5000 seconds. .... 129

Figure 7-5: Force generated as a result of hydraulic fracture pressure. a) Natural fracture at a long distance away from wellbore. b) Natural fracture close to wellbore. The longer the natural fracture distance from wellbore, the higher the hydraulic fracture force. .... 132

Figure 7-6: (a) Sample with hydraulic fracture just arrived at natural fractures. (b) Parallel bond forces. Orange shows compressive and green shows tensile forces. Each force is shown by a small line segment. The thicker the line, the higher the force. Tensile forces at the intersection point between hydraulic and natural fractures as well as at the natural fracture tip further away from wellbore have highest magnitudes..... 132

Figure 7-7: Natural fracture tip under compression ..... 133

Figure 7-8: The greater the force (F) or the arm (d), the greater the Torque (T).  $T = rF\sin\phi = |F|d$ . (Serway & Jewett, 2013) ..... 134

Figure 7-9: Rotational moment generated as a result of forces. a) Low permeability natural fracture. b) High permeability natural fracture. In the case of low permeability, the fracture is pushed more towards the centre. .... 135

Figure 7-10: Hydraulic fracturing in the presence of natural fractures. (a) Two natural fractures on either side of wellbore. (b) One natural fracture set at 30°. (c) Two natural fracture sets at 30° and -50°. .... 139

Figure 7-11: a: Hydraulic fracturing with no natural fracture in sample. b: Hydraulic fracturing in the presence of one set of natural fractures which their normal is at 30° orientation with respect to the direction of  $\sigma_H$ . c: Hydraulic fracturing in the presence of two sets of natural fractures. .... 141

Figure 7-12: Brinell Hardness Number in different shale formations in United Stated. (Stegent et al, 2011) ..... 144

# List of Tables

Table 2-1: Hydrostone Hydraulic fracture test results for different angles of approach and stress state. After (Blanton, 1982).....	23
Table 2-2: Laboratory experimental results on Coconino sandstone. (Warpinski & Teufel, 1987) .....	27
Table 3-1: Mechanical Properties of two oil shales from Western USA. After (Eseme et al., 2007)....	38
Table 3-2: Micro mechanical properties of Particles and Parallel Bonds. After (Fatahi, 2014).....	39
Table 3-3: Macro-mechanical properties of real and simulated Lean and Rich Shales. After (Fatahi, 2014) .....	41
Table 4-1: Parameters of Simulation at Steady State Condition. (Fatahi & Hossain, 2016).....	71
Table 4-2: Simulation time (t) and Dimensionless Time ( $t_D$ ). (Fatahi & Hossain, 2016) .....	72
Table 4-3: : Parameters of Simulation (Fatahi & Hossain, 2016) .....	75
Table 4-4: Simulation time (t) and dimensionless time ( $t_D$ ). (Fatahi & Hossain, 2016) .....	77
Table 4-5: Values of first 50 $\lambda_n$ . (Fatahi & Hossain, 2016).....	78
Table 5-1: Micro-mechanical properties of the samples (Fatahi et al, 2016) .....	81
Table 5-2: Mechanical properties of real and simulated samples (Fatahi et al, 2016) .....	82
Table 5-3: Flow rate, fluid viscosity, rock matrix permeability and rock porosity (Fatahi et al, 2016)	82
Table 5-4: Sample and wellbore dimensions (Fatahi et al, 2016) .....	92
Table 5-5: Principal Stresses and notch direction (Fatahi et al, 2016) .....	92
Table 5-6: Experimental versus simulated initiation and breakdown pressures. (Fatahi et al, 2016) .	99
Table 6-1: Hydro-mechanical properties of synthetic sample and natural fracture filling materials. (Sarmadivaleh, 2012) .....	106
Table 6-2: Synthetic and simulated sample mechanical properties .....	107
Table 6-3: Summary of test parameters and test results.....	117
Table 7-1: Constant test variables; a: sample side length; R: wellbore diameter; $\sigma_H$ : maximum horizontal stress; $K_m$ : matrix permeability. ....	124
Table 7-2: Variable parameters and test results; b: distance from centre of wellbore to centre of fracture; l: natural fracture length; $\alpha$ : angle between natural fracture normal and maximum horizontal stress direction; $\sigma_h$ : minimum horizontal stress; $K_n$ : natural fracture permeability .....	136

# Nomenclature

<i>Symbol</i>	<i>Description</i>
$ba\_Ec$	<i>Particle young's modulus</i>
$ba\_fric$	<i>Particle friction</i>
$ba\_krat$	<i>Particle normal to shear stiffness ratio</i>
$ba\_rho$	<i>Particle density</i>
$c_t$	<i>Total Compressibility</i>
$pb\_coh\_mean$	<i>Parallel bond cohesion strength</i>
$pa\_Ec$	<i>Parallel bond young's modulus</i>
$pb\_krat$	<i>Parallel bond normal to shear stiffness ratio</i>
$pb\_mcf$	<i>Parallel bond moment contribution factor</i>
$pb\_phi$	<i>Parallel bond friction angle</i>
$pb\_sn\_mean$	<i>Parallel bond normal strength</i>
$pb\_sn\_sdev$	<i>Parallel bond normal strength standard deviation</i>
$k$	<i>Permeability</i>
$k_{ic}$	<i>Critical stress intensity factor</i>
$h_f$	<i>fracture height</i>
$l$	<i>fracture half-length</i>
$p_w$	<i>wellbore fluid pressure</i>
$phi$	<i>Porosity</i>
$q$	<i>Fluid flow rate</i>
$r_c$	<i>Fracture tip process zone radius</i>
$t_D$	<i>Dimensionless time</i>
$x_D$	<i>Dimensionless position</i>
$C_b$	<i>rock bulk compressibility</i>

$C_r$	<i>rock matrix compressibility</i>
$DEM$	<i>Distinct Element Method</i>
$E$	<i>Young's modulus</i>
$ISIP$	<i>Instantaneous Shut-In Pressure</i>
$J_0$	<i>first kind of Bessel function of order zero</i>
$\mathcal{L}$	<i>normalized crack length</i>
$P_0$	<i>Pore pressure</i>
$P_b$	<i>breakdown pressure</i>
$P_{bl}$	<i>Lower bound of breakdown pressure</i>
$P_{bu}$	<i>Upper bound of breakdown pressure</i>
$P_{c0}$	<i>hydraulic fracturing tensile strength</i>
$P_D$	<i>Dimensionless Pressure</i>
$P_i$	<i>Initial Pressure</i>
$P_{iso}$	<i>far-field isotropic stress component</i>
$P_{net}$	<i>Net pressure in fracture</i>
$PFC2D$	<i>Particle Flow Code In Two Dimensions</i>
$R$	<i>wellbore diameter</i>
$R_e$	<i>External Radius</i>
$R_w$	<i>Wellbore Radius</i>
$S$	<i>Total or confining normal stress</i>
$T$	<i>Tensile strength</i>
$UCS$	<i>Unconfined compressive strength</i>
$Y_0$	<i>second kind of Bessel function of order zero</i>
$\alpha$	<i>Biot's poro-elastic constant</i>
$\alpha^2$	<i>hydraulic diffusivity</i>
$\mu$	<i>Fluid Viscosity</i>
$\nu$	<i>Poisson's ratio</i>

$\sigma_{eff}$	<i>Effective stress</i>
$\sigma_h$	<i>Minimum horizontal stress</i>
$\sigma_H$	<i>Maximum horizontal stress</i>
$\Delta P_D$	<i>delta dimensionless pressure</i>
$\Delta t$	<i>Time step</i>
$\Gamma$	<i>effective fracture surface energy</i>

## **Publications related to this thesis**

Fatahi, H., Hossain, M. M., & Sarmadivaleh, M. (2017). Numerical and experimental investigation of the interaction of natural and propagated hydraulic fracture. *Journal of Natural Gas Science and Engineering* 37, 409-427.

Fatahi, H., Hossain, M. M., Fallahzadeh, S. H., & Mostofi, M. (2016). Numerical simulation for the determination of hydraulic fracture initiation and breakdown pressure using distinct element method. *Journal of Natural Gas Science and Engineering* 33, 1219-1232.

Fatahi, H., & Hossain, M. M. (2016). Fluid flow through porous media using distinct element based numerical method. *Journal of Petroleum Exploration and Production Technology* 6, 217-242. DOI 10.1007/s13202-015-0179-5

Fatahi, H. (2014). Simulation of shale mechanical properties in PFC2d and calibration of them against lab results for tensile, uni-axial and confined compression tests; *Society of Petroleum Engineers* SPE-173464-STU. SPE Annual Technical Conference and Exhibition, 27-29 October. Amsterdam, The Netherlands.

# 1

## Introduction

World population growth, migration towards cities, advancement in lifestyle standards, improvement in access to technology, and so on, are all demanding more and more energy. The U.S. Census Bureau has estimated that world population will reach 9 billion by 2042, as shown in Figure 1-1 (U.S. Census Bureau, 2015). This corresponds to a 1.5 billion increase in population compared to 2015. Even though there are a lot of activities around developing renewable energies such as solar, wind and so on, these energies alone cannot cope with the worldwide increasing demand for energy. The U.S. Energy Information Administration (EIA) has estimated that from now until 2040 there will be a significant increase in energy consumption for all sources of energy, as shown in Figure 1-2 (EIA, 2016). The increase in consumption is especially noticeable for renewables, liquid fuels and natural gas. These trends raise the question: are there enough reserves for liquid and natural gas sources of energy? The answer is yes, but not in the way we are used to. As shown in the resource triangle in Figure 1-3, conventional reservoirs are on top of the triangle, with very limited availability of other resources. Moving from the tip of the triangle to the base of it, you see an increase in the size of resources. Oil, shale and gas hydrate resources are the most abundant ones, sitting at the base of the triangle. Currently, conventional reservoirs are the main sources for oil and gas production. Based on the EIA report (Administration, 2016), the current global consumption of petroleum and other liquids is 96 million barrels per day. Around 40 million barrels are produced by OPEC countries from conventional reservoirs. These reservoirs are mainly carbonate and sandstone reservoirs with high permeability values. But most of these reservoirs are entering their second phase of life, where their pressures are significantly dropping and they need enhanced oil recovery methods. With the current massive production from these reservoirs, soon they will be depleted. Figure 1-3 shows that the only way to respond to worldwide energy demand and compensate for conventional reservoir production decline is to move downward from the tip of the triangle and develop other sources of energy. The United States is currently a pioneer in this regard, and they already are producing from multiple shale

plays such as Eagle Ford, Haynesville, Bakken, Utica and others. Exploiting these reservoirs is not easy and requires advanced technology and excellent management. These reservoirs have extremely low permeability values, in the range of nano to micro-Darcies, and will not flow easily. To overcome this issue, horizontal drilling with massive multistage hydraulic fracturing technology has been used. In the last decade, pumping pressure capacity, fluid chemistry, proppants and so on have brought great improvements. Advancements in micro-seismic have made it possible to track hydraulic fracture growth and live propagation during the fracturing operation. But there is still one issue with these reservoirs; they are very heterogeneous both laterally and vertically. Most of the reservoirs contain natural fractures. Natural fractures were created either because of tectonic activities or because of liquid expulsion from the reservoirs. As a result, their sizes can be quite different, ranging from micro fractures to joints and faults. In spite of great improvements in all aspects to develop these reservoirs, fracture design and simulation is still lagging behind. Most fracture simulators available have been developed for conventional reservoirs. These simulators oversimplify the situation and with few modifications, use the conventional procedures to simulate unconventional hydraulic fracture propagation. As mentioned earlier, most of the unconventional reservoirs are very heterogeneous, and a hydraulic fracture will branch out as it moves away from the wellbore. A branch-out can happen because of many parameters, the main one being interaction with natural fractures and stepping at bedding planes. Most commercial fracture simulators only take into account the effect of leak-off to these natural fractures and still simulate a simple bi-wing fracture. These conventional simulators assume that natural fractures open once a threshold pressure is reached, and ignore the dynamic change of stresses within the formation. This is far from reality and what is observed using micro-seismic events. As a result, there is still a great need for a more realistic fracture simulator to take into account the presence of natural fractures.

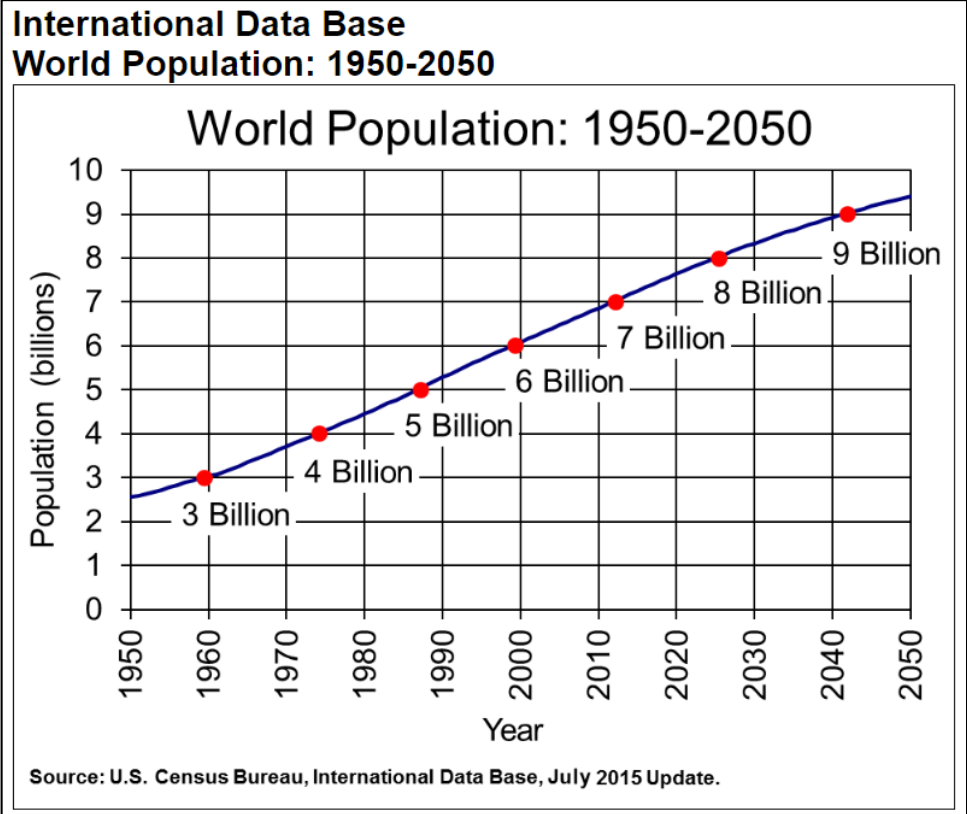


Figure 1-1: World population growth, (U.S. Census Bureau, 2015)

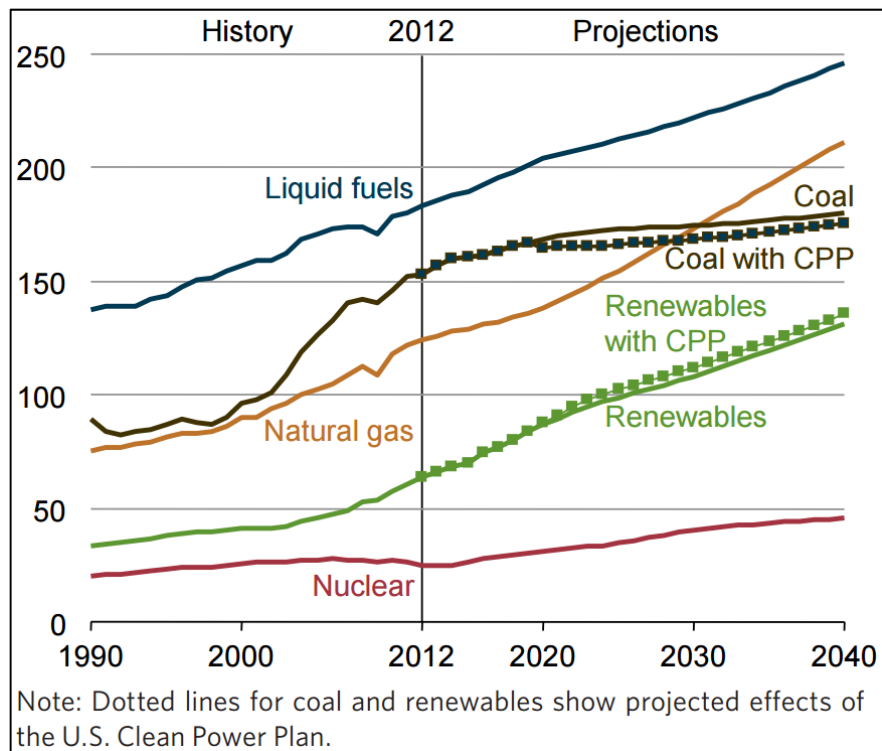


Figure 1-2: Total world energy consumption by energy source, 1990–2040 (Quadrillion Btu), (EIA, 2016)

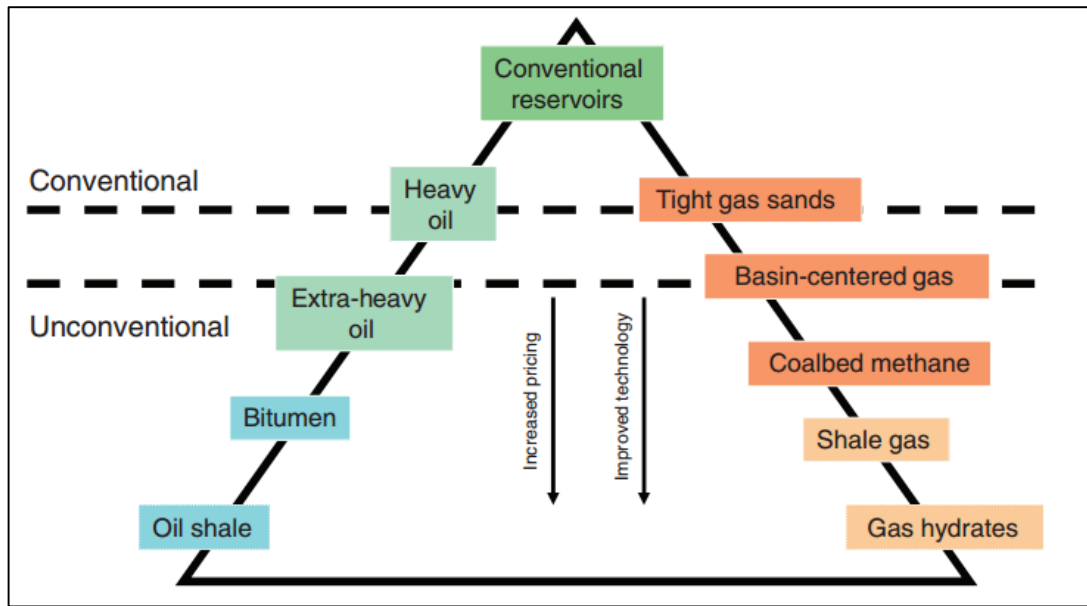


Figure 1-3: Resource Triangle, (Chan et al, 2012)

The greatest limitation to any simulation software such as fracture simulators was the computation power. To overcome this issue, those simulators used algorithms to simplify the situation and to increase computation speed. One of these simplifications was to use continuum-based algorithms such as finite element methods to simulate the discontinuous medium of rocks. Moor has predicted that computation speed doubles nearly every two years. Figure 1-4 shows computation cost per USD1000. It shows that for the same cost, computation has increased by  $10^{11}$  times (Seth, 2016) during 1950 to 2015. Although there have been great improvements in computation speed since those early commercial simulators were developed, they don't take full advantage of this improvement and are still relying on original algorithms and simplifications. Discontinuous simulators such as Distinct Element Methods (DEM) that are based on Discrete Element Methods require a high computation speed. This might be the reason that held back these simulators from being used for the design of hydraulic fracturing. But with current processors and improvements in computation speed, these simulators can now be easily run on personal computers. Using these Discrete-based methods, the physics of fracturing can be better captured and can more realistically simulate the fracturing mechanism, as will be shown in this study.



- Simulation of hydraulic fracture initiation and propagation, and investigation of influencing parameters and validation by comparison against laboratory analysis;
- Simulation of the interaction mechanism of hydraulic fractures and natural fractures, and comparison against laboratory analysis;
- Sensitivity analysis to investigate the effect of different parameters on the interaction mechanism and propagation behaviour of induced hydraulic fractures.

## **1.2. Significance of this research**

As discussed at the beginning of this chapter, it is becoming more and more important to develop unconventional reservoirs in response to the worldwide increase in demand for energy. Currently the best or probably the only way to exploit these reservoirs is to use horizontal drilling with multistage hydraulic fracturing. Millions of gallons of fracturing fluid with a few million pounds of proppant (sand, ceramics and so on) have to be pumped into each well drilled in these formations to increase the contact area between the wellbore and the formation. These unconventional reservoirs often contain natural fractures. The presence of natural fractures can influence the propagation path of hydraulic fractures once they intersect, and as a result, fluid and proppants movement inside the fracture is affected. Therefore, their influence needs to be properly investigated to design a successful hydraulic fracturing operation and maximise well production with the lowest possible cost. Currently hydraulic fracturing operation in these reservoirs is mostly simulated by continuum based simulators. Most of these simulators are based on analytical derivations that study the interaction mechanism in a pseudo-static manner. This study, however, can be distinguished from other similar studies in the following significant features:

- Simulation is based on the Distinct Element Method to appreciate the discontinuous nature of rocks.

- Hydraulic fracturing is simulated under dynamic conditions of fluid flow and stress changes, as the hydraulic fracture propagates and interacts with natural fractures.
- Simulation is based on simple particle–particle interaction and force-displacement between particles. This characteristic removes the dependency of the simulation on analytical derivation regarding fracture advancement and the interaction mechanism, and hence eliminates the errors inherited from analytical derivations.
- Simulation takes account of the fluid leak-off into the formation rock and natural fractures, and its effect on stress changes. Most analytical derivations and associated numerical simulations ignore fluid leaks to simplify derivations.
- The effect of different parameters such as in-situ stress states, natural fracture properties, rock mechanical properties, and injection fluid properties, can be easily simulated.

Better understanding of the interaction mechanism can help to better design the hydraulic fracturing operation to lower the cost of stimulation and increase the safety of performing these operations.

### **1.3. Outline of Thesis**

The thesis is divided into eight chapters. Chapter 1 presents a background on the necessity of hydraulic fracturing operations, the objectives of this study, the research significance and an outline of the thesis.

The first part of Chapter 2 surveys the literature on hydraulic fracture initiation and breakdown pressure. The second part reviews the literature on the interaction mechanism between hydraulic fractures and natural fractures.

Chapter 3 demonstrates how to simulate a rock sample using DEM with the desired mechanical properties of rock. Simulation results are compared against the properties of real samples to validate the accuracy of simulation.

Chapter 4 explains the fluid flow algorithm. Analytical equations are developed for two cases of linear and radial fluid flow in porous media. Simulation results are compared against analytical results to validate the accuracy of fluid flow.

Chapter 5 shows the procedure for simulating hydraulic fractures. Simulation is used to study the initiation and breakdown pressure as well as the fracture propagation path. The results are compared against the laboratory results to validate the accuracy of the model in this regard.

Chapter 6 demonstrates how the simulation is used to study the interaction mechanism between hydraulic fractures and natural fractures. Results of the simulation are compared against the experimental results for calibration purposes.

Chapters 3, 4, 5 and 6, together, elaborate how the model is developed and calibrated. The chapters progressively show the model's evolution and calibration. In a sequential process, the model that is calibrated in each chapter is used in the next chapter for further development and calibration.

The final model described in Chapter 6 is used for sensitivity analysis in Chapter 7, regarding the interaction mechanism between hydraulic fractures and natural fractures. In this chapter, the effect of different parameters such as the permeability of natural fractures, principal stress contrasts, natural fracture size, and the angle and distance from the wellbore, are described.

Chapter 8 presents the conclusions and recommendations for future work.

# 2

## **Mechanics of Hydraulic Fracture Initiation, Propagation and Interaction with Natural Fracture**

To perform hydraulic fracturing, firstly, a well is drilled down to the desired formation. It is then cased, cemented and perforated. Tubing is then run down to the formation and the zone of interest is isolated with plugs. Fracturing fluid is pumped down the tubing and through perforations into the formation. The fracturing fluid is then pressurized with multiple pumps on the surface, up to a few thousand psi, such as 10 or 15 kpsi. The pressurized fluid causes tensile stress in the formation rock and causes the rock to fracture.

Figure 2-1 demonstrates pressure and flow rate versus time since the beginning of the flow injection to create a hydraulic fracture. At the beginning of the flow injection, the pressure increases in a linear trend up to the initiation point. At the initiation point, hydraulic fracture is initiated. This introduces extra volume to the wellbore and causes the pressure increase to deviate from a linear trend. Pressure increases to a maximum value, which is referred to as breakdown pressure. After breakdown pressure, the wellbore pressure starts to decline and reaches a horizontal trend. Pressure at this stage is referred to as propagation pressure. If the injection rate is stopped, the wellbore pressure will suddenly decline and reaches a value referred to as instantaneous shut-in pressure (ISIP). The amount of this pressure decline is related to a frictional pressure drop inside the wellbore and, perforations and near wellbore region. After ISIP, the pressure continues to decline steeply. Once the fracture is closed, the rate of decline reduces. This is represented on the pressure curve as a deflection point and is referred to as closure pressure. Re-injecting fluid into the wellbore increases the pressure linearly until the fracture re-opens. After this stage, the pressure increase rate reduces until fracture propagation pressure is reached. Propagation pressure does not always have a flat trend. It can decrease in the case of penny shaped or vertical radial fractures. Or it can increase if the fracture

hits a boundary, such as formation boundaries or natural fractures. If fracturing fluid is loaded with proppant, proppant settlement and screen-out can also lead to an increase in fracture propagation pressure.

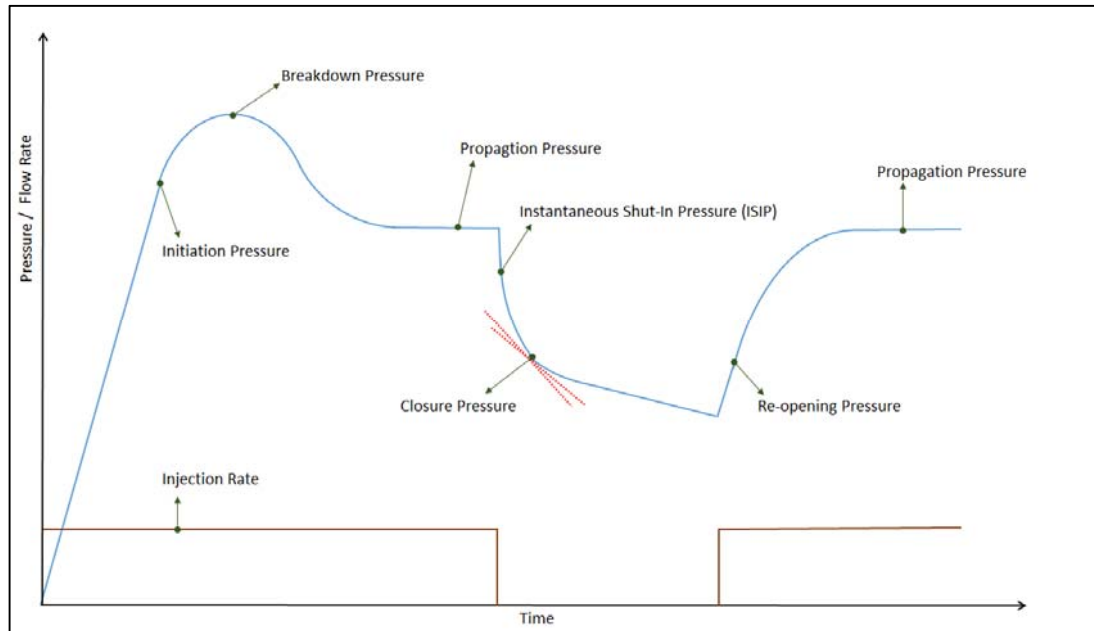


Figure 2-1: Pressure/flow rate versus time since the beginning of flow injection to create a hydraulic fracture, propagate, close and re-open it.

This chapter reviews the literature regarding initiation pressure, breakdown pressure and the interaction between hydraulic fractures and natural fractures. The first part is related to initiation and breakdown pressure. The second part reviews studies related to the mechanism of hydraulic and natural fracture interaction.

## 2.1. Initiation and Breakdown Pressure

Hydraulic fracturing is an inevitable process for economic development of most unconventional oil and gas fields. To design this process efficiently, it is essential to have a proper understanding of the characteristics of formation, such as its mechanical properties, prevailing in-situ stresses, well configuration (e.g. vertical, horizontal and/or deviated well), and some critical parameters such as breakdown pressure and propagation pressure. An accurate estimation of the breakdown pressure is extremely important for a proper determination of how much horsepower will be required on site. The number of pump trucks required is in direct relationship to the

amount of horsepower required. Overestimating this parameter will cause extra expenditure by companies. Underestimation of this parameter can cause operation failure, as the formation may not break down because of an inadequate number of pump trucks used to perform the onsite operation based on the underestimated breakdown pressure. This parameter can vary from formation to formation or even within a formation. For example, the breakdown pressure gradient is typically 1.2 to 1.3 psi/ft in the western part of Eagle Ford shale in USA, and hydraulic fracturing was not very successful in this area. Given that each well can cost USD10+ million, the importance of this parameter is evident. Hubbert and Willis (1957) derived an expression for breakdown pressure for the case of a vertical fracture initiated from a vertical well, in an impermeable infinite elastic medium known as the elastic criterion, as given by Equation (2-1):

$$P_b = 3\sigma_h - \sigma_H + T - P_0 \quad (2-1)$$

Where;

$P_b$ : breakdown pressure

$\sigma_h$ : Minimum horizontal stress

$\sigma_H$ : Maximum horizontal stress

$T$ : Tensile strength

$P_0$ : Pore pressure

Reservoir rock typically consists of a porous, permeable and elastic medium; upon injection of hydraulic fracturing fluid inside a wellbore, some of this fluid will leak-off into the reservoir rock, and will change its pore pressure. Haimson and Fairhurst (1967) derived an equation to take into account the permeation of fluid into the reservoir rock, or, to put it another way, to take into account the poro-elastic effect known as the poro-elastic criterion. Based on this criterion, they provided the expression of breakdown pressure, as given by Equation (2-2):

$$P_b = \frac{3\sigma_h - \sigma_H + T - 2\eta P_0}{2(1 - \eta)} \quad (2-2)$$

In the derivation of equations (2-1) and (2-2), Terzaghi effective stress ( $\sigma_{eff} = S - P_0$ ), is used, in which  $S$  is the total or confining normal stress and  $\eta$  is a property of the rock, and is defined as:

$$\eta = \frac{\alpha(1 - 2\nu)}{2(1 - \nu)} \quad (2-3)$$

Where  $\nu$  is Poisson's ratio and  $\alpha$  is Biot's poro-elastic constant and is defined as:

$$\alpha = 1 - \frac{C_r}{C_b} \quad (2-4)$$

Where  $C_r$  is rock matrix compressibility and  $C_b$  is rock bulk compressibility. However, Equation (2-2) does not convert back to Equation (2-1) when the rock permeability is zero. To overcome this inconsistency, Schmitt and Zoback (1989) have defined a general effective stress law ( $\sigma_{eff} = S - \beta P_0$ ), where  $\beta$  is a constant that they calculated from experiments to account for the effect of pore pressure. This constant is different for different rocks. Based on this new definition, they derived new forms of Equations (2-1) and (2-2) which are given in Equations (2-5) and (2-6) respectively.

$$P_b = 3\sigma_h - \sigma_H + T - \beta P_0 \quad (2-5)$$

$$P_b = \frac{3\sigma_h - \sigma_H + T - \frac{\eta P_0}{2}}{(1 + \beta - \frac{\eta}{2})} \quad (2-6)$$

If both  $\alpha$  and  $\beta$  approach zero, Equation (2-6) will convert back to equation (2-5) and solves the inconsistency that was mentioned earlier. Haimson and Huang (1989) re-worked the problem on this assumption and proposed that porosity and therefore  $\beta$  will not approach zero at the wellbore wall. They conducted eight hydraulic fracturing experiments on cylindrical samples, with five series under no pore pressure on different types of rocks, and three series conducted on porous Indiana limestone under initial pore pressure. To be able to compare the results of the experimental work with those of the analytical work, they separately measured the rock properties  $\nu$  (dimensionless),  $\phi$  (%),  $k$  (md),  $\alpha$  (dimensionless), and  $\eta$  (dimensionless) in the laboratory under controlled conditions; they also mentioned that they could not directly measure the properties that are dependent on the porosity under a changing stress field during hydraulic fracturing. Under no initial pore pressure and low porosity and low permeability rocks, the results matched perfectly with the poro-elastic criterion. The rest of the results fell between poro-elastic and elastic predicted results but were still closer to the poro-elastic criterion. They concluded that the elastic criterion can be used as an upper bound and the poro-elastic criterion as the lower bound for the prediction of results.

Abou Sayed, Brechtel and Clifton (1978) performed burst tests on cylindrical shale samples that were cored from Gray Shale section at a depth of 823-845 m. They proposed Equation (2-7) to determine the tensile strength of the rock. In this equation,  $w$  is the ratio of the outer diameter to the inner diameter of the cylindrical samples.  $P_i$  is the internal pressure at failure.

$$T = P_i \frac{w^2 + 1}{w^2 - 1} \quad (2-7)$$

The tensile strength for the samples ranged from 2.3 MPa to 22.3 Mpa, which is a wide range, and using these tensile strengths in either of Equations (2-1) or (2-2) can result in significant error in determination of  $\sigma_H$ . They noticed that the shale samples have natural fractures in them, and this is the reason why the tensile strength varies over a wide range. They concluded that this condition also exists in real field situations, and neither Equation (2-1) nor Equation (2-2) can be used to determine  $\sigma_H$ . They suggested determining  $\sigma_H$  based on breakdown pressure, as shown in Equation (2-8), using the concept of linear elastic fracture mechanics:

$$\begin{aligned} & \left( \frac{G(l/r)}{F(l/r)} \cos(2\theta) - \cos^2\theta \right) (\sigma_H - \sigma_h) \\ & = \sigma_h - P_b + \frac{K_{Ic}}{F(l/r) (l\pi)^{1/2}} \end{aligned} \quad (2-8)$$

Where  $l$  is the half-length of a bi-wing crack intersecting the borehole with radius  $r$ .  $G$  and  $F$  are functions of  $(l/R)$  and  $\theta$  is the angle between the direction of crack and maximum horizontal stress.  $K_{Ic}$  is the critical stress intensity factor. This equation is for the case when the minimum principle stress is one of the horizontal principle stresses for the known direction and length of the crack. They suggested inducing a crack of the known length. The minimum horizontal stress is derived from the shut-in pressure.

Daneshy (1978) has derived a relation for the propagation of fracture in three dimensions, as shown in Equation (2-9):

$$p - \sigma_h = \sqrt{\frac{3E\gamma}{2(1-\nu^2)} \cdot \frac{(L^2 + h_f^2)[E(k)]^2}{L[2(L^2 + h_f^2)E(k) - L^2K(k)]}} \quad (2-9)$$

Where  $E$  is Young's modulus,  $\gamma$  is effective fracture surface energy,  $L$  is fracture extent (length of a two dimensional fracture or radius of a penny shaped fracture),  $h_f$  is fracture height,  $E(k)$  is the complete elliptical integral of the second kind,  $K(k)$  is the complete elliptical integral of the first kind, and  $k$  is the parameter of the elliptic integral. This equation shows that as the length of the fracture increases, the pressure decreases. It was also shown experimentally in Figure 2-2, in which the volume of injected fluid is assumed to have a direct relation with the length of created hydraulic fracture.

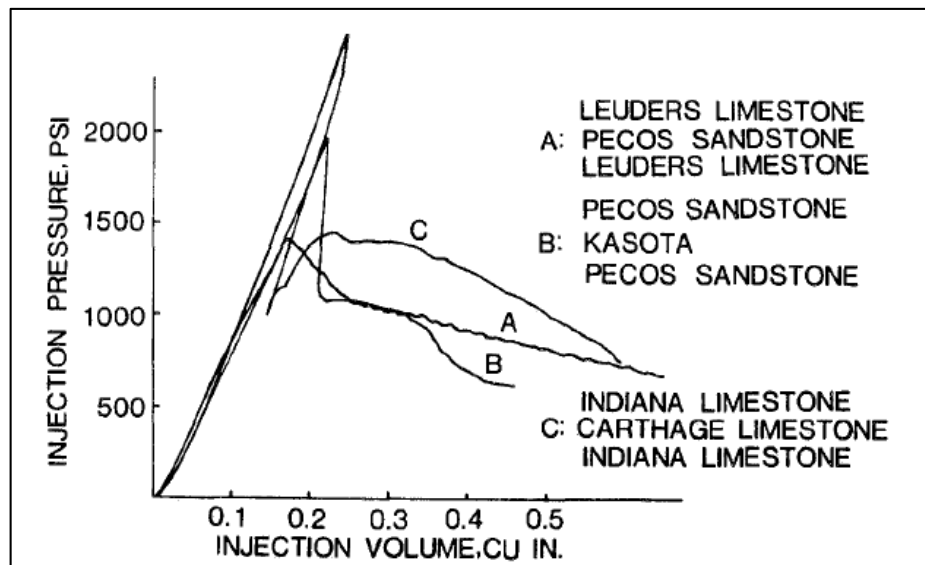


Figure 2-2: Fluid pressure variation during fracturing of layered samples. After (Daneshy, 1978)

Rummel (1987) used the concept of linear elastic fracture mechanics to derive an expression for breakdown pressure. He assumed that the wellbore axis is parallel to  $\sigma_v$ . The wellbore is assumed to be circular with a bi-wing crack in the direction of  $\sigma_H$  and with a half-length of  $l$ , as shown in Figure 2-3:

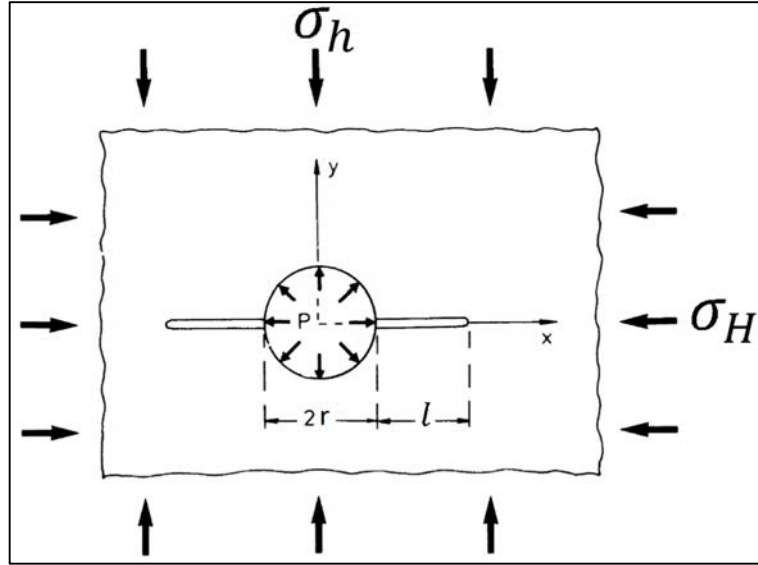


Figure 2-3: Circular borehole drilled in an intact infinite medium with a bi-wing crack of half-length  $l$  in the direction of  $\sigma_H$ . After (Rummel, 1987)

He further assumed that crack propagation depends on the mode  $I$  stress intensity factor, which is a superposition of individual stress components as shown in Equation (2-10), and that fluid leak-off from the surface of the crack is not considered:

$$K_I(\sigma_H, \sigma_h, p_w, p_a) = K_I(\sigma_H) + K_I(\sigma_h) + K_I(p_w) + K_I(p_a) \quad (2-10)$$

In Equation (2-10),  $p_w$  is the wellbore fluid pressure and  $p_a = p_a(x, 0)$  is the fluid pressure distribution inside the fracture. Derivation of individual components and addition of them in a single term results in Equation (2-11):

$$P_b = T + k_1 \sigma_h + k_2 \sigma_H \quad (2-11)$$

In Equation (2-11),  $T = K_{Ic}/f(R, a)$ , with  $K_{Ic}$  being the fracture toughness, and functions  $f$ ,  $k_1$  and  $k_2$  depend on the wellbore diameter  $R$  and the crack half-length  $l$ . A detailed explanation of the derivations and procedure can be found in Rummel (1987).

Medline and Masse (1979) derived the expressions for fracture initiation pressure in the case of penetrating and non-penetrating fluids in spherical and cylindrical wellbore geometries, as shown in Figure 2-4:

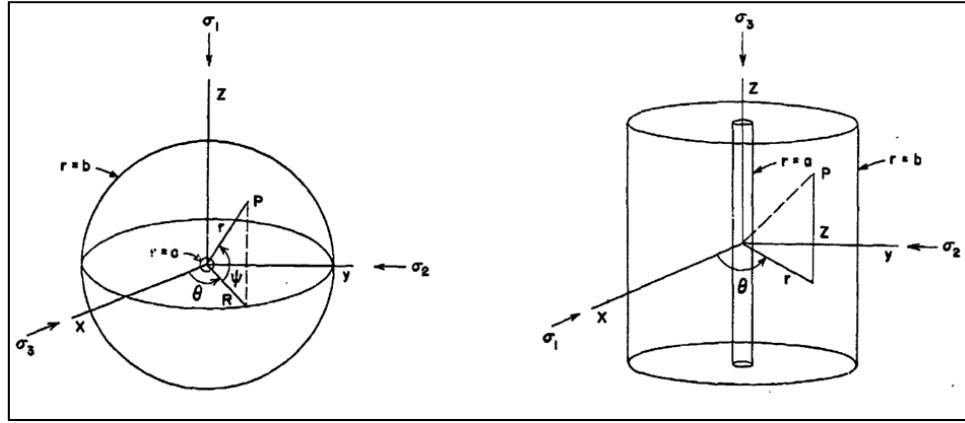


Figure 2-4: Spherical (left) and cylindrical (right) holes in the sample (Medlin & Masse, 1979)

Hollow spherical geometry with non-penetrating fracturing fluid:

$$P_{ini} = 2(T + \sigma_t) \quad (2-12)$$

Hollow spherical geometry with penetrating fracturing fluid:

$$P_{ini} = \frac{2(T + \sigma_t)}{3 - 2\alpha\left(\frac{1 - 2\nu}{1 - \nu}\right)} \quad (2-13)$$

Hollow cylindrical geometry with non-penetrating fracturing fluid:

$$P_{ini} = T + \sigma_t \quad (2-14)$$

Hollow cylindrical geometry with penetrating fracturing fluid:

$$P_{ini} = \frac{T + \sigma_t}{2 - \alpha\left(\frac{1 - 2\nu}{1 - \nu}\right)} \quad (2-15)$$

For the spherical geometry,  $\sigma_t$  is defined as:

$$\sigma_t = \frac{3}{2(7 - 5\nu)} [(9 - 5\nu)\sigma_1 - (1 + 5\nu)\sigma_2 + (-1 + 5\nu)\sigma_3] \quad (2-16)$$

And for cylindrical geometry,  $\sigma_t$  is defined as:

$$\sigma_t = -\sigma_1 + 3\sigma_2 \quad (2-17)$$

Equations (2-14) and (2-15) are same as (2-1) and (2-2) respectively, with zero pore pressure.

Medlin and Masse (1979) also performed extensive experimental studies on four different rock types to verify the theoretical derivations they made. They observed an excellent match between theory and experiment at low confinement pressure. At higher confinement pressure, theoretical values were higher than experimental values. They commented that lower experimental results are due to weakening of the rock at higher compressive stresses, as the rock starts to develop micro cracks, and as a result has lower tensile strength.

Boyce, Doe and Majer (1984) performed experimental investigation on salt rocks that were obtained from Avery Island salt dome in Louisiana, to test if salt formations follow the elastic derivation for breakdown pressure. The experiments they carried out on prismatic rocks subjected to three principle stresses demonstrated that the breakdown pressure was independent of the ratio of horizontal stresses, and nearly constant when minimum horizontal stress was kept constant and maximum horizontal stress was increased, as shown in Figure 2-5. Based on the elasticity equation it is expected that as the maximum horizontal stress increases, breakdown pressure decreases. Boyce et al.'s experimental investigation inferred that the salt formations do not follow elasticity equations, and consequently hydraulic fracturing cannot be used as the only means of predicting the values of stresses in these formations, as it is generally used for brittle rocks.

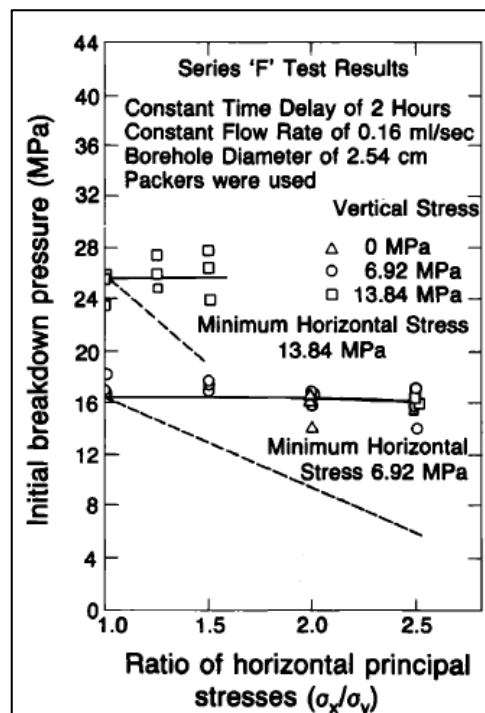


Figure 2-5: Breakdown pressure as a function of horizontal stress ratio for minimum horizontal stresses of 6.9 and 13.8 MPa. Dashed lines show expected decline in breakdown pressure for elastic rock. After (Boyce et al, 1984)

Haimson and Zhao (1991) have carried out experimental laboratory studies on Indiana limestone and Lac du Bonnet granite under zero confining stress and zero pore pressure, to investigate the effect of borehole size and pressurisation rate on the hydraulic fracturing tensile strength, which they termed  $P_{c0}$ . Figure 2-6 and Figure 2-7 show the effect of borehole size and pressurisation rate respectively on  $P_{c0}$ . Decreasing borehole size or increasing pressurisation rate will increase  $P_{c0}$ . Their findings suggest that the hydraulic fracturing tensile strength is not a constant value, and if elastic or poro-elastic equations are to be used for breakdown or maximum horizontal stress calculations, then a proper value of tensile strength should be used. This tensile strength can be different for different sizes of boreholes and pressurisation rates. This value can also be different from the tensile strength that is obtained from other methods, such as the direct tension or Brazilian test.

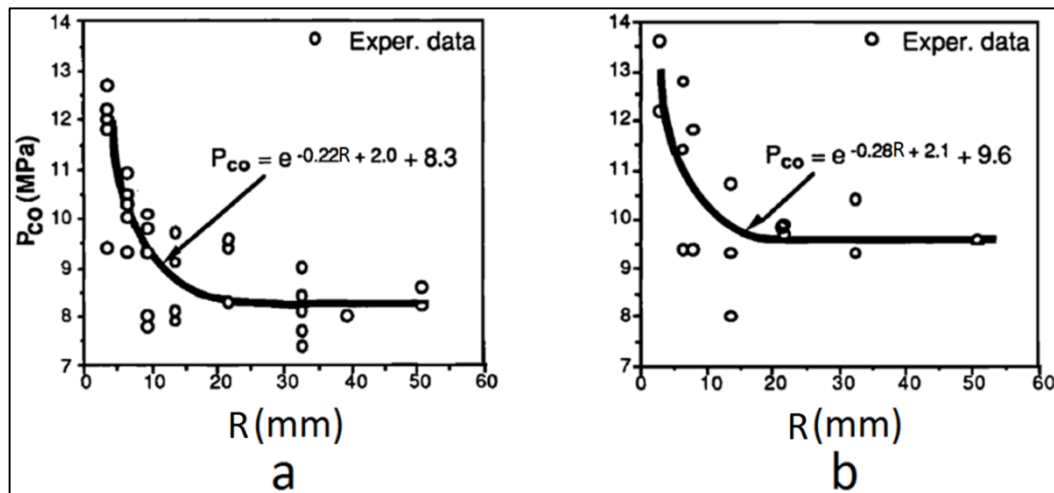


Figure 2-6: Effect of borehole size on  $P_{c0}$ . a) Lac du Bonnet Granite, b) Indiana limestone. After (Haimson & Zhao, 1991)

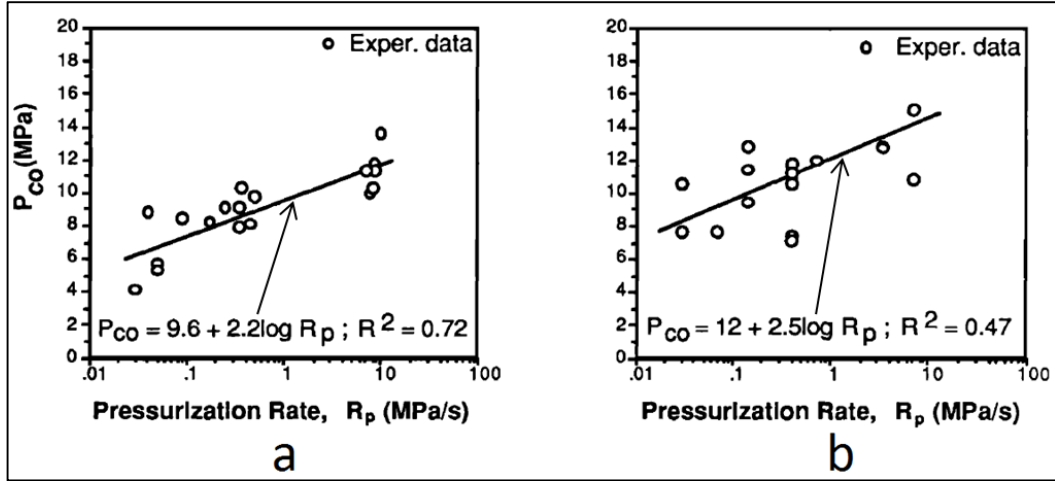


Figure 2-7: Effect of pressurisation rate on  $P_{c0}$ . a) Ldb granite, b) Indiana limestone. After (Haimson & Zhao, 1991)

The scale of some critical parameters such as low permeability, low flow rate and large borehole diameter are generally considered arbitrary, without a fine line. A standard needs to be in place to set a bench mark for these values. Detournay and Cheng (1992) derived a mathematical model regarding the effect of borehole size and flow rate on breakdown pressure, as shown in Equation (2-18):

$$p_b - p_0 = \frac{3\sigma_3 - \sigma_1 - 2p_0 + T}{1 + (1 - 2\eta)h(\zeta)} \quad (2-18)$$

$\zeta$  is a parameter which depends on pressurisation rate, size of the borehole, diffusivity of the fluid into the rock, and mechanical properties of the rock and fluid. They have defined pressurisation rate as slow, fast and transient regimes based on the value of  $\zeta$ . A slow regime is when  $\zeta \rightarrow 0$ , and the breakdown equation will simplify to Equation (2-19), which is the same as the poro-elastic criterion.

$$p_{bl} - p_0 = \frac{3\sigma_3 - \sigma_1 - 2p_0 + T}{2(1 - \eta)} \quad (2-19)$$

If  $\zeta \rightarrow \infty$ , it will be a fast pressurization regime, and breakdown equation will simplify to Equation (2-20) which is the same as the elastic criterion.

$$p_{bu} - p_0 = 3\sigma_3 - \sigma_1 - 2p_0 + T \quad (2-20)$$

This is the reason why in some experiments data are best fitted with the elastic criterion, and some are best fitted with the poro-elastic criterion. These two criteria

are the lower " $p_{bl}$ " and upper " $p_{bu}$ " bounds of the breakdown pressure. So both criteria are correct, with the transient regime falling in between these two criteria.

Zhao, Kim and Haimson (1996) have performed experimental analysis on Lac du Bonnet granite to test the effect of a horizontal stress contrast on fracture initiation and breakdown pressure. Their results showed that if horizontal stresses have different magnitudes, fracture initiation pressure is less than fracture breakdown pressure. In their tests they noticed that fracture propagation is in a controlled state before pressure reaches the breakdown pressure. "Controlled" here means that, if borehole pressurisation stops, fracture growth will stop immediately. But after breakdown pressure is reached, fracture propagation is uncontrolled, which means that, if borehole pressurisation stops, the fracture can still grow to some extent. Their tests also showed that under isotropic horizontal stresses, fracture initiation and breakdown pressure are the same, and fracture propagation is uncontrolled once it is initiated. They suggested that the maximum horizontal stress determined using fracture breakdown pressure can result in underestimation of this stress.

Garagash and Detournay (1996) analysed the effect of the pressurisation rate on breakdown pressure in impermeable rocks. They considered two scenarios of an edge crack with half-length of  $l \ll r$ , and a Griffith crack with half crack length of  $l \gg r$ , where  $r$  is the wellbore radius. Based on their derivations, breakdown pressure depends on pressurisation rate. They assumed three cases of slow, transient and fast pressurisation rate. In the case of slow pressurisation rate, breakdown pressure is the lowest and is considered as the lower bound, which is shown in Equation (2-21):

$$p_{bl} = p_{iso} + T/2^n \quad (2-21)$$

$p_{iso}$  is the far-field isotropic stress component.  $n$  is equal to 0 for a Griffith crack and 1 for an edge crack. In the case of a fast pressurisation rate, breakdown pressure is highest and is considered as the upper bound. The upper bound for edge crack and Griffith crack are given by Equations (2-22) and (2-23) respectively.

$$p_{bu} = 2p_{iso} + T \quad (2-22)$$

$$p_{bu} = \pi l T / 2r \quad (2-23)$$

As can be seen from Equation (2-23), the upper bound of the breakdown pressure for a Griffith crack approaches  $\infty$  as the crack length approaches  $\infty$ .

Detournay and Carbonell (1997) state that classical equations ((2-1) and (2-2)) cannot explain the dependency of breakdown pressure on the wellbore radius and pressurisation rate which was seen in experimental results. Based on the experimental results, increasing pressurisation rate or decreasing wellbore radius will increase fracture initiation pressure. They also mention that the breakdown pressure prediction based on the classical equations is not the breakdown pressure but is the initiation pressure. The breakdown pressure can be same as or different from initiation pressure, depending on the pressurisation rate and initial crack length. They have performed analytical analysis based on fracture mechanics to determine a relationship between fracture length and initiation pressure, as shown in Equation (2-24):

$$p_*(\mathcal{L}; s) = \alpha_k(\mathcal{L}; s)T_* + \alpha_p(\mathcal{L}; s)P_0 - \alpha_s(\mathcal{L}; s)S_0 - \alpha_p(\mathcal{L}; s)p_0 \quad (2-24)$$

Where  $\mathcal{L}$  is the normalised crack length, which is equal to  $l/r$ ;  $l$  is the fracture half-length;  $r$  is the wellbore radius; and  $s$  is the dimensionless pressure, which is equal to  $\frac{p_c - p_0}{p_w - p_0}$ . If  $s$  is zero, the pressurisation is fast; and if it is 1, the rate is slow. Figure 2-8 shows wellbore pressure versus normalised crack length for slow pressurisation rate (a), and fast pressurization rate (b). Curves 1 and 2 are for the cases of isotropic and non-isotropic far field stresses respectively, and curve 3 is for the case of reopening test. As it can be seen from Figure 2-8, for the case of a fast pressurisation rate, the wellbore pressure tends to increase after a certain length of crack is reached, and can go beyond the pressure that initiated the fracture. However, it should be noted in this case that pressure will not increase to infinity, because increasing the crack length will introduce more volume that receives fluid; and at a certain stage during fracturing, the regime will change from fast to transient, and eventually to a slow pressurisation regime, and will cause the pressure to decline.

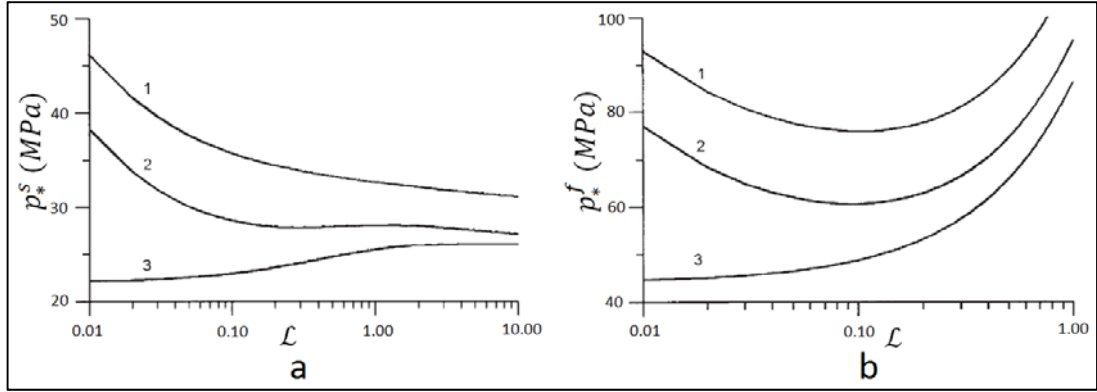


Figure 2-8: Wellbore pressure versus normalised fracture length for three cases of 1) isotropic far field stress, 2) non-isotropic far field stress, and 3) reopening test. (a) Slow pressurisation (b) Fast pressurisation. After (Detournay & Carbonell, 1997)

If the initial crack length is very small ( $\mathcal{L} \ll 1$ ), the condition of propagation becomes:

$$p_i(s) = \frac{1}{1+s} \frac{K_{IC}}{\sqrt{l_0} I^*} + \frac{2}{1+s} P_0 - \frac{4}{1+s} S_0 - \frac{1-s}{1+s} p_0 \quad (2-25)$$

Equation (2-25) is similar to the classical breakdown criterion. If ( $s=0$ ), the equation will convert back to the elastic criterion; and if ( $s=1$ ) it will convert to the poro-elastic criterion.

Lhomme and de Pater (2002) developed a method to study fracture initiation and propagation in an elastic homogenous permeable material. They assumed the fracture to be penny shaped. The finite difference method was then used to simulate their model in FLAC software. They have validated the results by comparing them against laboratory results. Their laboratory tests were conducted on Colton Sandstone in a tri-axial stress cell. In this model, the fracture path was axi-symmetric, and was known as a-priori. Simulated initiation and breakdown pressures were consistently lower than experimental results.

Pak and Chan (2004) developed an implicit finite element numerical simulation. In their simulation, the fracture is symmetric with respect to the wellbore. They developed this simulation based on their thermo-hydro-mechanical analytical model. Model results were compared against Golder Associates' (Golder Associates Ltd., 1994) laboratory test results. These laboratory tests were conducted on oil sands in a tri-axial stress cell. Although experimental and numerical breakdown pressures were close, the fracture propagation pattern was not the same.

Chudnovsky et al. (2008) developed a numerical method based on an assumed penny-shaped hydraulic fracture growth. The model simulates the fracture as axisymmetric. The model considered two cases of constant and variable fracture toughness with respect to the hydraulic fracture radius size. Model results were compared to Wu et al.'s (2008) laboratory test results. Laboratory tests were conducted on edible-grade gelatine in a tri-axial stress cell. This material is brittle, elastic and impermeable. In these tests, fracture initiation was observed to be same as fracture breakdown pressure. Comparison of the results showed that variable fracture toughness results are more realistic and closer to the experimental outcome.

Lakirouhani, Bungler and Detournay (2008) developed an analytical model for initiation of hydraulic fracture from a vertical borehole. The great strength of their model is using dimensionless parameters in their derivations to simplify calculations. They assumed the fracturing medium to be elastic and impermeable and that the crack has an initial half-length of  $l$ . They have shown that fracture initiation depends on dimensionless fluid compressibility,  $C = \frac{r}{(E'U)^{1/2}}$ , dimensionless fracture viscosity  $M = \mu' \left( \frac{E'^3 Q_0}{K'^4} \right)$ , and dimensionless deviatoric in-situ stress,  $D = \sigma_d \frac{(E'U)^{1/4}}{K'}$ . Equation (2-26) shows the relationship between dimensionless fracture length ( $\mathcal{L}$ ) and dimensionless time  $\tau$  for the case of an inviscid fluid. Functions,  $g_1$ ,  $g_2$ ,  $f_1$  and  $f_2$  can be solved numerically using a displacement discontinuity equation.

$$\tau = (2\pi\mathcal{L}^2 g_1(\mathcal{L}/C) + 1) \left( \frac{1}{2^{5/2}\mathcal{L}^{1/2}f_1(\mathcal{L}/C)} + D \frac{f_2(\mathcal{L}/C)}{f_1(\mathcal{L}/C)} \right) - 2\pi\mathcal{L}^2 D g_2(\mathcal{L}/C) \quad (2-26)$$

Figure 2-9 shows dimensionless wellbore pressure ( $\Pi$ ) and dimensionless fracture length ( $\mathcal{L}$ ) versus dimensionless time  $\tau$  for  $M=0.1$  and  $C=0.4$ . In this case the fracture breakdown pressure is greater than the fracture initiation pressure.

Figure 2-10 shows dimensionless breakdown and initiation pressure difference versus dimensionless viscosity for two different fluid compressibilities. This figure shows that as the compressibility increases, the pressure difference decreases.

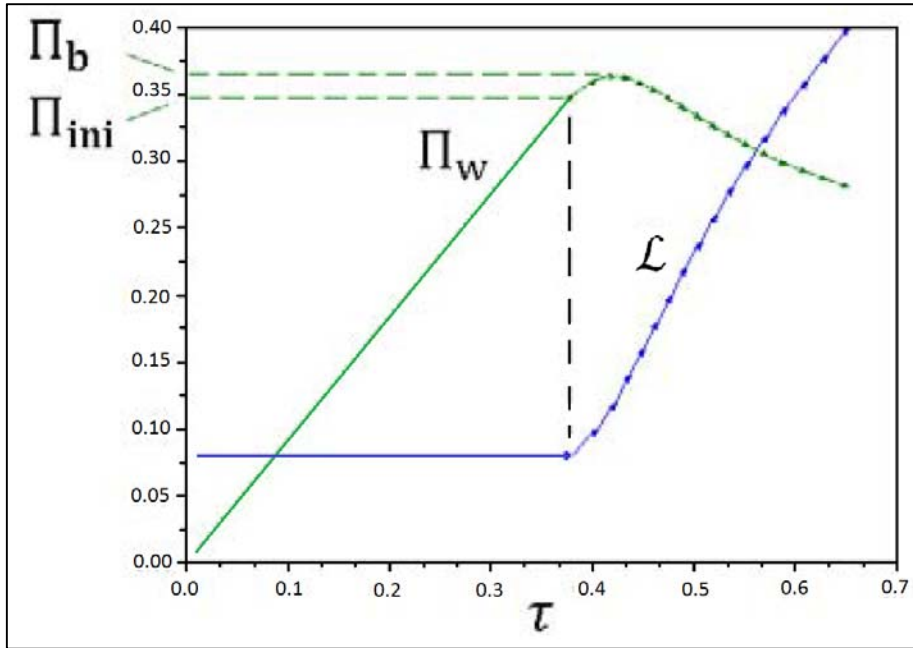


Figure 2-9: Dimensionless wellbore pressure ( $\Pi$ ) and dimensionless fracture length ( $\mathcal{L}$ ) versus dimensionless time  $\tau$  for  $M=0.1$  and  $C=0.4$ . After (Lakirouhani et al., 2008)

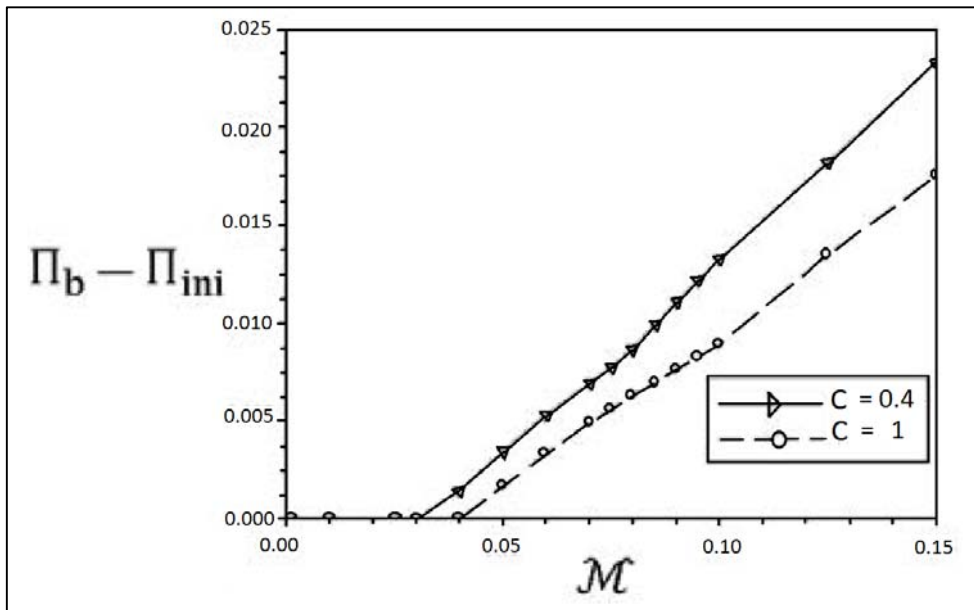


Figure 2-10: Dimensionless breakdown and initiation pressure difference versus dimensionless viscosity. After (Lakirouhani et al., 2008)

Zhang, Jeffrey, Bungler and Thiercelin (2010) developed a two dimensional numerical model to study the initiation and growth of hydraulic fracture from a vertical borehole in an impermeable rock. The wellbore was intersected by initial flaws. They considered two cases of toughness-dominated and viscous-dominated fracturing regimes to investigate the tortuosity of the created fracture in each case. In their model, the wellbore has an initial flaw that can be either bi-wing or single-wing,

with an angle of  $\Theta$  with respect to the direction of minimum horizontal stress, and the well is parallel to one of the principle stresses, as shown in Figure 2-11.

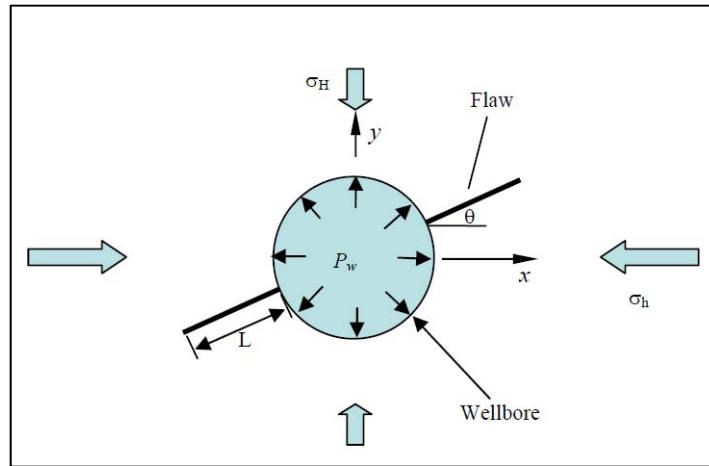


Figure 2-11: Wellbore with an initial flaw. After (Zhang et al., 2010)

Zhang et al.'s numerical scheme coupled fluid flow and rock deformation in an implicit manner. In the toughness-dominated case, the fluid pressure is assumed to be constant in the fracture and equal to wellbore pressure. In the viscous-dominated schemes, fluid flow is considered in the fracture with a pressure profile. The fluid is assumed to be incompressible. They have shown that in both cases the fracture will re-orient itself with the direction of maximum horizontal stress. For the viscous-dominated case, the higher the viscosity, the lower the degree of turning of the fracture, and as a result less fracture tortuosity. Fracture tortuosity is important, as it affects the fracture opening profile and proppant transport. To take into account the effect of injection rate, viscosity and other parameters, they used a dimensionless number, as shown in Equation (2-27):

$$\chi_F = \frac{(\sigma_H - \sigma_h)\sqrt{r}}{(\mu' Q_{in} E'^3)^{1/4}} \quad (2-27)$$

$E'$  is the plane strain modulus and  $\mu' = 12\mu$ . They showed that fractures will have same trajectory as long as they have same value of  $\chi_F$ , provided other parameters that are not included in  $\chi_F$  are kept constant, as shown in Figure 2-12.

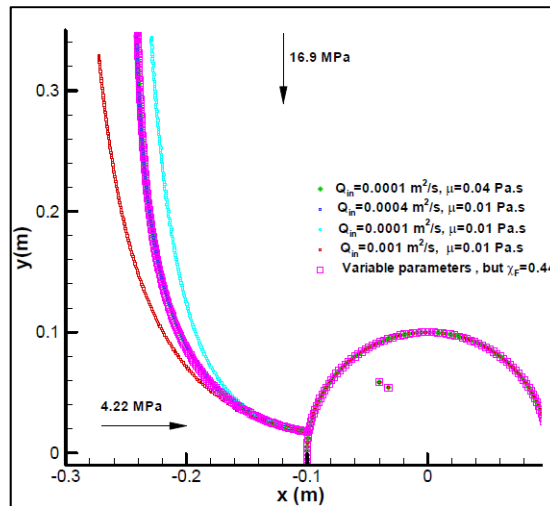


Figure 2-12: Fracture trajectory for different sets of injection rate and fluid viscosity. After (Zhang et al., 2010)

Lecampion (2012) performed analytical analysis to study fracture initiation, breakdown and propagation, and has shown that, depending on parameters that affect hydraulic fracture, initiation and breakdown pressure can be different. Continuing the earlier numerical studies (Gordeliy & Detournay, 2011; Lakirouhani et al, 2008; Lecampion & Detournay, 2007) and using his analytical derivations, Lecampion built a numerical model based on the Displacement Discontinuity Method. He discretised the continuity equation based on one dimensional finite volume method. In his model, the time step was calculated for an assumed constant fracture increment. He then compared his numerical results to Zhao's (1995) experimental result. Zhao conducted extensive experimental tests on Lac du Bonnet Granite. Hydraulic fracturing tests were performed in a tri-axial stress cell. Numerical-experimental comparison was done for two cases of variable borehole size and variable pressurisation rate. For both cases, the numerical model and the experiments showed the same trend. However, the numerical results were consistently higher than the experimental results.

To summarise, this section has presented a review of analytical, experimental and numerical investigations of initiation and breakdown pressure. The early studies began by presenting the classical equations for breakdown pressure, known as elastic and poro-elastic criteria. Soon after they were presented, experimental studies were carried out by other researchers to prove their accuracy. It was found that neither of the equations could be applied for all situations encountered by the experimental studies. Different researchers proposed different methodologies to overcome the

inconsistency between the theoretical and experimental results. Later, it was realised that neither of the equations are applicable in all situations, but that the elastic criterion shows the upper bound of the breakdown pressure, and the poro-elastic criterion shows the lower bound of the breakdown pressure. It was also realised that what was calculated based on these criteria as breakdown pressure was actually initiation pressure. Breakdown pressure can be different from initiation pressure. The magnitude of breakdown pressure is dependent on test parameters such as injection flow rate, fluid viscosity, fluid compressibility, wellbore radius, in-situ stresses and so on. The most comprehensive study was carried out by Lakirouhani et al. (2008). They incorporated test variables into dimensionless parameters to better understand initiation and breakdown pressure and what could cause a difference between the two pressures.

The models presented in this review show the great achievements of researchers in this area. The review explains how the analytical equations were first formulated and have evolved through time since 1950s. Most of the numerical methods that were developed were also based on these analytical equations. One of the limitations of these analytical equations is that they studied the physics of the problem in a static manner. However, injection of fluid into the wellbore causes a dynamic change in the system, such as changing pore pressure in the formation, wellbore radius and so on. As soon as a fracture initiates from the wellbore wall, the state of stress changes around the wellbore, and Kirsch equations cannot be applied to analyse the situation anymore. Numerical models that are based on these analytical equations can inherit the same limitations. To overcome these issues, a more robust numerical equation is needed to study the physics of the problem in a dynamic mode, to appreciate the dynamic changes that occur to the system while the fluid is injected and after the fracture is initiated. The numerical code presented in this study is based on DEM methods and does not rely on the aforementioned analytical methods. The method only relies on force displacement between particles. Since, during each time-step, the particle positions and forces on them are updated, the system simulates the situation in a dynamic mode. It also appreciates the changes that occur during injection, such as changing pore pressure, wellbore radius and so on.

## **2.2. Interaction Mechanism of Hydraulic and Natural Fracture**

Naturally fractured reservoirs can present many challenges during the initiation and propagation of hydraulic fracturing. The challenges include: the causes of higher fluid leak-off; branch-out of a propagated hydraulic fracture as it moves away from the wellbore and interacts with natural fractures; arresting of propagated hydraulic fracture once it intersects with the natural fractures; and fracture turning and twisting. Excessive leak-off or fracture turning upon arriving at natural fractures can be either beneficial or detrimental to the success of hydraulic fracturing treatment. Leak-off can cause premature dehydration of slurry and early screen out. Turning of the fracture can also be detrimental, as proppants cannot be easily transported, and settle down at the point of turning, causing early screen out. On the other hand, fluid leak-off to the natural fracture can open or shear the natural fracture, and as a result increase the aperture of natural fractures. This in turn can lead to an increase in the permeability of natural fractures. So designing a successful fracturing treatment in these reservoirs requires a proper understanding of the mechanism of the interaction between natural and hydraulic fractures. Many researchers have devoted some time to studying and understanding this behaviour analytically, numerically or experimentally. Daneshy (1974) has divided natural flaws into three groups based on their length with respect to the length of hydraulic fracture: small, medium and large, with two subdivisions of open and closed flaws. Both open and closed small flaws have no effect on the overall orientation of the hydraulic fractures. Open flaws on the other hand can reduce the effective surface energy that is required to extend the hydraulic fracture. Examples of small sized flaws are crystals, matrix boundaries and small sized natural fractures. Medium flaws can affect the orientation of the hydraulic fracture locally in their zone of influence, but have no effect on the overall orientation of the hydraulic fracture. In this case, the hydraulic fracture can either cross the natural flaws or it can encircle them. Large flaws cannot be encircled. If these flaws are open, the normal stress around them is zero. In this case, the hydraulic fracture will change its direction to be parallel to the direction of natural flaws, and after it passes the zone of influence, it can either continue or reorient to the original orientation. In the case of a large closed flaw, a hydraulic fracture can

cross it. Figure 2-13 demonstrates this situation. Daneshy (1974) also mentioned that the interaction behaviour depends on: the weakness plane strength; weakness plane angle with respect to the minimum principle stress; and deviatoric stress magnitude. Daneshy has verified his discussion experimentally in granite rocks with small, medium and large flaws.

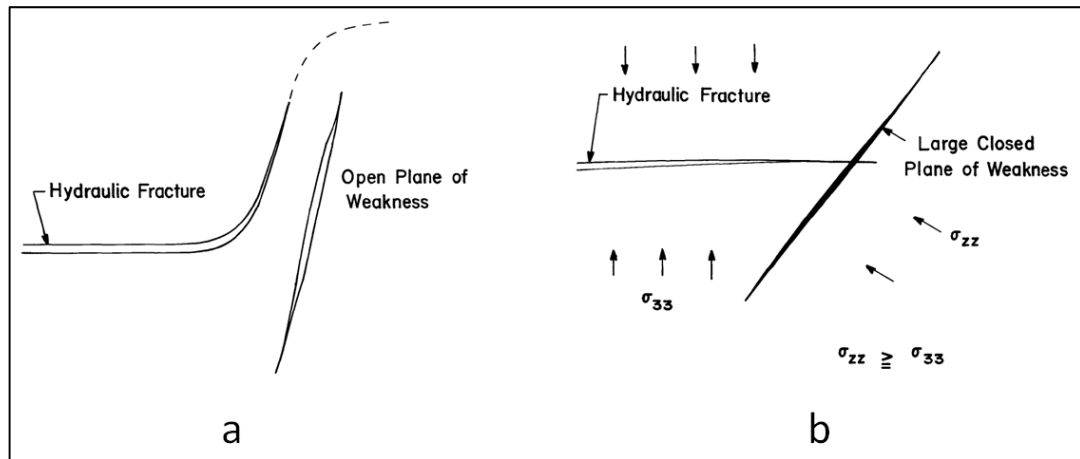


Figure 2-13: Extension of hydraulic fracture near a-large open flaw, b-large closed flaw. (Daneshy, 1974)

Hanson, Shaffer and Anderson (1981) performed experimental studies on Nugget Sandstone and Indiana limestone samples to investigate the effect of the natural interface friction coefficient, material Young's modulus, and the presence of natural flaws in addition to the main natural interface on the interaction mechanism for an un-bonded interface. Their set-up was designed in such a way that the hydraulic fracture arrived at the natural interface at a  $90^{\circ}$  angle. They found that for the hydraulic fracture to cross the natural interface, a threshold normal stress should act on the natural interface. Below this threshold interface, the hydraulic fracture can be arrested at the natural interface. Lubricating the natural interface can reduce the friction coefficient, and increase the threshold normal stress for crossing. They also found that lowering the Young's modulus on the other side of the interface opposite to the side that contains the hydraulic fracture will result in arresting the hydraulic fracture. The presence of natural interfaces in addition to the main natural interface had the same effect as lowering the Young's modulus on the opposite side. Figure 2-14 shows a three blocks assembly to study the effect of the natural interface's presence on hydraulic fracture interaction. The top block is composed of three rock blocks that show the case with two perpendicular natural interfaces. As shown on the

right hand side of Figure 2-14, the hydraulic fracture was arrested once it arrived at the top interface, but it crossed the lower interface. In this set-up, there was a vertical load on the blocks but the blocks were free on the sides.

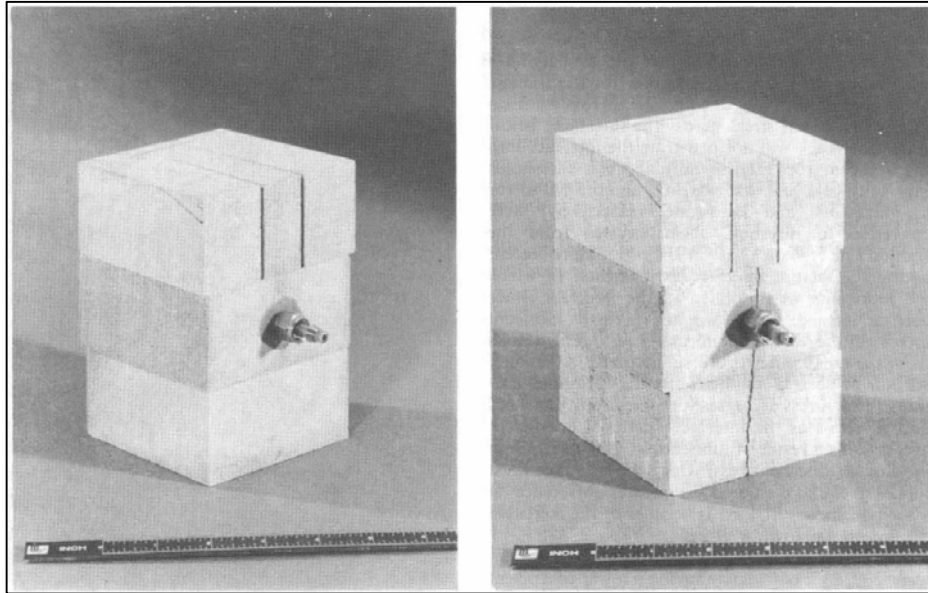


Figure 2-14: Effect of natural interfaces on hydraulic fracture propagation. (Hanson et al., 1981)

Blanton (1982) performed experimental studies for the interaction mechanism between a hydraulic fracture and natural fractures in Hydrostone prismatic rocks. Figure 2-15 shows the schematic view of the sample, natural fracture, hydraulic fracture, and the stress state around the sample on the left hand side. On the right hand side a sample that was tested is shown. First, the minimum and maximum horizontal stresses were 5 and 20 Mpa, and the hydraulic fracture arrived at the natural fracture and crossed it. Then the direction of stresses was changed and the hydraulic fracture arrived at the natural fracture at 30° and was arrested at the natural fracture. The results of Blanton's tests are shown in Table 2-1.

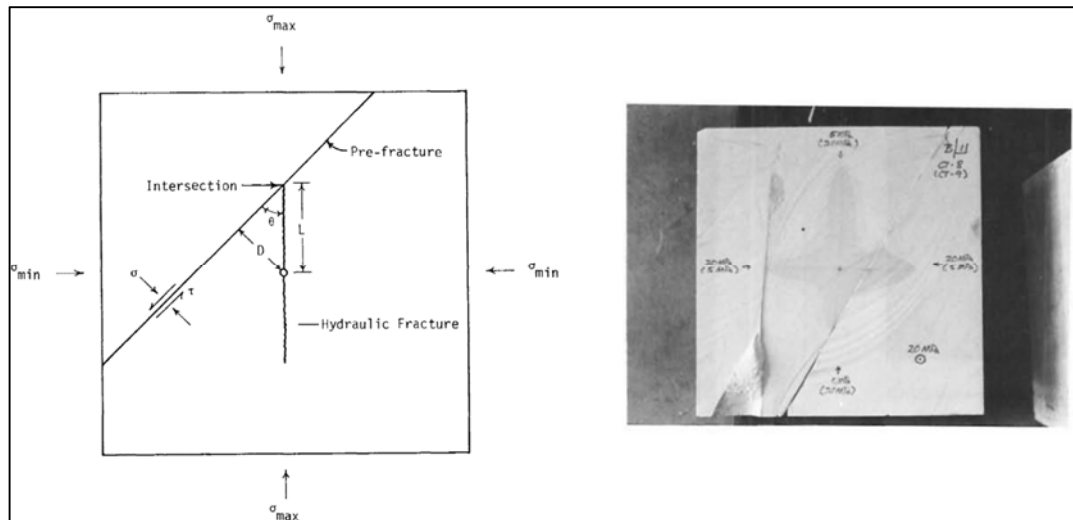


Figure 2-15: Schematic view of the tests on left and a sample tested on the right for 60° and 30° interaction angles. (Blanton, 1982)

Table 2-1: Hydrostone Hydraulic fracture test results for different angles of approach and stress state. After (Blanton, 1982)

Block #	Test #	Pre-Fracture Orientation	Horizontal Stresses		Horizontal Differential Stress, $\sigma_{\max} - \sigma_{\min}$ (psi)	Type of Interaction
			$\sigma_{\max}$	$\sigma_{\min}$		
1	CT - 4	60°	1740	1450	290	Opening
1	CT - 7	30°	2755	1450	1305	Opening
2	CT - 8	60°	2900	725	2175	Crossing
2	CT - 9	30°	2900	725	2175	Arrest
3	CT - 11	45°	2900	725	2175	Arrest
3	CT - 12	45°	2610	725	1885	Arrest
4	CT - 13	45°	2320	725	1595	Arrest
4	CT - 14	45°	2030	725	1305	Arrest
5	CT - 20	90°	2030	725	1305	Crossing
6	CT - 21	60°	2030	725	1305	Arrest
7	CT - 22	45°	1450	725	725	Opening

Blanton then proposed that for the hydraulic fracture to be able to open the natural fracture, the pressure at the intersection should be equal to normal stress acting on the natural fracture plane, as shown in Equation (2-28).

$$p = \sigma \quad (2-28)$$

For the left hand side of Equation (2-28), the penny shaped extension criterion based on Sack's criterion (1946) is used; and the right hand side is solved based on stress states and the angle of approach. After rearranging, the opening criterion is expressed as shown in Equation (2-29):

$$\sigma_{max} - \sigma_{min} = \left( \frac{\pi E \gamma}{4(1 - \nu^2)L} \right)^{1/2} / \sin^2 \theta \quad (2-29)$$

The test results as well as the opening criteria based on Equation (2-29) for three values of  $\gamma$  are shown in Figure 2-16.

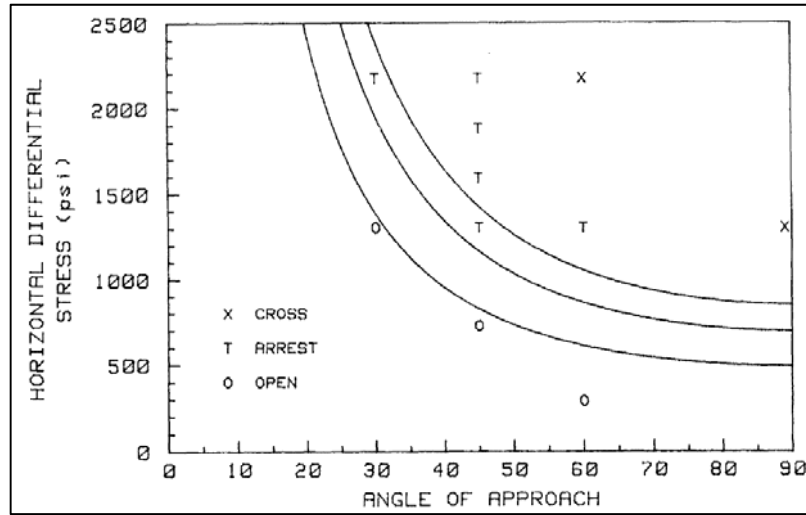


Figure 2-16: Opening criteria, from left to right  $\gamma = 0.2, 0.4$  and  $0.6$  psi.in, (Blanton, 1982)

If the pressure is not enough to open the natural fracture, it might be able to cause shear slippage on the natural fracture surface. In this case the normal stress on the fracture plane will be reduced by pressure in the fracture. The shearing criterion is shown in Equation (2-30):

$$\tau = \mu(\sigma - p) \quad (2-30)$$

By substituting appropriate equations for  $\tau$ ,  $\sigma$  and  $p$ , Equation (2-30) will convert to :

$$\sigma_{max} - \sigma_{min} = \left( \frac{\pi E \gamma}{4(1 - \nu^2)L} \right)^{1/2} / \left( \sin^2 \theta - \frac{\sin 2\theta}{2\mu} \right) \quad (2-31)$$

The sensitivity analysis for Equation (2-31) for different values of  $\gamma$  and  $\mu$  are shown in Figure 2-17.

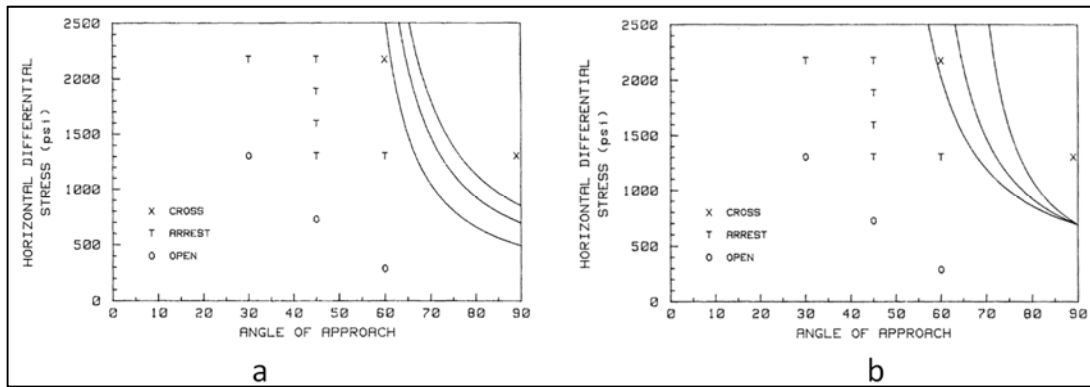


Figure 2-17: Arresting criteria for a-  $\mu = 0.75$  and  $\gamma = 0.2, 0.4$  and  $0.6$  psi.in, b-  $\gamma = 0.4$  psi.in and  $\mu = 1.0, 0.75$  and  $0.5$  from left to right, (Blanton, 1982)

Blanton has further improved his criterion in a later paper (Blanton, 1986). In this paper he assumes that a temporary arrest of hydraulic fracture occurs, when the hydraulic fracture intersects the natural fracture. The pressure then starts to increase to a point where either opening or crossing occurs. He assumes the natural interface to have three sections of open, slippage and normal zone, as shown in Figure 2-18. He has shown that if re-initiation is to happen, it should happen at point  $x_0$ , which will be in the slippage zone, and the criterion is:

$$\frac{\sigma_{max} - \sigma_{min}}{\cos 2\theta - b \sin 2\theta} < -T \quad (2-32)$$

Where,

$$b = \frac{1}{2c} \left[ v(x_0) - \frac{x_0 - 1}{\mu} \right]$$

$$v(x) = \frac{1}{\pi} \left[ (x + 1) \ln \left( \frac{x + 1 + c}{x + 1} \right)^2 + (x - 1) \ln \left( \frac{x - 1 - c}{x - 1} \right)^2 + c \ln \left( \frac{x + 1 + c}{x - 1 - c} \right)^2 \right]$$

If the value of  $c$  approaches zero, it means no slippage zone is present. This causes  $b$  to tend toward infinity, and based on Equation (2-32), crossing will occur. If  $c$  tends to infinity the term for  $b$  will simplify to:

$$b = \frac{1}{2\pi} \ln \left[ \frac{1 + (1 + e^{\pi/2\mu})^{1/2}}{1 - (1 + e^{\pi/2\mu})^{1/2}} \right]^2$$

The above equation shows that the value of  $b$  will depend on the natural interface friction coefficient for the case when  $c$  is very large.

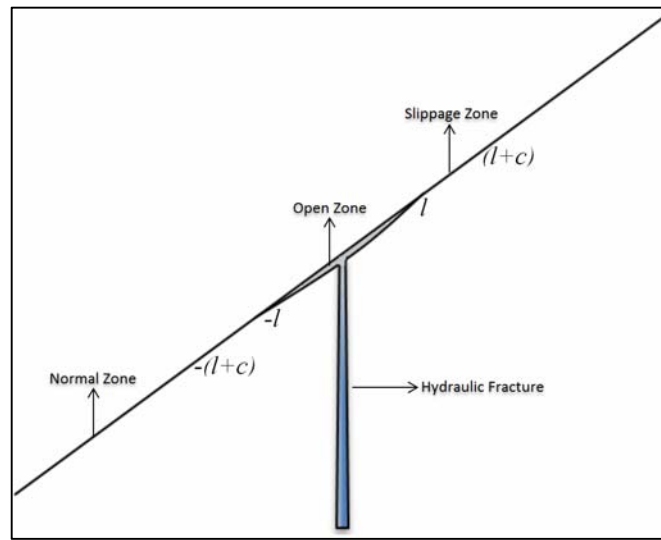


Figure 2-18: Hydraulic fracture intersecting natural fracture.

Blanton (1986) has plotted the crossing criterion for three values of  $b$  to compare his experimental results with analytical criterion, as shown in Figure 2-19. Hydraulic fracture interaction experiments were made on hydrostone blocks. On the left hand side of the curves, opening will occur, and on the right hand side, crossing will take place. The best curve is the one for  $b = 0.2$ , which is the asymptotic value of  $b$  for the hydrostone that he used.

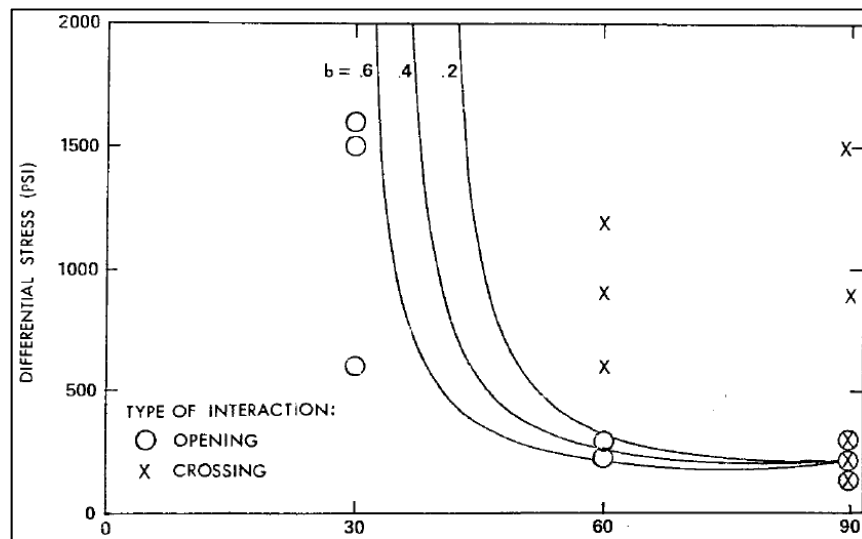


Figure 2-19: Interaction criteria versus experimental results comparison, (Blanton, 1986)

Warpinski and Teufel (1987) have performed experimental tests for the investigation of the interaction mode of hydraulic and natural interfaces in the field and in the laboratory. In their tests, they have shown the effect of differential stress and angle of approach on the interaction mode. From their results, it is clear that at lower values of differential stress, dilation occurs, and at higher values, crossing or shear slippage takes place. They also derived analytical expressions to explain the interaction mode. Equation (2-33) is the opening criterion.  $p_{net}$  is the net pressure in the fracture, which is equal to actual pressure in the fracture minus minimum horizontal stress. If the condition in Equation (2-33) is met, the fracture will dilate. Equation (2-34) is the criterion for the slippage. For the slippage to occur, the condition of Equation (2-33) should not meet, and the condition of Equation (2-34) should meet. Results of experimental studies are presented in Table 2-2.

$$p_{net} \geq \frac{\sigma_{max} - \sigma_{min}}{2 * (1 - \cos 2\theta)} \quad (2-33)$$

$$\sigma_{max} - \sigma_{min} \leq \frac{2\tau_0 - 2\mu_f p_{net}}{\sin 2\theta + \mu_f \cos 2\theta - \mu_f} \quad (2-34)$$

Table 2-2: Laboratory experimental results on Coconino sandstone. (Warpinski & Teufel, 1987)

Test	Joint Orientation (degrees)	$\sigma_{Hmax}$ (psi)	$\sigma_{Hmin}$ (psi)	$\Delta\sigma_H$ (psi)	Result
3	30	1000	500	500	Dilated Joint
4	30	1500	500	1000	Dilated Joint
7	30	2000	500	1500	Shear Slippage
5	60	1000	500	500	Dilated Joint
9	60	1500	500	1000	Dilated Joint
6	60	2000	500	1500	Crossed Joint
11	90	1000	500	500	Dilated Joint
8	90	1500	500	1000	Crossed Joint
12	90	2000	500	1500	Crossed Joint

Renshaw and Pollard (1995) have studied the case of a hydraulic fracture approaching a natural fracture at right angles. They believed that if the interface is bonded, the fracture will propagate right through it and the interface has no effect on the propagating path of the hydraulic fracture. They developed a criterion called compressional crossing for a cohesion less interface with a friction coefficient of  $\mu_f$ . The logic behind this criterion is that the compressional stress on the interface is of great enough strength to prevent the slippage on the interface, as shown mathematically in Equation (2-35), and will allow the tensile stress to be transferred to the opposite side of the interface. The reason that  $\sigma_{max}$  is used on the right hand side of Equation (2-35) is that the hydraulic fracture propagates in the direction of  $\sigma_{max}$ .

$$|\tau_{interface}| < -\mu_f \sigma_{max} \quad (2-35)$$

Based on this criterion, if slippage occurs, crossing will not happen. This criterion also suggests that re-initiation of the fracture on the other side of the interface will not definitely happen in the exact path of the hydraulic fracture; rather, it can have some offset and this re-initiation can happen before the hydraulic fracture arrives at the natural interface. Taking into account the stress distribution around the fracture tip and using Equation (2-35), the compressional crossing criterion developed by Renshaw and Pollard (1995) is:

$$\frac{-\sigma_{max}}{T - \sigma_{min}} > \frac{1 + \mu_f}{3\mu_f} \quad (2-36)$$

If the criterion in Equation (2-36) is satisfied, crossing will occur; otherwise, slippage will take place and hydraulic fracture cannot cross the natural interface. In this equation, tensile strength has a positive sign and compressive horizontal stresses have a negative sign. One of the main assumptions in the derivation of this criterion is the presence of a critical zone around the fracture tip with radius  $r_c$  where inelastic deformation takes place, known as the fracture process zone. Without this assumption, there will be stress singularity at the fracture tip. Based on the literature, Renshaw and Pollard assumed that stresses within this zone are less than or equal to stresses at the critical radius. They performed experimental studies on anchoring

cement and Rock hard and got a very good match between the experimental and analytical results. The problem with their criterion is that the hydraulic fracture should always approach the natural interface at right angles, and the natural interface is orthogonal to the maximum stress direction. In reality, hydraulic fracture can arrive at the natural interface at different angles, and natural interfaces are not necessarily orthogonal to the maximum stress direction.

Zhou, Chen, Jin and Zhang (2008) have performed experimental studies on synthetic cement samples to study the effect of deviatoric stress, angle of approach and natural interface aperture on the interaction behaviour of the hydraulic and natural interface. They used three papers with different thicknesses to resemble three types of interfaces. Their results show that at a higher angle of approach and deviatoric stress, a hydraulic fracture has a higher tendency to cross the natural interface, while at low angles of approach and deviatoric stress, it will dilate the natural interface. They also showed that under similar conditions of stress state and angle of approach, a hydraulic fracture has a higher tendency to cross the natural interface with a lower aperture and dilate the natural interfaces with a larger aperture.

Gu and Weng (2010) and Gu et al. (2011; 2012) have extended Renshaw and Pollard's criterion for the cases where the natural interface has cohesion and for non-orthogonal angles of approach. They assumed that the fracture re-initiates on the natural interface surface when the value of the maximum principal stress is equal to the tensile strength of the rock, as shown in Equation (2-37):

$$\sigma_1 = T \quad (2-37)$$

Inserting the appropriate values for  $\sigma_1$  and T will result in Equation (2-38):

$$\begin{aligned} \cos^2 \frac{\delta}{2} K^2 + 2 \left[ \left( \frac{\sigma_{max} - \sigma_{min}}{2} \right) \sin \frac{\delta}{2} \sin \frac{3\delta}{2} - T \right. \\ \left. + \frac{\sigma_{max} + \sigma_{min}}{2} \right] K \\ \left. + \left[ \left( T - \frac{\sigma_{max} + \sigma_{min}}{2} \right)^2 - \left( \frac{\sigma_{max} - \sigma_{min}}{2} \right)^2 \right] = 0 \end{aligned} \quad (2-38)$$

In Equation (2-38),  $\delta = \Theta$  or  $\delta = \Theta - \pi$ ,  $K = \frac{K_I}{\sqrt{2\pi r_c}} \cos \delta$ , and solving this equation will give two values for  $K$ , one of which results in maximum principle stress and is the valid answer.

Gu and Weng (2010) and Gu et al. (2011; 2012) also assumed that for re-initiation to occur, there should be no slip on the natural interface surface, as shown in Equation (2-39):

$$|\tau_{interface}| < S_0 - \mu_f \sigma_{n,interface} \quad (2-39)$$

The main difference between Equations (2-35) and (2-39) is the inclusion of natural interface cohesion  $S_0$  in Equation (2-39). Normal and shear stresses on the interface are shown in Equations (2-40) and (2-41). Again,  $\delta = \Theta$  or  $\delta = \Theta - \pi$ , and insertion of these equations in Equation (2-39) will give the no slip criterion.

$$\begin{aligned} \tau_{interface} = & K \sin \frac{\delta}{2} \sin \frac{3\delta}{2} \sin 2\theta + K \sin \frac{\delta}{2} \cos \frac{3\delta}{2} \cos 2\theta \\ & - \frac{\sigma_{max} - \sigma_{min}}{2} \sin 2\theta \end{aligned} \quad (2-40)$$

$$\begin{aligned} \sigma_{n,interface} = & K + K \sin \frac{\delta}{2} \sin \frac{3\delta}{2} \cos 2\theta - K \sin \frac{\delta}{2} \cos \frac{3\delta}{2} \sin 2\theta \\ & + \frac{\sigma_{max} + \sigma_{min}}{2} - \frac{\sigma_{max} - \sigma_{min}}{2} \cos 2\theta \end{aligned} \quad (2-41)$$

They mentioned that the Renshaw and Pollard criterion can also be extended in the form of an equation to include the effect of cohesion of natural interface.

$$\frac{\frac{S_0}{\mu_f} - \sigma_{max}}{T - \sigma_{min}} > \frac{1 + \mu_f}{3\mu_f} \quad (2-42)$$

Gu et al. (2011; 2012) have verified their criterion by conducting experimental studies on Colton Sandstone. Their results agreed very well with their criterion, as shown in Figure 2-20. They also compared their criterion with the experimental results of Blanton (1982) and Zhou et al (2008) and showed that their criterion agrees very well with these results.

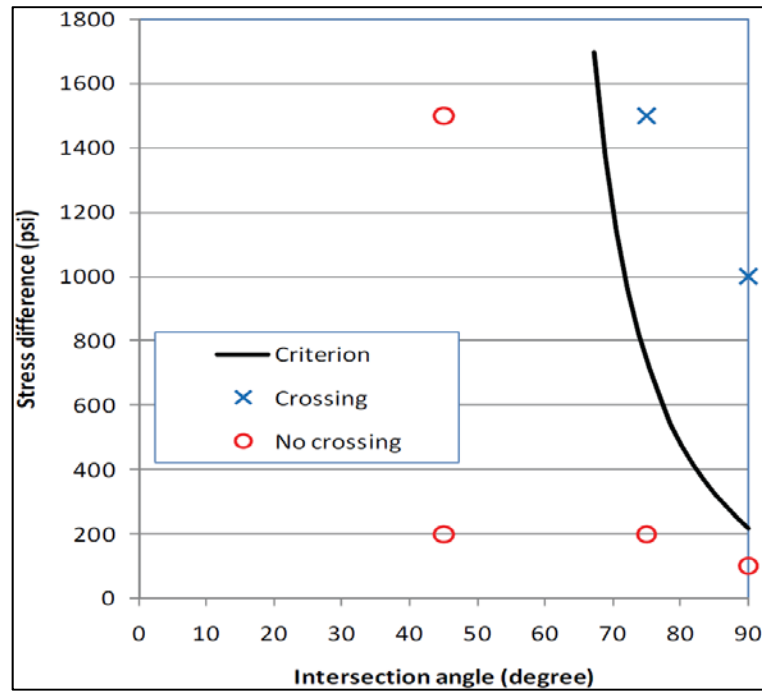


Figure 2-20: Comparison of analytical and experimental results for hydraulic fracture interacting with natural interface in Colton sandstone. (Gu et al, 2011)

This section has summarised the studies that have been conducted regarding hydraulic and natural fracture interaction by a few researchers. It is shown that since the 1970s, a great improvement has been achieved in the understanding of the interaction between hydraulic and natural fractures. Extensive experimental studies conducted have helped to improve the analytical conclusions. However, as in the previous section, the analytical investigations were performed for a static scenario. Hydraulic fracturing, its propagation and interaction with natural interfaces is a dynamic process. As the hydraulic fracture propagates, the stress regime at different locations within the sample, especially at the natural interface plane, undergoes continuous changes. Fracture re-initiation on the opposite side of the natural interface with respect to the side of hydraulic fracture can occur before the hydraulic fracture intersects with the natural interface. Numerical simulations that are based on the aforementioned analytical derivations inherit the same limitations. The DEM simulation presented in this study takes into account the dynamic process of hydraulic fracturing. The model results were validated with extensive experimental studies. The simulation is not based on analytical equations that describe the interaction mechanism. Rather, it is based on force-displacement between sample particles. Continuous updating of particle positions and forces between particles and

boundary plates during each time step makes the model dynamic and allows for the continuous change of stresses within the sample.

To create the simulation model, first a rock sample needs to be simulated that has the same mechanical properties as real rock samples. The next chapter explains and presents how rock samples with desired mechanical properties are simulated.

# 3

## Simulation of Rock's Mechanical Properties

This chapter explains how the mechanical properties of a rock sample are simulated and adjusted in the DEM numerical tool (PFC2D) to match with the mechanical properties of a real sample. Most parts of this chapter are based on the author's own paper, "Simulation of Shale Mechanical Properties in PFC2D and Calibration of them Against Lab Results for Tensile, Uni-axial and Confined Compression Tests", published in the *SPE Annual Technical Conference and Exhibition*, 27-29 October 2014, Amsterdam, The Netherlands. A brief summary of the Discrete Element Method, Distinct Element Method and commercial software PFC2D are provided in the first part of the chapter. In the next part, matching rock mechanical properties are explained.

### 3.1. Introduction to Discrete Element Method, Distinct Element Method (DEM) and PFC2D

Reservoir rock consists of grains, pores which are filled with pore fluids, and possibly joints and faults, or in a general sense, discontinuities, which may or may not be filled with cement. If the size of discontinuities is not in the scale of the reservoir rock, a continuum based model may be accurate enough for simulation by incorporating some modification into the model to include the effect of these features. However, if the size of discontinuities is comparable with the size of the rock, continuum based models may lose accuracy. In this case, discontinuous models provide better results (Morris et al, 2003). One of these discontinuous models is based on the Discrete Element Method, which is a family of numerical methods that defines the domain as a combination of independent elements. This method is mostly used for granular media, fractured rock systems, systems composed of multiple

bodies in mechanical engineering, and also fluid mechanics. During the 1970s–1980s, this method developed rapidly for geological and engineering applications. The major breakthrough was by Cundall in 1971 in his study of rock’s mechanical properties. In 1979, Cundall and Stark applied this method for soil mechanics. In the Discrete Element Method, the independent particles can be either rigid or deformable, and can have a circular or polygonal shape (Jing & Stephansson, 2007). A great advantage of Discrete Element Method compared to the continuum based model is that meshes are built by individual elements and there is no need for re-meshing as the simulation progresses. Figure 3-1 shows a structure that has been modelled by the Discrete Element Method and Finite Element Method. It is evident from this figure that in the case of the Finite Element Method, meshes are rigid, and if a fracture initiates, the model needs to be re-meshed. On the other hand, in the model that is constructed based on the Discrete Element Method, there is no need for re-meshing (Tavarez & Plesha, 2007) and this characteristic is because of these properties of the Discrete Element Method:

- Rotation, finite displacement and complete detachment of discretised bodies are allowed;
- While the calculation progresses, new contacts can be automatically recognised. (Morris et al., 2003)

Four basic classes of computer programs can be defined based on the definition of the Discrete Element Method (Cundall & Hart, 1992):

1. Distinct Element Programs;
2. Modal Methods;
3. Discontinuous deformation analysis;
4. Momentum-exchange methods.

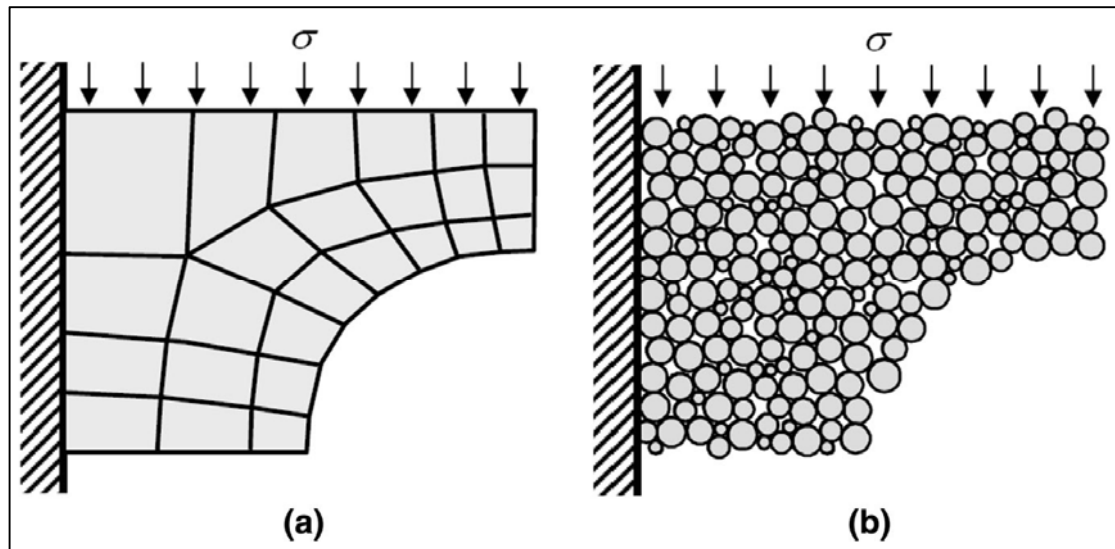


Figure 3-1: A sample that has been simulated by: a- Finite Element Method, b- Discrete Element Method. (Tavarez & Plesha, 2007)

Figure 3-2 shows a summary of the characteristics of the Discrete Element Method classes, as well as the Limit Equilibrium, Limit Analysis Method.

Distinct element programs have been developed based on the Distinct Element Method (DEM) which is a sub-classification of the Discrete Element Method. In this method, contacts are deformable and discretised elements can be either rigid or deformable (Cundall & Hart, 1992). The solution scheme is based on explicit time stepping, of which time steps are chosen to be so small that the disturbances introduced by a single particle cannot propagate beyond neighbouring particles (Cundall & Strack, 1979). Detailed descriptions of the method can be found in Cundall (1988) and Hart et al., (1988) papers.

PFC2d (Particle Flow Code in two dimensions) is a DEM based commercial software developed by Itasca Consulting Group. In this software, discretised bodies are composed of rigid circular particles that can have a random distribution of radius size from a range defined by the user. The analysis is based on the Force–Displacement calculation for individual particles and applying Newton’s second law for calculating velocity and position of particles in each time step (Itasca, 2008). Figure 3-3 depicts the general algorithm used in PFC2D.

For Each Method			Class 1	Class 2	Class 3	Class 4	LELA		
Rigid contacts		Deformable contacts	▲	●	▲	●	▲	●	▲
Rigid bodies		Deformable bodies	●	●	●	●	▲	●	▲
Small disp.		Large displacement	●	●	●	●	▲	●	▲
Small strain		Large strain	●	●	●	●	▲	▲	▲
Few bodies		Many bodies	●	●	●	■	●	●	■
Linear material		Nonlinear material	●	●	■	●	▲	▲	▲
No fracture		Fracture	●	■	●	●	▲	▲	▲
Loose packing		Dense packing	●	●	■	▲	●	■	▲
Static		Dynamic	●	●	●	■	▲	●	▲
Forces only		Forces & displacement	▲	●	▲	●	▲	●	▲

**Key**

- ▲ Does not allow it or not applicable
- Can model it but may be inefficient or not well-suited
- Models it well

Class 1: Distinct element method  
Class 2: Modal methods  
Class 3: Discontinuous deformational  
Class 4: Momentum exchange methods  
LELA: Limit Equilibrium; Limit Analysis

Figure 3-2: Characteristics of Discrete Element Method classes as well as Limit Equilibrium Limit Analysis. After (Cundall & Hart, 1992)

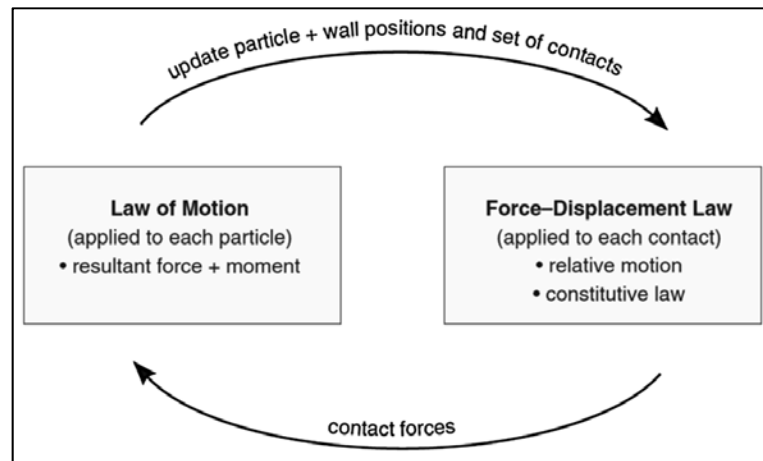


Figure 3-3: Algorithm used in PFC2D for force, velocity and displacement calculation. (Itasca, 2008)

Figure 3-4 shows particle-particle interaction in PFC2D. Each particle in contact with another particle can cause normal and tangential forces. The magnitude of these

forces depends on the overlap of particles, elastic properties of particles, contact model and contact model properties. More information about the formulation and analysis procedure can be found in the PFC2D manual (Itasca, 2008).

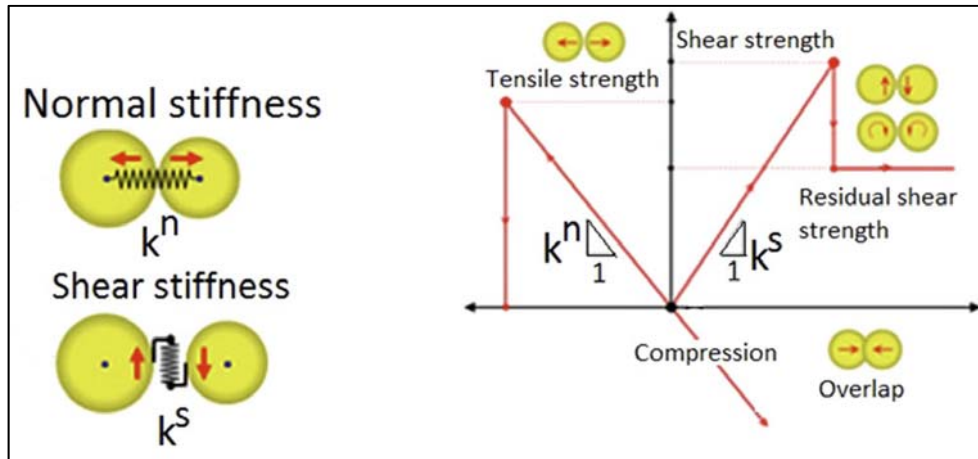


Figure 3-4: Particle-particle interaction analogy and concept in PFC2D. After (Huynh, 2014)

### 3.2. Simulating Rocks in PFC2D

To simulate a rock model in PFC2d, in the first step particles are generated and placed next to each other. These particles are then joined together by one type of bonding model (contact bond, parallel bond, and so on) available in PFC2D. In this study, a parallel bond is chosen to connect the particles to each other, as it is more similar to the cement bonding found in real samples. Particles and bonds joining them have micro mechanical properties. These properties include:

- Particle density,  $ba\_rho$ ;
- Particle young's modulus,  $ba\_Ec$ ;
- Particle friction,  $ba\_fric$ ;
- Particle normal to shear stiffness ratio,  $ba\_krat$ ;
- Parallel bond young's modulus,  $pa\_Ec$ ;
- Parallel bond normal strength,  $pb\_sn\_mean$ ;
- Parallel bond cohesion strength,  $pb\_coh\_mean$ ;
- Parallel bond friction angle,  $pb\_phi$ ;
- Parallel bond normal to shear stiffness ratio,  $pb\_krat$ .

Properties of the particles and the bonds between them are not necessarily similar to the macro mechanical properties of samples. In real samples, grains and cement connecting them have different properties than the rock sample as a whole. Simulated sample micro mechanical properties should be adjusted in a trial and error fashion to match the macro mechanical properties of the simulated sample against the mechanical properties of a real sample. In this chapter, the mechanical properties of two oil shales from Western USA are simulated. The mechanical properties of these shales are presented in Table 3-1:

Table 3-1: Mechanical Properties of two oil shales from Western USA. After (Eseme et al., 2007)

Property	Unit	Lean Shale	Rich Shale
Young's Modulus	GPa	16±2	4.5±0.5
Unconfined Compressive Strength	MPa	125±25	50±30
Poisson's Ratio	---	0.2	0.35
Friction angle	°	40.5±0.5	20
Cohesion	MPa	28±7	28±7
Tensile Strength	MPa	13±1	9.5±1.5

Simulated rock samples had a height and width of 60 and 30 mm, respectively. Samples were generated with a random combination of particle sizes with a minimum particle radius of 0.3mm. The maximum to minimum particle radius ratio was set at 1.66. These samples were then bounded between plates that are called walls in PFC2D and were subjected to the following simulated tests to drive their macro mechanical properties:

- Direct tension test;
- Uni-axial compression test;
- Confined compression test (tests at 10, 15, 20 and 25 MPa confinement stresses).

From these tests, unconfined Young's modulus, Poisson's ratio, compressive strengths, and confined compressive strengths were derived. Detailed information about these tests can be found in the PFC2D manual (Itasca, 2008). Compressive

strengths at different confined stresses were plotted in Mohr's diagram to calculate cohesion and the internal friction coefficient of the samples. As mentioned earlier, micro mechanical properties of particles and parallel bonds are adjusted to be able to reproduce the mechanical properties of real samples. The micro mechanical properties of bonds and particles are presented in Table 3-2. To make sure that the simulated results were reproducible, tests were done using 5 different seed numbers. Simulations based on different seed numbers gave very close results. Averages of these results were calculated as the final results.

Table 3-2: Micro mechanical properties of Particles and Parallel Bonds. After (Fatahi, 2014)

Property	Unit	Lean Shale	Rich Shale
Particle Properties			
<i>ba_rho</i>	Kg/m <sup>3</sup>	2400	1800
<i>ba_Ec</i>	GPa	10.5	3.5
<i>ba_fric</i>		0.8	2
<i>ba_krat</i>		1.5	
Parallel Bond Properties			
<i>pb_add</i>		1	1
<i>pb_Ec</i>	GPa	10.5	3
<i>pb_sn_mean</i>	MPa	145	40
<i>pb_sn_sdev</i>	MPa	0	0
<i>pb_mcf</i>		1	1
<i>pb_coh_mean</i>	MPa	85	40
<i>pb_coh_sdev</i>	MPa	0	0
<i>pb_phi</i>	°	60	5
<i>pb_krat</i>		1.5	2

Figure 3-5a and Figure 3-5c show direct tension tests for Lean and Rich shales respectively. In these figures, the horizontal axis shows time and the vertical axis shows stress in MPa. Figure 3-5b and Figure 3-5d show the unconfined compressive strength test of Lean and Rich shales, respectively. These figures show that lean shale has higher tensile and compressive strengths than rich shale.

Figure 3-6a and Figure 3-6b show confined compressive strength tests of Lean and Rich shales at 10 MPa confinement stress. Figure 3-6c and Figure 3-6d show confined compressive strength tests of lean and rich shales at 20 MPa confinement stress. These figures show that compressive stresses near the pick are to some extent flattened out. This is due to the more plastic behaviour of rich shales. Figures indicate as well that pick stresses are lower for Rich shale than Lean shale.

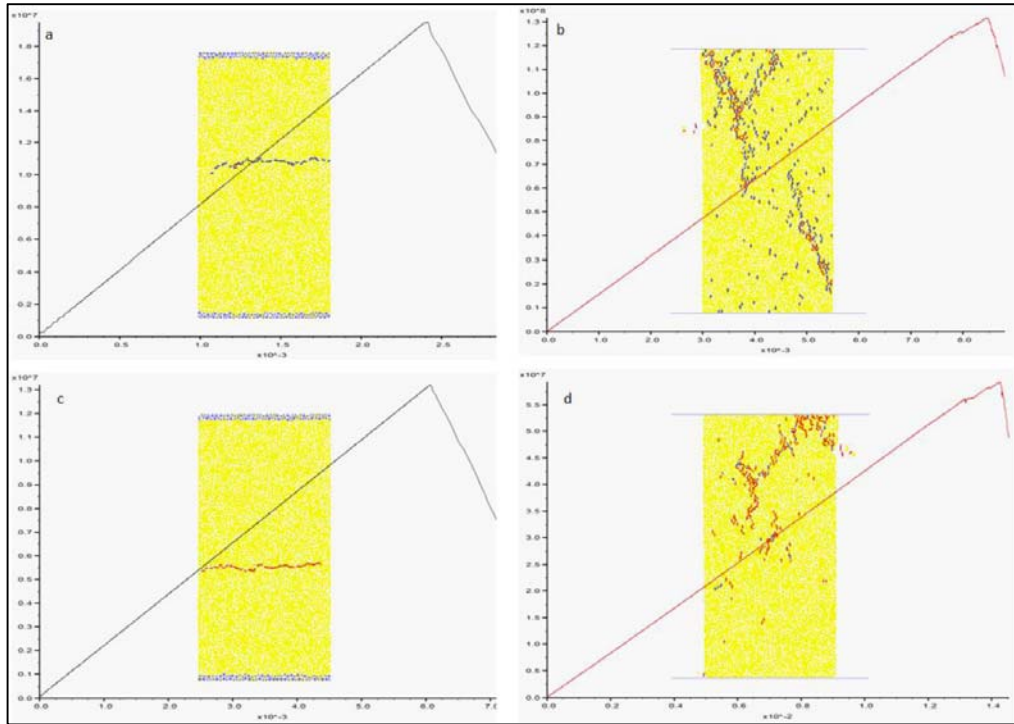


Figure 3-5: a- Direct tension test of Lean shale; b- Uniaxial compression test of Lean shale; c- Direct tension test of Rich shale; d- Uniaxial compression test of Rich shale. (Fatahi, 2014)

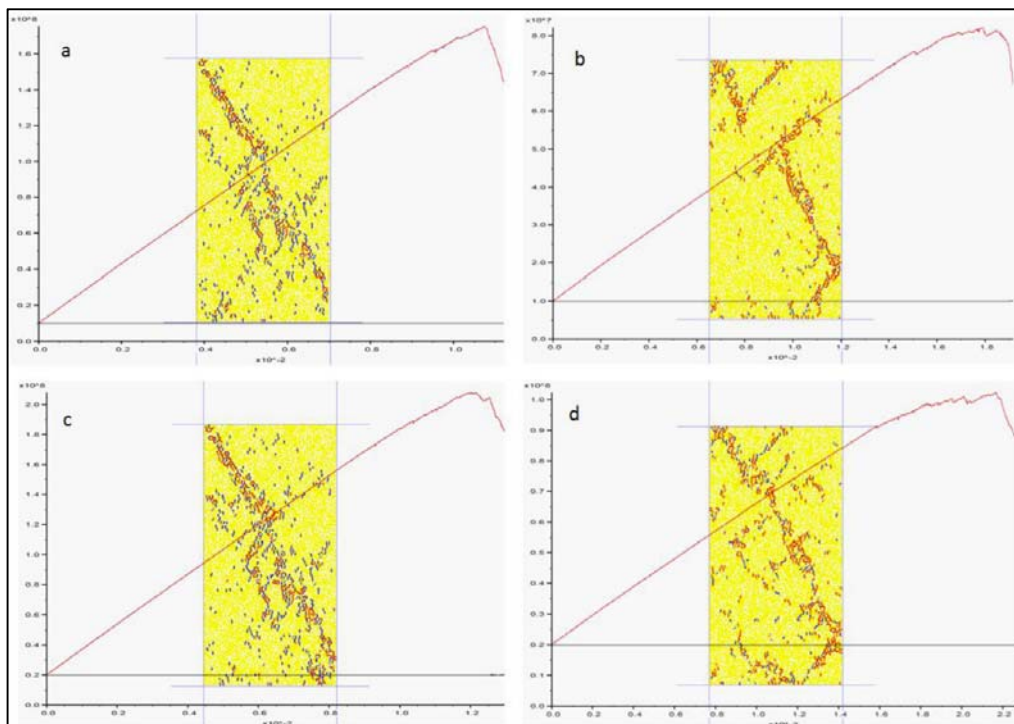


Figure 3-6: a- Confined compression test of Lean shale (10 MPa confinement stress); b- Confined compression test of Rich shale (10 MPa confinement stress); c- Confined compression test of Lean shale (20 MPa confinement stress); d- Confined compression test of Rich shale (20 MPa confinement stress). (Fatahi, 2014)

Table 3-3 presents the mechanical properties of real and simulated Lean and Rich oil shales. All properties except tensile strength show a very close agreement between real and simulated results. Discrepancies between the tensile strength of real and simulated samples can be due to the nature of real rock samples. Rocks often have micro or nano size natural fractures. These fractures might not be visible to the naked eye, but they can act as stress concentration zones and weaken the rock sample. As a result, real samples have a lower tensile strength than simulated samples that don't have these defects. The reason that this discrepancy is not seen in other tests is that all other properties are derived based on compressive tests. In the compressive tests, the micro and nano size fractures close down under compression and their effect is reduced to a large extent.

Table 3-3: Macro-mechanical properties of real and simulated Lean and Rich Shales. After (Fatahi, 2014)

Property	Unit	Lean Shale	Simulated Lean shale	Rich Shale	Simulated Rich Shale
Tensile Strength	MPa	13±1	21±1	9.5±1.5	15±2
UCS	MPa	125±25	125±7	50±30	58±2
E	GPa	16±2	16±0.2	4.5±0.5	4±0
v		0.2	0.2±0	0.35	0.32±0
Cohesion	MPa	28±7	30±3	28±7	21±1
Φ	°	40.5±0.5	39±3	20	20±2

To summarise, this chapter has demonstrated how to match the mechanical properties of simulated rock samples against real rock sample properties. In the next chapter, fluid flow in simulated samples is presented. Validation of results will be through comparison against analytical results.

# 4

## Simulation of Fluid Flow using DEM

The procedure to simulate a rock sample in PFC2D with the same mechanical properties as real rock samples is described in Chapter 3. Chapter 4 describes the algorithm and concepts that are used to match fluid flow properties of simulated samples. If not impossible, it might be very hard to measure pressure versus time and distance in a real sample during a transient flow regime. Drilling a hole through the sample to place pressure sensors and cementing the holes afterwards might disturb the homogeneity of samples. Also, there will be limitations as to how many pressure transducers can be implemented in the sample. To overcome these issues, the validation of simulation results in this chapter is based on the analytical results. The governing partial differential equation for fluid flow was solved to derive pertinent equations for transient flow regimes for two cases of linear and radial fluid flow regimes. In the linear flow regime, a prismatic sample with initial pore pressure is considered. At time zero, pressure at one end is kept at initial pore pressure, and at the other end it is dropped to zero. Transient pressure behaviour at subsequent times is derived. In the radial fluid flow regime, the sample is at initial pore pressure. At time zero, the wellbore starts to produce at a constant flow rate. Transient pressure behaviour at subsequent times is derived.

In the first part of this chapter, the algorithm of fluid flow for simulated samples is presented. In the second part, the derivation of analytical equations for the two cases of linear and radial fluid flow is explained. In the last part, comparison and validation of simulation results against analytical results are presented. This chapter is based on author's paper "Fluid flow through porous media using distinct element based numerical method" published in the *Journal of Petroleum Exploration and Production Technology* (Fatahi & Hossain, 2016).

## 4.1. Distinct Element Method Fluid Flow

In PFC2D, the porous medium, through which the fluid flows, is considered to be composed of individual circular particles, which are connected together by contact or parallel bonds. The void space between the particles is assumed to be filled with fluid, which flows between these void spaces. To characterise fluid flow between these void spaces, it is required to define the domain term. A domain is defined as a closed loop polygon by particles that are connected to each other, as illustrated in Figure 4-1. Each side of the polygon is a line segment connecting centres of two particles that are connected by contact bonds.

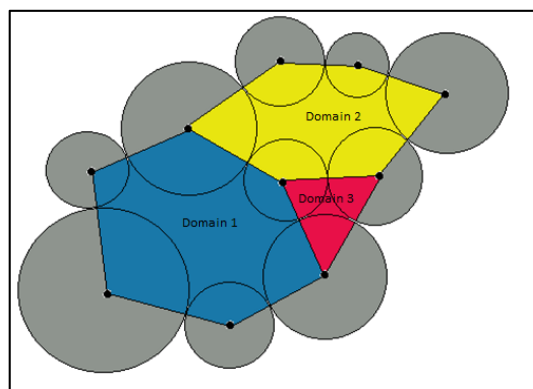


Figure 4-1: Particles and Domains. (Fatahi & Hossain, 2016)

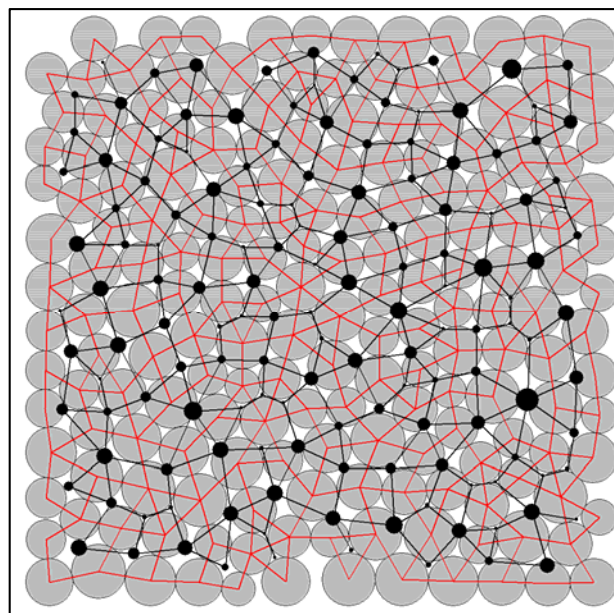


Figure 4-2: A sample composed of grey particles. Black circles are centres of domains and their size is based on size of domain volume. Black lines connect each domain to its neighbouring domains. Red lines show boundaries of each domain. (Fatahi & Hossain, 2016)

Figure 4-1 shows 10 particles and 3 domains. Particles are in grey colour. Domain 1 is in blue, domain 2 is in yellow, and domain 3 is in red. Figure 4-2 shows a sample which is a compacted bonded assembly of particles. In this figure particles are in grey. Black circles show the centres of domains. The size of black circles is in direct relationship to the volumes of domains, with the biggest size showing the largest domain volume, and the smallest size showing the smallest domain volume. Black lines show the connection of each domain to its neighbouring domains. Red lines show the boundaries of domains, and they connect the centres of particles that build the domain.

Fluid flow happens between the domains through a parallelepiped centred at the contact point between each pair of particles. The parallelepiped length is the sum of two particles' radii. The aperture between parallel plates is denoted as “ $w$ ”. The depth of the parallelepiped is equal to unity.

Figure 4-3-a shows two domains connected by the parallelepiped. Domains are denoted as  $Domain_i$  and  $Domain_j$ , and the parallelepiped connecting them is shown as a rectangle in red. Figure 4-3b shows the parallelepiped. The aperture of the parallelepiped is  $w$  and its length is  $L_p$ . The depth of the parallelepiped which is in the out-of-plane direction is equal to one.

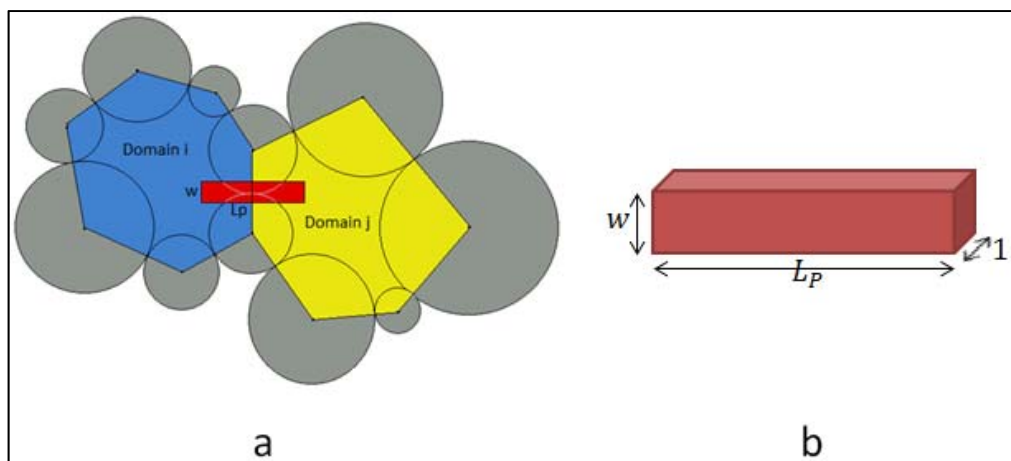


Figure 4-3: a- Parallelepiped connecting two domains. Parallelepiped is shown in red. b- Parallelepiped with length  $L_p$ , width  $w$ , and depth 1. (Fatahi & Hossain, 2016)

Fluid flow through the parallelepiped is governed by the Poiseuille's Equation for fluid flow through parallel plates, as shown by equation (4-1):

$$q = \frac{w^3}{12\mu} \frac{P_i - P_j}{L_p} \quad (4-1)$$

Where;

$q$ : Flow Rate

$P_i$ : Pressure in Domain  $i$

$P_j$ : Pressure in Domain  $j$

$\mu$ : Fluid Viscosity

$L_p$ : Parallelepiped Length

The parallelepiped can be defined between two particles only if they are in contact. However, after they have been initialised they will exist even if particles detach from each other. When particles are in contact, the aperture of the parallelepiped will be zero. But to take into account the macroscopic permeability of the rock and to overcome the 2D limitation of the simulation, “ $w$ ” will be set to a number greater than zero.

After setting the initial value for the aperture, its value should also take into account the nature of the contact between its two adjacent particles. That means if particles are still in contact and apply a compressive force on each other, “ $w$ ” can be found by Equation (4-2):

$$w = \frac{w_0 F_0}{F - F_0} \quad (4-2)$$

$w_0$  is the initial aperture.  $F_0$  is the fixed value and is the amount of normal force that changes the aperture to half of its initial value.  $F$  is the compressive force between particles and its value can change. If the value of  $F$  is much lower than  $F_0$  value, the value of  $w$  would not change appreciably. If the value of  $F$  is negative (i.e. particles’ bond is under tension) the aperture value is obtained by Equation (4-3):

$$w = w_0 + m \times g \quad (4-3)$$

In this equation,  $g$  denotes the gap or the distance between particles;  $m$  is a calibration constant, and can have a value between zero to one.

The macroscopic permeability value of the rock can be reproduced by adjusting the values of  $w_0$ ,  $F_0$  and  $m$ . Each domain has pressure communication with the other

surrounding domains. Total flow in and out of each domain is  $\sum_{i=1}^n q_i$ , with “ $n$ ” being the number of surrounding domains that is different for each individual domain, with a minimum value of one, and the maximum value can be any number greater than zero. The total flow volume into a domain in one time step is given by Equation (4-4):

$$\Delta V_{Domain} = \Delta t \times \sum_{i=1}^n q_i \quad (4-4)$$

“ $n$ ” is different for different domains and is equal to the number of surrounding domains, and  $\Delta t$  is the time step.

In each time step, domains experience a mechanical volume change because of the movement of particles. These movements are because of changes that occur in forces between the particles. Total pressure change in one time step for a single domain is:

$$\Delta P = \frac{K_f}{V_d} (\Delta t \times \sum_{i=1}^n q - \Delta V_d) \quad (4-5)$$

$\Delta V_d$  is mechanical volume change of the domain,  $V_d$  is the volume of the domain, and  $K_f$  is the bulk modulus of the fluid.

After a sample is generated, it will be enclosed by four frictionless plates, as shown in Figure 4-4. These plates can move independently of each other toward or away from the sample. Plates have no interaction with each other and only interact with particles of the sample. The purpose of these plates is to introduce principal stresses on the specimen to resemble tectonic stresses that are present underground.

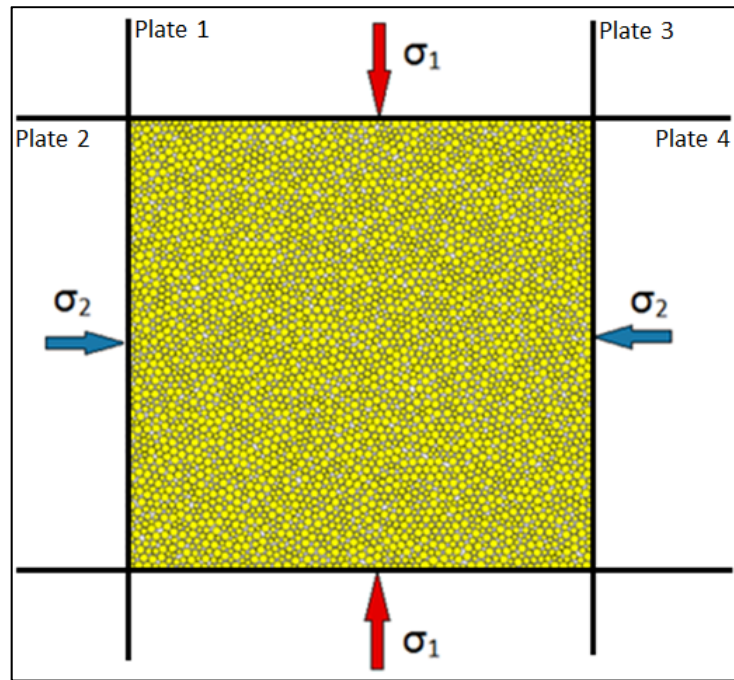


Figure 4-4: Sample with principle stresses acting on its sides. (Fatahi & Hossain, 2016)

Because of principal stresses, particles exert normal and tangential forces on each other. In addition to these forces, fluid inside the pore spaces also exerts some force on particles. Figure 4-5a shows a domain with pressure  $P_i$ , and Figure 4-5b shows particle 1 and forces on it that are generated because of pressure in the domain. The resultant of these forces is  $F$ .

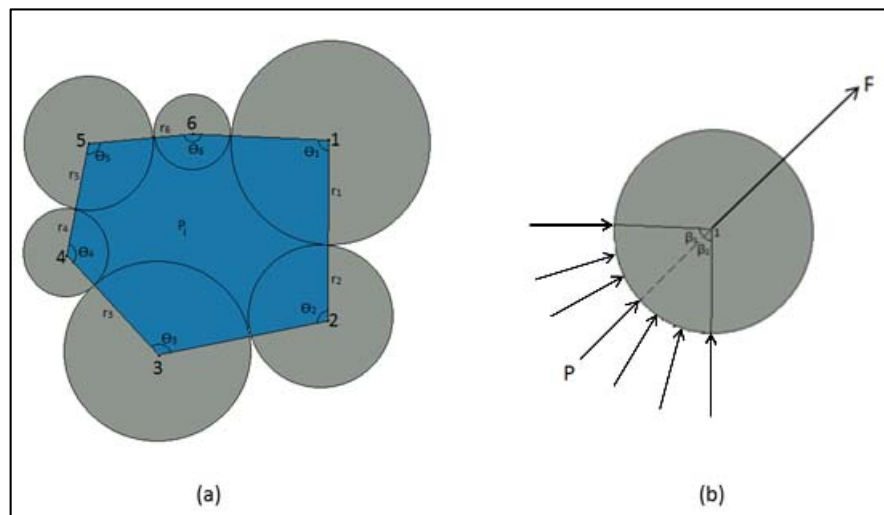


Figure 4-5: a) Domain with pressure  $P$ ; b) Pressure applied to part of particle 1 that is exposed to domain 1 and generated force  $F$  because of pressure  $P$ . (Fatahi & Hossain, 2016)

The magnitude of force that is exerted on particle 1 by fluid pressure in domain i is the product of pressure by the area of the particle that is exposed to domain i.

$$F = P \times A = P_i \times (1 \times r_1 \times \theta_1) = P_i r_1 \theta_1 \quad (4-6)$$

The depth of the particle is equal to 1. So the area is equal to 1 multiplied by the length of the arc. The length of the arc is equal to the radius of the particle multiplied by the angle that forms between the lines joining the centre of the particle to its neighbouring particles. The direction of force is outward from the domain in the direction of the line that divides the arc into two halves.

$$\beta_1 = \beta_2 = \frac{\theta_1}{2} \quad (4-7)$$

If  $\theta$  in Equation (4-6) is greater than  $\pi$ , then it should be subtracted from  $2\pi$  and the result be substituted instead of  $\theta$ . This is shown in Figure 4-6. It is evident from the figure that forces that are applied to the shaded section of the particle will balance each other out. The net force that remains on the particle as a result of pressure in domain i will be equal to the forces that are applied on the arc between the dashed lines. Also from the figure, it can be seen that  $\beta = 2\pi - \theta$ .

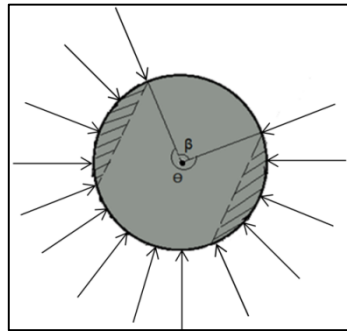


Figure 4-6:  $\theta$  is greater than  $\pi$ . The value of  $\theta$  should be replaced by  $\beta$  in (4-6). (Fatahi & Hossain, 2016)

Domain volumes will be updated in every time step. The solution to fluid flow alternates between flow through parallelepipeds and pressure adjustments between domains. This means that in each time step, the fluid flow through parallelepipeds is calculated and the total net flow to or from each domain will causes pressure change in the domains. For stability analysis, a critical time step needs to be calculated. The

procedure is to first calculate the critical time step for each domain, and then take the minimum time step of all critical time steps as the global time step.

In every time step, total flow into a domain because of pressure perturbation  $\Delta P_p$  is calculated by Equation (4-8).

$$q = \frac{Nw^3\Delta P_p}{24\mu\bar{R}} \quad (4-8)$$

$N$  is the number of parallelepipeds for each domain, and  $\bar{R}$  is the average of radius of particles that surround the domain. Solving for  $\Delta P_p$ :

$$\Delta P_p = \frac{24q\mu\bar{R}}{Nw^3} \quad (4-9)$$

The pressure disturbance applied to the domain because of the above flow rate is:

$$\Delta P_r = \frac{K_f}{V_d} (\Delta t \times Q - \Delta V_d) \quad (4-10)$$

To confirm stability, the pressure response needs to be less than or equal to pressure perturbation:

$$\Delta P_r \leq \Delta P_p \quad (4-11)$$

If we replace Equation (4-9) and Equation (4-10) in Equation (4-11), we will get Equation (4-12):

$$\frac{K_f}{V_d} (Q \times \Delta t - \Delta V_d) \leq \frac{24q\mu\bar{R}}{Nw^3} \quad (4-12)$$

Solving Equation (4-12) for  $\Delta t$  will result in Equation (4-13):

$$\Delta t \leq \frac{24\mu\bar{R}V_d}{NK_fw^3} + \frac{\Delta V_d}{Q} \quad (4-13)$$

To simplify the right hand side of Equation (4-13),  $\frac{\Delta V_d}{Q}$  is neglected and the remaining terms are multiplied by a safety factor:

$$\Delta t \leq \frac{24\mu\bar{R}V_d}{NK_fw^3} \times S.F. \quad (4-14)$$

The fluid flow calculation is explicit in time. To summarise:

- The reservoir is built from individual particles. These particles are connected together by either contact or parallel bond;
- Tectonic stresses are applied on the reservoir;
- Domains are created. Wellbore is one of these domains;
- Domain volumes are calculated;
- Domain pressures are set;
- Wellbore flow rate is set.

Once the fluid flow is started, in every time step:

- An initial time step is fed into the model and will be adjusted by the model to be not too big or too small.
- Wellbore flow rate causes wellbore pressure to drop. Equation (4-4) is used to calculate this pressure drop.
- A loop cycle goes through all domains. Aperture of the parallelepiped connecting each two domain is calculated by Equation (4-2) or Equation (4-3), depending on the nature of the force between the particles.
- Pressure difference between each two domain is calculated.
- Flow rate between each two domain is calculated by Equation (4-8).
- Equation (4-10) is used to calculate pressure change in domains as a result of flow rate between them.
- Domain pressures are updated.
- Pressure force on particles is updated.
- Particles positions are updated.
- Local time steps for fluid flow between each two domains is calculated by Equation (4-14), and the minimum of all time steps is chosen as the global time step to be used as the new value of time step.
- Calculation cycles are continued (end point of calculation cycles depends on the desired fluid flow time that is set by user. Simulation flow time is set to zero at the beginning of simulation. In every cycle the time step is added to simulation flow time. Once the simulation flow time is equal to desired fluid flow time, calculations will end).

Figure 4-7 shows the algorithm for fluid flow calculation. In every time step, fluid flow between domains and pressure change at domains is calculated and domain pressures are updated. The loop in this figure does not mean that the calculations are iterative. Every one cycle of calculations progresses the fluid flow one step in time. Addition of the time steps in all calculation cycles shows how long fluid has flown in the porous medium.

As can be concluded from this section, fluid flow is at a microscopic level and is independent of the reservoir geometry. This independence is because fluid flows between domains and domain can be created for any reservoir shape. This characteristic makes this method applicable for any reservoir geometry. Also, this method is independent of flow type (linear, radial, etc.) and flow regime (transient, late transient, steady state or semi-steady state) and can be applied for any flow type and flow regime.

A discontinuity such as a fracture or a joint has a permeability that can be different from the matrix permeability. These discontinuities can be incorporated into the system by using a smooth joint model. Domain pipes that are on a smooth joint can have different apertures ( $w$ ) and by adjusting these apertures, discontinuity permeability can be reproduced. In this way, the only difference between the parallelepipeds that represent discontinuity and the parallelepipeds that represent pore throat, is their aperture. Following this method simplifies the incorporation of discontinuities without the need to develop a whole new system to describe fluid flow. Analytical models, on the other hand, may require development of whole new solution, as a new type of discontinuity is presented in the system. Figure 4-8 illustrates a sample with two sets of joints with dip angles of  $60^\circ$  and  $-20^\circ$ .

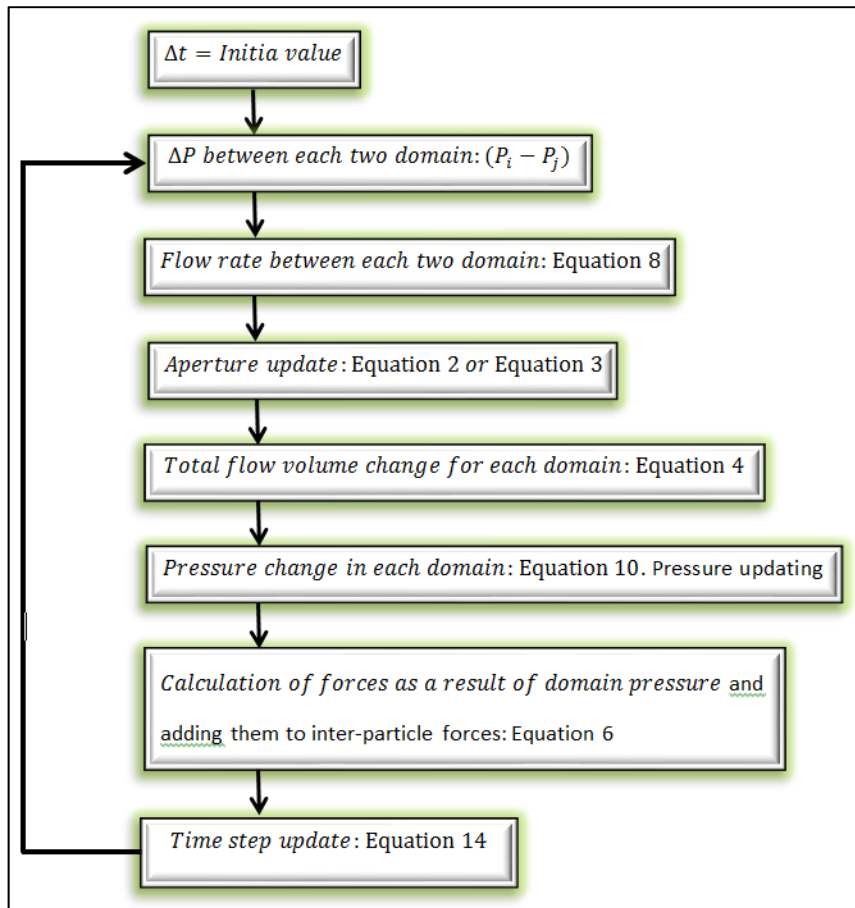


Figure 4-7: Algorithm of fluid flow calculation. Calculations are explicit in time. (Fatahi & Hossain, 2016)

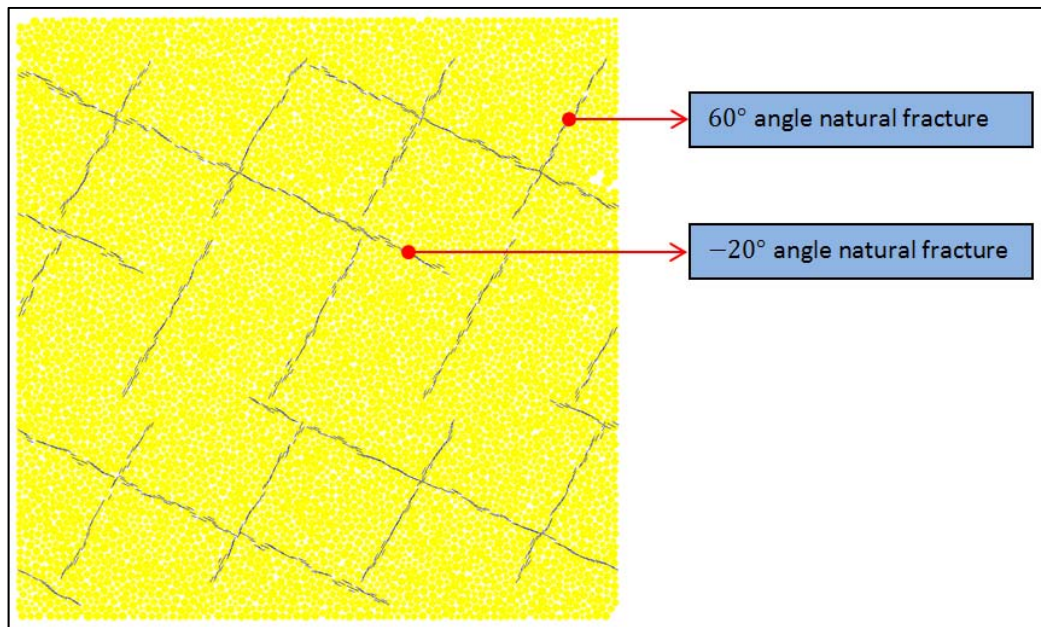


Figure 4-8: Sample with two sets of natural fractures. (Fatahi & Hossain, 2016)

## 4.2. Analytical Methods

To validate the numerical model, two cases of linear fluid flow and radial fluid flow in a porous medium are considered. The formation in both cases is finite. For each case, boundary and initial conditions as well as derivation of analytical formulas are presented in sections 4.2.1 and 4.2.2. Solutions of both cases are used in the comparison section to compare the results of the numerical model against analytical models.

### 4.2.1. Linear Fluid Flow Condition

One dimensional fluid flow is considered in a sample with dimensions of  $L \times H \times W$ . Initial pore pressure of the sample is set equal to  $P_i$ . Boundaries have constant pressure. Pressure at one end of the sample is  $P_1$  and on the other end is  $P_2$ . Equation (4-15) shows the initial condition. Equation (4-16) and Equation (4-17) show boundary conditions:

$$P(x, t = 0) = P_i = f(x) \quad (4-15)$$

$$P(x = 0, t > 0) = P_1 \quad (4-16)$$

$$P(x = L, t > 0) = P_2 \quad (4-17)$$

Equation (4-18) shows the linear form of the pressure diffusion equation in porous media:

$$\frac{\partial P}{\partial t} = \alpha^2 \frac{\partial^2 P}{\partial x^2}, t \geq 0, 0 \leq x \leq L \quad (4-18)$$

$\alpha^2$  is called hydraulic diffusivity and is equal to fluid mobility divided by fluid storability:

$$\alpha^2 = \frac{k}{\varphi \mu c_t} \quad (4-19)$$

Equation (4-18) can be solved by separation of variables to get an expression for pressure function where its variables are time and location. Equation (4-18) can be solved easily for a homogenous boundary condition, that is, with boundary condition values set to zero. But in this situation, one or both boundary condition values can be a pressure above zero. To overcome this problem and convert it to a homogenous

boundary condition equation, the pressure function can be assumed to be composed of two parts, one being time-independent and the other part being time-dependent:

$$P(x, t) = v(x) + w(x, t) \quad (4-20)$$

In Equation (4-20),  $v(x)$  is the steady state pressure equation that is independent of time and aids to change the boundary conditions of the problem to homogenous boundary conditions.  $w(x, t)$  is the transient part of pressure function, and its value will change with respect to time.

Because  $v(x)$  is part of the pressure function equation, it should satisfy the diffusivity equation as well.  $v(x)$  is independent of time and its derivative with respect to time is zero, as shown in Equation (4-21):

$$\frac{\partial v}{\partial t} = 0 \quad (4-21)$$

Replacing  $P(x, t)$  by  $v(x)$  in Equation (4-18) and using Equation (4-21) gives:

$$\alpha^2 \frac{\partial^2 v}{\partial x^2} = 0 \quad (4-22)$$

The solution of Equation (4-22) is:

$$v(x) = c_1 x + c_2$$

Rewriting the boundary conditions for  $v(x)$ ,  $P(0, t) = v(0) = P_1$  and  $(L, t) = v(L) = P_2$ . Values of  $c_1$  and  $c_2$  can be determined by these two boundary values:

$$\begin{aligned} v(0) &= P_1 = c_1 \times 0 + c_2 = c_2 \\ v(L) &= P_2 = c_1 \times L + c_2 = c_1 \times L + P_1 \rightarrow c_1 = \frac{P_2 - P_1}{L} \\ v(x) &= \frac{P_2 - P_1}{L} x + P_1 \end{aligned} \quad (4-23)$$

The steady state part of the pressure equation is determined. The next step is to find the transient part of the pressure equation. The boundary values for the transient part are calculated as follows:

$$\begin{aligned} P(0, t) &= P_1 = v(0) + w(0, t) \rightarrow w(0, t) = P_1 - v(0) = 0 \rightarrow w(0, t) = 0 \\ w(x = 0, t > 0) &= 0 \end{aligned} \quad (4-24)$$

$$P(L, t) = P_2 = v(L) + w(L, t) \rightarrow w(L, t) = P_2 - v(L) = 0 \rightarrow w(L, t) = 0$$

$$w(x = L, t > 0) = 0 \quad (4-25)$$

$$P(x, 0) = f(x) = P_i = v(x) + w(x, 0) \rightarrow w(x, 0) = f(x) - v(x)$$

$$= P_i - \left(P_1 + \frac{P_2 - P_1}{L}x\right)$$

$$w(x, t = 0) = P_i - \left(P_1 + \frac{P_2 - P_1}{L}x\right) \quad (4-26)$$

As  $w(x, t)$  is also part of the pressure equation, it should satisfy the partial differential pressure diffusivity equation:

$$\frac{\partial w}{\partial t} = \alpha^2 \frac{\partial^2 w}{\partial x^2}, \quad 0 \leq x \leq L, \quad t \geq 0 \quad (4-27)$$

This equation can be solved by the method of separation of variables. If  $w(x, t)$  is denoted as a multiplication of two functions where one of them is only dependent on  $x$  and the other is dependent on time, then:

$$w(x, t) = X(x) \times T(t) \quad (4-28)$$

Partial derivatives of  $w(x, t)$  with respect to time ( $t$ ) and position ( $x$ ) are:

$$\frac{\partial^2 w}{\partial x^2} = T(t) \frac{\partial^2 X}{\partial x^2} \quad (4-29)$$

$$\frac{\partial w}{\partial t} = X(x) \frac{\partial T}{\partial t} \quad (4-30)$$

Substitution of Equation (4-29) and Equation (4-30) into Equation (4-27) gives:

$$X \frac{\partial T}{\partial t} = \alpha^2 T \frac{\partial^2 X}{\partial x^2} \quad (4-31)$$

If either  $X(x)$  or  $T(t)$  is zero, then the solution of  $w(x, t)$  is the trivial solution of  $w(x, t) = 0$ . So both of these functions are different from zero and both sides of Equation (4-31) can be divided by  $X(x)T(t)$  to give:

$$\frac{1}{\alpha^2 T} \frac{\partial T}{\partial t} = \frac{1}{X} \frac{\partial^2 X}{\partial x^2} \quad (4-32)$$

Sides of (4-32) are independent of each other. The left hand side is a function of time ( $t$ ) and the right hand side is a function of position ( $x$ ). So in order for the equation to

hold for any  $t$  and  $x$ , both sides should be equal to a constant. If sides are equated to  $-\lambda$  ( $-\lambda$  can be any positive or negative number but the negative sign makes calculations simpler) it will result in:

$$X'' + \lambda X = 0 \tag{4-33}$$

And,

$$T' + \alpha^2 \lambda T = 0 \tag{4-34}$$

So  $W(x, t)$  is decomposed to a homogenous second order ordinary differential equation for  $X(x)$  and a homogenous first order ordinary differential equation for  $T(t)$ . Solving for boundary conditions:

$$w(0, t) = 0 \rightarrow X(0)T(t) = 0 \rightarrow X(0) = 0 \text{ or } T(t) = 0$$

$$w(L, t) = 0 \rightarrow X(L)T(t) = 0 \rightarrow X(L) = 0 \text{ or } T(t) = 0$$

$T(t) = 0$  will make both of the conditions satisfy but it also causes  $w(x, t)$  equation to be zero, which is a trivial solution and not the desired solution. Therefore;

$$X(x = 0) = 0 \tag{4-35}$$

$$X(x = L) = 0 \tag{4-36}$$

To solve Equation (4-33) there are three options for  $\lambda$ :

Option 1:  $\lambda < 0$

Option 2:  $\lambda = 0$

Option 3:  $\lambda > 0$

The three options will be considered individually to decide which option will give the correct answer:

**Option 1:  $\lambda < 0$**

$\lambda = -\delta^2$  so the characteristic equation is:  $r^2 - \delta^2 = 0$  and roots are  $r = \pm\delta$ .

This gives the general solution as:

$$X(x) = D_1 e^{\delta x} + D_2 e^{-\delta x} \quad (4-37)$$

Putting the first boundary condition from Equation (4-35) into Equation (4-37) gives:

$$X(0) = 0 = D_1 + D_2 \rightarrow D_1 = -D_2 \quad (4-38)$$

Putting the second boundary condition from Equation (4-36) into Equation (4-37) gives:

$$X(L) = 0 = D_1 e^{\delta L} + D_2 e^{-\delta L} = D_1 (e^{\delta L} + e^{-\delta L}) \quad (4-39)$$

$(e^{\delta L} + e^{-\delta L}) \neq 0$  and for Equation (4-39) to hold,  $D_1$  should be zero, which causes  $D_2$  to be zero as well. This will result in  $X(x) = 0$  which in turn causes  $w(x, t) = 0$ , which is a trivial solution. So this means that option 1 is not valid and  $\lambda$  cannot be a negative value.

### **Option 2: $\lambda = 0$**

This option will result in Equation (4-40) for  $X(x)$ :

$$X(x) = D_1 + D_2 x \quad (4-40)$$

Applying the first boundary condition will result in:

$$X(0) = 0 = D_1 \rightarrow D_1 = 0$$

And applying the second boundary condition will result in:

$$X(L) = 0 = D_1 + D_2 L = D_2 L \rightarrow D_2 = 0$$

This will result in  $X(x) = 0$  which in turn causes  $w(x, t) = 0$ , which is a trivial solution. So this means that option 2 is not valid and  $\lambda$  cannot be zero, and only option 3 remains.

### **Option3: $\lambda > 0$**

$\lambda = \delta^2$ , so the characteristic equation is:  $r^2 + \delta^2 = 0$ , and roots are  $r = \pm \delta i$ . So based on the roots of the characteristic equation, the general solution is:

$$X(x) = D_1 \cos(\delta x) + D_2 \sin(\delta x) \quad (4-41)$$

By imposing the boundary conditions:

$$X(0) = 0 = D_1 \cos(0) + D_2 \sin(0) = D_1 \rightarrow D_1 = 0$$

$$X(L) = 0 = D_1 \cos(\delta L) + D_2 \sin(\delta L) = D_2 \sin(\delta L)$$

For  $D_2 \sin(\delta L) = 0$  to be valid, either  $D_2 = 0$  or  $\sin(\delta L) = 0$ . If  $D_2 = 0$ , it will result in  $X(x) = 0$  which in turn causes  $w(x, t) = 0$  which is a trivial solution. So this means that  $\sin(\delta L) = 0$ , which implies that  $\delta L = \pi, 2\pi, 3\pi, \dots, n\pi$ . Solving for  $\delta$  will give:  $\delta = \frac{\pi}{L}, \frac{2\pi}{L}, \dots, \frac{n\pi}{L}$ .

So based on the above three options being analysed, the value of  $\lambda$  should be greater than zero. The values of  $\lambda$  that satisfy (4-41) are eigenvalues of this equation and are:

$$\lambda = \delta^2 = \frac{n^2 \pi^2}{L^2}, \quad n = 1, 2, 3, \dots \quad (4-42)$$

For each of eigenvalues there will be an eigenfunction. The  $n^{\text{th}}$  eigenfunction is:

$$X_n(x) = \sin \frac{n\pi x}{L}, n = 1, 2, 3, \dots \quad (4-43)$$

Inserting the value of  $\lambda$  from Equation (4-42) into Equation (4-34) will give:

$$T' + \alpha^2 \frac{n^2 \pi^2}{L^2} T = 0 \quad (4-44)$$

Solving Equation (4-44) will give  $T(t)$  for  $n^{\text{th}}$  eigenvalue:

$$T_n(t) = C_n e^{-\frac{\alpha^2 n^2 \pi^2}{L^2} t}, \quad n = 1, 2, 3, \dots \quad (4-45)$$

The  $n^{\text{th}}$  eigenfunction for  $w(x, t)$  is the product of Equation (4-43) and Equation (4-45):

$$w_n(x, t) = X_n(x)T_n(t) = C_n e^{-\frac{\alpha^2 n^2 \pi^2}{L^2} t} \sin \frac{n\pi x}{L}, \quad n = 1, 2, 3, \dots \quad (4-46)$$

The summation of all solutions for different eigenvalues is also a solution of  $w(x, t)$ .

As a result,  $w(x, t)$  can be shown as:

$$w(x, t) = \sum_{n=1}^{\infty} X_n(x)T_n(t) = \sum_{n=1}^{\infty} C_n e^{-\frac{\alpha^2 n^2 \pi^2}{L^2} t} \sin \frac{n\pi x}{L}, \quad n = 1, 2, 3, \dots \quad (4-47)$$

Applying the initial condition of  $w(x, 0) = f(x) - v(x)$  gives:

$$w(x, 0) = \sum_{n=1}^{\infty} C_n \sin \frac{n\pi x}{L} = f(x) - v(x), \quad n = 1, 2, 3, \dots \quad (4-48)$$

Equation (4-48) is "sine" Fourier series. The coefficients  $C_n$  which are the "sine" Fourier coefficients are:

$$\begin{aligned} C_n &= \frac{2}{L} \int_0^L (f(x) - v(x)) \sin \frac{n\pi x}{L} dx = \frac{2}{L} \int_0^L \left( P_i - \left( P_1 + \frac{P_2 - P_1}{L} x \right) \right) \sin \frac{n\pi x}{L} dx \\ &= \frac{2}{L} \int_0^L (P_i - P_1) \sin \frac{n\pi x}{L} dx + \frac{2}{L} \int_0^L \left( \frac{P_1 - P_2}{L} x \right) \sin \frac{n\pi x}{L} dx \\ &= \frac{2-L}{L n\pi} \cos \left( \frac{n\pi x}{L} \right) (P_i - P_1) \Big|_0^L + \frac{2}{L^2} (P_1 - P_2) \int_0^L x \times \sin \frac{n\pi x}{L} dx \\ &= \frac{2(P_i - P_1)(1 - \cos(n\pi))}{n\pi} \\ &\quad + \frac{2}{L^2} (P_1 - P_2) \left( -\frac{L^2(-\sin(n\pi)) + \cos(n\pi) \times n\pi}{n^2\pi^2} \right), \\ n &= 1, 2, 3, \dots \end{aligned}$$

$$\begin{aligned} C_n &= \frac{2(P_i - P_1)(1 - (-1)^n)}{n\pi} + 2(P_2 - P_1) \left( \frac{(-1)^n}{n\pi} \right), n \\ &= 1, 2, 3, \dots \end{aligned} \quad (4-49)$$

Inserting Equation (4-49) into Equation (4-47):

$$\begin{aligned} w(x, t) &= \sum_{n=1}^{\infty} \left( \frac{2(P_i - P_1)(1 - (-1)^n)}{n\pi} \right. \\ &\quad \left. + 2(P_2 - P_1) \left( \frac{(-1)^n}{n\pi} \right) \right) e^{-\frac{\alpha^2 n^2 \pi^2}{L^2} t} \sin \frac{n\pi x}{L}, n \\ &= 1, 2, 3, \dots \end{aligned} \quad (4-50)$$

Inserting Equation (4-23) and Equation (4-50) in Equation (4-20) gives:

$$\begin{aligned}
P(x, t) = & \left( P_1 + \frac{P_2 - P_1}{L} x \right) \\
& + \sum_{n=1}^{\infty} \left( \frac{2(P_i - P_1)(1 - (-1)^n)}{n\pi} \right. \\
& \left. + 2(P_2 - P_1) \left( \frac{(-1)^n}{n\pi} \right) \right) e^{-\frac{\alpha^2 n^2 \pi^2}{L^2} t} \sin \frac{n\pi x}{L}, \\
& n = 1, 2, 3, \dots
\end{aligned} \tag{4-51}$$

To simplify calculations, the concept of dimensionless parameters is used. Dimensionless pressure, position and time are defined as:

$$P_D = \frac{P_1 - P(x, t)}{P_1 - P_2} \tag{4-52}$$

$$x_D = \frac{x}{L} \tag{4-53}$$

$$t_D = \frac{t \times \alpha^2}{L^2} \tag{4-54}$$

If  $P_1$  is set equal to  $P_i$  and  $P_2$  is set equal to zero, after re-arranging Equation (4-51) and using Equation (4-52), Equation (4-53) and Equation (4-54), dimensionless pressure is:

$$P_D = x_D + \frac{2}{\pi} \sum_{n=1}^{\infty} \frac{(-1)^n}{n} e^{-n^2 \pi^2 t_D} \sin(n\pi x_D), \quad n = 1, 2, 3, \dots \tag{4-55}$$

Equation (4-55) is the dimensionless form of the pressure diffusion equation of laminar fluid flow in a sample with initial pore pressure of  $P_i$  and constant boundary pressures of  $P_1 = P_i$  and  $P_2 = 0$ .

Equation (4-55) is used in section “4.3. Comparison of Numerical and Analytical Models” for validation of numerical results.

### 4.2.2. Radial fluid flow

Radial fluid flow is considered for a sample with external radius ( $R_e$ ) and wellbore radius ( $R_w$ ). Initial pore pressure is  $P_i$ . Pressure at outer boundary ( $R_e$ ) is kept

constant at  $P_i$  while wellbore pressure changes to ensure constant wellbore flow rate. Equation (4-56) and Equation (4-57) show inner and outer boundary conditions. Equation (4-58) is the initial condition.

$$\begin{aligned} \left( \frac{2\pi kh}{\mu} R \frac{\partial P}{\partial R} \right) \Big|_{(R=R_w, t>0)} &= Q = \text{constant} \\ &= \frac{2\pi kh(P_e - P_w|_{\text{steady state}})}{\mu \ln\left(\frac{R_e}{R_w}\right)} \end{aligned} \quad (4-56)$$

$$P(R_e, t > 0) = P_i \quad (4-57)$$

$$P(R, t = 0) = P_i \quad (4-58)$$

The radial form of pressure diffusion equation in porous media is shown in Equation (4-59):

$$\frac{1}{R} \frac{\partial}{\partial R} \left( R \frac{\partial P}{\partial R} \right) = \frac{\varphi \mu c_t}{k} \frac{\partial P}{\partial t}, \quad t \geq 0, \quad R_w \leq R \leq R_e \quad (4-59)$$

To simplify Equation (4-59) and boundary conditions, the following dimensionless parameters are defined:

$$R_D = \frac{R}{R_w} \quad (4-60)$$

$$t_D = \frac{kt}{\varphi \mu c R_w^2} \quad (4-61)$$

$$\Delta P_D = \frac{2\pi kh(P_i - P)}{\mu Q} \quad (4-62)$$

$R_D$  is dimensionless radius,  $t_D$  is dimensionless time and  $\Delta P_D$  is delta dimensionless pressure. Inserting Equations (4-60), (4-61) and (4-62) into Equation (4-59), will simplify it to Equation (4-63):

$$\frac{1}{R_D} \frac{\partial}{\partial R_D} \left( R_D \frac{\partial \Delta P_D}{\partial R_D} \right) = \frac{\partial \Delta P_D}{\partial t_D}, \quad t_D \geq 0, \quad 1 \leq R_D \leq R_{De} \quad (4-63)$$

Boundary conditions and Initial condition will simplify to:

$$\Delta P_D(R_D = 1, t_D) = \ln(R_{De}), \quad R_D \frac{\partial \Delta P_D}{\partial R_D} \Big|_{(R_D=1, t_D)} = -1 \quad (4-64)$$

$$\Delta P_D(R_D = R_{De}, t_D) = 0 \quad (4-65)$$

$$\Delta P_D(R_D, 0) = 0 \quad (4-66)$$

Equation (4-63) can be solved in the same way as linear form of the equation has been solved by assuming that the equation is composed of two parts of steady state and unsteady state.

$$\Delta P_D(R_D, t_D) = S(R_D) + U(R_D, t_D) \quad (4-67)$$

$S(R_D)$  is the steady state part of the equation and  $U(R_D, t_D)$  is the unsteady state part of the equation. Steady state part of the equation should satisfy initial and boundary conditions as well as pressure diffusion equation. As the steady state solution is independent of time, the right hand side of the diffusivity equation is equal to zero.

$$\frac{1}{R_D} \frac{\partial}{\partial R_D} \left( R_D \frac{\partial S(R_D)}{\partial R_D} \right) = 0, \quad t_D \geq 0, \quad 1 \leq R_D \leq R_{De} \quad (4-68)$$

$$S(R_D = 1) = \ln(R_{De}) \quad (4-69)$$

$$S(R_D = R_{De}) = 0 \quad (4-70)$$

Solving Equation (4-68) gives:

$$S(R_D) = C_1 \ln(R_D) + C_2 \quad (4-71)$$

Inserting boundary conditions from Equations (4-69) and (4-70) into Equation (4-68) results in  $C_2 = \ln(R_{De})$  and  $C_1 = -1$  and therefore;

$$S(R_D) = -\ln\left(\frac{R_D}{R_{De}}\right) \quad (4-72)$$

The steady state part of the dimensionless pressure equation is solved. The unsteady state part needs to be solved. But first its boundary and initial conditions need to be determined. Using the second part of Equation (4-64):

$$\begin{aligned} R_D \frac{\partial \Delta P_D}{\partial R_D} \Big|_{(R_D=1, t_D)} = -1 &\rightarrow R_D \frac{\partial (S + U)}{\partial R_D} \Big|_{(R_D=1, t_D)} = R_D \left( -\frac{1}{R_D} + \frac{\partial (U)}{\partial R_D} \right) \Big|_{(R_D=1, t_D)} \\ &= -1 \rightarrow R_D \frac{\partial (U)}{\partial R_D} \Big|_{(R_D=1, t_D)} = 0 \end{aligned}$$

Therefore;

$$R_D \frac{\partial (U)}{\partial R_D} \Big|_{(R_D=1, t_D)} = 0 \quad (4-73)$$

Inserting Equations (4-65) and (4-70) into Equation (4-67), gives:

$$\begin{aligned} \Delta P_D(R_{De}, t_D) = 0 = S(R_{De}) + U(R_{De}, t_D) = 0 + U(R_{De}, t_D) &\rightarrow U(R_{De}, t_D) = 0 \\ U(R_{De}, t_D) &= 0 \end{aligned} \quad (4-74)$$

Inserting Equations (4-66) and (4-72) into Equation (4-67), gives:

$$\begin{aligned} \Delta P_D(R_D, 0) = 0 = S(R_D) + U(R_D, 0) = -\ln\left(\frac{R_D}{R_{De}}\right) + U(R_D, 0) &\rightarrow \\ U(R_D, 0) = \ln\left(\frac{R_D}{R_{De}}\right) & \\ U(R_D, 0) = \ln\left(\frac{R_D}{R_{De}}\right) & \end{aligned} \quad (4-75)$$

Equations (4-73) and (4-74) are the boundary conditions for the unsteady state equation and Equation (4-75) is its initial condition.

Same as what has been done to solve the transient part of the pressure equation for linear flow, in here the concept of separation of variables is used to solve  $U(R_D, t_D)$ .  $U(R_D, t_D)$  can be shown to be a multiplication of two functions with one being dependent on time and the other dependent on space or radius.

$$U_D(R_D, t_D) = T(t_D)X(R_D) \quad (4-76)$$

By applying boundary conditions from Equations (4-73) and (4-74) to Equation (4-76):

$$U(R_D = 1, t_D) = 0 = T(t_D)X(1) \rightarrow T(t_D) = 0 \text{ or } X(1) = 0$$

$$U(R_{De}, t_D) = 0 = T(t_D)X(R_{De}) \rightarrow T(t_D) = 0 \text{ or } X(R_{De}) = 0$$

If  $T(t_D) = 0$  then  $U(R_D, t_D) = 0$  which is not of interest. Therefore;

$$X(R_D = 1) = 0 \tag{4-77}$$

$$X(R_{De}) = 0 \tag{4-78}$$

As  $U_D(R_D, t_D)$  is part of dimensionless pressure equation, so it should satisfy the dimensionless partial differential equation:

$$\frac{1}{R_D} \frac{\partial}{\partial R_D} \left( R_D \frac{\partial U_D}{\partial R_D} \right) = \frac{\partial U_D}{\partial t_D}, \quad t_D \geq 0, \quad 1 \leq R_D \leq R_{De} \tag{4-79}$$

Partial derivatives of  $U_D(R_D, t_D)$  with respect to time and space are:

$$\frac{1}{R_D} \frac{\partial}{\partial R_D} \left( R_D \frac{\partial U_D}{\partial R_D} \right) = T(t_D) \frac{1}{R_D} \frac{d}{dR_D} \left( R_D \frac{dX}{dR_D} \right) \tag{4-80}$$

$$\frac{\partial U_D}{\partial t_D} = X(R_D) \frac{dT}{dt_D} \tag{4-81}$$

Substitution of Equations (4-80) and (4-81) into Equation (4-79) gives:

$$T(t_D) \frac{1}{R_D} \frac{d}{dR_D} \left( R_D \frac{dX}{dR_D} \right) = X(R_D) \frac{dT}{dt_D} \tag{4-82}$$

If either of  $T(t_D)$  or  $X(R_D)$  is equal to zero then  $U_D(R_D, t_D)$  will be equal to zero which is not of interest. Therefore, both  $T(t_D)$  and  $X(R_D)$  are different from zero. If both sides of Equation (4-82) are divided by  $T(t_D) \times X(R_D)$ , it gives:

$$\frac{1}{R_D X(R_D)} \frac{d}{dR_D} \left( R_D \frac{dX}{dR_D} \right) = \frac{1}{T(t_D)} \frac{dT}{dt_D} \tag{4-83}$$

Sides of Equation (4-83) are independent of each other. The left hand side is dependent on location or radius and the right hand side is dependent on time. In order for Equation (4-83) to hold for any time and location, both sides should be equal to a constant. Sides can be equated to  $Y$ . Same arguments can be made about the sign of  $Y$  as before for the linear pressure diffusion equation. In here it can be shown that  $Y$

should be a negative value  $-\lambda^2$  for equation to hold. So equating both sides to  $-\lambda^2$  will give:

$$\frac{1}{T(t_D)} \frac{dT}{dt_D} = -\lambda^2 \quad (4-84)$$

Solving Equation (4-84) gives:

$$T(t_D) = Ae^{-\lambda^2 t_D} \quad (4-85)$$

In Equation (4-85), A is a constant.

$$\begin{aligned} \frac{1}{R_D X(R_D)} \frac{d}{dR_D} \left( R_D \frac{dX}{dR_D} \right) &= -\lambda^2 \rightarrow \frac{d^2 X}{dR_D^2} + \frac{1}{R_D} \frac{dX}{dR_D} + \lambda^2 X = 0 \\ \frac{d^2 X}{dR_D^2} + \frac{1}{R_D} \frac{dX}{dR_D} + \lambda^2 X &= 0 \end{aligned} \quad (4-86)$$

Equation (4-86) can be solved in maple as shown below:

$$\begin{aligned} dsolve \left( diff(diff(X(R), R), R) + \frac{1}{R} \cdot diff(X(R), R) + \text{lambda}^2 * X(R) = 0 \right) \\ X(R) = \_C1 \text{BesselJ}(0, \lambda R) + \_C2 \text{BesselY}(0, \lambda R) \end{aligned}$$

So the answer to Equation (4-86) is:

$$X(R_D) = C_1 J_0(\lambda R_D) + C_2 Y_0(\lambda R_D) \quad (4-87)$$

$J_0$  in Equation (4-87) is first kind of Bessel function of order zero and  $Y_0$  is second kind of Bessel function of order zero. To determine constants of the equation, boundary conditions from Equations (4-73) and (4-74) are applied to Equation (4-87):

$$\begin{aligned} R_D \frac{\partial(U)}{\partial R_D} \Big|_{(R_D=1, t_D)} = 0 &= R_D \frac{\partial(C_1 J_0(\lambda R_D) + C_2 Y_0(\lambda R_D))}{\partial R_D} \Big|_{(R_D=1, t_D)} \\ &\rightarrow R_D (-C_1 \lambda J_1(\lambda R_D) - C_2 \lambda Y_1(\lambda R_D)) \Big|_{(R_D=1, t_D)} = 0 \\ &\rightarrow C_1 J_1(\lambda) + C_2 Y_1(\lambda) = 0 \end{aligned}$$

$$C_1 J_1(\lambda) + C_2 Y_1(\lambda) = 0 \quad (4-88)$$

$$C_1 J_0(\lambda R_{De}) + C_2 Y_0(\lambda R_{De}) = 0 \quad (4-89)$$

Solving Equation (4-88) for  $C_2$  gives:

$$C_2 = -\frac{C_1 J_1(\lambda)}{Y_1(\lambda)}$$

Replacing above equation in Equation (4-89) gives:

$$\begin{aligned} C_1 J_0(\lambda R_{De}) - \frac{C_1 J_1(\lambda)}{Y_1(\lambda)} Y_0(\lambda R_{De}) = 0 &\rightarrow C_1 (J_0(\lambda R_{De}) Y_1(\lambda) - J_1(\lambda) Y_0(\lambda R_{De})) = 0 \\ \rightarrow C_1 = 0 \text{ or } J_0(\lambda R_{De}) Y_0(\lambda) - J_0(\lambda) Y_0(\lambda R_{De}) = 0 \end{aligned}$$

If  $C_1 = 0$ , it implies that  $C_2 = 0$  and as a result  $X(R) = 0$  which is not of interest. Therefore;

$$Y_1(\lambda) J_0(\lambda R_{De}) - J_1(\lambda) Y_0(\lambda R_{De}) = 0 \quad (4-90)$$

Knowing  $R_{De}$ , Equation (4-90) can be solved to get the value of  $\lambda$ . There are infinite numbers of  $\lambda$  that will satisfy this equation and they are called eigenvalues of this equation. Eigenvalues are represented as  $\lambda_n$ . For every  $\lambda_n$  there is a  $C_{1n}$ ,  $C_{2n}$  and as a result there is a  $X_n(R)$ :

$$C_{2n} = -\frac{C_{1n} J_1(\lambda_n)}{Y_1(\lambda_n)} \quad (4-91)$$

$$\begin{aligned} X_n(R_D) &= C_{1n} J_0(\lambda_n R_D) - \frac{C_{1n} J_1(\lambda_n)}{Y_1(\lambda_n)} Y_0(\lambda_n R_D) \\ &= C_n (Y_1(\lambda_n) J_0(\lambda_n R_D) - J_1(\lambda_n) Y_0(\lambda_n R_D)) \end{aligned} \quad (4-92)$$

As every  $X_n(R_D)$  is a solution for Equation (4-76), their summation is also a solution for Equation (4-76). Inserting Equations (4-85) and (4-92) into Equation (4-76) gives:

$$\begin{aligned} U_D(R_D, t_D) &= \sum_{n=1}^{\infty} C_n (Y_1(\lambda_n) J_0(\lambda_n R_D) \\ &\quad - J_1(\lambda_n) Y_0(\lambda_n R_D)) e^{-\lambda_n^2 t_D} \end{aligned} \quad (4-93)$$

Applying the initial condition from Equation (4-75) to Equation (4-93) gives:

$$\sum_{n=1}^{\infty} C_n (Y_1(\lambda_n) J_0(\lambda_n R_D) - J_1(\lambda_n) Y_0(\lambda_n R_D)) = \ln\left(\frac{R_D}{R_{De}}\right) \quad (4-94)$$

$C_n$  can be shown to be:

$$C_n = \frac{\pi J_0^2(\lambda_n R_{De})}{\lambda_n (J_1^2(\lambda_n) - J_0^2(\lambda_n R_{De}))} \quad (4-95)$$

Inserting Equation (4-95) into Equation (4-93) gives:

$$U_D(R_D, t_D) = \sum_{n=1}^{\infty} \frac{\pi J_0^2(\lambda_n R_{De})}{\lambda_n (J_1^2(\lambda_n) - J_0^2(\lambda_n R_{De}))} (Y_1(\lambda_n) J_0(\lambda_n R_D) - J_1(\lambda_n) Y_0(\lambda_n R_D)) e^{-\lambda_n^2 t_D} \quad (4-96)$$

Equation (4-96) is the final solution of the un-steady state part of pressure equation. Inserting Equations (4-72) and (4-96) into Equation (4-67) gives the final solution to pressure equation:

$$\begin{aligned} \Delta P_D(R_D, t_D) = & -\ln\left(\frac{R_D}{R_{De}}\right) \\ & + \sum_{n=1}^{\infty} \frac{\pi J_0^2(\lambda_n R_{De})}{\lambda_n (J_1^2(\lambda_n) - J_0^2(\lambda_n R_{De}))} (Y_1(\lambda_n) J_0(\lambda_n R_D) \\ & - J_1(\lambda_n) Y_0(\lambda_n R_D)) e^{-\lambda_n^2 t_D} \end{aligned} \quad (4-97)$$

Dimensionless pressure is defined as:

$$P_D(R_D, t_D) = \frac{P_i - P}{P_i - P_w|_{(steady\ state)}} \quad (4-98)$$

Wellbore flow rate at any time is constant and is equal to steady state flow rate. Steady state flow rate is:

$$Q = \frac{2\pi kh(P_i - P_w|_{steady\ state})}{\mu \ln\left(\frac{R_e}{R_w}\right)} \quad (4-99)$$

Inserting Equation (4-99) into Equation (4-62) gives:

$$\begin{aligned} \Delta P_D &= \frac{2\pi kh(P_i - P)}{\mu Q} = \frac{2\pi kh(P_i - P)}{\mu \frac{2\pi kh(P_i - P_w|_{steady\ state})}{\mu \ln\left(\frac{R_e}{R_w}\right)}} = \frac{P_i - P}{P_i - P_w|_{steady\ state}} \ln(R_{De}) \\ &= P_D \ln(R_{De}) \\ \Delta P_D &= P_D \ln(R_{De}) \end{aligned} \quad (4-100)$$

Inserting Equation (4-100) into Equation (4-97) gives:

$$\begin{aligned}
P_D \ln(R_{De}) &= -\ln\left(\frac{R_D}{R_{De}}\right) + \sum_{n=1}^{\infty} \frac{\pi J_0^2(\lambda_n R_{De})}{\lambda_n (J_1^2(\lambda_n) - J_0^2(\lambda_n R_{De}))} (Y_1(\lambda_n) J_0(\lambda_n R_D) \\
&\quad - J_1(\lambda_n) Y_0(\lambda_n R_D)) e^{-\lambda_n^2 t_D} \\
\rightarrow P_D &= 1 - \frac{\ln(R_D)}{\ln(R_{De})} \\
&\quad + \frac{\sum_{n=1}^{\infty} \frac{\pi J_0^2(\lambda_n R_{De})}{\lambda_n (J_1^2(\lambda_n) - J_0^2(\lambda_n R_{De}))} (Y_1(\lambda_n) J_0(\lambda_n R_D) - J_1(\lambda_n) Y_0(\lambda_n R_D)) e^{-\lambda_n^2 t_D}}{\ln(R_{De})} \\
P_D &= 1 - \frac{\ln(R_D)}{\ln(R_{De})} + \\
&\quad \frac{\sum_{n=1}^{\infty} \frac{\pi J_0^2(\lambda_n R_{De})}{\lambda_n (J_1^2(\lambda_n) - J_0^2(\lambda_n R_{De}))} (Y_1(\lambda_n) J_0(\lambda_n R_D) - J_1(\lambda_n) Y_0(\lambda_n R_D)) e^{-\lambda_n^2 t_D}}{\ln(R_{De})}
\end{aligned}$$

(4-101)

Equation (4-101) is the dimensionless pressure distribution across a circular finite reservoir with constant outer boundary pressure and constant wellbore flow rate. Equation (4-101) will be used in section 4.3. “Comparison of Numerical and Analytical Models” for validation of numerical results.

## 4.3. Comparison of Numerical and Analytical Models

### 4.3.1. Linear Fluid Flow with Constant Boundary Pressures

Figure 4-9 shows a sample before setting the pore pressure (a) and the same sample with pore pressure being set (b). The right hand side of the sample in (b) has no pore pressure, as its pore pressure is set equal to zero and will be kept at zero during fluid flow. The left hand side pressure will be kept constant at initial pressure. The sample

length is 14 meters, its height is 14 meters, and its width, which is an out-of-plane dimension, is equal to one meter. The sample length between the left boundary and the right boundary is 13.5 meters. Brown circles in Figure 4-9(b) show domain pressure.

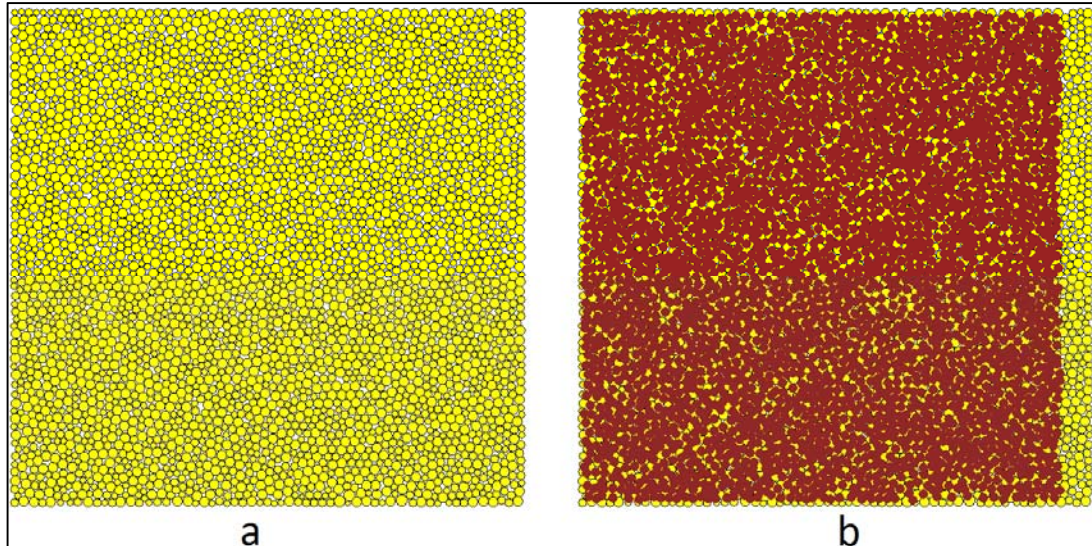


Figure 4-9: a) Sample. Each yellow circle shows a particle; b) Sample after setting pore pressure. Each brown circle shows the domain pore pressure. (Fatahi & Hossain, 2016)

Figure 4-10 shows the simulation results at four different times. Each point shows the pressure of a domain. The vertical axis shows pressure in Mega Pascals (MPa) and horizontal axes show the x and y position of the domain. The pressure at the left hand side is kept constant at initial pressure and pressure at the right hand side is kept constant at zero. At the beginning of simulation, flow rate on the left hand side is zero, as the pressure reduction wave has not reached it, and the flow rate on the right hand side is  $1.101 \times 10^{-3} \text{ m}^3/\text{s}$ . The flow rate quickly drops on the right hand side as the pressure on the right hand side starts to fall down. As soon as the pressure reduction wave reaches the left hand side, the flow rate on the left hand side starts to increase. The flow rate keeps increasing on the left and falling on the right until a steady state flow rate is established. At steady state conditions, the flow rate on both sides is equal to  $1.365 \times 10^{-3} \text{ m}^3/\text{s}$ . Figure 4-11 shows pressure distribution across the sample, with each point representing the pressure of its domain. At  $t = 15067 \text{ seconds}$  a steady state flow regime is established.

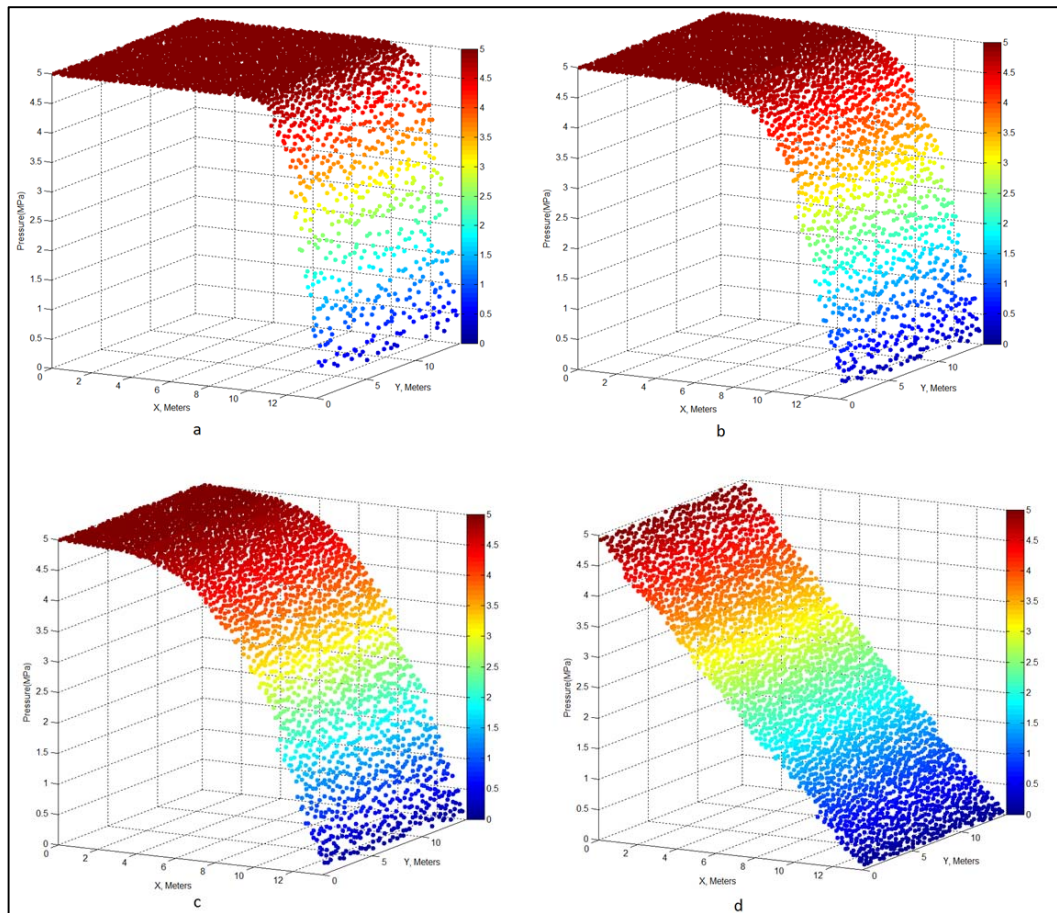


Figure 4-10: Simulation results at four different times; a:t=67 seconds, b:t=267 seconds, c:t=667 seconds and d:t=15067 seconds. (Fatahi & Hossain, 2016)

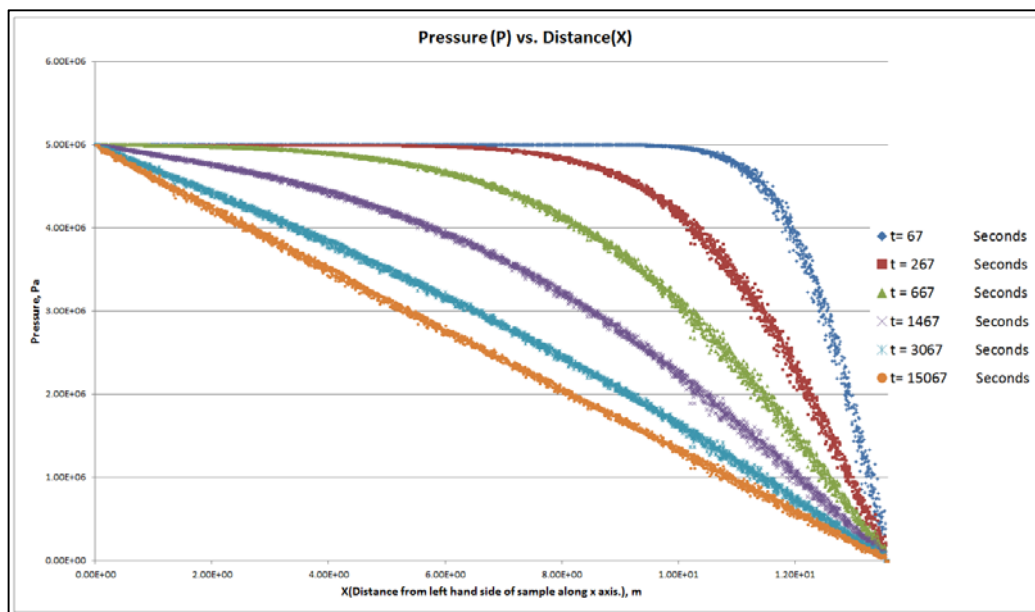


Figure 4-11: Simulation results. Pressure of domains against linear distance from left hand side of sample at different times. As time increases, domain pressures decrease until a steady state condition is established. (Fatahi & Hossain, 2016)

To make sure that the simulation results are correct, they are compared against the analytical results. To do so, data in Figure 4-11 are converted to a dimensionless form by using Equations (4-52) to (4-54).

Table 4-1: Parameters of Simulation at Steady State Condition. (Fatahi & Hossain, 2016)

Parameter	Metric System		Imperial System	
	$q$	$1.37E - 05$	$m^3/s$	$7.42E + 00$
$P_1$	$5.00E + 06$	$Pa$	$7.25E + 02$	$psia$
$P_2$	0	$Pa$	$0.00E + 00$	$psia$
$A$	14	$m^2$	150.69	$ft^2$
$\mu$	1	$Pa.Sec$	1000	$cp$
$L$	13.5	$m$	42.29	$ft$
$c$	$1.00E - 09$	$Pa^{-1}$	$6.90E - 06$	$psia^{-1}$
$\phi$	0.2	v/v	0.2	v/v

The permeability of the simulated sample can be obtained by using Darcy's equation for linear flow in steady state conditions, as given by Equation (4-102).

$$q = \frac{0.001127kA(P_1 - P_2)}{\mu L} \quad (4-102)$$

By inserting the values of different parameters from Table 4-1 into Equation (4-102), permeability is found to be  $2.67 \times 10^3 \text{ md}$ . To confirm that this is the correct value, another simulation has been conducted with a different initial pressure of  $8.00 \text{ MPa}$ . Steady state flow rate was  $2.18 \times 10^{-5} \text{ m}^3/\text{s}$ . The rest of the parameters were kept constant. By inserting new values for initial pressure and flow rate, permeability is calculated to be  $2.67 \times 10^3 \text{ md}$ , which is the same as the value calculated before. Dimensionless times and position are also inserted in (4-55) to compare simulated and analytical results. Equation (4-103) is the dimensionless time in field units. Table 4-2 shows simulation time in seconds and day, and calculated dimensionless time.

$$t_D = \frac{0.006336kt}{\phi\mu c_t L^2} \quad (4-103)$$

The units for different parameters are:

$k$ :  $\text{md}$

$t$ :  $\text{day}$

$\mu$ :  $\text{cp}$

$c_t$ :  $\text{psi}^{-1}$

$L$ :  $\text{ft}$

Table 4-2: Simulation time ( $t$ ) and Dimensionless Time ( $t_D$ ). (Fatahi & Hossain, 2016)

$t$ (Seconds)	$t$ (Day)	$t_D$
67	0.00078	0.00484
267	0.00309	0.01931
667	0.00772	0.04823
1467	0.01698	0.10608
3067	0.03550	0.22178
15067	0.17439	1.08951

Figure 4-12 shows the results of simulation in the dimensionless form compared with the analytical results. It shows that data from the simulation match very well with the analytical results, and validates the model for linear fluid flow.

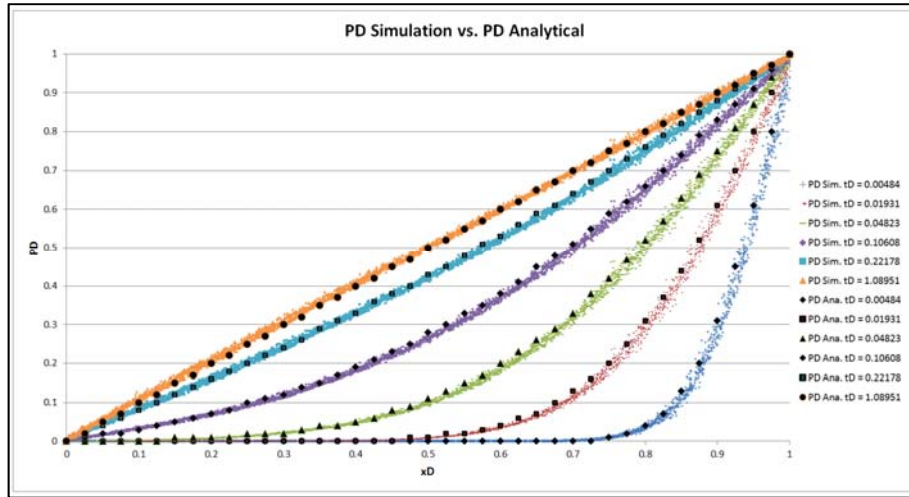


Figure 4-12: Simulated versus analytical results. Vertical axis shows dimensionless pressure and horizontal axis shows dimensionless position. On each curve coloured dots are simulation results and black dots are analytical results. (Fatahi & Hossain, 2016)

### 4.3.2. Radial Fluid Flow

Radial fluid flow is simulated for a reservoir with constant external boundary pressure and constant wellbore flow rate. Figure 4-13a shows the reservoir with wellbore in the centre. Figure 4-13b shows the reservoir with boundary pressure set. Pressure at distances more than external radius  $R_e$  is constant. The wellbore radius is  $R_w$  and the height of the reservoir which is an out-of-plane dimension is equal to one. Each brown circle represents the pore pressure of a domain which is kept constant at  $7\text{ MPa}$  at distances greater than external radius.

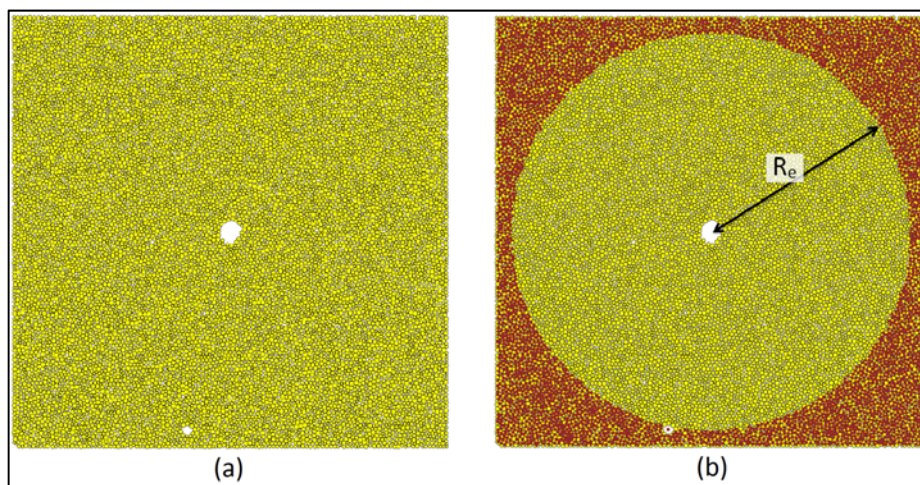


Figure 4-13: a) Reservoir with wellbore at centre; b) Reservoir with boundary pressure of  $7\text{ MPa}$ . Brown circles show domain pressure. (Fatahi & Hossain, 2016)

Figure 4-14 shows the reservoir with initial pore pressure set to 7 MPa. The initial and boundary pressures are equal.

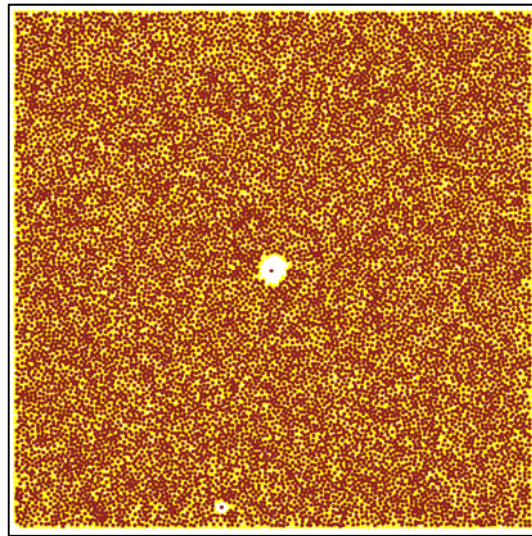


Figure 4-14: Reservoir with initial pore pressure set to 7 MPa. (Fatahi & Hossain, 2016)

Figure 4-15 shows simulation results within the external radius of the reservoir. Before starting production from the wellbore, the pressure across the whole reservoir is the same and equal to  $P_i$ . As production starts with a constant wellbore flow rate, pressure starts to decrease near the wellbore. As simulations continue, the pressure reduction wave propagates towards the outer boundary. Before pressure reduction arrives at the outer boundary, the flow rate at outer boundary is zero. As soon as the pressure reduces near the outer boundary, the flow rate starts to increase. The flow rate keeps rising until steady state condition is reached. At steady state condition, the outer boundary flow rate is equal to the wellbore flow rate.

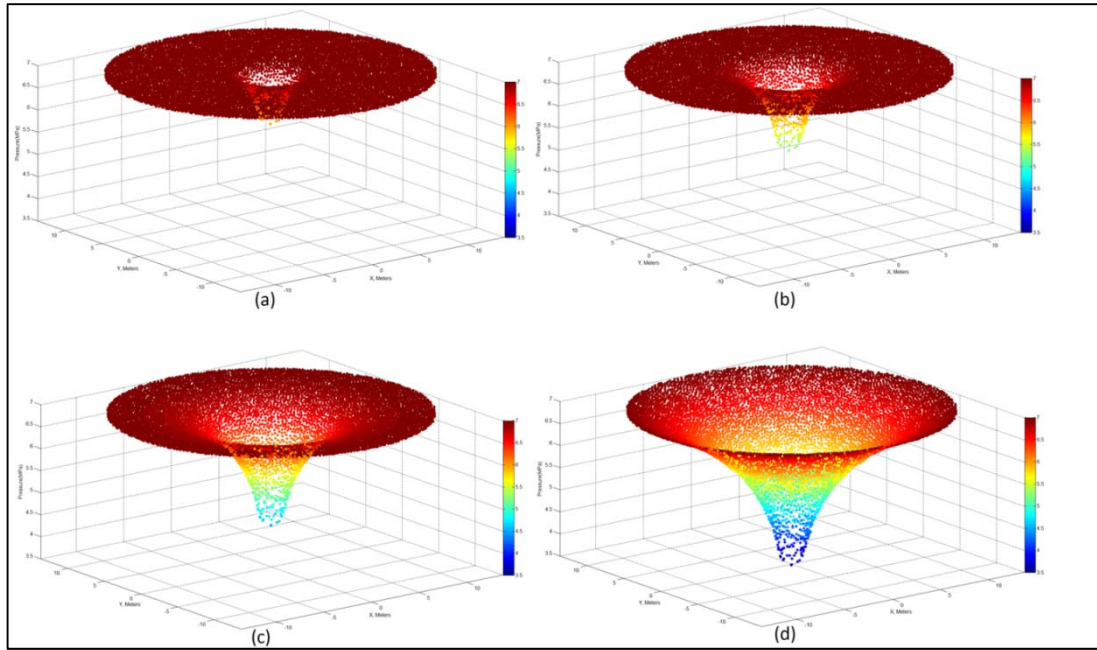


Figure 4-15: Simulation results at four different times; a:  $t=120.03$  seconds; b:  $t=420.03$ ; c:  $t=1420.03$  and d:  $t=24086.70$  seconds (Fatahi & Hossain, 2016)

Table 4-3 shows simulation parameters:

Table 4-3: : Parameters of Simulation (Fatahi & Hossain, 2016)

Parameter	Metric System		Imperial System	
$q$	$2.00E - 05$	$m^3/s$	$7.42E + 00$	$bbl/day$
$P_i$	$7.00E + 06$	$Pa$	$1.02E + 03$	$psia$
$P_e$	$7.00E + 06$	$Pa$	$1.02E + 03$	$psia$
$P_{w steady\ state}$	$3.49E + 06$	$Pa$	$5.06E + 02$	$psia$
$r_w$	$9.64E - 01$	$m$	3.16	$ft$
$r_e$	$1.38E + 01$	$m$	45.11	$ft$
$\mu$	1	$Pa.Sec$	1000	$cp$
$h$	1	$m$	3.28	$ft$
$c$	$1.00E - 09$	$Pa^{-1}$	$6.90E - 06$	$psia^{-1}$
$\phi$	0.2	v/v	0.2	v/v

At steady state condition, the wellbore pressure becomes constant and equal to  $3.49 \times 10^6 \text{ Pa}$  and is used to determine the permeability of the reservoir. Steady state radial flow in field units is:

$$Q|_{steady\ state} = \frac{0.00708kh(P_e - P_w)}{\mu \ln\left(\frac{R_e}{R_w}\right)} \quad (4-104)$$

The units for different parameters are:

$k: md$

$P: psia$

$\mu: cp$

$h: ft$

$R: ft$

Using Equation (4-104), permeability is found to be equal to  $2.44 \times 10^3 \text{ md}$ .

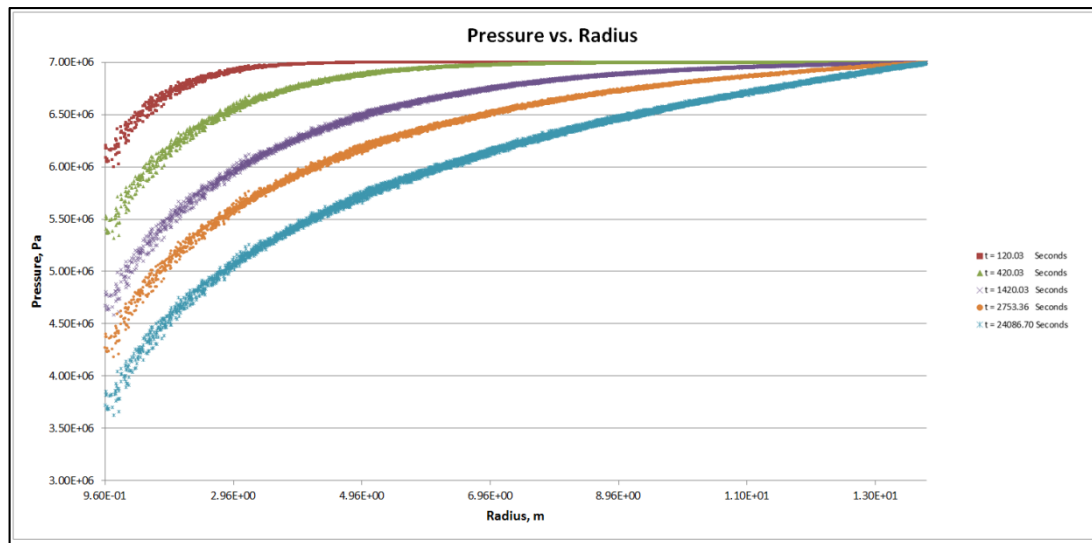


Figure 4-16: Simulation results of pressure vs. radius. (Fatahi & Hossain, 2016)

Figure 4-16 shows the simulation results of pressure versus radius. The vertical axis shows pressure in  $\text{Pa}$  and the horizontal axis shows the radius in meters. Each point shows the pressure of its domain versus the radial distance of the domain with respect to the wellbore centre. The figure shows that pressure at the outer boundary is kept constant, while the wellbore pressure keeps reducing until a steady state is

reached. To make sure that the simulated results are correct, they are compared against the analytical results. To do so, Equation (4-101) is used to find the dimensionless pressure versus the dimensionless radius. In this equation, dimensionless time is required, which is calculated by Equation (4-105):

$$t_D = \frac{0.000264kt}{\phi\mu c_t r_w^2} \quad (4-105)$$

The units for different parameters in Equation (4-105) are:

$k:md$

$t:hr$

$\mu:cp$

$c_t:psi^{-1}$

$r_w:ft$

Table 4-4 shows simulation time in the left column and calculated dimensionless time in the right column.

Table 4-4: Simulation time (t) and dimensionless time (t<sub>D</sub>). (Fatahi & Hossain, 2016)

<b>t(Seconds)</b>	<b>t<sub>D</sub></b>
120.03	1.67
420.03	5.84
1420.03	19.75
2753.36	38.29
24086.70	334.97

Equation (4-101) also requires values of  $\lambda_n$ , which are the roots of Equation (4-90). A plot of  $[Y_1(\lambda)J_0(\lambda R_{De}) - J_1(\lambda)Y_0(\lambda R_{De})]$  versus  $\lambda$  is drawn in Maple and is shown in Figure 4-17.  $R_{De}$  is equal to 14.26. It is evident from the graph that the values of the function approach zero very quickly as the value of  $\lambda$  increases. So to solve Equation (4-101), only the first few roots of the function will be sufficient to get acceptable results. This equation is solved in maple for first 50 roots. The values of  $\lambda$  are shown in Table 4-5:

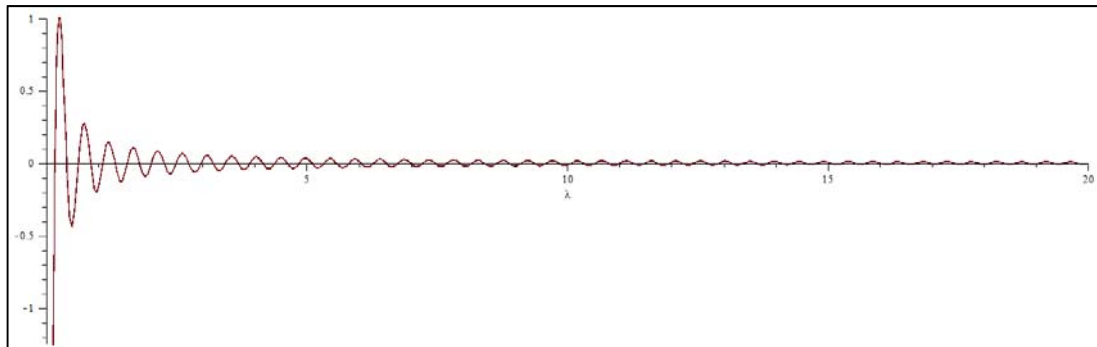


Figure 4-17:  $[Y_1(\lambda)J_0(\lambda R_{De}) - J_1(\lambda)Y_0(\lambda R_{De})]$  vs.  $\lambda$ . The function approaches zero very quickly as the value of  $\lambda$  increases. (Fatahi & Hossain, 2016)

Table 4-5: Values of first 50  $\lambda_n$ . (Fatahi & Hossain, 2016)

n	$\lambda_n$								
1	0.170	11	2.499	21	4.863	31	7.230	41	9.598
2	0.395	12	2.735	22	5.099	32	7.467	42	9.835
3	0.624	13	2.971	23	5.336	33	7.704	43	10.072
4	0.855	14	3.207	24	5.573	34	7.941	44	10.309
5	1.088	15	3.444	25	5.810	35	8.177	45	10.546
6	1.322	16	3.680	26	6.046	36	8.414	46	10.783
7	1.557	17	3.916	27	6.283	37	8.651	47	11.020
8	1.792	18	4.153	28	6.520	38	8.888	48	11.256
9	2.027	19	4.390	29	6.757	39	9.125	49	11.493
10	2.263	20	4.626	30	6.993	40	9.362	50	11.730

The simulation and analytical dimensionless pressures versus dimensionless radius are calculated and plotted in Figure 4-18. This plot shows that the simulation results match with the analytical results very well, and validates the applicability of the model for radial fluid flow.

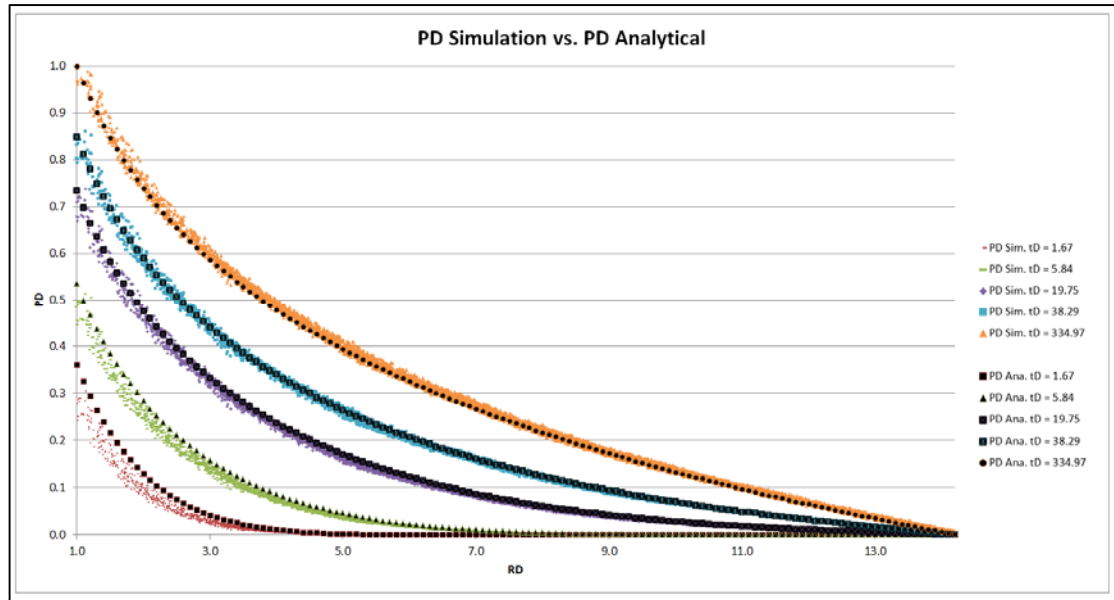


Figure 4-18: Simulated dimensionless pressure and analytical dimensionless pressure vs. dimensionless radius. (Fatahi & Hossain, 2016)

This chapter has presented the algorithm that was used to simulate fluid flow in the DEM based numerical model using PFC2D software. To validate the accuracy of simulation results, two scenarios of linear and radial fluid flow were considered. Analytical equations for these two scenarios were derived. The simulation results show very close agreement with the analytical results. Validation of fluid flow was an important step in the model development, as fluid flow and fluid–rock interaction are important components of hydraulic fracturing. The model developed from this chapter is used in the next chapter to simulate hydraulic fracturing initiation and breakdown pressure, as well as the hydraulic fracturing propagation path.

# 5

## Hydraulic Fracture Initiation Pressure, Breakdown Pressure and Propagation Path

Chapters 3 and 4 covered the validation of simulated rock's mechanical properties and fluid flow in rock samples. In this chapter the same procedure as described in previous chapters is used to prepare three samples to simulate two sandstones and one synthetic mortar sample. These three samples are then used to simulate hydraulic fracturing operation. Results of the simulation are compared against hydraulic fracturing in the laboratory for validation. The simulated hydraulic fracture initiation, breakdown and propagation path are validated. This chapter is based on the author's original paper "Numerical simulation for the determination of hydraulic fracture initiation and breakdown pressure using distinct element method" published in *Journal of Natural Gas Science and Engineering* (Fatahi, Hossain, Fallahzadeh and Mostofi; 2016).

### 5.1. Simulated Samples: Mechanical and Fluid Flow Properties

Simulated rock samples should exhibit the same mechanical properties as real samples. To calibrate the mechanical properties of simulated samples, a series of tests of uniaxial compressive strength and confined compressive strength were performed, as explained in Chapter 3. Simulated samples have a height of 95.25 mm and a width of 38.1 mm. These are the standard dimensions that were used for the real samples to testing their mechanical properties. In this simulation, the minimum particle radius was chosen as 0.3 mm and the ratio of maximum to minimum particle radius was 1.66. Simulated samples have two sets of mechanical properties. One set belongs to particles and bonds between particles, known as micro-mechanical properties. The second set is the mechanical properties of the bulk of the sample, which are called macro-mechanical properties. This is analogous to real rocks that are composed of grains. For example, a real sandstone rock is composed of sand

grains that are connected together by cement. Sand grains and cements have different mechanical and physical properties than sandstone. Grains have a density of 2.65 g/cc, while bulk density depends on porosity. To calibrate the macro-mechanical properties of the simulated samples, their micro-mechanical properties need to be adjusted. Table 5-1 shows the micro-mechanical properties of particles and bonds between particles. The macro-mechanical properties of the simulated rocks are presented in Table 5-2, and show close agreement with the experimental results. Simulation uses a seed number to generate random particles. To ensure the model results and to make sure that they are reproducible, a few simulations were performed. For each simulation the seed number was changed to generate simulated samples with different particle arrangements. The macro-mechanical properties of the samples generated based on different seed numbers were very close. The reported values in Table 5-2 are average of five simulation test results. Test plugs in different direction and from different parts of real samples were chosen for mechanical testing. The test results showed that the mechanical properties were the same in all directions and in all parts of the samples. This ensured that samples were homogenous and isotropic.

Table 5-1: Micro-mechanical properties of the samples (Fatahi et al, 2016)

Property	Unit	Value		
		Sandstone 1	Sandstone 2	Mortar
<i>Particle Young's Modulus</i>	<i>GPa</i>	11	5.5	18
<i>Particle Friction Coefficient</i>	---	0	0	0
<i>Particle Normal to Shear stiffness ratio</i>	---	1.5	1.5	0.9
<i>Parallel bond Young's Modulus</i>	<i>GPa</i>	11	5.5	18
<i>Parallel bond Normal Strength</i>	<i>MPa</i>	1000	800	1000
<i>Parallel bond moment contribution factor</i>	---	1	1	1
<i>Parallel bond cohesion strength</i>	<i>MPa</i>	51	30	60
<i>Parallel bond friction angle</i>	°	80	64	66
<i>Parallel bond normal to shear stiffness ratio</i>	---	1.5	1.5	0.9

Table 5-2: Mechanical properties of real and simulated samples (Fatahi et al, 2016)

Sample Type, ID	UCS (MPa)	Young's Modulus E (GPa)	Poisson's Ratio	Cohesion (MPa)	Internal Friction coefficient (°)
<i>Sandstone 1</i>	41.37	14.71	0.31	6.73	54
<i>Simulated Sandstone 1</i>	39.88	14.31	0.31	7.5	54
<i>Sandstone 2</i>	42.60	73.50	0.33	9.90	40.28
<i>Simulated Sandstone 2</i>	40.76	72.91	0.31	10.0	39.6
<i>Mortar</i>	79.50	27.70	0.2	17.40	44.3
<i>Simulated Mortar</i>	79	27.6	0.2	17	46

After preparing samples with the desired mechanical properties, the next stage is to set their fluid flow properties. In this stage, the porosity and permeability of the simulated samples should be matched against the porosity and permeability of real samples. In the laboratory these two parameters were measured on cylindrical dry samples. Samples were placed in a Helium Poro/Permeameter apparatus. The apparatus is capable of applying boundary pressure on the sample. Permeability was measured using the pulse decay method that uses helium as the flowing fluid. Using different pressures, it then extrapolated gas permeability versus reciprocal of pressure to calculate liquid permeability. Porosity was measured by the apparatus using Boyle's law. These parameters are reported in Table 5-3 for different samples.

Table 5-3: Flow rate, fluid viscosity, rock matrix permeability and rock porosity (Fatahi et al, 2016)

Sample Type, ID	Flow Rate (cc/min)	Viscosity (cp)	Permeability (md)	Porosity (%)
<i>Sandstone 1.1</i>	0.1	100000	3	20
<i>Sandstone 1.2</i>	0.1	100000	3	20
<i>Sandstone 2.5</i>	0.1	100000	0.40	12
<i>Sandstone 2.7</i>	0.1	100000	0.40	12
<i>Mortar</i>	0.1	100000	0.02	15

## 5.2. Simulation of Hydraulic Fracturing

The aim of this chapter is to investigate fracture initiation and breakdown pressure, fracture propagation with respect to the direction of minimum and maximum horizontal stresses, and comparison of results against laboratory results. Samples that were calibrated for their mechanical and fluid flow properties, as described in the previous section, are used again in this stage of the study. To simulate the borehole, particles in the centre of the sample were removed. The sample was then subjected to minimum and maximum horizontal stresses. The next stage is to inject fluid into the borehole and monitor the wellbore pressure versus time. At the beginning of the simulation, the fluid volume into the borehole is zero. At each time-step, a constant volume of fluid is added to the borehole to simulate a constant injection fluid flow rate. Also, at each time step, the fluid leak-off volume from the borehole into the sample is calculated. Compressibility equations are used to calculate pressure change in each time step. At each time step, the forces on particles because of pressure and boundary condition stresses are calculated. These forces will move particles with respect to each other. As the pressure rises, the borehole starts to expand. Particles at the borehole wall start to move away from each other. This puts the particle bonds under tensile and shear forces. Once the tensile or shear forces on bonds exceed the tensile or shear bond strength, these bonds will break. The first bond breakage between particles on the borehole wall corresponds to fracture initiation. Breakage of bonds one after each other corresponds to fracture propagation. At the initial state, the pressure inside the borehole and sample is zero. Fluid pressure inside the sample at top, bottom, left and right boundaries is kept constant at zero Pa. This is a drained test on a dry sample, and fluid can move out of the sample at each boundary.

The simulation process is shown in Figure 5-1 for Sandstone 1.1. Figure 5-1a shows the sample that is enclosed by four frictionless plates. These plates introduce the maximum and minimum horizontal stresses on the sample. These plates only interact with sample particles. They don't interact with each other and can move freely with respect to each other. Plates are controlled by a servo control mechanism that moves them toward or away from the sample to keep constant stresses on it. Figure 5-1b

shows the sample with a small vertical crack. On the right hand side in this figure, the picture is zoomed-in to show a better view of the crack. For incorporation of the crack, the bond between the particles is broken and replaced with a smooth joint bond that has no strength. Information about bonds between the particles is elaborated in PFC2D manual (Itasca, 2008). Figure 5-1c shows the start of fluid injection into the wellbore. The vertical axis shows the wellbore pressure in Pascals. The horizontal axis shows the time since the beginning of fluid injection. The blue circles show the normalized fluid pressure with biggest circle showing the highest pressure and smaller circles showing lower pressures. Figure 5-1d shows the fracture initiation with a closed up view at the right hand side. The fracture is shown as a red coloured line segment between two particles. The fracture initiates when the force on the particles pushes them away from each other and causes the bond between them to break. At this time the pressure starts to deviate from the linear trend. The reason for this deviation is that as the fracture initiates, the aperture of the parallelepiped between particles increases and fluid can easily flow through the parallelepiped away from wellbore and causes depressurization of the wellbore. Figure 5-1e shows the propagation of the fracture. It is seen from Figure 5-1e that even though the fracture has started, the pressure is still rising. This demonstrates that in this case, fracture breakdown and initiation pressures are different. Figure 5-1f shows the fracture breakdown pressure stage. This is the maximum pressure that the wellbore can experience. It should be noted that this is the pressure in the wellbore and not inside the fracture. The pressure inside the fracture is lower than the wellbore pressure. Figure 5-1g shows the stages where the fracture arrived at the top boundary (left), bottom boundary (right), and a zoomed-in view of the fracture and pressure profile at the bottom. It can be seen from the pressure profile that nearly one-fourth of the fracture at each side away from the wellbore has no fluid pressure. This is known as the fluid lag zone or the zone that the fracturing fluid has not penetrated yet.

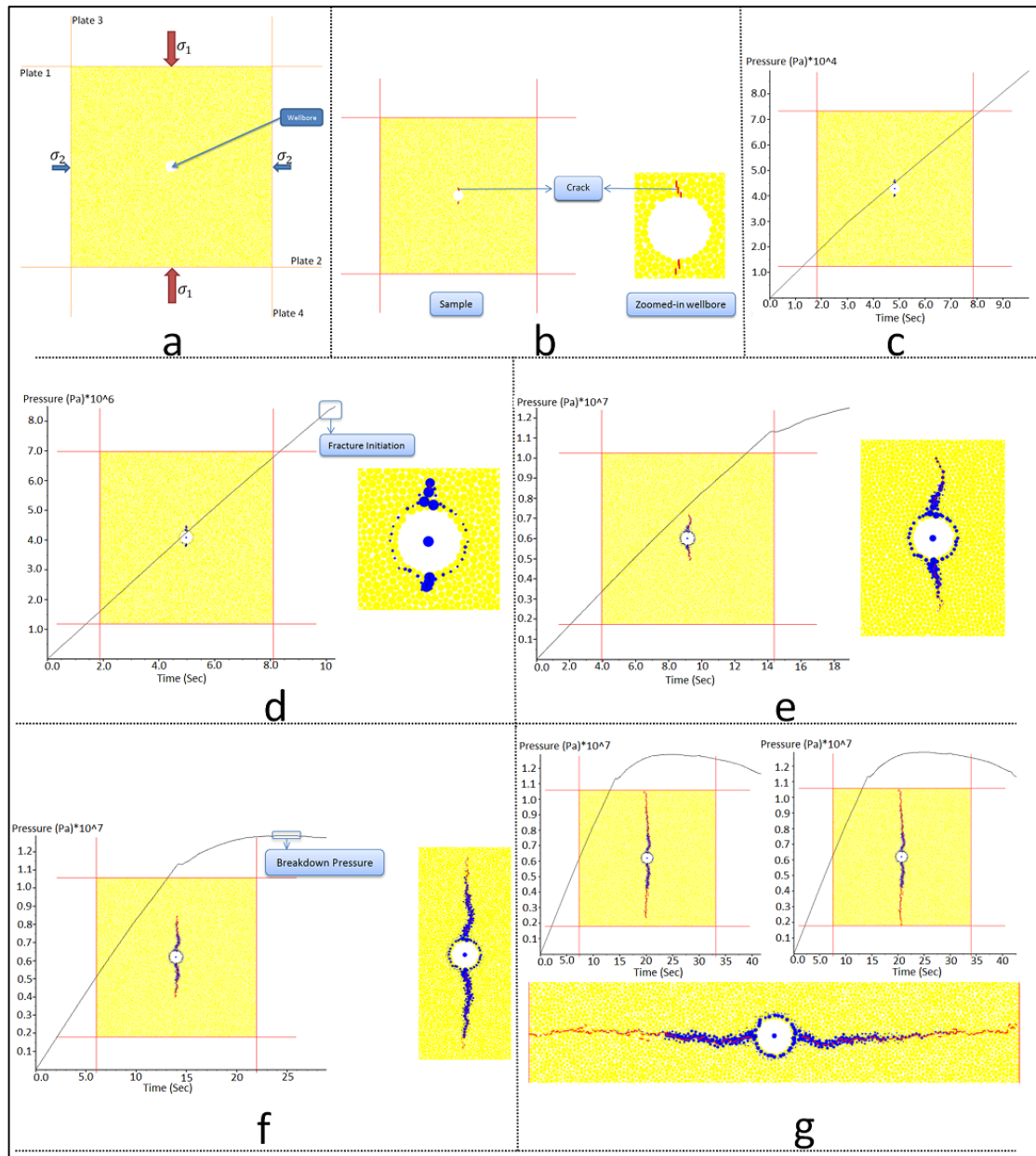


Figure 5-1: a-Sample with wellbore in the middle and four plates around it for stress installation. Horizontal maximum and minimum stresses are applied on the sample. b- Sample with vertical crack on left and zoomed in view at right. This represents the initial crack in the direction of maximum horizontal stress in Sandstone 1.1. C- Beginning of fluid injection into the wellbore. Blue circles show normalised fluid pressure with the biggest circle showing the highest pressure. The vertical axis shows the wellbore pressure and the horizontal axis shows time elapsed since the beginning of fluid injection. The black diagonal line shows pressure versus time. d- Onset of fracture initiation. The red line shows created fracture. The pressure profile starts to deviate from a linear trend with the creation of the first fracture. e- Fracture propagation. Bonds between particles break one after the other. f- Fracture breakdown pressure is the maximum pressure that the wellbore experiences. g- Fracture arriving at top boundary (left), arriving at bottom boundary (right), and zoomed-in view of fracture with pressure profile rotated 90° clockwise. (Fatahi et al, 2016)

Figure 5-2 shows the extended flow period after fracture arrived at boundaries. At this stage the volume of the fluid injected into the wellbore is equal to the volume of

fluid flow inside fracture and out of the sample. The rate of wellbore pressure drop was high at the beginning but it gradually decreased and becomes zero at steady state condition. At steady state condition, the wellbore pressure is equal to pressure required to keep the fracture open plus frictional pressure drop across the fracture. Because of the very low permeability of the sample and high fluid viscosity, the rate of leak off is very low but still considered to happen.

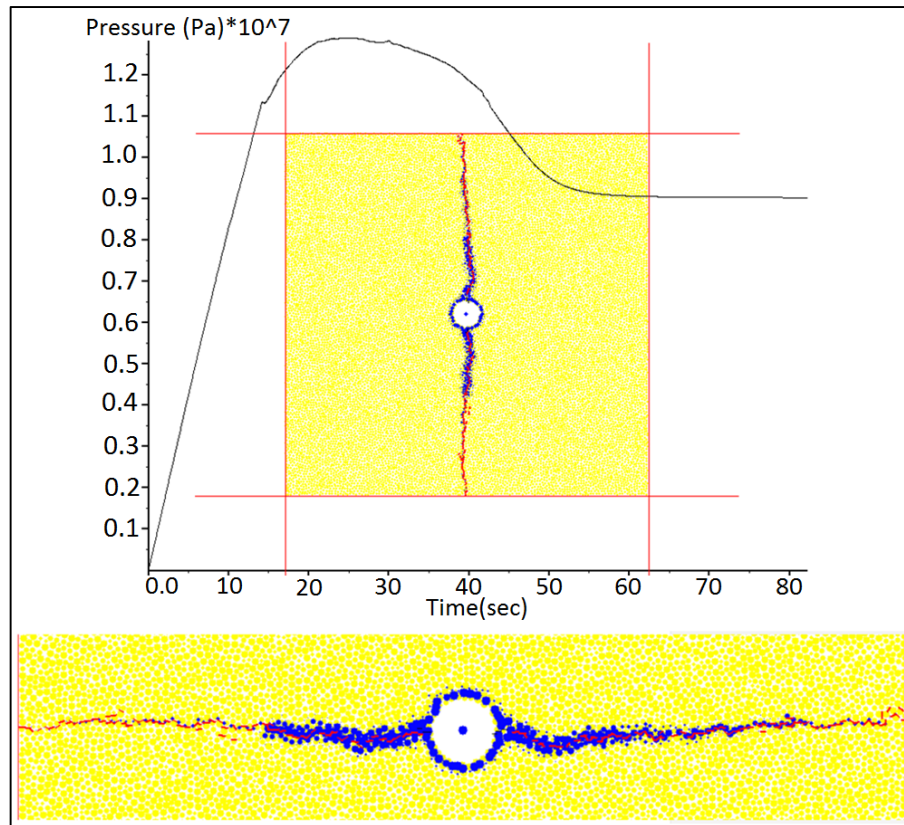


Figure 5-2: Stabilised flow through the fracture after the fracture arrived at the top and bottom boundaries. Pressure decline rate is high at the beginning when the fracture arrived at the boundaries. It gradually levelled off and got a constant value. The stabilised pressure value is equal to the pressure that is required to keep the fracture open, plus the frictional pressure drop inside the fracture. The bottom part of the figure shows the pressure profile inside the fracture. Bottom picture is rotated 90° clockwise. (Fatahi et al, 2016)

### 5.3. Laboratory Experiments

A rigorous experimental study was carried out in order to validate the simulation results. This study was carried out using True Tri-axial Stress Cell (TTSC). The experimental setup was developed based on the setup considered in a previous study conducted by Sarmadivaleh (Sarmadivaleh, 2012; Sarmadivaleh & Rasouli, 2014). Detailed information about equipment, sample preparation, mechanical property tests

and test procedure can be found in these references. A brief description of the equipment and test procedure is presented here.

Figure 5-3 shows a schematic view of the sample after preparation. A wellbore in the middle of one side of the sample was drilled all the way to the opposite side. The top part of the hole was plugged and the middle section was left open, with a vertical crack along the wellbore axis. The bottom part was cased using a steel pipe.

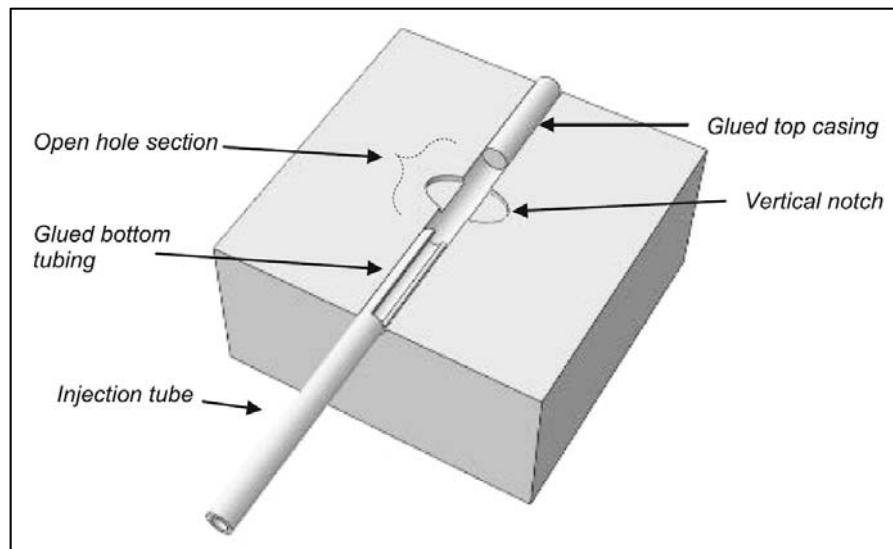


Figure 5-3: Schematic view of the sample showing the wellbore, top plug, bottom injection tubing and notch along the wellbore. (Sarmadivaleh & Rasouli, 2014)

Figure 5-4 shows a laboratory view of the TTSC equipment. The top part of the picture shows the whole apparatus. The bottom part of the picture shows the sample placement in the equipment. The sample is placed in the centre. Four spacers are placed between the sample and the loading plates. Loading plates are connected to loading rams. These rams will apply the horizontal stresses on the sample. Another spacer is placed on top of the sample. A hydraulic jack is then put on top of this spacer to apply the vertical stress on the sample. This configuration allows three independent stresses to be applied to the sample to simulate a realistic underground situation. The bottom part of the sample is connected to a pipe assembly. This pipe system is connected to a pump to inject fluid into the sample. Figure 5-5 shows the schematic view of the equipment configuration and sample placement. The top part of the figure shows the top view of the equipment. The bottom part shows the side

view. The injection line has two pressure transducers close to the wellbore. There is a check between these two transducers. These transducers are connected to a computer to record pressure versus time.

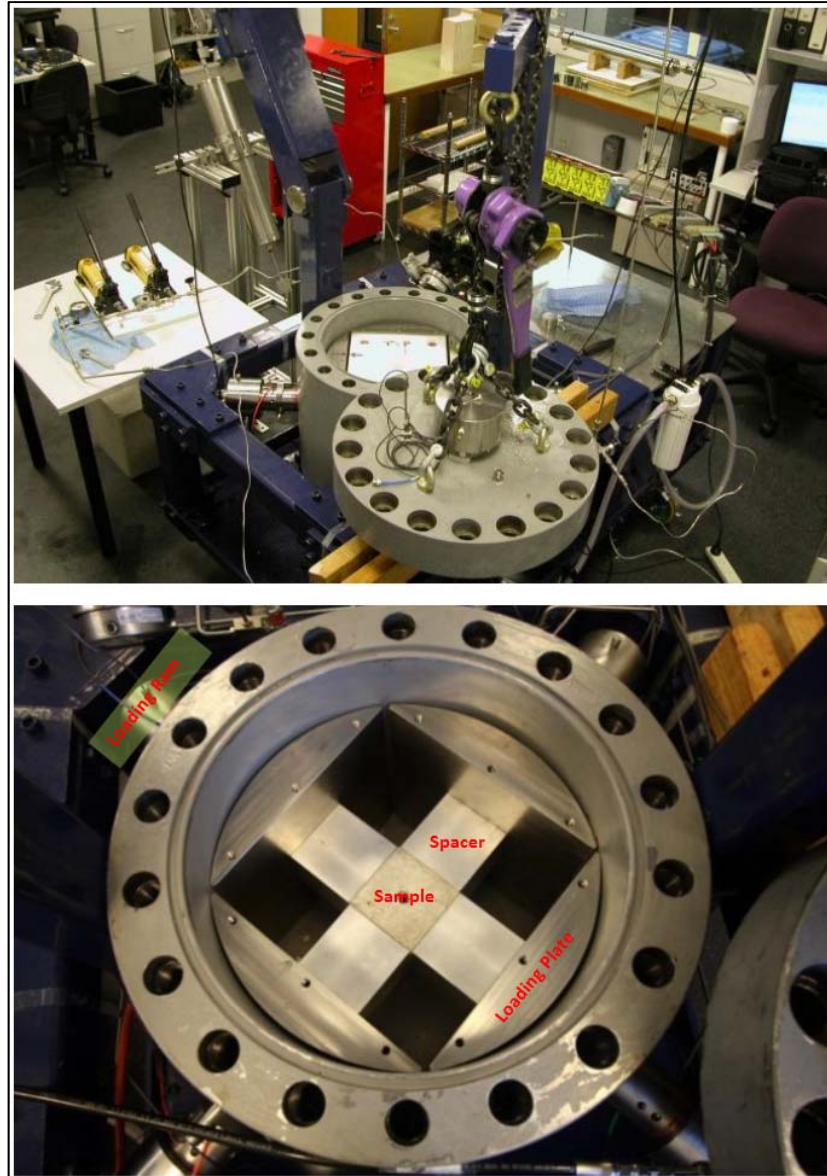


Figure 5-4: Laboratory picture of True Triaxial Stress Cell. The top view shows the whole apparatus. The bottom picture shows a 10 cm sample in the centre. Four spacers are placed between the sample and the loading plates. The loading plates are connected to loading rams. After (Sarmadivaleh, 2012)

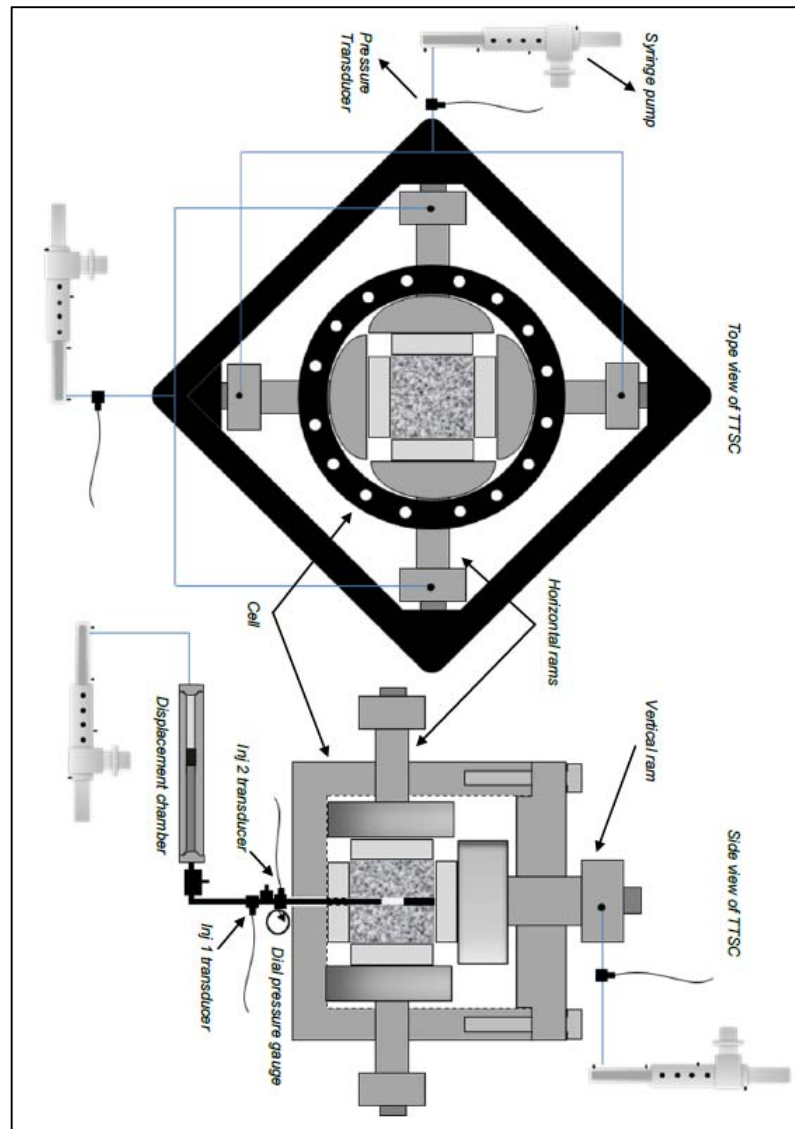


Figure 5-5: Schematic view of True Tri-axial Stress Cell. Top view of the apparatus is shown on the top. Side view of the apparatus is shown at the bottom. (Sarmadivaleh, 2012)

Figure 5-6 shows the cartoon representation of pressure-time profile of laboratory hydraulic fracturing. There are two red and blue curves showing the pressure versus time. The blue curve shows the pressure recorded by the pressure transducer represented as “Inj 2 transducer” in the bottom part of Figure 5-5. The red curve shows the pressure recorded by the pressure transducer represented as “Inj 1 transducer”. As shown in Figure 5-6, these two curves fall on each other before fracture initiation. The reason is that, before fracture initiation, the flow rate across the chock is negligible. As a result, the pressure drop across the chock is very small. During this stage, the fluid is being compressed in the system. Once the fracture initiates, extra volume is introduced to the wellbore volume that can receive fluid.

This causes a fluid flow across the chock and as a result, a pressure drop across it. This causes the two red and blue curves to separate by the amount of pressure drop across the chock. To help identify initiation pressure with more accuracy, the pressurisation rate is also plotted. Before initiation, the pressurisation rate is constant. After initiation, the pressurisation rate drops. The reason is that the fluid injection rate is constant, but the volume of the system is increasing. The wellbore pressure can still increase to a maximum value that can be different from the initiation pressure. This is known as “Breakdown Pressure.” Whether breakdown pressure and initiation pressure are the same or different will depend on the test parameters. These parameters are flow rate, fluid viscosity, stress state and so on. The difference between the two pressures has been analytically studied by Lakirouhani et al. (2008). At this pressure, the wellbore pressurisation rate is zero. After breakdown pressure, the wellbore pressure declines and the pressurisation rate gets a negative value. The wellbore pressure drops to a stabilised pressure. At this stage one or both wings of the fracture have arrived at the boundary. Stabilised pressure is the pressure that is required to keep the fracture open plus pressure drop across the fracture because of fluid flow. At this stage, the pressurisation rate is zero.

In the numerical simulation, a hydraulic fracture will always propagate in a horizontal direction because of the 2D limitation of the software. The created fracture is parallel to the wellbore axis. To simulate this situation in the laboratory, the vertical stress is greater than the horizontal stresses. This forces the created fracture to be vertical and propagate in the horizontal direction.

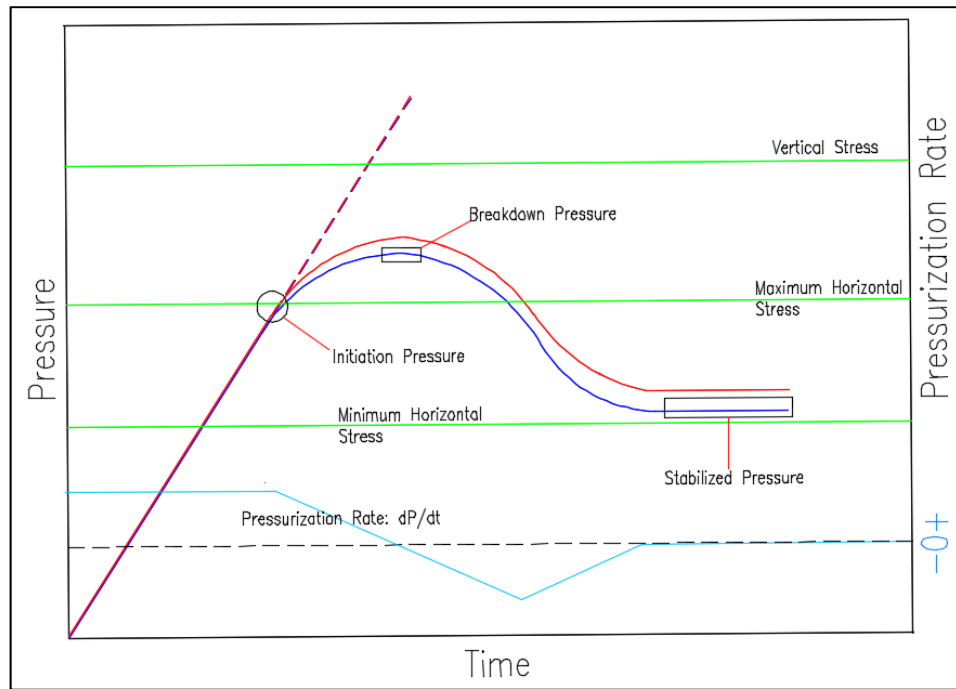


Figure 5-6: Hydraulic fracturing pressure profile. In the laboratory two pressure gauges are installed near the borehole with a chock between them. The blue curve shows the pressure from the gauge closest to the borehole. The red curve shows the pressure before the chock. Before fracture initiation, both curves fall on each other. During this time, the pressurisation rate is constant. After initiation, the pressurisation rate drops and the two red and blue curves separate. Breakdown pressure is the maximum pressure that the borehole experiences. (Fatahi et al, 2016)

Cubical samples of side lengths specified in Table 5-4 were prepared. This table also shows the wellbore diameter and wellbore section length. Table 5-3 shows fluid flow rate and viscosity as well as sample permeability and porosity. Lab experiments should properly represent field scale operations; therefore, dimensional analyses should be carried out and appropriate scaling laws should be followed. In order to develop the fracturing scaling laws, the fracturing mechanisms, which consist of different fracture propagation regimes, must be analysed. It is the various fracturing mechanisms through which the fracturing fluid energy is consumed. An unlimited number of fracturing mechanisms may exist in one specific fracturing process. However, one of these mechanisms would be the main energy dissipation source at one time, which is the main fracture propagation regime (Bunger, 2005). Considering the main propagation regime, fluid viscosity and injection rate and the fracture propagation time could be evaluated using the scaling laws. This requires knowledge of the sample and borehole sizes, as well as its hydro-mechanical properties. Further description of the process of running scaled hydraulic fracturing test can be found in

Fallahzadeh, James Cornwell, Rasouli and Hossain (2015). Table 5-5 shows the principal stresses and notch directions for each of the samples.

Table 5-4: Sample and wellbore dimensions (Fatahi et al, 2016)

Sample Type, ID	Sample Length (cm)	Sample Height (cm)	Sample Width (cm)	Wellbore Diameter (cm)	Wellbore Length (cm)
<i>Sandstone 1.1</i>	10	10	10	0.6	4
<i>Sandstone 1.2</i>	10	10	10	0.6	4
<i>Sandstone 2.5</i>	5	5	5	0.65	2
<i>Sandstone 2.7</i>	5	5	5	0.65	2
<i>Mortar</i>	10	10	10	0.7	4

Table 5-5: Principal Stresses and notch direction (Fatahi et al, 2016)

Sample Type, ID	$\sigma_v$ (MPa)	$\sigma_H$ (MPa)	$\sigma_h$ (MPa)	Notch status
<i>Sandstone 1.1</i>	17.93	13.79	6.89	In direction of $\sigma_H$
<i>Sandstone 1.2</i>	11.03	6.89	3.45	In direction of $\sigma_h$
<i>Sandstone 2.5</i>	10.34	0	0	No notch
<i>Sandstone 2.7</i>	10.34	6.89	3.45	In direction of $\sigma_H$
<i>Mortar</i>	20.68	13.79	6.89	In direction of $\sigma_H$

Figure 5-7 shows Sandstone 2.7 before and after hydraulic fracturing. Figure 5-7a shows the initial state of the sample. Figure 5-7b shows the sample with a wellbore drilled through it. A saw was used to create the initial crack along the wellbore axis. Figure 5-7c shows the sample with the injection pipe glued at the top. The bottom part was plugged by a piece of solid steel bar. Figure 5-7b & c show the state of stresses that were applied to the sample. Maximum horizontal stress was applied in the direction of the initial crack. Figure 5-7d, e & f show the sample after hydraulic fracturing. The hydraulic fracture was initiated and propagated in the direction of maximum horizontal stress.

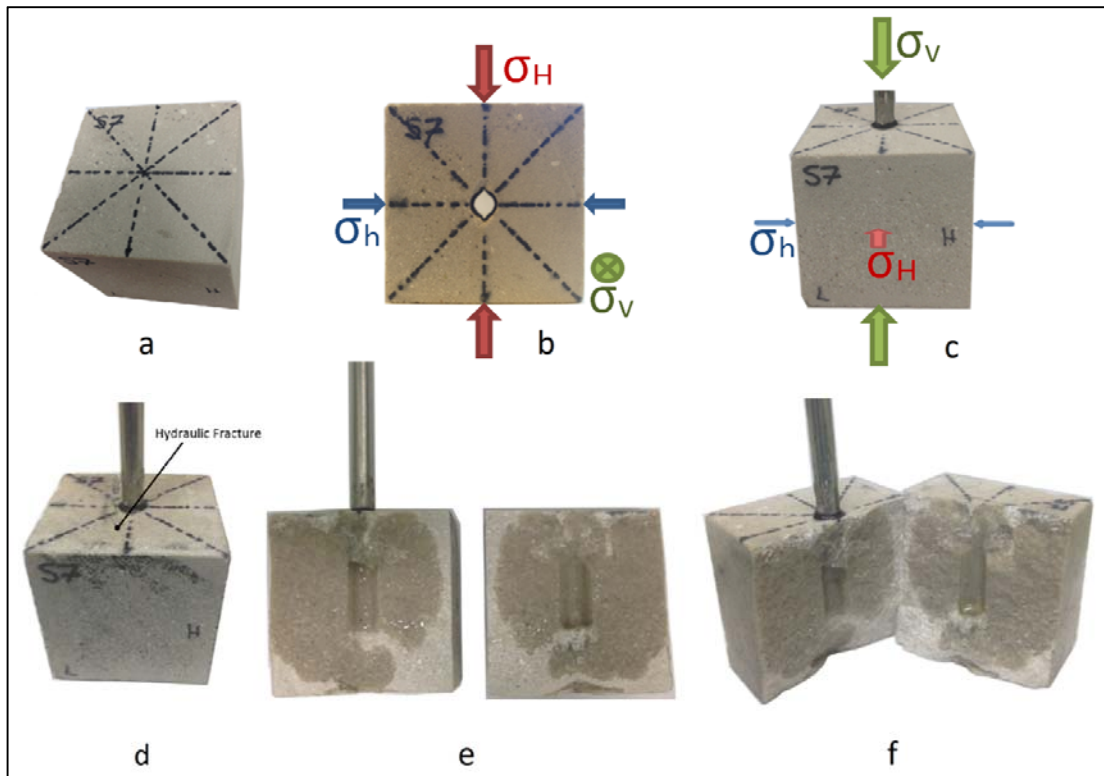


Figure 5-7: Sandstone 2.7. a) Prismatic sample; b) sample with hole drilled through and vertical notch; c) injection tubing glued to the sample; d, e, f) sample after hydraulic fracturing test. Figures b and c show the direction of principal stresses. The hydraulic fracture was created and propagated in the direction of maximum horizontal stress. (Fatahi et al, 2016)

Figure 5-8 shows other samples tested. As can be seen from Figure 5-8a, the left wing of the fracture has deviated from the direction of maximum horizontal stress for Sandstone 1.1. This can be due to the heterogeneous nature of the rock, as real rock samples are not homogenous. The right wing aligned itself very well in the direction of maximum horizontal stress. Figure 5-8b shows Sandstone 1.2. In this sample, the small initial crack is aligned in the direction of minimum horizontal stress, whereas the fracture initiated and propagated in the direction of maximum horizontal stress. As can be seen, the fracture is straight bi-wing with a small tortuosity along the path. Figure 5-8c shows Sandstone 2.5. This sample had no initial crack and no horizontal stress. Figure 5-8d shows a synthetic mortar sample. This sample has two slabs on each side that were cemented to the sample. The slabs were created similar to the main sample with the same composition. The small crack was in the direction of maximum horizontal stress, and a bi-wing fracture was created in the direction of the initial small crack.

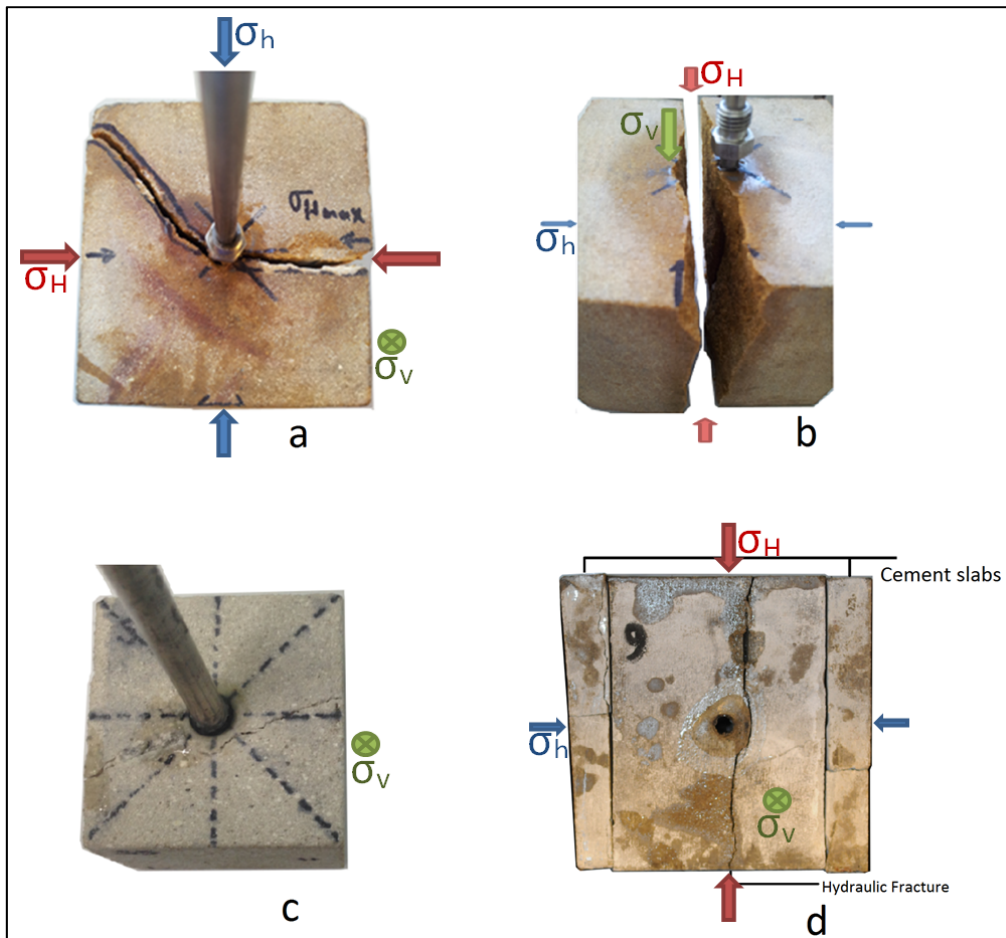


Figure 5-8: a- Sandstone 1.1; b- Sandstone 1.2; C- Sandstone 2.5; d- mortar sample. b and d show the hydraulic fracture aligned itself very well in the direction of  $\sigma_H$ . For Sandstone 1.1, one wing of the hydraulic fracture deviated away from  $\sigma_H$  direction. Sample 2.5 had no horizontal stresses. (Fatahi et al, 2016)

## 5.4. Comparison between Numerical Simulation and Experimental Studies

This section compares the experimental and numerical simulation results. The simulated results are close to the experimental results. These results are presented in Table 5-6. The percentage differences between the simulation and experimental results are calculated by subtracting the simulation results from the experimental results and dividing the difference by the experimental results and then multiply it by 100. Table 5-6 shows that differences are less than 10%. The smallest difference belongs to the mortar sample. The reason is that synthetic samples are more homogenous than real rock samples. The fluctuation for the experimental breakdown pressure for same samples under the same testing conditions is observed in many other studies (Asadi et al., 2012; Boyce et al., 1984; Gan et al., 2013; Haimson &

Fairhurst, 1969; Haimson & Huang, 1989; Haimson & Zhao, 1991; Lhomme, 2005; Martin, 1993; Rummel, 1987; Schmitt & Zoback, 1989; Zhao, 1995; Zhao et al., 1996; Zoback et al., 1977).

Figure 5-9 shows experimental and simulation pressure-time curves for Sandston 1.1 and 1.2. These rocks were tested in the early days that TTSC was installed. At the beginning, there was only one pressure transducer near the borehole. This is the reason that there is only one curve showing borehole pressure. At that time, the injection pump was manually controlled and the rate could not be controlled perfectly. Pressure fluctuations before breakdown pressure were a result of this issue. From these curves, the initiation pressures could not be inferred. Only the breakdown pressure, which is the highest pressure on the pressure-time curve, can be picked. These issues were remedied after these tests. Better pressure-time curves were recorded later, and are shown in Figure 5-10 and Figure 5-11. In Figure 5-9 a & c, the borehole pressure is shown in blue. The principal stresses are in green. Figure 5-9 b & d show the simulation pressure-time curve. In these figures, the state of the sample after hydraulic fracturing is shown. Figure 5-10 shows the test results for the mortar sample. This sample has been experimentally studied by Sarmadivaleh (Sarmadivaleh, 2012). As shown on the experimental plot, inferring the initiation pressure is not straightforward. So a different initiation pressure from what has been inferred by Sarmadivaleh (Sarmadivaleh, 2012) was picked up. The picked point is where the two dotted red lines cross each other. As shown on the plot, this is the time at which the difference between Inj1 and Inj2 pressures started to increase. Figure 5-10 and Table 5-6 show that experimental and numerical initiations and breakdown pressures are very close to each other. Figure 5-11 shows the test results for Sandstone 2.5 and 2.7. Figure 5-11 a & c show Inj1 and Inj2 pressure transducer results in red and blue respectively. Principal stresses are shown in green. Pressurisation rates are shown in cyan. The initiation point is where the two dotted lines cross each other. Figure 5-11c shows big fluctuations in the pressurisation rate after fracture initiation. This might be because of some noise in the pressure readings, and some disturbance at pressure transducer and PC connection points. Figure 5-11 b & d show the simulation test results for sandstones 2.5 and 2.7 respectively. It also shows the state of the simulated sample after the fracturing test.

Figure 5-11 shows the closeness of values for the numerical simulation and experimental test results.

The major difference between the simulated and experimental pressure-time curves is the short time for the simulated samples. The simulated test intervals are two orders of magnitude lower than the experimental test interval times. For the real samples, the injection system consists of the volume of oil in the injection pump and pipes, the volume of fracturing fluid in the fracturing fluid reservoir and pipes, and the volume of the wellbore. The volume of the wellbore is observed to be very small compared to the volume of the rest of the system. As the pressure builds up in the system, the oil and fracturing fluid will compress. Meanwhile the injection system that consists of pump, pipes and fracturing fluid reservoir, will expand. This compression and expansion causes an extra volume of fluid to be stored in the system. Once the fracture starts and reaches the boundary, it takes a long time for the whole system to depressurise. On the other hand, in simulation, the injection system only considers the volume of the wellbore. So the volume of the fluid that is stored in the injection system will be very small and will take only few seconds to depressurise. In this study, the focus was more on the fracture pattern and the initiation and breakdown pressures. To match the time of the simulated hydraulic fracturing with the experimental one, extra tests need to be carried out to calculate the exact volume of oil and fracturing fluid in the system, the volume of pumps and pipes, and establish the relationship between the expansion of the volume of the injection system and injection pressure.

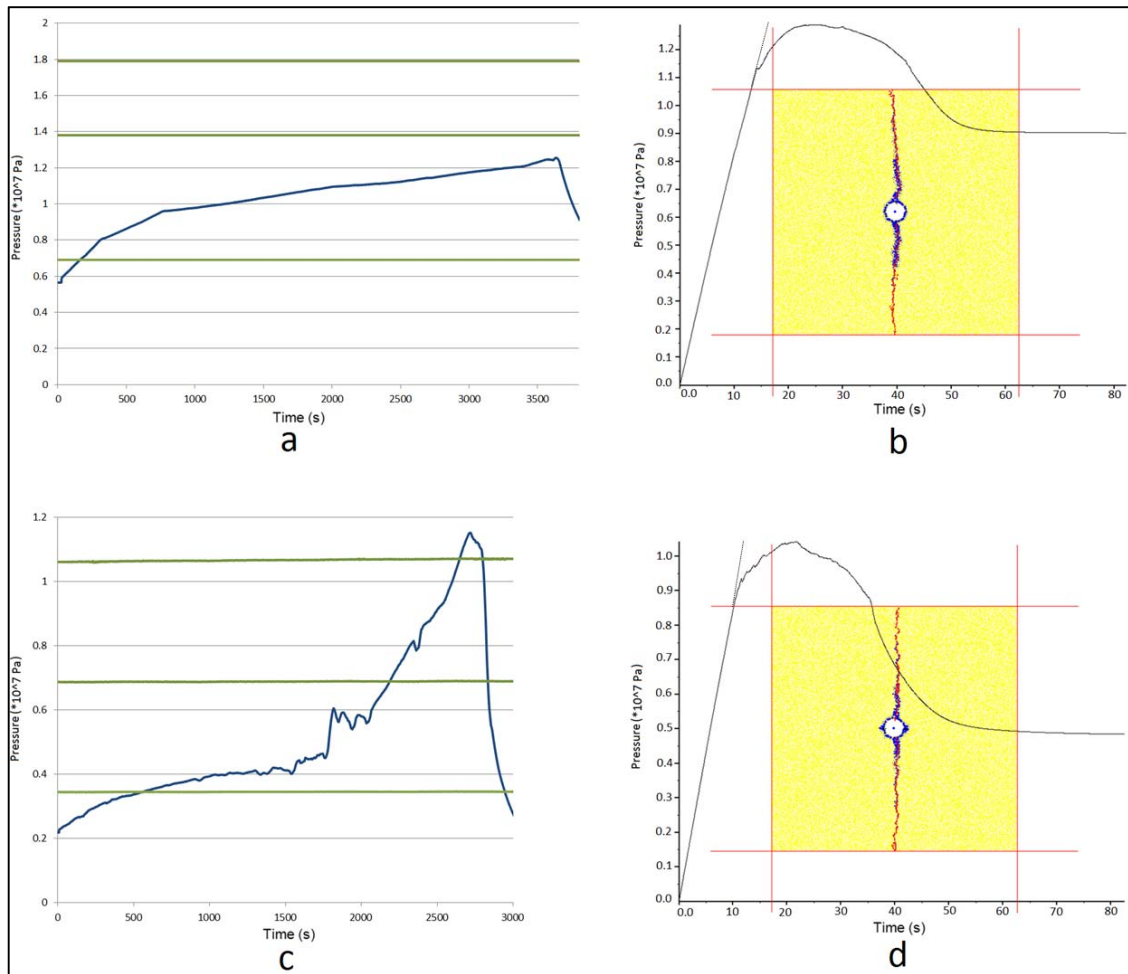


Figure 5-9: a- Experimental pressure vs time for hydraulic fracturing Sandstone 1.1; b- Simulated pressure vs time for hydraulic fracturing Sandstone 1.1; c- Experimental pressure vs time for hydraulic fracturing Sandstone 1.2; d- Simulated Pressure vs time for hydraulic fracturing Sandstone 1.2. For each sample, simulated and experimental breakdown pressure values are very close. In the experimental plots green curves show principal stresses. The blue curve shows borehole pressure. (Fatahi et al, 2016)

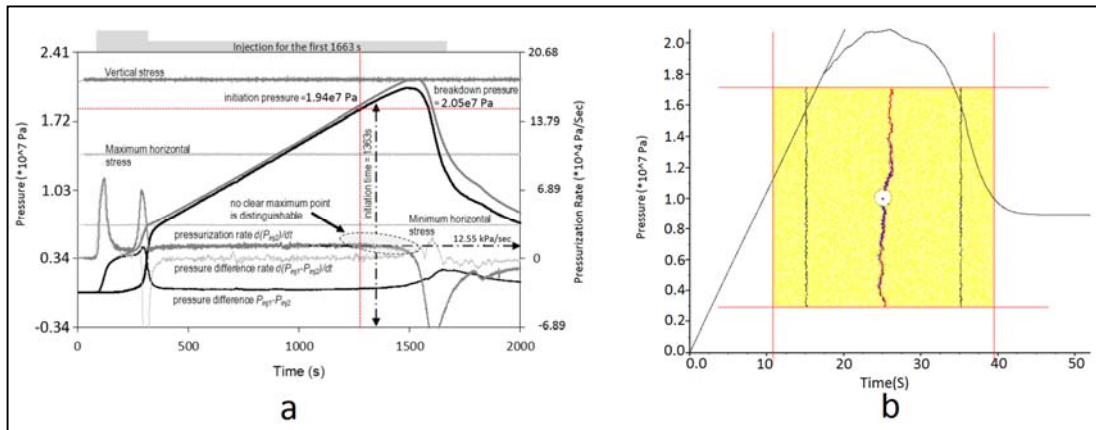


Figure 5-10: a- Experimental pressure vs time for hydraulic fracturing of mortar sample. After Sarmadivaleh (Sarmadivaleh, 2012); b- Simulated pressure vs time for hydraulic fracturing of mortar sample. Experimental and simulated initiation and breakdown pressures are very close. (Fatahi et al, 2016)

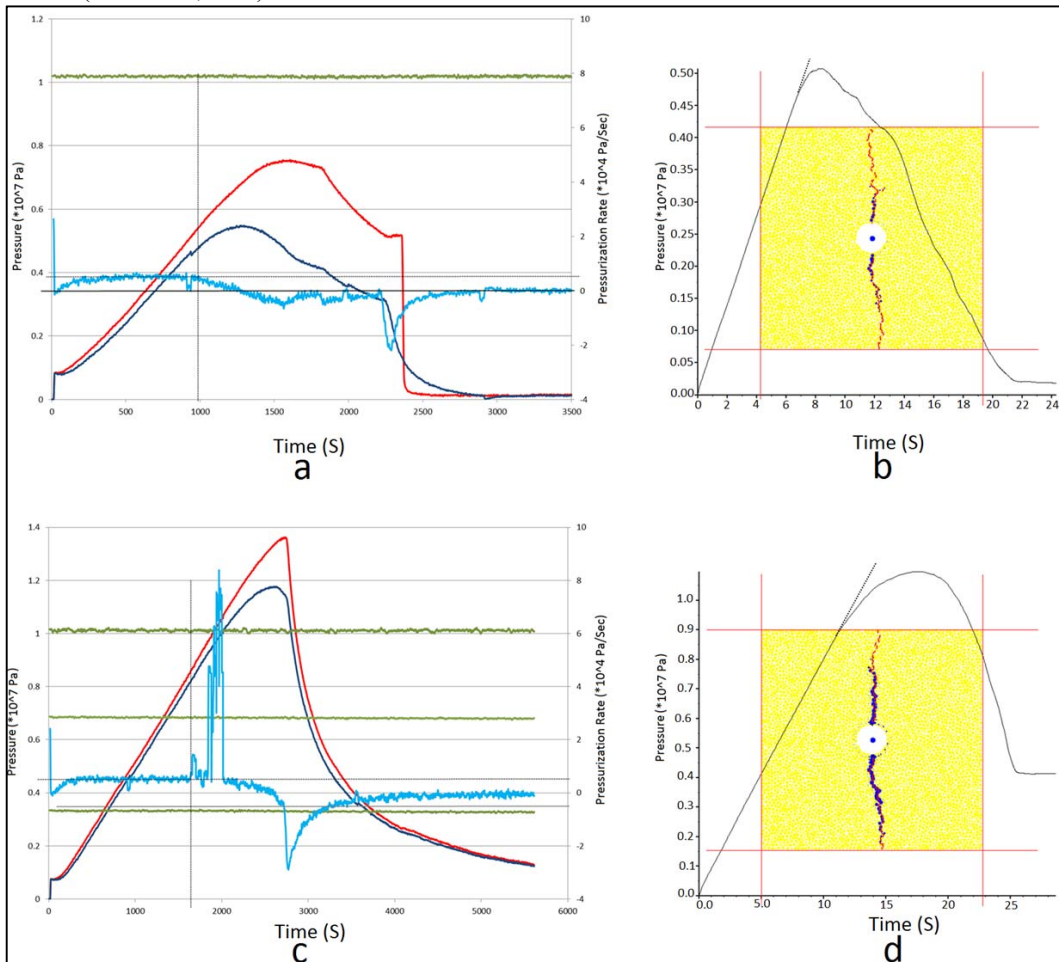


Figure 5-11: Pressure-time curve of hydraulic fracturing. a- Experimental pressure profile of Sandstone 2.5; b- Simulated pressure profile of Sandstone 2.5 c- Experimental pressure profile of Sandstone 2.7; d- Simulated pressure profile of Sandstone 2.7. In experimental plots, red and blue curves show pressure reading from Inj1 and Inj2 pressure transducers respectively. Green curves show principal stresses. Cyan curve shows pressurization rate calculated from Inj2 pressure transducer readings. (Fatahi et al, 2016)

Table 5-6: Experimental versus simulated initiation and breakdown pressures. (Fatahi et al, 2016)

Sample Type, ID	Simulated Initiation pressure (MPa)	Experimental Initiation Pressure (MPa)	% Difference	Simulated Breakdown pressure (MPa)	Experimental Breakdown Pressure (MPa)	% Difference
<i>Sandstone 1.1</i>	11.30	Not recognisable	---	12.91	12.50	-3.28
<i>Sandstone 1.2</i>	8.70	Not recognisable	---	10.44	11.51	9.30
<i>Sandstone 2.5</i>	4.54	4.66	2.58	5.09	5.48	7.12
<i>Sandstone 2.7</i>	8.90	8.1	-9.88	11.03	11.79	6.45
<i>Mortar</i>	18.0	18.3	1.64	20.91	20.55	1.75

This section presents the simulation model that was used to study the fracture initiation and breakdown pressure during hydraulic fracturing tests. It also describes the propagation path of the hydraulic fracture with respect to the principal stresses. The accuracy of the model was justified by comparing the simulation results with the experimental results. The model has the ability to overcome some of the limitations that prevail in existing analytical models, such as zero leak-off or ambiguity of the pressure profile inside the fracture. The conclusions of the current study are summarised below:

- The initiation and breakdown pressure are not necessarily the same. Once initiation occurs, the pressure can still increase to reach the breakdown pressure. In other words, the fracture breakdown pressure is generally higher to some extent than the fracture initiation pressure.
- Initiation pressure can be inferred from the plot of pressure–time and pressurisation rate–time plots.
- Once initiation occurs, the pressure–time plot deviates from a linear trend. The pressurisation rate decreases after initiation time.
- Breakdown pressure is the maximum pressure on the pressure–time plot.
- The pressurisation rate at breakdown time is zero.

- The fracture propagates predominantly in the direction of the maximum horizontal in-situ stress, provided the vertical stress is the maximum principal stress.

The model validated in this chapter is used in the next chapter to investigate the interaction mechanism between hydraulic and natural fractures. The simulation results will be validated through comparison with the experimental results.

# 6

## **Numerical and Experimental Investigation of the Interaction of Natural and Propagated Hydraulic Fracture**

Chapter 5 comprehensively discusses the numerical modelling of formation breakdown pressure, hydraulic fracture initiation and propagation, and demonstrates that the numerical model simulates hydraulic fracturing initiation and breakdown pressure as well as the fracture propagation path with great precision. This chapter describes the interaction of hydraulic and natural fractures using the developed simulation model. The simulation results are validated by comparison with experimental studies. The experimental results are found to be in very good agreement with the simulation results. The study demonstrates that the Distinct Element Method numerical model can be used as an alternative to laboratory experiments to investigate the interaction mechanisms of hydraulic and natural fractures with greater confidence. Both experimental and numerical simulation tests demonstrate that an increase in angle between the plane of a natural fracture and the direction of maximum horizontal stress increases the chance of a hydraulic fracture crossing the natural fractures. At low angles, a hydraulic fracture is most likely to be arrested at the plane of the natural fracture, and/or cause a shear slippage at the plane of the natural fracture. Natural fracture filling materials also have a great effect on the interaction mechanism. Weakly bonded natural fracture surfaces increase the chance of shear slippage occurring, and arrest the propagation of hydraulic fractures even at an angle of interaction as high as 90°.

The first part of the chapter describes how the simulation model is used to investigate the mechanism of the interaction between hydraulic and natural fractures. The second part of the chapter explains the experimental procedure and the laboratory tests of the interaction mechanism. In the last part, the simulation and experimental results are compared and discussed thoroughly. This chapter is based on the author's

original paper “Numerical and experimental investigation of the interaction of natural and propagated hydraulic fracture” published in *Journal of Natural Gas Science and Engineering* (Fatahi, Hossain and Sarmadivaleh; 2017).

## **6.1. Simulation of the Interaction of Hydraulic and Natural Fractures**

Interaction between hydraulic and natural fractures depends on many parameters. Among these parameters are: rock’s mechanical properties (e.g. Young’s modulus, Poisson’s ratio, Uni-axial compressive strength etc.); fracturing fluid properties (e.g. viscosity, leak-off properties, bulk modulus etc.); natural fracture properties (e.g. cohesion, friction, fracture orientations, fracture sizes etc); state of stresses (e.g. in situ stresses, deviatoric stresses, stress regime etc.); and the geometry of the fracture. Figure 6-1 shows a cartoon representation of the geometry of a simplified case that is normally studied in the laboratory. The same geometry is used in this study. In this figure, the wellbore is shown as a white circle in the middle of the sample with diameter “ $R$ ”. Two natural fractures are present above and below the wellbore at a distance of “ $b$ ” with lengths of “ $l$ ”. The hydraulic fracture is considered to be a bi-wing fracture, and is shown as two red triangles filled with orange. The angle between the hydraulic and natural fractures is considered to be  $(\pi/2 - \alpha)$ , where  $\alpha$  is the angle of the natural fracture with the direction of minimum horizontal stress. Sample lengths are shown as “ $a$ ”. Maximum and minimum horizontal stresses are shown respectively as “ $\sigma_H$ ” and “ $\sigma_h$ ”.

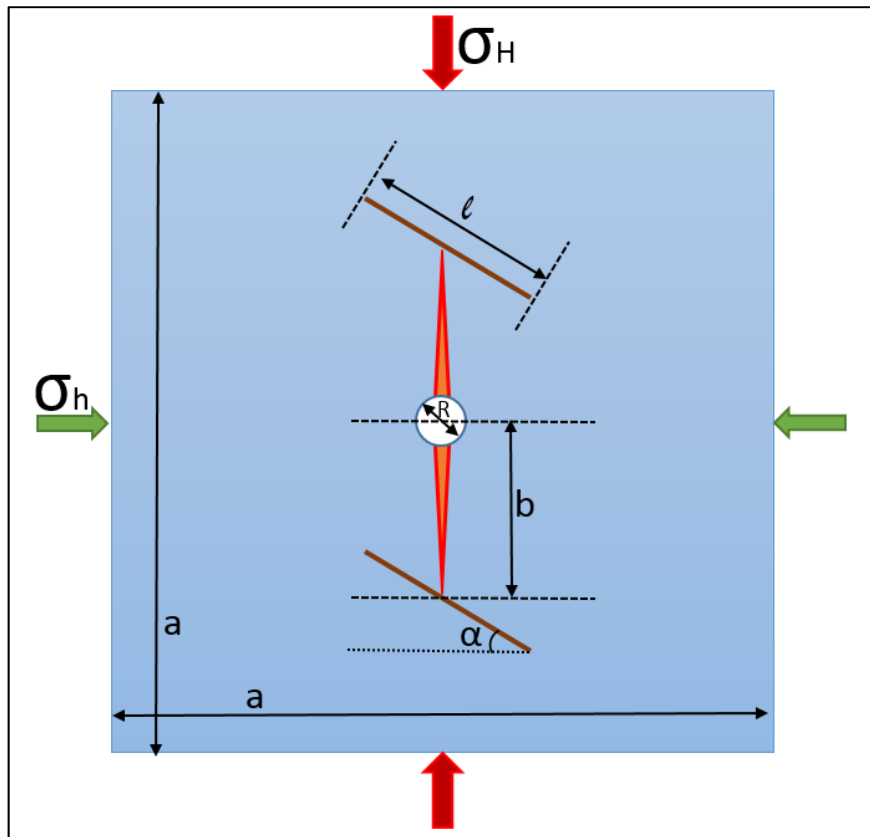


Figure 6-1: Geometry of a hydraulic and natural fracture interaction. a: Sample dimension; b: Natural fracture distance from centre of the wellbore; R: wellbore diameter; l: natural fracture size;  $\alpha$ : natural fracture angle;  $\sigma_H$ : Maximum horizontal stress; and  $\sigma_h$ : Minimum horizontal stress.

Figure 6-2 shows a simulated result of the interaction between hydraulic and natural fractures at  $90^\circ$  angles, and describes how a propagated hydraulic fracture may interact with the natural fracture and align with the direction parallel to the direction of minimum horizontal stress. Figure 6-2a shows the final result of simulation without showing the pressure. The wellbore is shown as white in the middle of the sample. The hydraulic fracture is shown as red dashed lines. The natural fracture is shown as black dashed lines. This figure demonstrates that the hydraulic fracture propagated in the direction of maximum horizontal stress, and crossed the natural fractures. Figure 6-2b shows the hydraulic fracture before it arrived at the natural fractures. Figure 6-2c shows that the lower wing of the hydraulic fracture arrived at the natural fracture. Figure 6-2d shows the final simulation result, with the pressure shown as blue circles with different sizes. The pressure circle sizes are normalised with respect to the highest pressure. The higher the pressure the bigger the circles are.

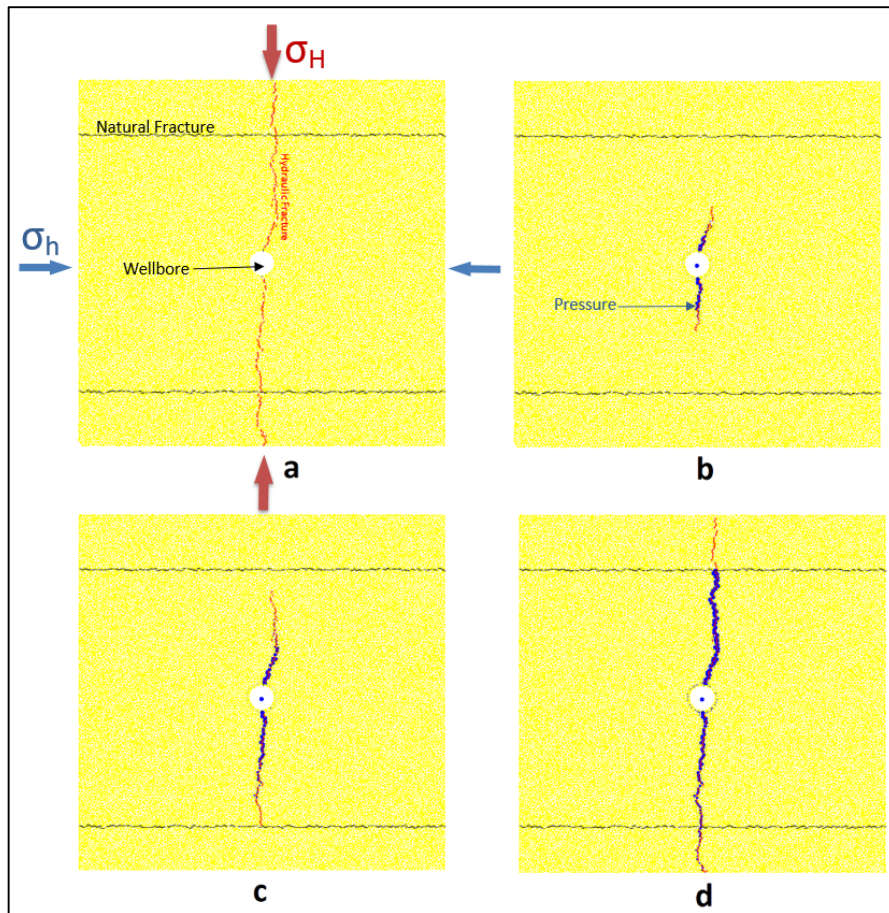


Figure 6-2: a) Sample in yellow colour. The natural fracture is shown as black dashed lines. The induced hydraulic fracture is shown as red dashed lines. The wellbore is shown as a white circle in the middle of the sample. b) Pressure is shown as blue circles. The larger the size of the circles the higher the pressure. The hydraulic fracture has not reached the natural fracture yet. c) The lower wing of the hydraulic fracture arrived at the natural fracture. d) Both wings of the hydraulic fracture have crossed the natural fractures. The hydraulic fracture propagated in the direction of maximum horizontal stress.

## 6.2. Experimental Studies

Synthetic mortar samples were considered for this study to make sure that the only heterogeneities in the samples are the synthetic natural fractures. Real samples may have some imperfections, such as hidden natural fractures or different grain diameters that can cause stress concentration. Stress concentration in one part of the sample can affect hydraulic fracture propagation and orientation, which consequently can affect test results.

A ratio of one to one was considered for sand and cement weight, and a weight percentage of 40% for water to cement ratio. Water, cement and sand were mixed for 15 minutes and poured into a mould that was sitting on a vibratory table. Vibration

intensity was controlled to make sure that there was no segregation of sand from slurry. Thin oil-coated galvanised steel plates were placed in the slurry that was poured into the mould in the desired location at the desired angle to create the natural fractures. The slurry was allowed to cure for 12 hours and then was removed from the mould, and placed in a water bath for 28 days. The water bath temperature was set at 25° C. Afterwards the samples were removed from the water bath; and were allowed to dry. The plates were then removed from the sample, and the sections that were separated by the plates were glued together using one of the two glues (white and brown) or cement slurry. These filling materials resemble the filling materials in the natural fractures (Sarmadivaleh, 2012).

Figure 6-3 shows two samples. The left sample has natural fractures of 90°, and the middle and right samples have natural fractures of 60° with respect to the anticipated hydraulic fracture propagation direction. A borehole is then drilled in the middle of the sample. One side of the hole was plugged by a solid steel rod. The middle part of the hole was left open, and the other side was cased by gluing a steel pipe. Once the samples were ready, they were placed (one at a time) in a True Triaxial Stress Cell (TTSC) that has the capability to impose three independent stresses on the sample to resemble vertical, minimum horizontal and maximum horizontal stresses. Fluid was then injected into the sample through a still pipe at a controlled rate to pressurise the borehole. This caused a fracture initiation and propagation and eventually interaction with the pre-existing synthetic natural fractures. To get the mechanical properties of the sample, samples with similar composition and similar preparation procedures were created. Then cylindrical plugs were removed from them. Uniaxial and tri-axial tests were conducted to drive the mechanical properties of the samples. The porosity and permeability of the samples were measured on cylindrical plugs in the Poro/Permeameter apparatus. Boyle's law was used for porosity measurement and the Pulse decay method was used for permeability measurements. Helium was used as the flowing fluid in these measurements. These properties as well as the shear properties of the glues used are shown in Table 6-1. The shear strength of the glues was determined by the manufacturer by a sandblasted aluminium lap shear test, and the shear property of the cement was determined by a direct shear test in the laboratory.

Table 6-2 shows the mechanical properties of the synthetic and simulated samples. Further details regarding the experimental study can be found in (Fatahi et al, 2016; Sarmadivaleh, 2012; Sarmadivaleh & Rasouli, 2015).

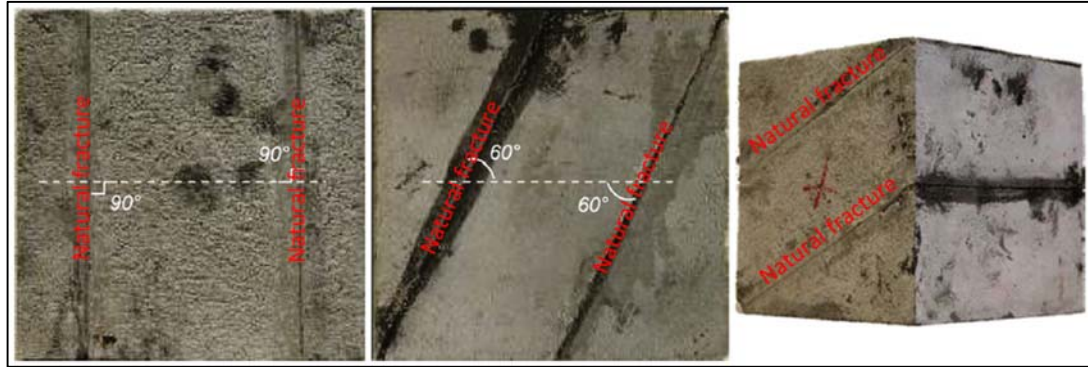


Figure 6-3: Two 10 cm samples with 90° (left) and 60° (middle and right) natural fractures with respect to the anticipated hydraulic fracture direction. (Sarmadivaleh & Rasouli, 2015)

Table 6-1: Hydro-mechanical properties of synthetic sample and natural fracture filling materials. (Sarmadivaleh, 2012)

Hydro-mechanical property	Value		Test method
Uni-axial compressive Strength, UCS psi (MPa)	11,530 ± 750 (79.5)		Unconfined compression test
Uni-axial poisson's ratio, $\nu$	0.197 ± 0.02		Unconfined compression test
Young's modulus, E, psi (GPa)	4.018 × 10 <sup>6</sup> ± 2 × 10 <sup>5</sup> (27.74)		Unconfined compression test
Internal friction coefficient, $\Phi$ (degrees)	44.3		Mohr circle, confined test
Cohesion, C <sub>c</sub> psi (MPa)	2524 (17.3)		Mohr circle, confined test
Tensile strength, T <sub>0</sub> , psi (MPa)	510±200 (3.5)		Brazilian tensile test
Fracture toughness, K <sub>IC</sub> , psi √in (MPa√m)	710±200 (0.78)		CSB
Natural interface shear Strength, $\tau_0$ , psi (MPa)	cement	290 (2)	*sandblasted aluminium lap shear test, Provided by manufacturer
	Brown glue	*70(0.5)	
	Black glue	*145(1)	
	White glue	3370 (26)	
Natural interface friction, $\mu_f$	0.698±0.006		Direct Shear Test
Porosity, $\Phi$ %	14.7±1		Two Boyle's cells
Permeability, K mD	0.018±0.005		Transient gas flood

Table 6-2: Synthetic and simulated sample mechanical properties

Sample Type, ID	UCS (MPa)	Young's Modulus E (GPa)	Poisson's Ratio	Cohesion (MPa)	Internal Friction coefficient ( $^{\circ}$ )
<i>Mortar</i>	79.50	27.70	0.2	17.4	44.3
<i>Simulated Mortar</i>	79	27.6	0.2	17	46

To perform an aluminium lap shear strength test, two aluminium plates of 2 in. width are overlapped 0.5 in. on each end of the plates and are epoxied together, as illustrated in Figure 6-4a. These two plates are then pulled apart in a direct tension test to evaluate the maximum shear strength that epoxy can tolerate. By knowing the area of the epoxied surface, the shear strength of epoxy is calculated by dividing the shear force by the shear surface area. Figure 6-4a shows the schematic view of the two aluminium plates that are epoxied together for the lap shear test. Figure 6-4b shows a simulated sample, prepared to perform an aluminium lap shear test. The contact strength between the particles in each of the top and bottom plates is set very high so that the plates do not fail under tensile force. The contact type between the particles of the top and bottom plates is set as a smooth joint model. The smooth joint contact properties are then adjusted to match its shear strength against the shear strength of cement and glues.

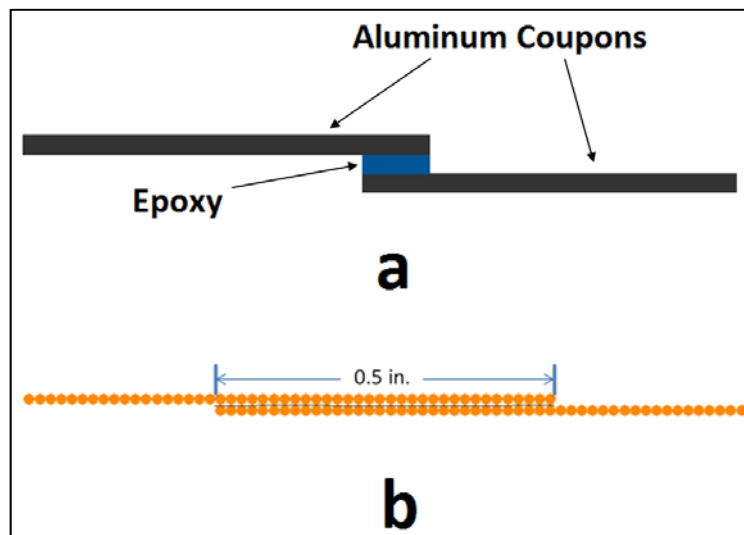


Figure 6-4: a) schematic view of the aluminium plates epoxied together (Technology, 2016); b) Simulated sample for aluminium lap shear strength test.

Figure 6-5a shows the schematic view of the plates and how they are pulled apart. Tensile force is increased linearly and is plotted against time. The maximum recorded force is then divided by the area of the epoxied section to calculate the shear strength of the epoxy. Figure 6-5b shows the simulated sample under a direct tension test. The tensile force is applied to the last particle on top and the bottom particle is fixed. The horizontal axis shows time and the vertical axis shows applied force. Force is slowly increased in a linear fashion until failure occurs. The value of the force at failure is then divided by the epoxied area to get the shear strength of the bonded section. Micro-mechanical properties of the smooth joint model are adjusted to reproduce the shear strength of the epoxy. For detailed information about the smooth joint model and its micro-mechanical properties, please refer to the PFC2D manual (Itasca, 2008).

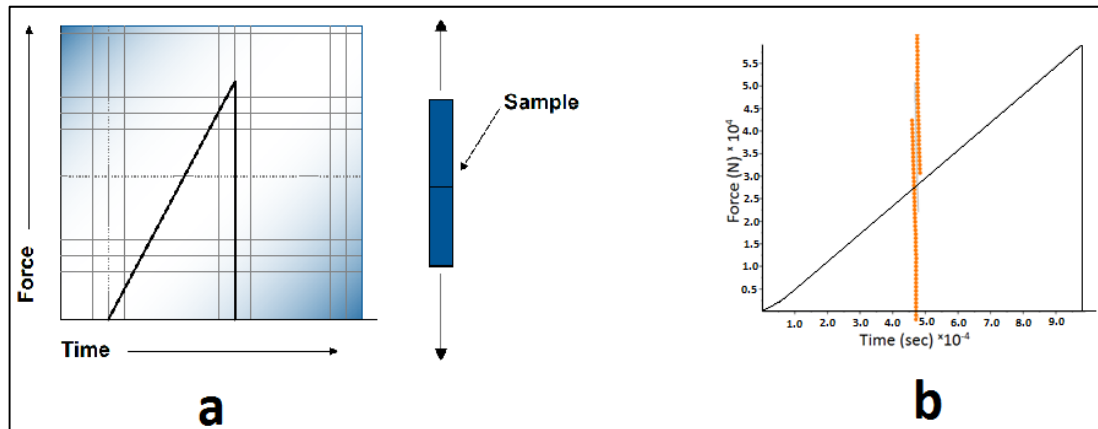


Figure 6-5: a) Schematic view of the sample and plot of Force versus Time. (Technology, 2016).  
b) Simulated sample under tension and its Force-Time relationship. At failure the tensile force will drop suddenly to zero value. The value of tensile force at failure is divided by the epoxied section's area to calculate the shear strength of the epoxy.

### 6.3. Results and discussion

This section presents the results of the interaction mechanism between the induced hydraulic fracture and natural fractures. Simulated results are compared with experimental results for the different interface filling materials and different interaction angles between natural and propagated hydraulic fractures. Note the term “angle,” especially in this section, will refer to the angle between the propagated hydraulic fracture and the natural fracture.

Figure 6-6 shows the results for the interaction angle of  $90^\circ$ . In this test, the filling material is brown glue. Figure 6-6a and Figure 6-6c show the experimental results and Figure 6-6b shows the simulated result. Both simulation and experimental results demonstrate that propagated hydraulic fractures are arrested at their intersection points with natural fractures. Figure 6-6c shows the sample with slabs detached from the main section using chisel and hammer. The main section is also split in half on the hydraulic fracture plane to describe the fracturing surface. A minor opening at the intersection point is observed in slab A, whereas slab B shows a complete arrest of hydraulic fracture. This slab was broken during the detachment process. The main section C shows a bi-wing hydraulic fracture.

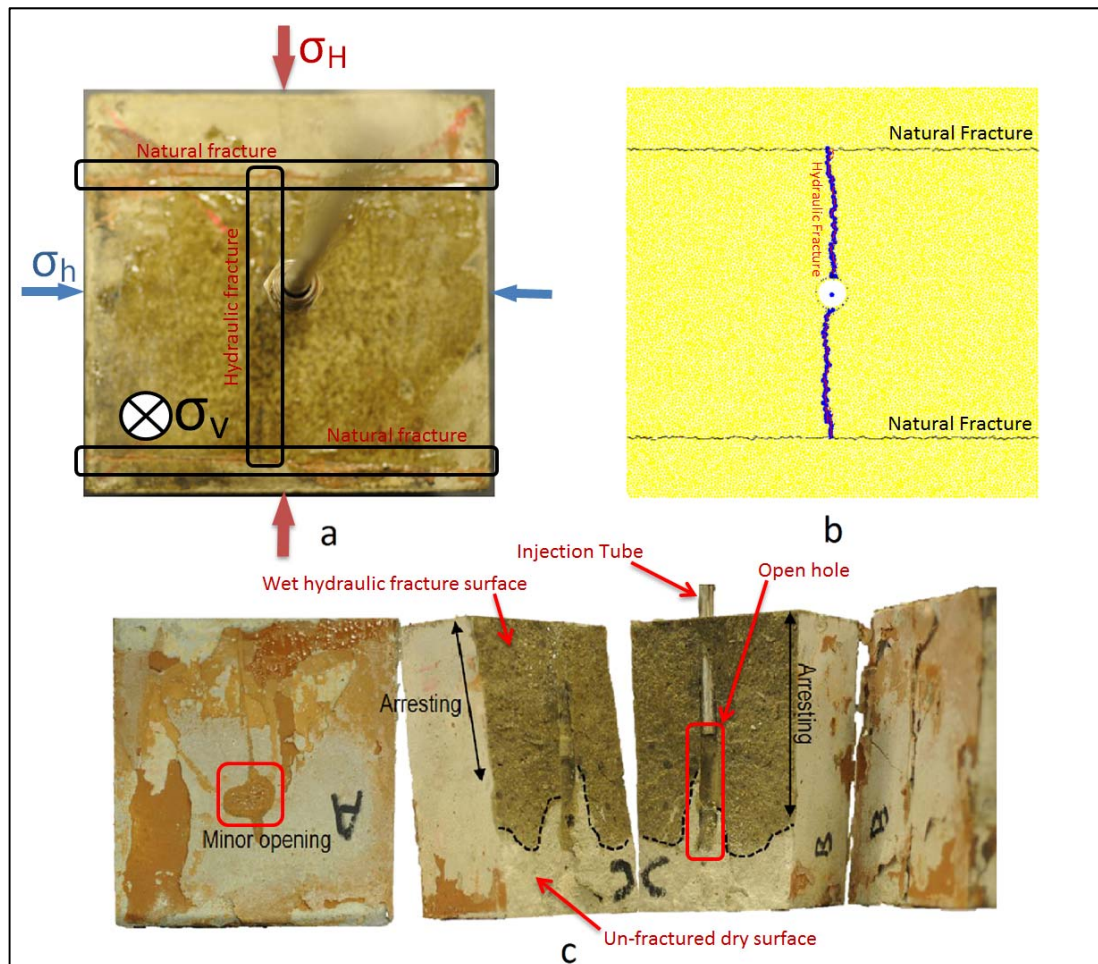


Figure 6-6: Brown glue as natural fracture filling material. a) Top view of the sample. The hydraulic fracture arrived at the natural fracture at  $90^\circ$ . The hydraulic fracture is arrested at the natural fracture. b) Simulated sample. It shows that the hydraulic fracture is arrested at the natural fracture. c) Sample opened to show the created hydraulic fracture. Slab A shows mainly arresting of the hydraulic fracture with minor opening. Slab B shows complete arresting of the hydraulic fracture. The slab was broken while trying to detach it from the main section C. Section C shows a bi-wing hydraulic fracture with the fracture surface shown in dark grey colour, as the fracturing fluid caused wetting of the fracture surface. Modified from (Sarmadivaleh, 2012)

Figure 6-7 shows a sample with white glue as the natural fracture filling material. Two tests were carried out with this sample. In the first test, as shown in Figure 6-7a, principal stresses were imposed in such a way that the hydraulic fracture initiated and propagated in a direction of  $30^\circ$  with respect to the natural fracture. No interaction was observed between the hydraulic fracture and the natural fracture. Figure 6-7b shows a simulation of this test with same result of no interaction. To facilitate the creation of hydraulic fractures, two sets of small notches on the borehole wall were created for both experimental and simulation tests. These two sets were orthogonal. The hydraulic fracture initiated and propagated in the direction of maximum horizontal principal stress, as one would anticipate. Figure 6-7c shows the result of the second test. In this test, the principal horizontal stresses were rotated  $90^\circ$  with respect to the test in Figure 6-7a (i.e. the hydraulic fracture propagated in the direction of maximum horizontal stress), and the minimum horizontal stress was halved. It is observed that the hydraulic fracture propagated in the direction of maximum horizontal stress and intersected the natural fracture at about  $60^\circ$ . Both wings of the hydraulic fracture crossed the natural fractures. The right wing shows a small offsetting at the intersection point. Figure 6-7d shows the simulated test condition with same interaction results.

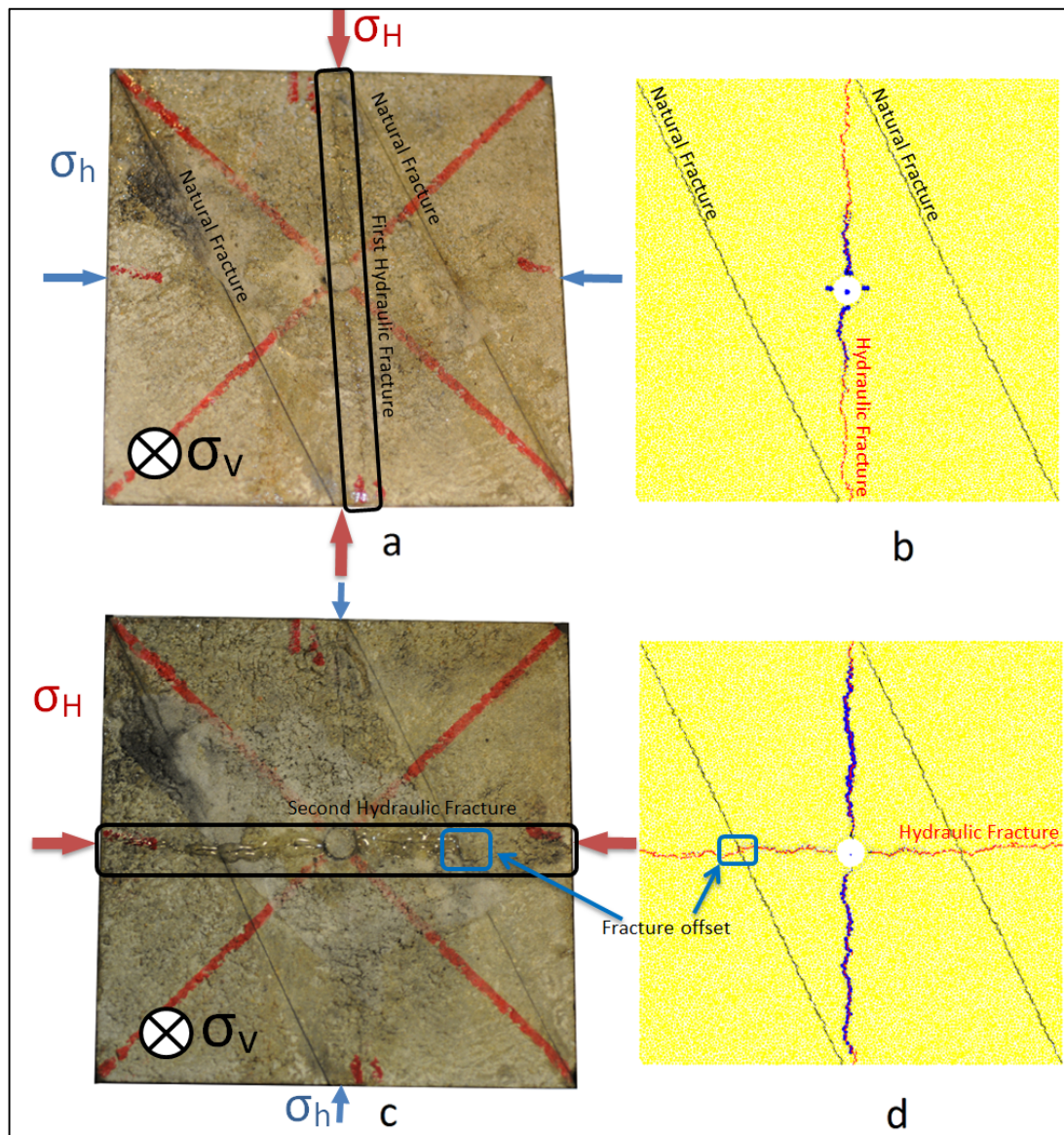


Figure 6-7: White glue as the natural fracture filling material. a) Experimental result for the natural fracture at  $30^\circ$  with respect to the hydraulic fracture. No interaction between hydraulic fracture and natural fracture occurred. b) Simulated fracturing test for the natural fracture at  $30^\circ$  with respect to the hydraulic fracture. No interaction between hydraulic fracture and natural fracture occurred. c) Experimental result for natural interface at  $60^\circ$  with respect to hydraulic fracture. Hydraulic fracture crossed natural fracture with small offset at right wing. d) Simulated fracturing test for the natural fracture at  $60^\circ$  with respect to hydraulic fracture. The hydraulic fracture crossed the natural fracture with a small offset at the left wing.

Figure 6-8 shows the simulation and experimental results for two cases of  $0^\circ$  and  $90^\circ$  orientation of the natural fractures with respect to the hydraulic fracture. Cement is the natural fracture filling material for both samples. Figure 6-8a shows the experimental result for the case that the hydraulic fracture was initiated and propagated parallel to the natural fracture. Figure 6-8b shows the simulation with the same interaction result. Both simulation and experimental results show that the

created hydraulic fracture is bi-wing in the direction of maximum horizontal stress. Figure 6-8c shows the experimental result for the case of a 90° interaction angle. The top wing is arrested at the intersection point and the bottom wing crossed the natural fracture. Figure 6-8d shows the simulation result for a 90° interaction angle. Simulation shows that the hydraulic fracture has crossed both top and bottom natural fractures. The discrepancy between the experimental and simulation results at the top natural fracture is due to the fact that in the experimental case, after the hydraulic fracture crossed the bottom boundary, it also intersected the boundary perpendicular to vertical stress direction. Fluid has leaked off at three boundaries and caused rapid depressurisation of the fracture fluid as well as loss of pressure energy. Consequently, the available remaining energy of the fracturing fluid was not good enough to cross the top boundary. In the simulated sample, no leak-off is considered in the out-of-plane dimension, which is considered to be a better representation of field conditions. In this case the target formation is considered to be bounded within two impermeable formations on top and bottom. It is very unlikely to fracture if the top and bottom formations have higher stress contrast with respect to the target formation. The chance of splitting at the interface between formations in the horizontal plane is also very slim, as overburden stress will clamp it down. The net result is that the fracture would be bounded in the target formation and the fracturing fluid would not lose its energy as readily as it did in the experimental test.

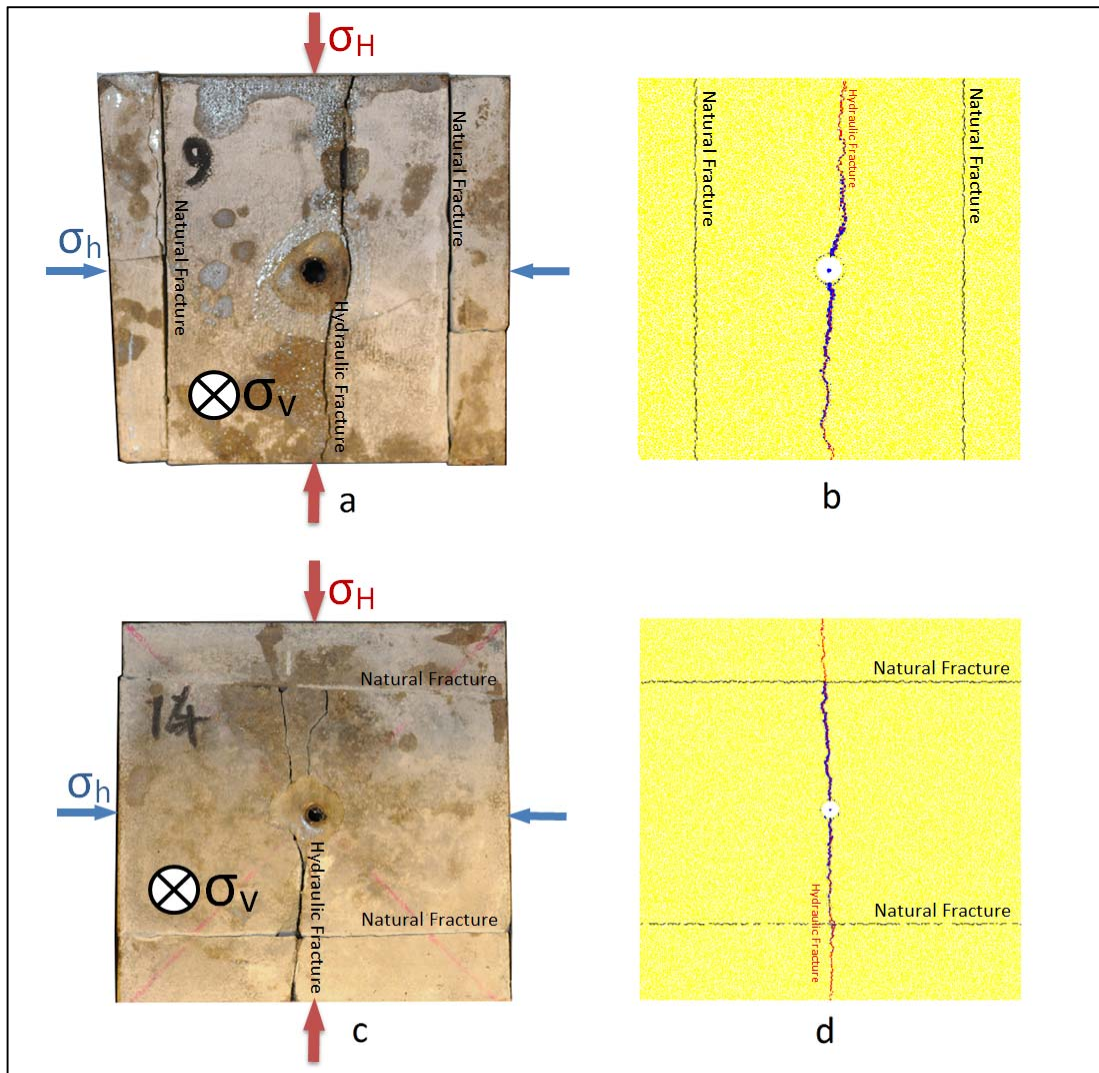


Figure 6-8: Cement as natural fracture filling material. a) Experimental result for the natural fracture at  $0^\circ$  with respect to the hydraulic fracture. No interaction between the hydraulic fracture and the natural fractures occurred. b) Simulated fracturing test for the natural fracture at  $0^\circ$  with respect to the hydraulic fracture. No interaction between the hydraulic fracture and the natural fractures occurred. c) Experimental result for the natural fracture at  $90^\circ$  with respect to the hydraulic fracture. The top wing arrested at the intersection point. The bottom wing crossed the natural fracture. d) Simulated result for the natural fracture at  $90^\circ$  with respect to the hydraulic fracture. Both wings crossed the natural fractures.

Figure 6-9 shows two tests for anticipated interaction angles of  $60^\circ$  and  $30^\circ$ . Figure 6-9a shows the experimental result for the anticipated  $60^\circ$  interaction angle. As predicted, the fracture has arrived at the natural fracture at  $60^\circ$ . The left wing got arrested and the right wing crossed the natural fracture. As in the previous case, excessive leak-off at three boundaries caused early depressurisation of the fracturing fluid. This caused the left wing to be arrested. Figure 6-9b shows the simulation result for a  $60^\circ$  interaction angle. It shows that both wings crossed the natural fractures with some degree of offsetting. Offset is larger at the left wing. Figure 6-9c

shows the experimental result for the planned interaction angle of  $30^\circ$ . However, the hydraulic fracture did not propagate in the planned direction. A few parameters could cause this deviation of hydraulic fracture from the planned direction, such as improper stress installation, defects in the sample, and misalignment of side slabs. The main reason could be that the opposite sample sides were not totally parallel. When the side slabs were cemented to the centre piece, a small misalignment could cause stress to be imposed more on the side slabs. This could cause stress rotation in the centre piece, which can impact the fracture initiation point and its propagation path. It then arrested at the natural fractures and caused shear slippage on them. Figure 6-9d shows the simulation result. From this figure it can be seen that fracture the initiated and propagated in the planned direction, parallel to the maximum horizontal stress and at  $30^\circ$  with respect to the natural fractures. The hydraulic fracture arrested at the natural fractures. It caused some shear slippage on the natural fractures' surfaces. To be able to benefit from the experimental result even though the whole physics of the problem could not be captured, a simulation was prepared with three natural fractures, as shown in Figure 6-9e. Two natural fractures were positioned at  $30^\circ$  with respect to the maximum horizontal stress, and the third one was positioned in the direction of the experimental hydraulic fracture. In this way, the third natural fracture allowed the fracturing fluid to arrive at similar interaction points to those in the experimental result. The aim was to observe whether the fluid pressurisation will cause initiation of a fracture at the intersection point on the opposite side of the natural fracture, or will cause shear slippage at the natural fractures. The fluid caused shear slippage at  $30^\circ$  natural fractures, as observed in the experimental case. This test further confirms the consistency between simulation and experimental results.

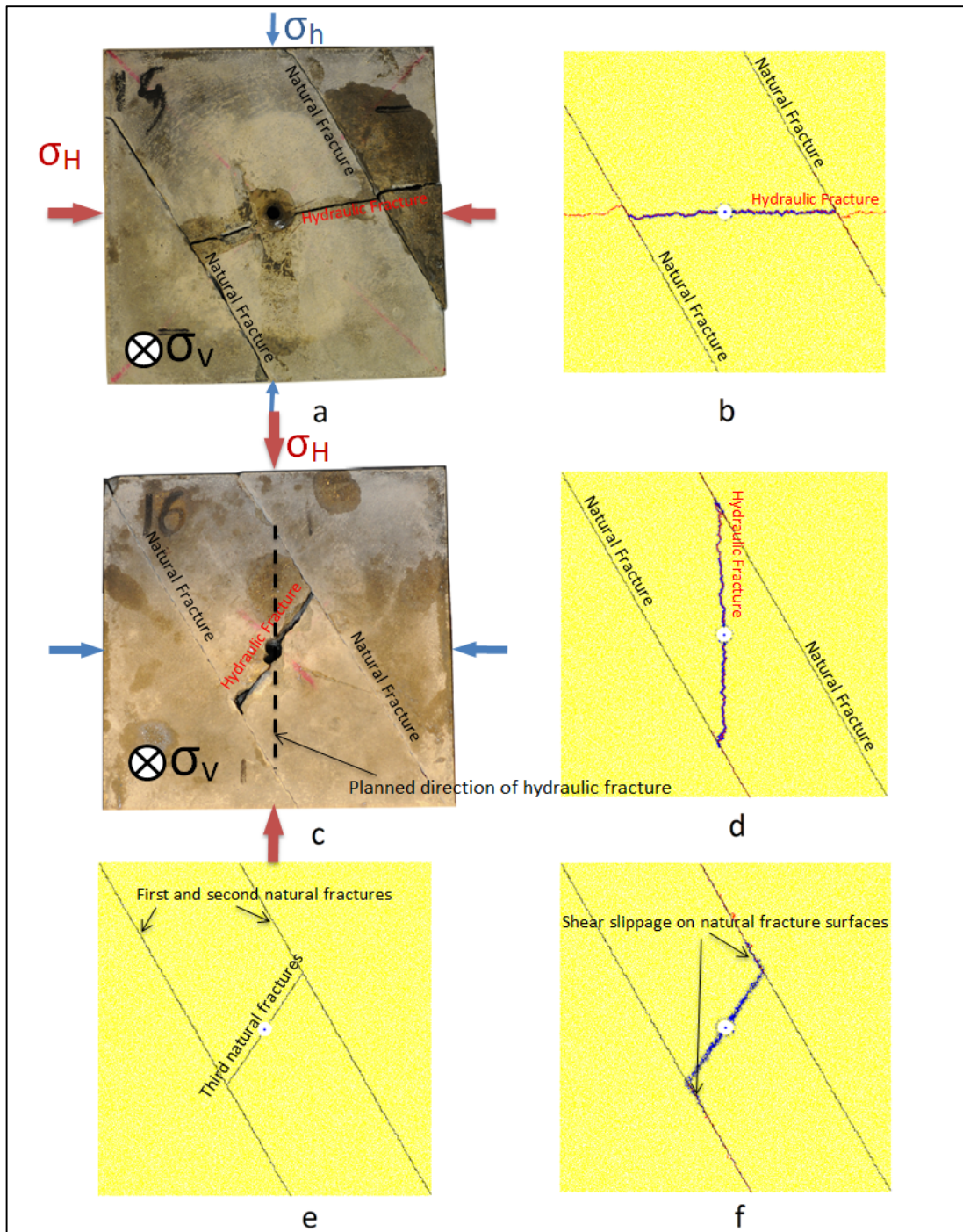


Figure 6-9: Cement as natural fracture filling material. a) Experimental result for natural fracture at  $60^\circ$  with respect to hydraulic fracture. Left wing of hydraulic fracture arrested at intersection point and right wing crossed natural fracture. b) Simulated fracturing test for the natural fracture at  $60^\circ$  with respect to the hydraulic fracture. Both wings crossed the natural fractures with small offsetting. Offset is larger at the left wing. c) Experimental result for natural fractures at anticipated  $30^\circ$  with respect to the hydraulic fracture. The hydraulic fracture didn't propagate in the desired direction. Both wings were arrested by natural fractures. d) Simulated result for anticipated natural fracture at  $30^\circ$  with respect to the hydraulic fracture. Both wings arrested at natural fractures. Shear slippage occurred at some intervals over natural fracture surfaces. e) Two natural fractures at  $30^\circ$  and a third one in the direction of experimental hydraulic fracture. f) Shear slippage at natural fracture surfaces.

Table 6-3 summarises the test parameters and results. This table, as well as the discussion above, clearly indicate that simulation results can replicate the experimental condition, and be capable of producing similar results. The major difference is the 2D characteristic of the simulation result. However, as discussed above, simulation is a better representation of field conditions than experiments. The reason is that in the simulation, there is no fluid leak-off out of the sample from the plane perpendicular to the vertical stress. This is similar to a reservoir formation that is sandwiched between two impermeable formations with higher stress contrast. Matrix permeability in the vertical direction doesn't allow excessive leak-off to barrier formations, as was observed in the experiments. In this case the fracture would be contained in the reservoir formation and the probability of fluid leak at formation interfaces would be very low. In the experiments, if the fracture arrives at the top and bottom surfaces that are perpendicular to the vertical stress, excessive fluid leak-off could depressurise the fluid, causing excessive fluid energy loss, which can significantly influence the outcome of the results. A remedy to this problem would be using samples with larger side lengths for experimental studies. But larger samples can introduce new problems. Creating synthetic homogenous large samples is very difficult. Handling and placement in the equipment and proper stress installation involve complex and tedious processes. If the opposing surfaces are not totally parallel, stress rotation and localisation can jeopardize the results. Another difficulty with experimental studies is that these tests are extremely time consuming and require very expensive experimental setup. This puts constraint on the number of tests that can be done. As a result, it is hardly possible to draw a strong conclusion that covers a wide range of test conditions. Simulation studies can overcome these limitations to a large extent. Large scale simulated samples can easily be developed without affecting the homogenous nature of the sample. Principal stresses can be controlled easily to make sure that there is no unwilling stress rotation. Tests can also be performed at a large frequency for a wide range of test conditions.

Table 6-3: Summary of test parameters and test results

			Interaction Results		
Test #	Natural fracture filling material	Interaction angle (°)	Simulation interaction result	Experimental Interaction result	Injection rate (cc/min)
1	Brown Glue	90	Arrest	Arrest	0.1
2	White Glue	30	Didn't intersect	Didn't intersect	0.1
3	White Glue	60	Cross	Cross	0.1
4	Cement	0	Didn't intersect	Didn't intersect	0.1
5	Cement	90	Cross	Cross-Arrest	0.1
6	Cement	60	Cross	Cross-Arrest	0.1
7	Cement	30	Arrest	Arrest	0.1
<b>Principal stresses</b>					
Test #	$\sigma_v$ (psi)	$\sigma_H$ (psi)	$\sigma_h$ (psi)	Sample side length (cm)	Fluid Viscosity (cp)
1	3000	2000	1000	10	100000
2	3000	2000	1000	10	100000
3	3000	2000	500	10	100000
4	3000	2000	1000	10	100000
5	3000	2000	1000	15	100000
6	3000	2000	1000	15	100000
7	3000	2000	1000	15	100000

To summarise the previous discussion and Table 6-3, the outcome of a propagated hydraulic fracture and its interaction with a natural fracture significantly depends on the orientation of natural fractures with respect to principal stresses and the natural fractures' filling material. Increasing the angle of natural fractures with respect to maximum horizontal stress increases the chance of crossing the natural fracture. Low

angles between the hydraulic fracture and natural fractures can cause shear slippage on the natural fracture planes. Filling material also plays a vital role. Weak planes increase the chance of shear slippage even at 90° orientation of natural fractures with respect to maximum horizontal stress as was observed in the case of the brown glue filling material. However, there are more parameters to be considered, such as deviatoric stress (i.e. the difference in the magnitude of maximum and minimum horizontal stress), the friction coefficient of the natural fracture, flow rate, fluid properties, and the rock's mechanical properties. The simulation developed for this study demonstrated that the results are very similar to experimental observations.

This chapter concludes the model development and validation. The simulation model developed will be used in the next chapter for sensitivity analysis to investigate the effect of different parameters on the interaction mechanism between hydraulic and natural fractures.

# 7

## Sensitivity Analysis

This chapter presents the results of the sensitivity analysis. The sample considered in the sensitivity studies has the same mechanical properties as the mortar sample considered during laboratory experiments, as described in Chapters 5 and 6. The main objectives of these sensitivity studies are, through investigation based on numerical simulation, to: understand comprehensively the propagation behaviour of hydraulic fractures; and identify the factors influencing the propagated hydraulic fracture, especially while interacting with the natural fractures in different scenarios. Figure 7-1 illustrates the schematic of the problem considered. The sample is prismatic in shape, with side lengths of  $a$ . A wellbore with diameter  $R$  is created in the centre of the sample. Natural fractures with side lengths  $l$  are created on each side of the wellbore with distance  $b$  from the centre of the wellbore. The natural fracture has an angle of  $\alpha$  with respect to  $\sigma_H$  direction.

The parameters considered for these studies are:

- Natural fracture permeability;
- Natural fracture orientation with respect to maximum horizontal stress direction;
- Natural fracture size;
- Natural fracture distance from wellbore;
- Horizontal stresses ratio.

The first part of this chapter describes the simulated results of the case when hydraulic fracturing is carried out in a sample without natural fractures under isotropic stress states. The second part presents sensitivity analysis results in the presence of two natural fractures on either side of the wellbore, to investigate the effect of different parameters on hydraulic and natural fracture interaction and the hydraulic fracture propagation path. In the last part of the chapter, hydraulic fracturing in the presence of abundant natural fractures is performed to investigate hydraulic fracture propagation behaviour.

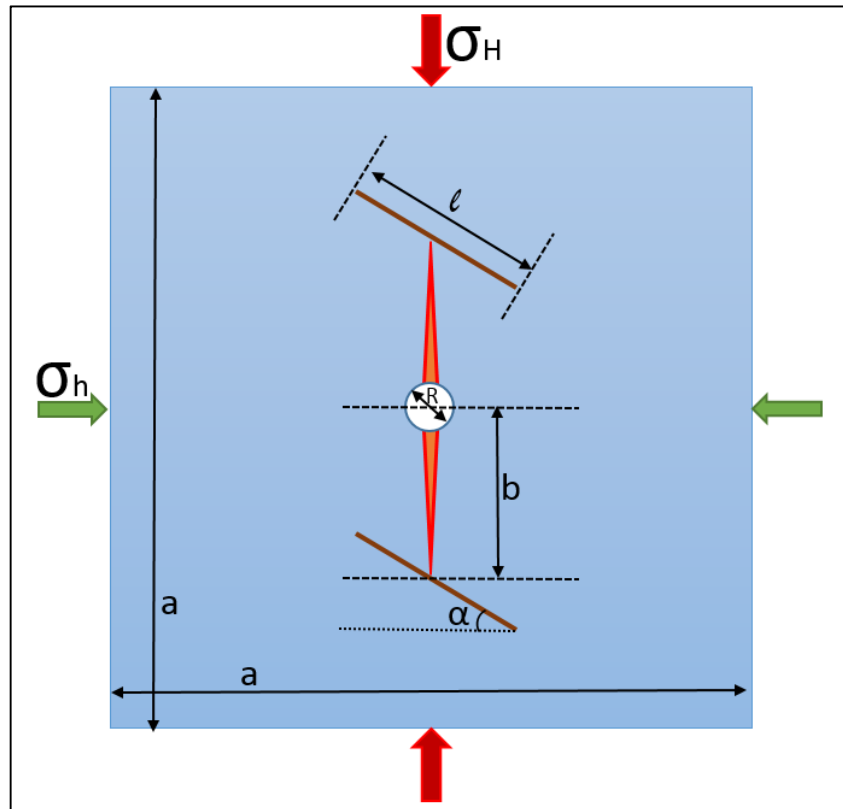


Figure 7-1: Geometry of a hydraulic and natural fracture interaction.  $a$ : sample dimension  $b$ : Natural fracture distance from centre of the wellbore;  $R$ : wellbore diameter;  $l$ : natural fracture size;  $\alpha$ : natural fracture angle;  $\sigma_H$ : Maximum horizontal stress; and  $\sigma_h$ : Minimum horizontal stress.

## 7.1. Isotropic Stress State

This section presents the results of hydraulic fracturing under isotropic horizontal stresses without any presence of natural fractures. Three isotropic stress states of 0, 6.89 MPa (1000 psi) and 13.79 MPa (2000 psi) are considered. For each isotropic stress state, two sensitivities are performed. The first sensitivity is performed for the case that two sets of notches are created at  $0^\circ$  and  $90^\circ$  at the wellbore wall. For the second sensitivity, notches are created at  $-45^\circ$  and  $+45^\circ$ . Figure 7-2a shows the 0 MPa isotropic stress state with notches at  $0^\circ$  and  $90^\circ$ . The hydraulic fracture is a bi-wing fracture. Although it was anticipated that two bi-wing fractures would start orthogonal to each other, only one bi-wing fracture was created. The reason is that when the first fracture initiated it started depressurising the wellbore. It also changed the stress orientation around the wellbore and increased stress concentration in all other directions, including the direction at  $90^\circ$  to the created hydraulic fracture

direction. The top wing reached the top boundary and the bottom wing stopped at roughly 1/6<sup>th</sup> the sample length from the bottom boundary. The reason is that once the top wing reached the top boundary, the wellbore and fracture depressurised fairly quickly and there wasn't enough energy left to propagate the bottom wing all the way to the bottom boundary. Because of the lack of horizontal stresses on the sample, the top fracture became wide very quickly as soon as it hit the top boundary. The same phenomenon seen in the case shown in Figure 7-2b. In this case, notches were created at  $-45^\circ$  and  $+45^\circ$  at the wellbore wall. The sample was under a 0 MPa isotropic stress state. The hydraulic fracture was a bi-wing fracture in the northeast-southwest direction. The north-eastern wing stopped just a short distance away from the wellbore. Both wings started at a  $45^\circ$  angle. The south-western wing deviated from the  $45^\circ$  angle direction at one-third the distance between the wellbore and sample edge and moved towards the bottom boundary. This might have been due to the sample edge and dimension effects. If the sample has an infinite length, the fracture could propagate at  $45^\circ$  for as long as pumping is continued, and the pressure is enough to propagate the fracture. Figure 7-2c and Figure 7-2d show hydraulic fracturing under a 6.89 MPa isotropic stress state, and Figure 7-2e and Figure 7-2f show hydraulic fracturing under a 13.79 MPa isotropic stress state. In all these four figures, the fractures are bi-wing and both wings have crossed the boundaries. An interesting effect is seen in Figure 7-2f. In this figure, the fracture initiated and propagated at  $-45^\circ$ . Although the samples were homogenous and the same sample was used for all simulations, random particle arrangement can affect stresses within the sample large enough to cause a change in the fracture initiation orientation. Also, from all these figures, it can be seen that the final wellbore pressure is higher for the case where the fracture initiated at either  $+45^\circ$  or  $-45^\circ$  with respect to  $90^\circ$ . This is due to the larger length of the hydraulic fracture and the higher frictional pressure inside the fracture. These simple simulation studies also demonstrate that the fracture propagation path is tortuous. In reality, a fracture also propagates in a tortuous path, and a direct smooth fracture doesn't happen, as was also confirmed by the laboratory tests in this study that are presented in Chapters 5 and 6. The simulation result, as presented in Figure 7-2a – Figure 7-2f, also demonstrates that increasing the isotropic stress state increases the hydraulic fracturing initiation and breakdown pressure.

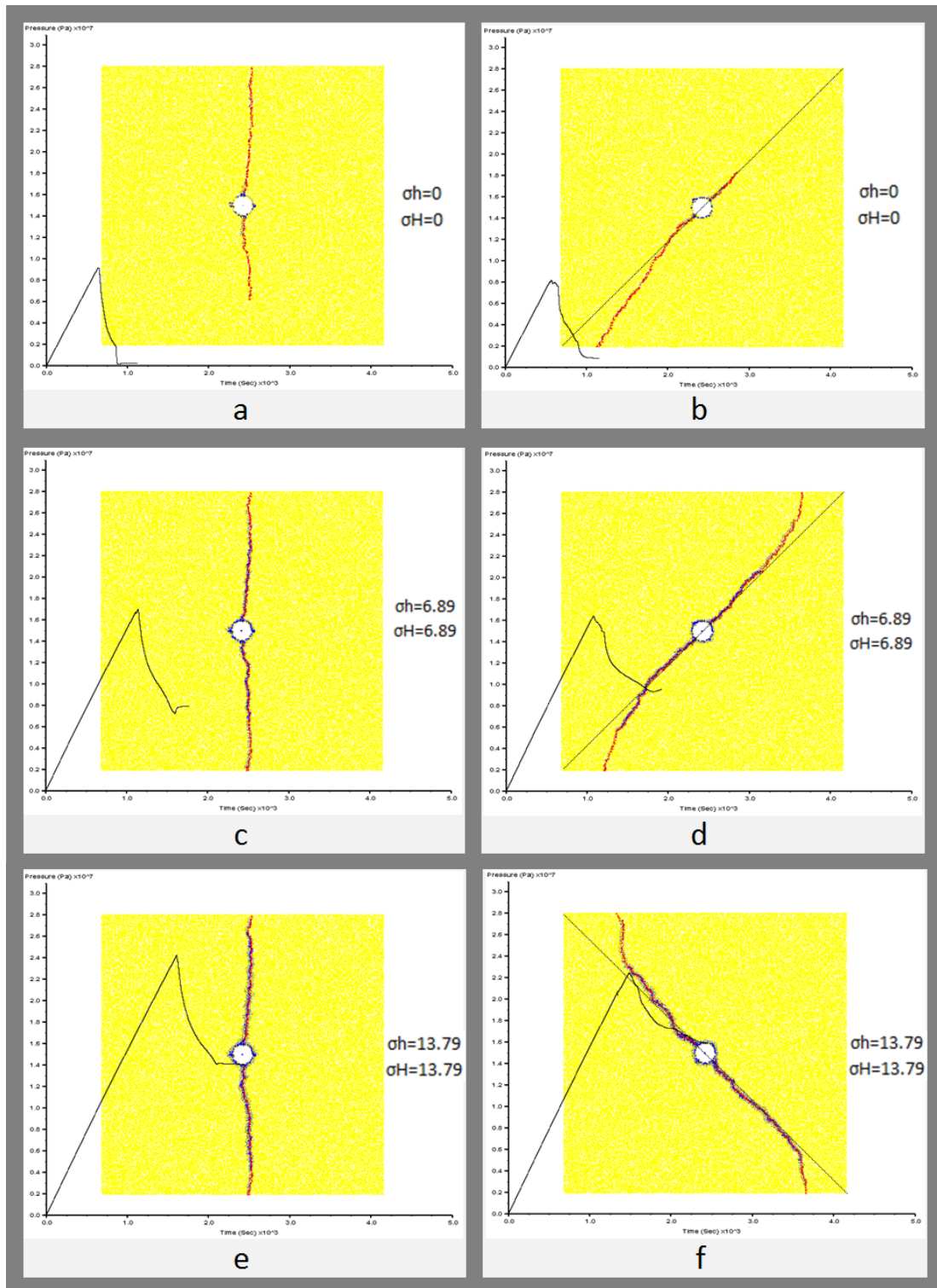


Figure 7-2: Isotropic stress state hydraulic fracturing. (a)- Zero horizontal stresses. Wellbore notches are created at  $0^\circ$  and  $90^\circ$ . (b)- Zero horizontal stresses. Wellbore notches are created at  $+45^\circ$  and  $-45^\circ$ . (c)- 6.89 MPa horizontal stresses. Wellbore notches are created at  $0^\circ$  and  $90^\circ$ . (d)- 6.89 MPa horizontal stresses. Wellbore notches are created at  $+45^\circ$  and  $-45^\circ$ . (e)- 13.79 MPa horizontal stresses. Wellbore notches are created at  $0^\circ$  and  $90^\circ$ . (f)- 13.79 MPa horizontal stresses. Wellbore notches are created at  $+45^\circ$  and  $-45^\circ$ . Dashed lines in (b), (d) and (f) connect the edges of sample and show the  $45^\circ$  angle direction.

Figure 7-3 shows breakdown pressure versus isotropic horizontal stresses for the different cases studied above. The blue line and dots show the breakdown pressure for the cases when a hydraulic fracture is propagated at 90° (north-south) direction. The red line and dots show breakdown pressure when a hydraulic fracture is propagated at +45° or -45°. The intercept of lines at 0 MPa horizontal stress shows the hydraulic fracturing tensile strength for the current testing conditions. It should be noted that rocks show different tensile strengths under different testing configurations and conditions. Tensile strengths can be determined based on direct tension, and Brazilian or wellbore pressurisation tests. But they all give different results. Even in the case of wellbore pressurisation, the hydraulic fracturing tensile strength depends on test conditions such as the injection rate in the wellbore, fluid flow compressibility, and so on. So the tensile strength indicated in Figure 7-3 only shows tensile strength for this test configuration and condition. From this figure, it can be seen that breakdown pressure increases in a linear fashion versus the horizontal stress. Again it should be noted here that breakdown pressure increases linearly. Such a linear trend of increasing breakdown pressure only happens as long as the sample does not go under plastic deformation as a result of increased horizontal stresses.

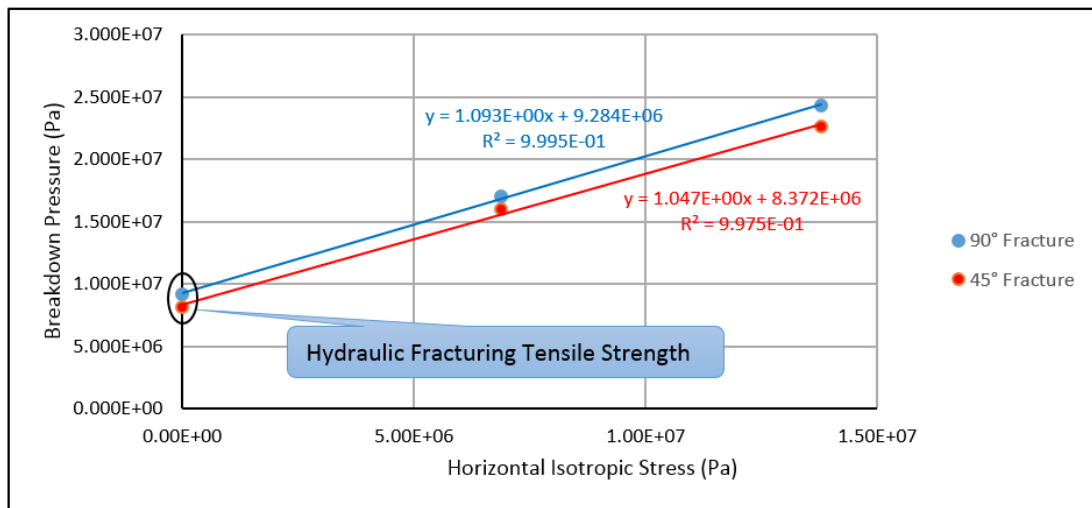


Figure 7-3: Breakdown pressure versus isotropic stress for two cases of 90° and 45° fracture propagation. The intercept shows hydraulic fracturing tensile strength.

## 7.2. Hydraulic Fracture Propagation in Presence of Natural Fractures

This section presents the results of the sensitivity analysis for hydraulic fracture propagation in the presence of two natural fractures on either side of the wellbore. An extensive number of tests were performed to investigate the effect of natural fracture permeability, interaction angle, magnitude of horizontal stresses, natural fracture size and natural fracture distance from the centre of the wellbore. Table 7-1 presents the base case parameters that were kept constant for tests. These parameters were also the same for the sensitivity analysis of isotropic horizontal stress state tests. The sample length is 15 cm, wellbore diameter is 1 cm,  $\sigma_H$  is 13.79 MPa (2000 psi), sample matrix permeability is 0.02 md, and wellbore fluid flow injection rate is 0.1 cc/min. Table 7-2 shows the test results, and variable parameters associated with each test. These variables are:

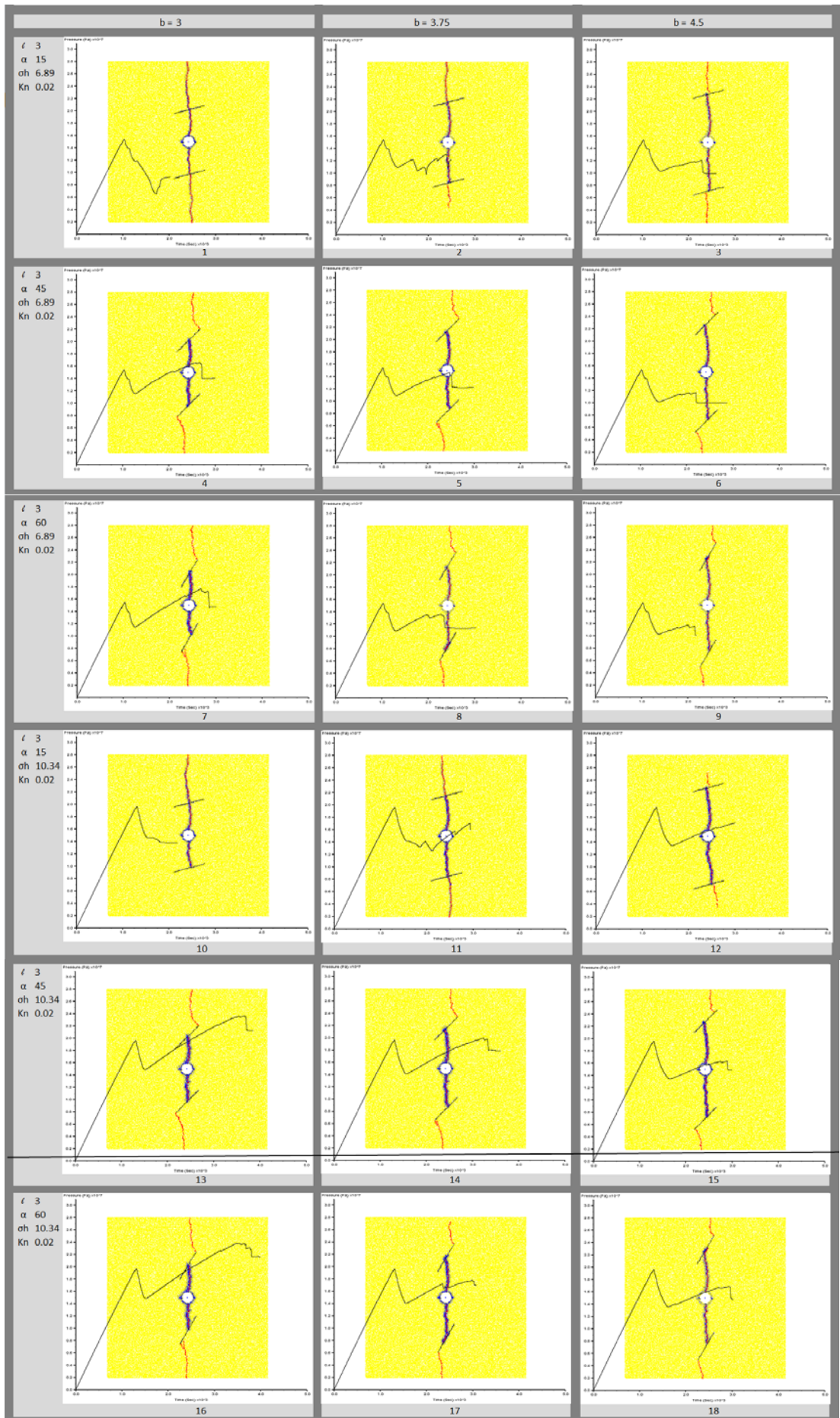
- ( $b$ , cm): Distance from the centre of the wellbore to the centre of the natural fracture. Three distances of 3, 3.75 and 4.5 cm were considered.
- ( $l$ , cm): Natural fracture length. It is mostly considered to be 3 cm. For some tests it changes to 4.5 cm.
- ( $\sigma_h$ , MPa): Minimum horizontal stress. Three stresses of 6.89 MPa, 10.34 MPa and 13.79 MPa were considered.
- ( $\alpha$ , °): Angle between the natural fracture plane and the direction of  $\sigma_h$ . Three angles of 15°, 45° and 60° were considered. Three tests with an angle of 0° were also performed.
- ( $K_n$ , md): Natural fracture permeability. Three permeability values of 0.02, 2 and 200 md were considered. These correspond to the natural fracture to matrix permeability ratios of 1, 100 and 10000.

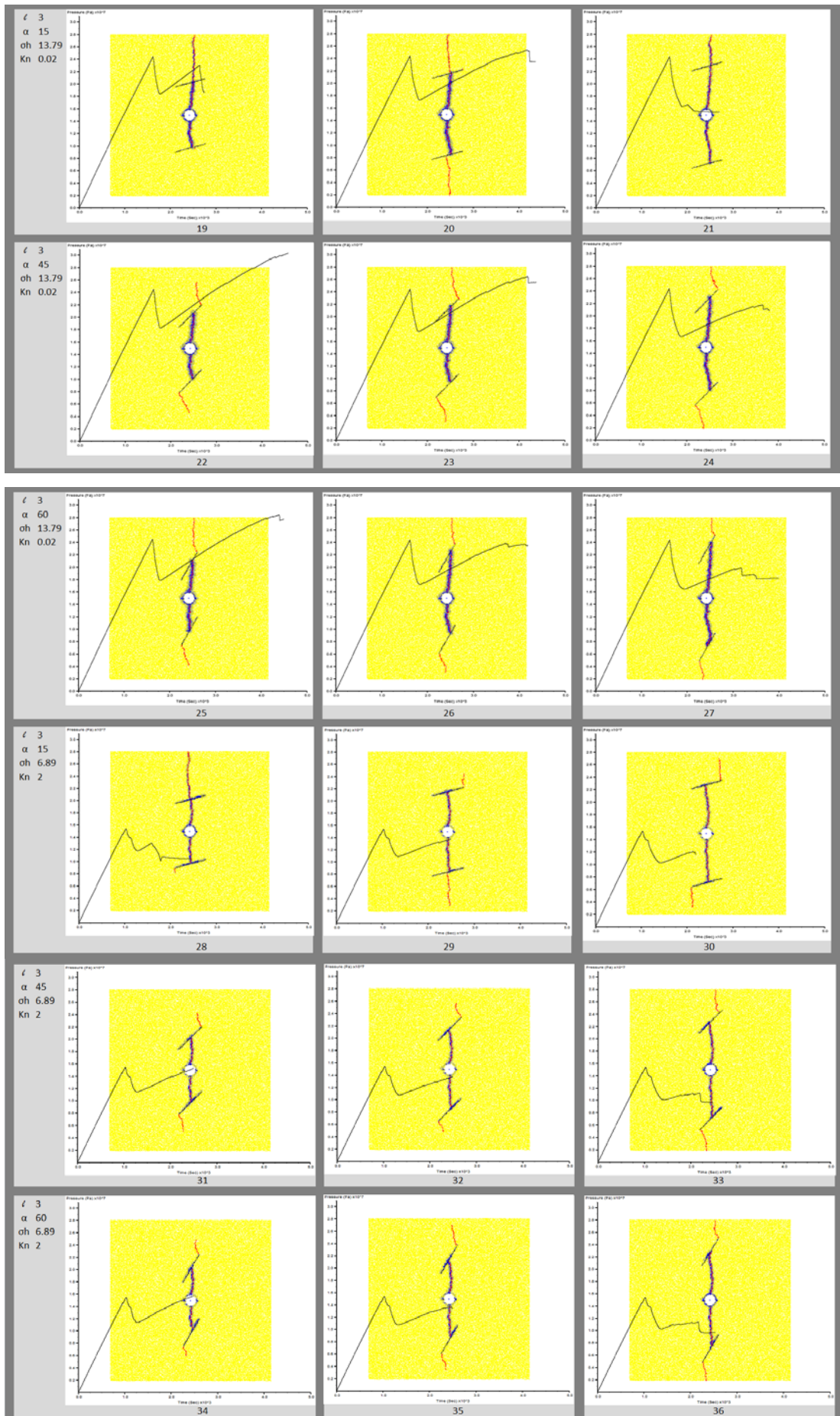
Table 7-1: Constant test variables;  $a$ : sample side length;  $R$ : wellbore diameter;  $\sigma_H$ : maximum horizontal stress;  $K_m$ : matrix permeability.

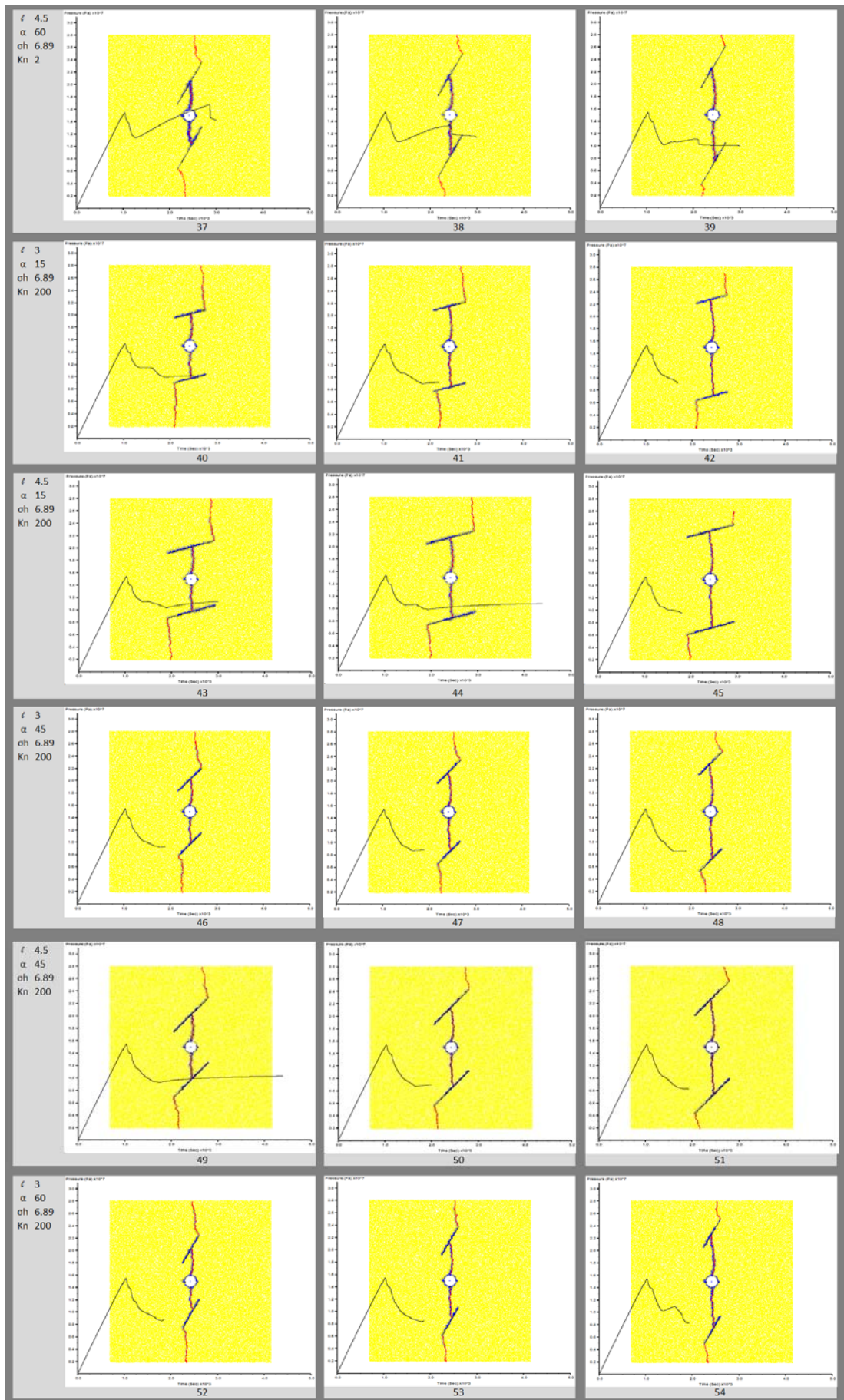
a, cm	R, cm	$\sigma_H$ , MPa	$K_m$ , md	flowRate, cc/min
15	1	13.79	0.02	0.1

A total number of 69 tests were performed. Test result images are shown in Figure 7-4. This figure shows three columns of images. The first column shows results for

the cases where the distance of natural fractures from the centre of the wellbore is 3 cm (short distance). The second column is for the cases where the distance of natural fractures from the centre of the wellbore is 3.75 cm (medium distance); and the third column shows results for the cases where the distance of natural fractures from the centre of the wellbore is 4.5 cm (long distance). As mentioned above, three natural fracture permeability values were considered for sensitivity analysis. As shown in Figure 7-4, tests 1 to 27 and 64 to 66 show hydraulic fracturing under 0.02 md natural fracture permeability. Tests 28 to 39 represent the cases with natural fracture permeability of 2 md, and tests 40 to 63 and 67 to 69 are for 200 md natural fracture permeability cases. The natural fracture length ( $l$ ), its angle ( $\alpha$ ) and its permeability ( $K_n$ ), as well as minimum horizontal stress ( $\sigma_h$ ) for the three images, are shown at the left hand side of images in each row.







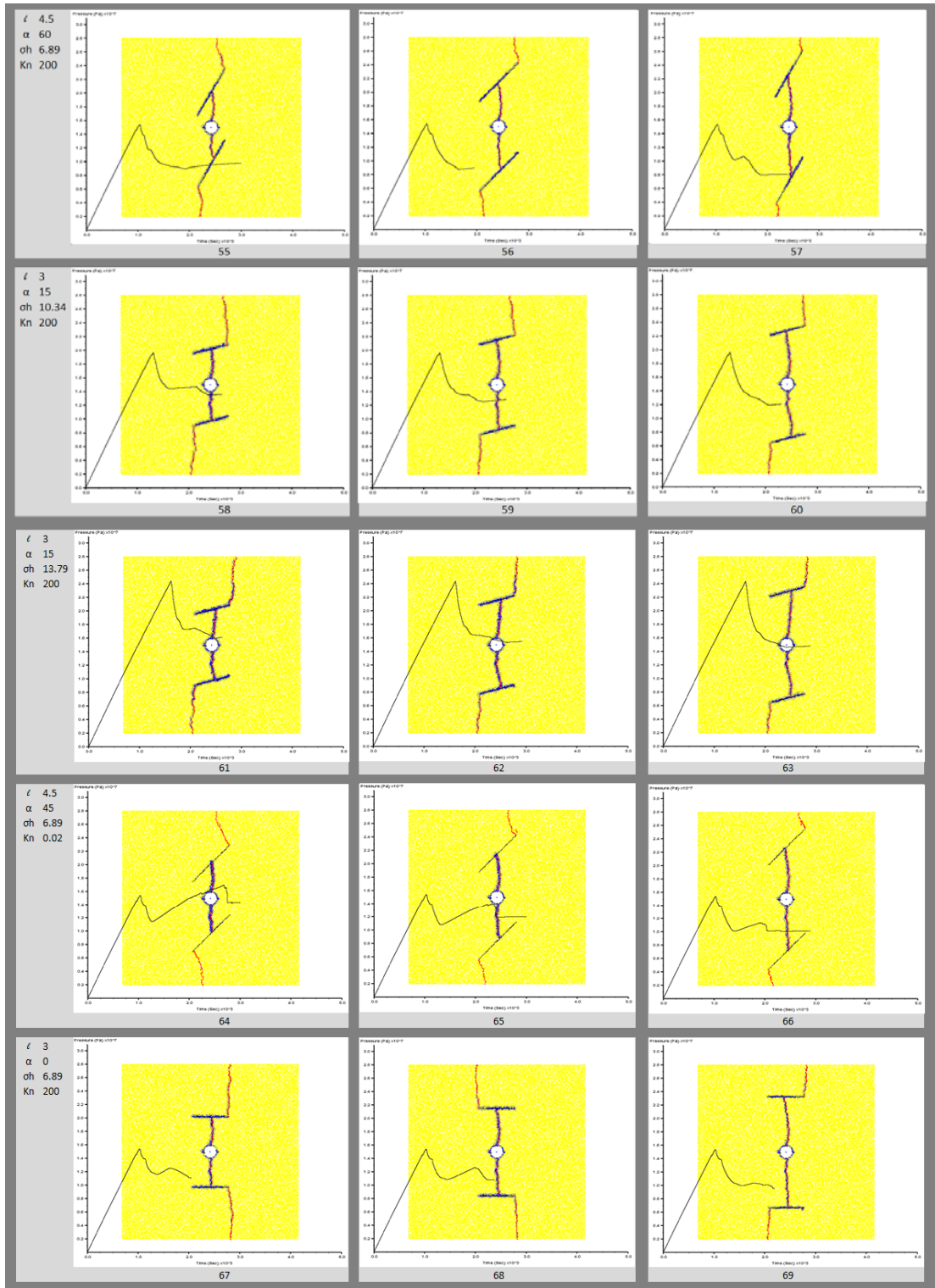


Figure 7-4: Test result images. Sample is shown in yellow. Hydraulic fracture is in red. Blue circles show pressure with bigger circles showing higher pressures. Black dashed lines show natural fractures. Plot shows wellbore pressure versus time. Vertical axis shows pressure in (Pa) and horizontal axis shows time in (sec). For all plots, maximum value for pressure axis is 31 MPa and maximum value for time axis is 5000 seconds.

Permeability is found to have a very significant and noticeable effect on the interaction mechanism and wellbore pressure behaviour. Permeability is found to be the most important parameter that affects the interaction mechanism.

At 200 md natural fracture permeability, which corresponds to 10000 times the matrix permeability, the interaction mechanism result is only “tip start,” which means that the hydraulic fracture re-initiates from the tip of the natural fractures. To investigate the interaction mechanism with the highest interaction angle of  $90^\circ$ , which corresponds to  $0^\circ$  angle between the direction of the natural fracture and the direction of minimum horizontal stress, three more tests were performed for the 200 md natural fractures. The results are shown in images 67 to 69 of Figure 7-4. It can be observed from these images that the re-initiation mechanism is “Tip Start” even at a  $90^\circ$  interaction angle. Other parameters have no effect on the interaction mechanism for the high permeability natural fractures. It is also observed that at this high permeability, the wellbore pressure does not show a noticeable rebound after the hydraulic fracture hits the natural fracture. Other parameters have an effect on the magnitude of breakdown pressure and test duration. For example, increasing  $\sigma_h$  increases both breakdown pressure and test duration.

At lower natural fracture permeability, values of 0.02 and 2 md, the interaction mechanism depends on other parameters besides natural fracture permeability. “Crossing”, “Tip Start” and “Offsetting” were observed at these lower permeability values. Tip Start is the interaction mechanism result for natural fracture angles of  $45^\circ$  and  $60^\circ$  at low permeability values of 0.02 and 2 md. For low angles of  $15^\circ$  the interaction mechanism depends mainly on permeability. Other parameters have secondary effects. At low natural fracture permeability of 0.02 md and low  $\sigma_h$  value of 6.89 MPa, the hydraulic fracture crosses natural fractures irrespective of other parameters such as natural fracture length and distance of natural fracture from the centre of the wellbore (Images 1 to 3). At higher  $\sigma_h$  values of 10.34 and 13.79 MPa, one wing of the natural fracture can get arrested, but the interaction mechanism is mainly crossing (Images 10 to 12 and 19 to 21). At intermediate natural fracture permeability of 2 md, one wing of the hydraulic fracture crosses the natural fracture and the other wing causes tip start for the natural fracture at distances of low and medium (Images 28 and 29). At a high natural fracture distance from the wellbore,

the interaction mechanism changes to tip start for both wings (Image 30). The reason for this is due to higher distances of the natural fracture from the wellbore, as the hydraulic fracture has a longer length. This corresponds to a larger area that the hydraulic fracture pressure acts on, and as a consequence creates a larger force. This larger force generates higher stress concentration at the tip of the natural fracture, causing the tip start mechanism. This phenomenon can be explained by Figure 7-5. This figure shows a cartoon representation of a hydraulic fracture half-length that has arrived at the natural fracture. As is shown, the hydraulic fracture pressure decreases by moving away from the wellbore. The force that is applied on the hydraulic fracture wall is the result of fracture pressure multiplied by fracture wall area. This corresponds to the area of the triangle that is created by the pressure profile and fracture wall length, as shown in Figure 7-5. As can be seen, the area of the triangle in Figure 7-5a is higher than the area of the triangle in Figure 7-5b. The lower the net force, the lower the stress concentration at the natural fracture tip. Also, as can be seen, there are two locations on the natural fracture with highest stress concentrations, shown by black ovals. This is shown in Figure 7-6. On the left hand side of this figure, the hydraulic fracture has just arrived at the natural fractures. On the right hand side of this figure, parallel bond forces are shown. Compressive forces are shown in orange, and tensile forces are shown in green. Each force is shown by a small line segment. The thickness of the line shows the force strength. The thicker the lines, the higher the force. Tensile forces are highest at the hydraulic and natural fracture intersection point, and at the tip further away from the wellbore. These two locations compete with each other, and mostly fracture re-initiation occurs from one of these two locations. However, this does not mean that the fracture cannot reinitiate from other places on the natural fracture plane. If there is a defect on the fracture that requires much lower energy for fracture initiation than from the tip or fracture interaction point, then the fracture can start from that weak location.

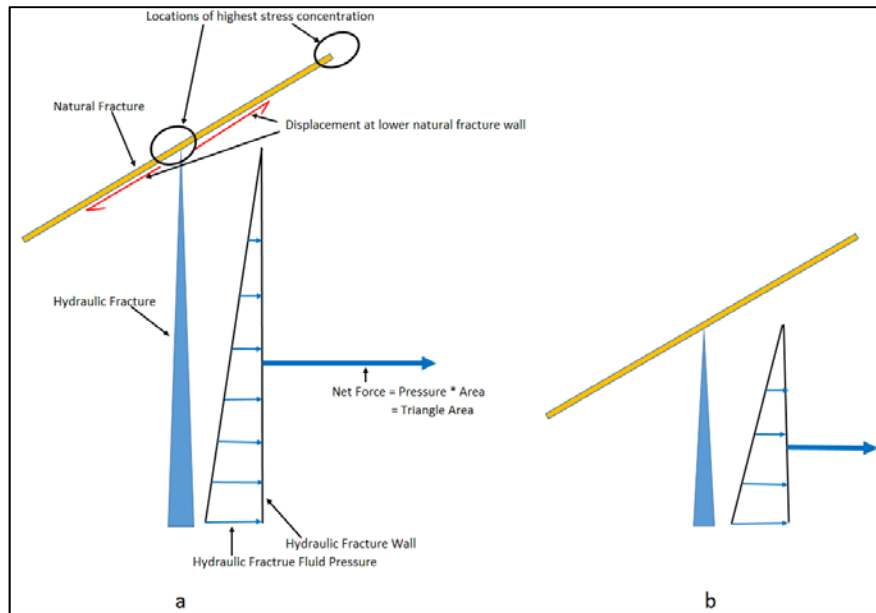


Figure 7-5: Force generated as a result of hydraulic fracture pressure. a) Natural fracture at a long distance away from wellbore. b) Natural fracture close to wellbore. The longer the natural fracture distance from wellbore, the higher the hydraulic fracture force.

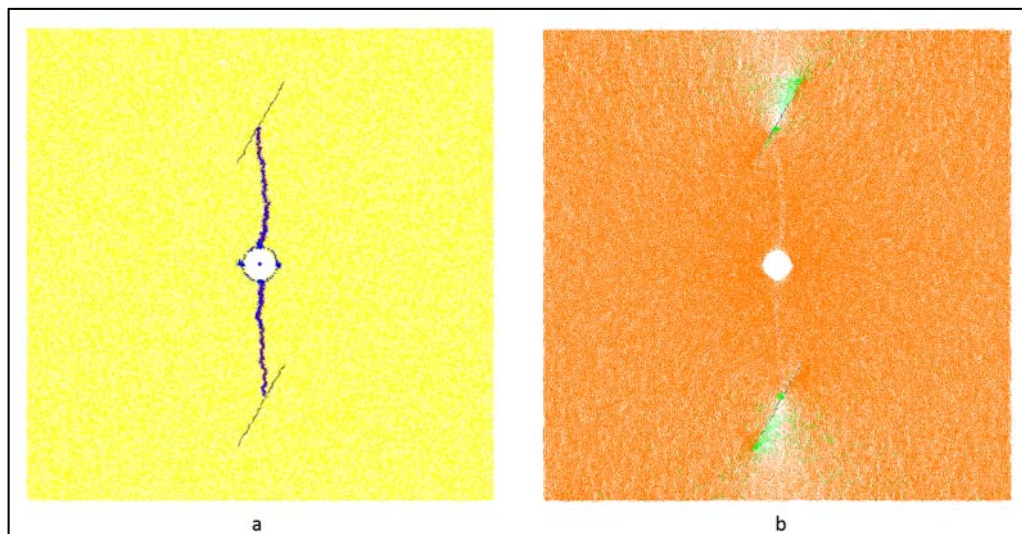


Figure 7-6: (a) Sample with hydraulic fracture just arrived at natural fractures. (b) Parallel bond forces. Orange shows compressive and green shows tensile forces. Each force is shown by a small line segment. The thicker the line, the higher the force. Tensile forces at the intersection point between hydraulic and natural fractures as well as at the natural fracture tip further away from wellbore have highest magnitudes.

Another main observation from the test results of Figure 7-4 is that the tip start always occurs from the tip which is further away from the wellbore. This is due to the fact that, as explained earlier, the tip which is closer to the wellbore can most likely be affected by hydraulic fracture compressive forces. Figure 7-7 shows how

the natural fracture tip which is closest to the wellbore is sandwiched between compressive forces from hydraulic fracture fluid pressure and minimum horizontal stress. These compressive forces prevent fracture re-initiation at this location.

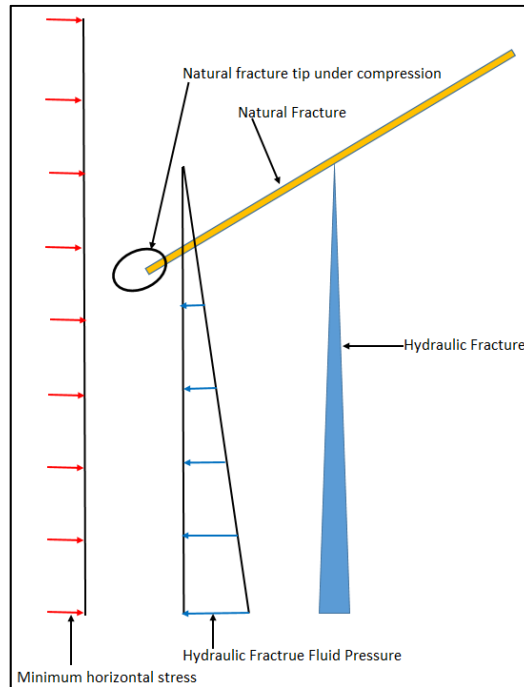


Figure 7-7: Natural fracture tip under compression

Figure 7-4 also shows that after fracture crossing, tip start or offsetting, the fracture continues to propagate in the initial hydraulic fracturing direction, which is the direction of  $\sigma_H$ . In few instances, such as images 8, 13, 22 and 25, after the fracture starts from tip, it moves a bit toward the centre of the sample, and as it gets closer to the centre it gradually re-adjusts its propagation path in the direction of  $\sigma_H$ . This behaviour is more noticeable for low permeability natural fractures with low angles. This again can analogously be explained by the concept of stress concentration and the torque and moment of rotation. In Figure 7-8, force F causes a rotational moment or torque at the nut. The magnitude of torque at the nut is equal to the magnitude of force  $|F|$  times the magnitude of arm (d). The greater the arm (d) or the force (F) the greater the torque (T). Figure 7-9a shows a low permeability natural fracture, and Figure 7-9b shows a high permeability natural fracture. In the case of a low permeability natural fracture, after the hydraulic fracture hits the natural fracture, fracturing fluid will not pressurise the natural fracture. The reason is that the fluid cannot move easily into the fracture. In this case, the torque at the tip of the natural

fracture is mostly the result of force that is applied on the hydraulic fracture wall. In Figure 7-9a, this force causes a clockwise torque at the tip of the natural fracture. This torque pushes the re-initiated fracture towards the centre of the sample. As the re-initiated fracture moves away from the tip, the effect of torque decreases and fracture re-orient itself in the direction of least resistance, which is parallel to the  $\sigma_H$  direction. In Figure 7-9b, high permeability of the natural fracture allows the fluid to flow inside the natural fracture. Consequently the natural fracture is pressurised. The pressure inside the fracture causes compressive forces on the sides of the natural fracture and increases the energy that is required for the re-initiated fracture to move towards the centre. As a result, the fracture tends to be straighter in the direction of  $\sigma_H$ . It should be noted that a competition between torque and compressive forces effect takes place here. If the torque effect is higher than the effect of compressive forces, the fracture tends to move towards the centre. This effect can be seen in images 46 to 48. In image 46, the natural fracture is 3cm away from the wellbore, and in image 48 it is 4.5 cm away. In this case, the torque in image 48 is more significant than the torque in image 46. In image 48, both force and distance increase with respect to image 46. As a result, the torque increases and pushes the fracture toward the centre.

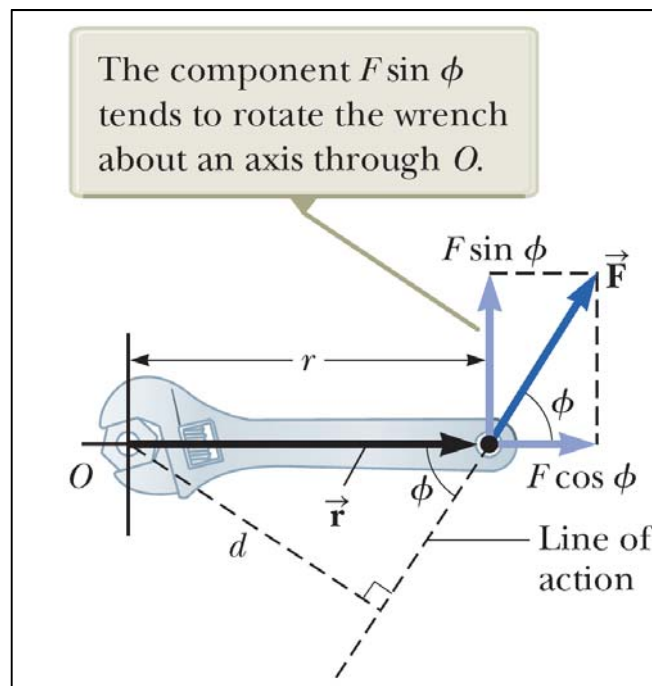


Figure 7-8: The greater the force ( $F$ ) or the arm ( $d$ ), the greater the Torque ( $T$ ).  $T = rF\sin\phi = |F|d$ . (Serway & Jewett, 2013)

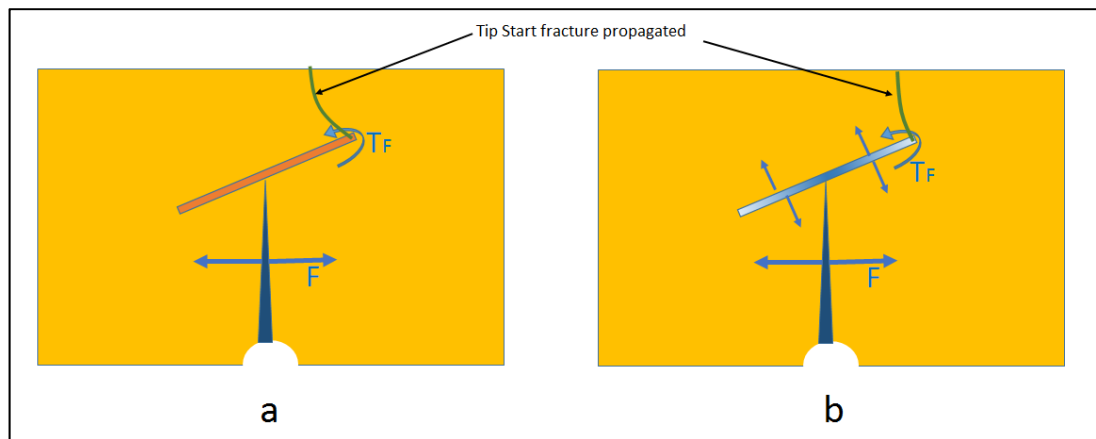


Figure 7-9: Rotational moment generated as a result of forces. a) Low permeability natural fracture. b) High permeability natural fracture. In the case of low permeability, the fracture is pushed more towards the centre.

Figure 7-4 also shows the hydraulic fracturing at different wellbore pressure profiles for different cases. In the images of Figure 7-4, the vertical axis shows pressure with a maximum value of 31 MPa, and the horizontal axis shows time in seconds with a maximum value of 5000 seconds. The axes' maximum is same for all images so that the pressure profile can be visually and easily compared between the different cases. In all cases pressure increases in a linear trend to the point where initiation and breakdown occurs. After breakdown, the pressure declines. Pressure decline continues until the hydraulic fracture intersects the natural fracture. At this stage the pressure continues to decline or starts to rebound, depending on the permeability of the natural fracture. If the permeability is high, pressure will continue to decline with a higher decline rate. If the permeability is low, pressure will rebound. If the natural fracture permeability is low, pressure rebound and increasing trend continues until crossing or tip start occurs as a result of stress concentration from hydraulic force inside the hydraulic fracture. If the permeability is high, the fracture stops and the natural fracture starts to pressurize. In this case, the pressure force inside the hydraulic fracture and natural fracture and fluid pressure at the tip of the natural fracture causes tip start fracture initiation. The pressure profile of images 1, 4 and 7 demonstrates that the crossing mechanism in image 1 required a lower pressure increase than that of the tip start mechanism, as shown in images 4 and 7. The pressure profile in Figure 7-4 also indicates that increasing the distance of the natural fracture from the wellbore decreases the amount of pressure increase which is required to re-initiate the fracture at the tip. This behaviour is seen in the most of the

images, such as images 4 to 6. These three images show that the peak of the pressure rebound is higher in image 4 with lower natural fracture distance, and it is lower in image 7 with higher natural fracture distance. The reason for this can be explained by Figure 7-5 and Figure 7-9. These two figures demonstrate that increasing the distance of the natural fracture from the wellbore increases the hydraulic force inside the hydraulic fracture. Increasing the natural fracture distance from the wellbore also increases the distance between the tip of the natural fracture and the point where the net hydraulic force is applied on the hydraulic fracture wall. These two effects generate higher stress concentration and higher torque (increasing force or arm increases torque) at the tip of the natural fracture.

Table 7-2: Variable parameters and test results; b: distance from centre of wellbore to centre of fracture; l: natural fracture length;  $\alpha$ : angle between natural fracture normal and maximum horizontal stress direction;  $\sigma_h$ : minimum horizontal stress; Kn: natural fracture permeability

Test#	b, cm	l, cm	$\alpha$ , °	$\sigma_h$ , MPa	Kn, md	Top Wing	Bottom Wing
1	3	3	15	6.89	0.02	Straight Cross	Straight Cross
2	3.75	3	15	6.89	0.02	Straight Cross	offset cross
3	4.5	3	15	6.89	0.02	offset cross	offset cross
4	3	3	45	6.89	0.02	Tip Start	Tip Start
5	3.75	3	45	6.89	0.02	Tip Start	Tip Start
6	4.5	3	45	6.89	0.02	Tip Start	Tip Start
7	3	3	60	6.89	0.02	Tip Start	Tip Start
8	3.75	3	60	6.89	0.02	Tip Start	Tip Start
9	4.5	3	60	6.89	0.02	Tip Start	Tip Start
10	3	3	15	10.34	0.02	Straight Cross	Arrest
11	3.75	3	15	10.34	0.02	Straight Cross	Straight Cross
12	4.5	3	15	10.34	0.02	offset cross	offset cross
13	3	3	45	10.34	0.02	Tip Start	Tip Start
14	3.75	3	45	10.34	0.02	Tip Start	Tip Start
15	4.5	3	45	10.34	0.02	Tip Start	Tip Start
16	3	3	60	10.34	0.02	Tip Start	Tip Start
17	3.75	3	60	10.34	0.02	Tip Start	Tip Start
18	4.5	3	60	10.34	0.02	Tip Start	Tip Start
19	3	3	15	13.79	0.02	Straight Cross	Arrest
20	3.75	3	15	13.79	0.02	Straight Cross	offset cross
21	4.5	3	15	13.79	0.02	Straight Cross	Arrest

22	3	3	45	13.79	0.02	Tip Start	Tip Start
23	3.75	3	45	13.79	0.02	Tip Start, offset cross	Tip Start
24	4.5	3	45	13.79	0.02	Tip Start	Tip Start, Parallel propagate
25	3	3	60	13.79	0.02	Tip Start	Tip Start
26	3.75	3	60	13.79	0.02	Tip Start	Tip Start
27	4.5	3	60	13.79	0.02	Tip Start	Parallel propagate, Tip Start
28	3	3	15	6.89	2	Straight Cross	Tip Start
29	3.75	3	15	6.89	2	Tip Start	offset cross
30	4.5	3	15	6.89	2	Tip Start	Tip Start
31	3	3	45	6.89	2	Tip Start	Tip Start
32	3.75	3	45	6.89	2	Tip Start	Tip Start
33	4.5	3	45	6.89	2	Tip Start	Tip Start
34	3	3	60	6.89	2	Tip Start	Tip Start
35	3.75	3	60	6.89	2	Tip Start	Tip Start
36	4.5	3	60	6.89	2	Tip Start	Tip Start
37	3	4.5	60	6.89	2	Tip Start	Tip Start
38	3.75	4.5	60	6.89	2	Tip Start	Tip Start
39	4.5	4.5	60	6.89	2	Tip Start	Tip Start
40	3	3	15	6.89	200	Tip Start	Tip Start
41	3.75	3	15	6.89	200	Tip Start	Tip Start
42	4.5	3	15	6.89	200	Tip Start	Tip Start
43	3	4.5	15	6.89	200	Tip Start	Tip Start
44	3.75	4.5	15	6.89	200	Tip Start	Tip Start
45	4.5	4.5	15	6.89	200	Tip Start	Tip Start
46	3	3	45	6.89	200	Tip Start	Tip Start
47	3.75	3	45	6.89	200	Tip Start	Tip Start
48	4.5	3	45	6.89	200	Tip Start	Tip Start
49	3	4.5	45	6.89	200	Tip Start	Tip Start
50	3.75	4.5	45	6.89	200	Tip Start	Tip Start
51	4.5	4.5	45	6.89	200	Tip Start	Tip Start
52	3	3	60	6.89	200	Tip Start	Tip Start
53	3.75	3	60	6.89	200	Tip Start	Tip Start
54	4.5	3	60	6.89	200	Tip Start	Tip Start

55	3	4.5	60	6.89	200	Tip Start	Tip Start
56	3.75	4.5	60	6.89	200	Tip Start	Tip Start
57	4.5	4.5	60	6.89	200	Tip Start	Tip Start
58	3	3	15	10.34	200	Tip Start	Tip Start
59	3.75	3	15	10.34	200	Tip Start	Tip Start
60	4.5	3	15	10.34	200	Tip Start	Tip Start
61	3	3	15	13.79	200	Tip Start	Tip Start
62	3.75	3	15	13.79	200	Tip Start	Tip Start
63	4.5	3	15	13.79	200	Tip Start	Tip Start
64	3	4.5	45	6.89	0.02	Tip Start	Tip Start
65	3.75	4.5	45	6.89	0.02	Tip Start	Tip Start
66	4.5	4.5	45	6.89	0.02	Tip Start	Tip Start
67	3	3	0	6.89	200	Tip Start	Tip Start
68	3.75	3	0	6.89	200	Tip Start	Tip Start
69	4.5	3	0	6.89	200	Tip Start	Tip Start

### 7.3. Hydraulic Fracturing in Presence of Abundant Natural Fractures

This section presents the results of a few sensitivity analyses regarding hydraulic fracture propagation in the presence of abundant natural fractures. Figure 7-10 shows three sensitivity results with sensitivity parameters presented below each image. The direction of maximum and minimum horizontal stresses is same as shown in Figure 7-1. Figure 7-10a shows fracture propagation in the presence of two natural fractures, the same as shown in the previous section. In this case, natural fracture permeability is 200 md, which corresponds to 10000 times matrix permeability. The hydraulic fracture intersects the natural fractures, pressurises them and causes tip start initiation and propagation. Both initial hydraulic fracture and re-initiated fractures propagate in the direction of maximum horizontal stress. Figure 7-10b shows hydraulic fracturing in the presence of a set of natural fractures with a 30° angle between the natural fracture and  $\sigma_h$  direction. The hydraulic fracture shows a step-stair propagation path. This image shows that the hydraulic fracture propagates away from the wellbore in both directions orthogonal to the wellbore. Figure 7-10c shows hydraulic fracturing in the presence of two sets of natural fractures. The first set has a 30° angle with

respect to the direction of  $\sigma_h$  and the second set has a  $-50^\circ$  angle with  $\sigma_h$  direction. The set with a  $30^\circ$  angle has a permeability of 200 md and the other set has a permeability of 20 md. To be able to discuss the process clearly, fractures that were involved in the fracture interaction are numbered. The hydraulic fracture first hit natural fractures 2 and 3 above and below the wellbore. No fracture initiation occurred from these two fractures. Fluid flowed from these fractures to fractures 5 and 6 and then to fractures 1 and 4. Three fracture initiations can be seen from the tip of fractures 4, 5 and 6. Fluid pressures at these tips are very small and the fluid pressure could not cause fracture re-initiation. Rather, it was the effect of stress concentration that caused the fracture re-initiation. Also from this image, it can be seen that the re-initiated fracture from the tip of fracture 6 has stopped and did not reach the boundary. The other two initiated fractures reached the boundaries.

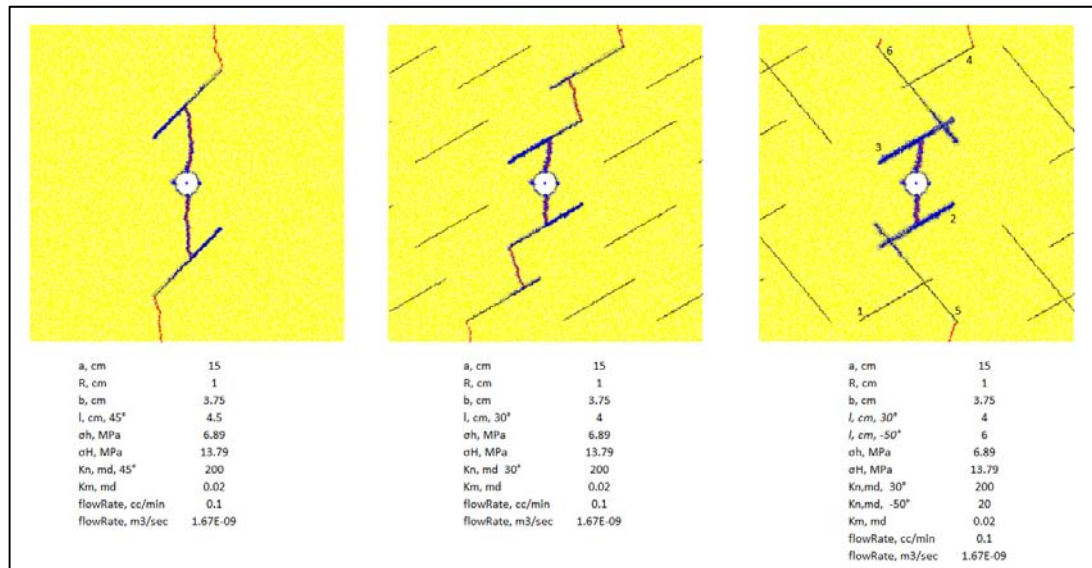


Figure 7-10: Hydraulic fracturing in the presence of natural fractures. (a) Two natural fractures on either side of wellbore. (b) One natural fracture set at  $30^\circ$ . (c) Two natural fracture sets at  $30^\circ$  and  $-50^\circ$ .

Figure 7-11 shows three more sensitivity analyses for a sample with a of 0.02 md, a width of 11 cm and a height of 22 cm. The directions of the principal stresses are same as shown in Figure 7-1. Figure 7-11a shows hydraulic fracturing in a sample with no natural fractures. After fracture breakdown, the wellbore pressure declines to reach a stabilised pressure value versus time. Figure 7-11b shows hydraulic fracturing in the presence of a set of natural fractures with 200 md permeability. The direction of natural fractures with respect to  $\sigma_h$  direction is  $30^\circ$ . This figure shows a

step-stair fracturing mechanism. That is, after the hydraulic fracture interacted with the natural fractures, it re-initiated from the tip of the natural fractures in a stair shape. After breakdown pressure, the wellbore pressure declined to reach a minimum value and then rebounded to get a stabilised pressure. No pressure rebound was observed during fracture propagation. This is due to the high permeability of natural fractures. Figure 7-11c shows hydraulic fracturing in the presence of two sets of natural fractures. The second set of natural fractures has a permeability of 20 md and their direction with respect to  $\sigma_h$  direction is  $-50^\circ$ . The hydraulic fracture has re-initiated from the tip of the natural fractures once it intersected both sets. The interaction of the hydraulic fracture with the natural fractures caused the wellbore pressure to rebound and increase. Two pressure rebounds are observed in this figure. The amount of the second pressure rebound is less than the first pressure rebound. This is consistent with what was observed from the results presented in Figure 7-4. From Figure 7-4, it can be concluded that the amount of pressure rebound is lower in the case of natural fractures that are further away from the wellbore.

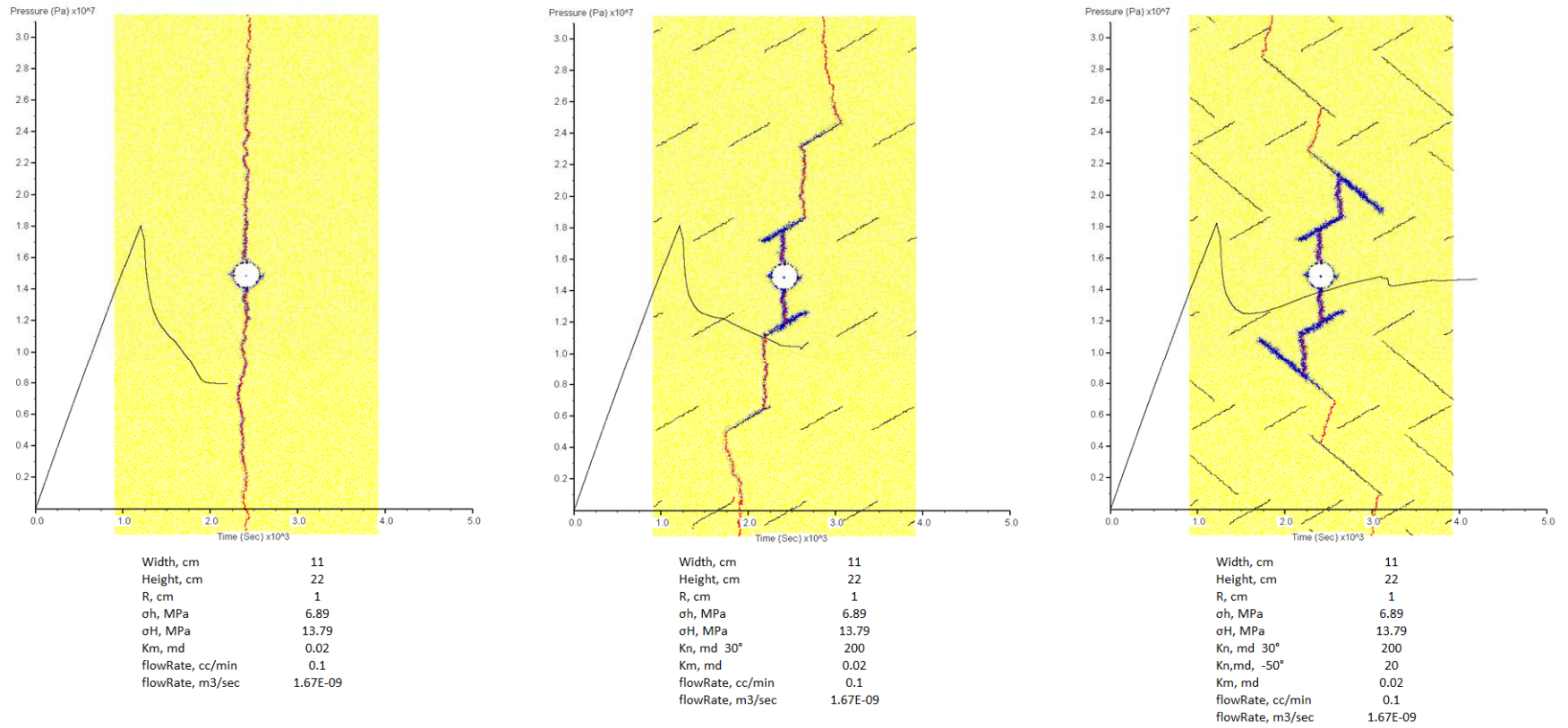


Figure 7-11: a: Hydraulic fracturing with no natural fracture in sample. b: Hydraulic fracturing in the presence of one set of natural fractures which their normal is at 30° orientation with respect to the direction of  $\sigma_H$ . c: Hydraulic fracturing in the presence of two sets of natural fractures.

This chapter presents the results of the sensitivity analysis for the interaction mechanism between a hydraulic fracture and natural fractures. The observations of the sensitivity analysis are summarised below:

- Increasing the natural fracture to matrix permeability ratio reduces the chance of crossing the natural fractures, and increases the chance of tip start propagation.
- Increasing the ratio of the natural fracture to matrix permeability ratio changes the re-initiation mechanism from crossing to tip start at a low angle of  $15^\circ$ .
- At a natural fracture to permeability ratio of 10,000, crossing did not occur even at high angles of approach.
- Decreasing the angle between natural fracture plane and  $\sigma_H$  decreases the chance of crossing the natural fracture and increases the chance of tip start propagation.
- Tip start occurs at the tip, which is further away from the wellbore.
- After crossing the natural fracture or tip start, the fracture continues to propagate in the initial direction and parallel to the direction of  $\sigma_H$ .
- Once the hydraulic fracture intersects the natural fractures, the wellbore pressure rises. Fracture propagation at this stage stops. Increasing the wellbore pressure and average fracture pressure re-initiates fracture propagation either by crossing the natural fracture or tip start.
- Increasing the fracture distance from the wellbore decreases the peak of the second pressure rise.
- Increasing  $\sigma_h$  value while keeping  $\sigma_H$  value at a constant level increases the initial fracture initiation and breakdown pressure. It also increases the re-initiation pressure significantly.
- Decreasing the permeability of the natural fracture increases the fracture re-initiation pressure.
- The tip start condition is observed to be a dominant mechanism, which occurs more than the natural fracture crossing mechanism.
- At low natural fracture permeability similar to matrix permeability, fluid will not pressurise natural fractures. In this case, stress concentration at the tip of

the natural fracture is created by pressure inside the hydraulic fracture.

Therefore, natural fracture pressure has no effect on the tip start mechanism.

Understanding the interaction mechanism is very important for low permeability formations such as shale oil or shale gas formations. Different interaction mechanisms are desired for different shale plays. Figure 7-12 demonstrates the Brinell Hardness Number for different shale formations in the United States. The higher the Brinell Hardness Number, the more brittle the formation. Figure 7-12 demonstrates that Barnett shale is the most brittle shale formation, and Bossier formation is the softest formation.

In brittle formations, created hydraulic fracture does not heal easily once the well has flowed back. As a result, a high volume of slick water with low proppant concentration is used. Once a hydraulic fracture interacts with natural fractures, water leaks off into the natural fractures and causes shear slippage. This shear slippage and re-alignment of natural fracture surface irregularities causes natural fractures to self-prop, and increases natural fractures' permeability. Because of this phenomenon, it is desirable that hydraulic fractures do not just cross natural fractures, but they re-initiate from the tip of natural fractures and cause a fracture branch out.

In soft formations such as Haynesville Shale, once the fluid inside the created hydraulic fracture has flowed back, the fracture can heal easily. As a result, a high viscosity fluid such as crossed-linked gel with high proppant concentration is required to compensate for the healing effect and to keep the fracture open. High viscosity fluid causes a high net pressure inside the fracture. High net pressure allows a wider fracture. As a result, higher proppant volume can be placed inside the fracture. In this case, it is desired that hydraulic fractures cross the natural fractures to prevent fluid leak-off and early screen out. It should be noted that if the hydraulic fracture diverts from its propagation path, proppants can settle at the interaction point, as they cannot turn into the natural fracture as easily as fluid does. This can lead to early screen out.

Another main observation from the sensitivity analysis is that, after the hydraulic fracture intersects natural fractures with low permeability, the wellbore pressure starts to increase. This pressure increase can be confused with pressure increase due

to proppant screen out, to which the response is to stop fluid injection. This confusion can lead to under-stimulation of the formation leading to lower stimulated volume, which means lower production.

These observations and results show the importance of the interaction mechanism of hydraulic fracture with natural fractures. In the first stage of a study to design hydraulic fracturing, a proper understanding of in-situ parameters such as stress state, natural fracture and rock mechanical properties is required. In the second stage, hydraulic fracturing in the presence of natural fractures should be simulated to understand the propagation path, interaction mechanism and wellbore pressure behaviour. After that, the simulation results should be compared against field results to calibrate the model and better understand uncertainties, in order to achieve a better design for the next fracturing operations. This is an optimisation process that should continue as long as financial and operational circumstances allow.

This concludes this chapter; in the next chapter the main study conclusions as well as recommendations for further study are presented.

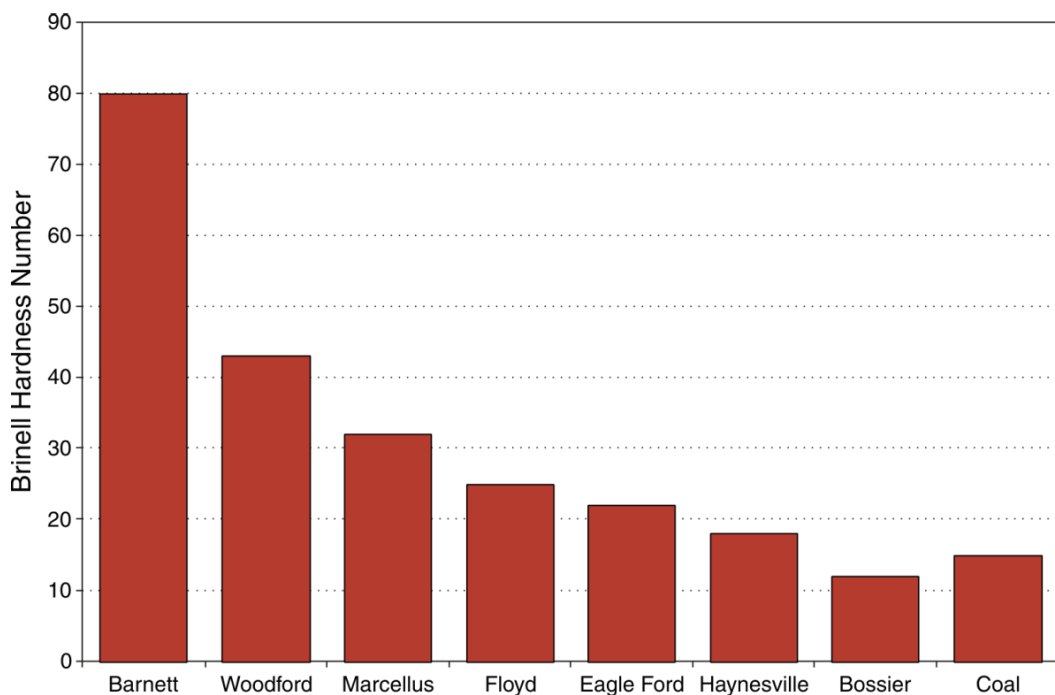


Figure 7-12: Brinell Hardness Number in different shale formations in United States. (Stegent et al, 2011)

# 8

## Conclusion and Recommendations

This study focuses on developing a numerical simulation in PFC2D to investigate the interaction mechanism of a hydraulic fracture with natural fractures. The numerical model is developed based on the Distinct Element Method, which itself is a sub-classification of the Discrete Element Method. The model development is presented in a systematic way, starting from the creation of a sample with the desired rock mechanical properties, and comparing the results with real sample results to validate the simulation outcome. Following this, the fluid flow model and algorithm and validation are presented to demonstrate how the fluid flow inside the sample and fracture works. Validation of the fluid flow is performed using analytical studies. The fracture initiation and breakdown pressure as well as fracture propagation behaviour are then studied. The model results are validated using the results from experimental studies. The model is taken one step ahead to simulate for better understanding of hydraulic fracture propagation and the natural fracture interaction mechanism. Model results are compared against laboratory experimental results to validate the simulation results. In the last step, a rigorous sensitivity analysis is performed using numerical simulation in order to investigate the influence of different parameters on the interaction mechanism. The following conclusions are based on this study.

### 8.1. Conclusions

- The fluid flow model and algorithm proposed in this study appear to be a viable tool which can easily handle complex scenarios such as reservoirs with natural discontinuities for any reservoir shape with any fluid flow regime.
- The fracture initiation pressure and breakdown pressure are not necessarily the same pressure. Once fracture initiation occurs, the pressure can still increase to reach breakdown pressure. In other words, the fracture breakdown

pressure is generally higher to some extent than the fracture initiation pressure.

- Fracture initiation pressure can be inferred from the plot of pressure–time and pressurization rate–time plots. Once fracture initiation occurs, the pressure–time plot deviates from a linear trend. The pressurisation rate decreases after initiation time.
- Breakdown pressure is the maximum pressure on the pressure–time plot. Pressurisation rate at breakdown time is zero.
- Both experimental and numerical results demonstrate that increasing the angle between the direction of maximum horizontal stress and natural fracture planes increases the chance of the propagated hydraulic fracture crossing the natural fractures. The results also show that the natural fracture’s filling material plays a vital role in the outcome of interaction between hydraulic and natural fracture. Weak filling materials increase the chance of shear slippage on natural fracture planes, while increasing the strength of filling material increases the chance of crossing the natural fractures.
- The experimental results show that if a hydraulic fracture crosses the boundary that is orthogonal to vertical stress, it can cause a rapid depressurisation of the fracturing fluid, resulting in rapid loss of fluid energy. This can affect the interaction behaviour of hydraulic and natural fractures, and cause the hydraulic fracture to arrest at the natural fracture planes. Numerical simulation appeared to handle this situation better and generate more accurate results.
- Misaligned gluing of slabs to the centre piece during preparation of laboratory testing samples can cause misleading interaction behaviour of natural and propagated hydraulic fractures, which highlights the importance of serious attention to a careful preparation of testing samples. The chance of such error is relatively thin for numerical modelling. The simulation model was found to be a better representation of the test scenario, which can generate more accurate results to interpret the interaction behaviour of natural and propagated hydraulic fractures.

- Increasing the ratio of natural fracture to matrix permeability reduces the chance of crossing the natural fracture, and increases the chance of tip start propagation.
- Increasing the ratio of natural fracture to matrix permeability changes the re-initiation mechanism from crossing the natural fracture to tip start at a low angle of  $15^\circ$ .
- At a natural fracture to permeability ratio of 10,000, crossing did not occur even at high angles of approach of  $90^\circ$ .
- Decreasing the angle between the natural fracture plane and the direction of  $\sigma_H$  decreases the chance of crossing the natural fracture and increases the chance of tip start propagation.
- Tip start occurs at the tip further away from the wellbore.
- After crossing the natural fracture or tip start, the fracture continues to propagate towards its initial direction which is parallel to the direction of  $\sigma_H$ .
- Once the hydraulic fracture intersects the natural fractures, the wellbore pressure can rise. Fracture propagation at this stage stops. Increasing the wellbore pressure and average fracture pressure re-initiates fracture propagation either by crossing the natural fracture or tip start.
- Increasing the fracture distance from the wellbore decreases the peak of the second pressure rise.
- Increasing  $\sigma_h$  value while keeping  $\sigma_H$  value at a constant level increases the initial initiation and breakdown pressure and the re-initiation pressure significantly.
- Decreasing the permeability of natural fracture increases the re-initiation pressure.
- The tip start condition is observed to be a dominant mechanism, which occurs more than the natural fracture crossing mechanism.
- At a low natural fracture permeability similar to matrix permeability, fluid will not pressurise natural fractures. In this case, stress concentration at the tip of the natural fracture is created by pressure inside the hydraulic fracture. Therefore, natural fracture pressure is not affected by the tip start mechanism.

## 8.2. Recommendations

- In the experimental tests, the natural fractures crossed the boundaries of the sample. This causes a different stress distribution in the case where natural fractures are contained within the sample. Future studies can be performed to come up with a solution to create natural fractures within the sample while maintaining control over the natural fracture properties.
- Experimental tests were conducted with dry samples. To consider the effect of pore pressure, future experimental tests need to be performed with samples saturated with fluid, and the pore pressure should be raised to the desired level.
- Tests were performed on cement samples. These samples have high Young's Modulus and low Poisson's ratio that makes them very brittle. A synthetic shale sample can be created using Yazid et al.'s methodology (as cited in Altowairqi et al., 2015a; b) to investigate fracture propagation in more ductile formations. Alternatively, a mixture of bentonite and gypsum can be used to study the effect of mechanical properties on fracture propagation in ductile formations.
- A large number of tests regarding fracturing and fracture propagation are reported so far in the literature. However, tests from one organisation to another and from one person to another are quite different. These differences makes the benchmarking and comparison very difficult, and in some cases irrelevant. A standard needs to be developed, such as the API standard, for these tests to make cross comparisons quicker and easier. Following this, a universal database can be created that captures all test parameters and results. With this resource, researchers will not repeat what has been done before. Rather, they will focus on what needs to be done to complete the database and push the frontiers.
- The current simulation was performed in PFC2D. While this gives a valuable insight into the fracture interaction mechanism, future work can be pursued to extend the model to PFC3D. A three-dimensional model will capture the physics of the problem more accurately.
- The current simulation considers single phase flow. While this is the main mechanism inside the hydraulic fracture, multiphase flow can occur inside the

matrix (rock). Although fluid flow into the matrix was not a major issue in this study, as it was done using high viscous fluid and a low permeability sample, to extend the model to more permeable formations, a multiphase flow needs to be incorporated.

# References

- Abou-Sayed, A. S., Brechtel, C. E. & Clifton, R. J. (1978). In situ stress determination by hydrofracturing: A fracture mechanics approach. *Journal of Geophysical Research: Solid Earth*, 83(B6), 2851-2862.
- Administration, U. S. E. I. (2016). Short-Term Energy Outlook. Available online: [https://www.eia.gov/forecasts/steo/pdf/steo\\_full.pdf](https://www.eia.gov/forecasts/steo/pdf/steo_full.pdf)
- Altowairqi, Y., Rezaee, R., Evans, B. & Urosevic, M. (2015a). Measuring elastic properties to determine the influence of TOC on Synthetic Shale Samples. *ASEG Extended Abstracts*, 2015(1), 1-5.
- Altowairqi, Y., Rezaee, R., Evans, B. & Urosevic, M. (2015b). Shale elastic property relationships as a function of total organic carbon content using synthetic samples. *Journal of Petroleum Science and Engineering*, 133, 392-400.
- Asadi, S., Bohlooli, B. & Malekijavan, M. R. (2012) Numerical investigation of fracture initiation and propagation of hydraulic fracturing based on fracture mechanics. *ISRM: International Society for Rock Mechanics*.
- Blanton, T. L. (1982) An experimental study of interaction between hydraulically induced and pre-existing fractures. *SPE: Society of Petroleum Engineers*.
- Blanton, T. L. (1986) Propagation of Hydraulically and Dynamically Induced Fractures in Naturally Fractured Reservoirs. *SPE: Society of Petroleum Engineers*.
- Boyce, G. H., Doe, T. W. & Majer, E. (1984) Laboratory hydraulic fracturing stress measurements in salt. *ARMA: American Rock Mechanics Association*.
- Bunger, A. P. (2005) Near-surface hydraulic fracture. [location]: University of Minnesota.
- Chan, P. B., Etherington, J. & Aguilera, R. (2012) Using the SPE/WPC/AAPG/SPEE/SEG PRMS to evaluate unconventional resources. *SPE: Society of Petroleum Engineers*, 4(2).
- Chudnovsky, A., Fan, F., Shulkin, Y., Zhang, H., Dudley, J. W. & Wong, G. K. (2008) Hydraulic fracture simulation revisited. *ARMA: American Rock Mechanics Association*.
- Cundall, P. A. (1988). Formulation of a three-dimensional distinct element model—Part I. A scheme to detect and represent contacts in a system composed of many polyhedral blocks. *International Journal of Rock Mechanics and Mining Sciences & Geomechanics Abstracts*, 25(3), 107-116.
- Cundall, P. A. & Hart, R. D. (1992). Numerical modelling of discontinua. *Engineering Computations*, 9(2), 101-113.

- Cundall, P. A. & Strack, O. D. L. (1979). A discrete numerical model for granular assemblies. *Geotechnique*, 29(1), 47-65.
- Daneshy, A. A. (1974). Hydraulic fracture propagation in the presence of planes of weakness. *SPE: Society of Petroleum Engineers*.
- Daneshy, A. A. (1978.) Hydraulic fracture propagation in layered formations. *SPE: Society of Petroleum Engineers*, 18(01).
- Detournay, E. & Carbonell, R. (1997). Fracture-mechanics analysis of the breakdown process in minifracture or leakoff test. *SPE: Society of Petroleum Engineers*, 12(03).
- Detournay, E. E. & Cheng, A. E. (1992) Influence of pressurization rate on the magnitude of the breakdown pressure. *ARMA: American Rock Mechanics Association*.
- Eseme, E., Urai, J. L., Krooss, B. M. & Littke, R. (2007). Review of mechanical properties of oil shales: Implications for exploitation and basin modelling. *Oil Shale*, 24(2), 159-174.
- Fallahzadeh, S. H., James Cornwell, A., Rasouli, V. & Hossain, M. (2015). The impacts of fracturing fluid viscosity and injection rate on the near wellbore hydraulic fracture propagation in cased perforated wellbores. *ARMA: American Rock Mechanics Association*.
- Fatahi, H. (2014). Simulation of shale mechanical properties in PFC2d and calibration of them against lab results for tensile, uni-axial and confined compression tests. *SPE: Society of Petroleum Engineers*.
- Fatahi, H. & Hossain, M. M. (2016). Fluid flow through porous media using distinct element based numerical method. *Journal of Petroleum Exploration and Production Technology*, 6(2), 217-242.
- Fatahi, H., Hossain, M. M., Fallahzadeh, S. H. & Mostofi, M. (2016). Numerical simulation for the determination of hydraulic fracture initiation and breakdown pressure using distinct element method. *Journal of Natural Gas Science and Engineering*, 33, 1219-1232.
- Gan, Q., Alpern, J. S., Marone, C., Connolly, P. & Elsworth, D. (2013). Breakdown pressures due to infiltration and exclusion in finite length boreholes. *ARMA: American Rock Mechanics Association*.
- Garagash, D. & Detournay, E. (1996). A Study of the breakdown process in hydraulic fracturing tests conducted in impermeable rocks. *ISRM: International Society for Rock Mechanics*.
- Gordeliy, E. & Detournay, E. (2011). A fixed grid algorithm for simulating the propagation of a shallow hydraulic fracture with a fluid lag. *International Journal for Numerical and Analytical Methods in Geomechanics*, 35(5), 602-629.

- Gu, H. & Weng, X. (2010). Criterion for fractures crossing frictional interfaces at non-orthogonal angles. *ARMA: American Rock Mechanics Association*.
- Gu, H., Weng, X., Lund, J. B., Mack, M. G., Ganguly, U. & Suarez-Rivera, R. (2011) Hydraulic fracture crossing natural fracture at non-orthogonal angles, a criterion, its validation and applications. *SPE: Society of Petroleum Engineers*.
- Gu, H., Weng, X., Lund, J. B., Mack, M. G., Ganguly, U. & Suarez-Rivera, R. (2012). Hydraulic fracture crossing natural fracture at nonorthogonal angles: A criterion and its validation. *SPE: Society of Petroleum Engineers*, 27(01), 20-26.
- Haimson, B. & Fairhurst, C. (1967). Initiation and extension of hydraulic fractures in rocks. *SPE: Society of Petroleum Engineers*, 7(03), 310-318.
- Haimson, B. & Fairhurst, C. (1969). Hydraulic fracturing in porous-permeable materials. *Journal of Petroleum Technology*, 21(07), 811-817.
- Haimson, B. C. & Huang, X. (1989) Hydraulic fracturing breakdown pressure and in situ stress at great depth. *ISRM: International Society for Rock Mechanics*.
- Haimson, B. C. & Zhao, Z. (1991) Effect of borehole size and pressurization rate on hydraulic fracturing breakdown pressure. *ARMA: American Rock Mechanics Association*.
- Hanson, M. E., Shaffer, R. J. & Anderson, G. D. (1981) Effects of various parameters on hydraulic fracturing geometry. *Society of Petroleum Engineers Journal*, 21(04), 435-443.
- Hart, R., Cundall, P. A. & Lemos, J. (1988). Formulation of a three-dimensional distinct element model—Part II. Mechanical calculations for motion and interaction of a system composed of many polyhedral blocks. *International Journal of Rock Mechanics and Mining Sciences & Geomechanics Abstracts*, 25(3), 117-125.
- Hubbert, M. K. & Willis, D. G. (1957) Mechanics Of hydraulic fracturing. *Society of Petroleum Engineers*.
- Huynh, K. D. V. (2014) *Discrete Element Method (DEM)*, 2014. Available online: <http://www.ngi.no/no/Innholdsbokser/Referansjeprojekter-LISTER-/Referanser/Discrete-Element-Method-DEM/>
- International Energy Outlook 2016*. Available online: [http://www.eia.gov/forecasts/ieo/pdf/0484\(2016\).pdf](http://www.eia.gov/forecasts/ieo/pdf/0484(2016).pdf)
- Itasca (2008) .Particle flow code in 2 dimensions. Fourth edition. [location]: *Itasca Consulting Group Inc*.
- Jing, L. & Stephansson, O. (2007). Fundamentals of Discrete Element Methods for rock engineering: Theory and applications. [location]: *Elsevier Science*.

- Lakirouhani, A., Bungler, A. & Detournay, E. (2008). Modeling initiation of hydraulic fractures from a wellbore. *ISRM: International Society for Rock Mechanics*.
- Lecampion, B. (2012). Hydraulic fracture initiation from an open-hole: wellbore size, pressurization rate and fluid-solid coupling effects. *ARMA: American Rock Mechanics Association*.
- Lecampion, B. & Detournay, E. (2007). An implicit algorithm for the propagation of a hydraulic fracture with a fluid lag. *Computer Methods in Applied Mechanics and Engineering*, 196(49–52), 4863-4880.
- Lhomme, T. P., de Pater, C. J. & Helfferich, P. H. (2002). Experimental study of hydraulic fracture initiation in Colton sandstone. *SPE: Society of Petroleum Engineers*.
- Lhomme, T. P. Y. (2005). Initiation of hydraulic fractures in natural sandstones. *TU Delft: Delft University of Technology*.
- Martin, C. D. (1993). The strength of massive Lac du Bonnet granite around underground openings. *Manitoba: University of Manitoba*.
- Medlin, W. L. & Masse, L. (1979). Laboratory investigation of fracture initiation pressure and orientation. *Society of Petroleum Engineers Journal*, 19(02), 129-144.
- Golder Associates Ltd. (1994). Laboratory Study of Hydraulic Fracture Propagation in Oil Sands, *Canada Centre for Mineral and Energy Technology (CANMET)*, Phase III: Final Report.
- Morris, J., Glenn, L. & Blair, S. (2003). The Distinct Element Method — Application to structures in jointed rock. In M. Griebel, & M. A. Schweitzer (Eds.), *Meshfree methods for partial differential equations*, pp. 291-306. Berlin, Heidelberg: Springer.
- Pak, A. & Chan, D. H. (2004). A fully implicit single phase T-H-M fracture model for modelling hydraulic fracturing in oil sands. *Journal of Canadian Petroleum Technology*, 43(06).
- Renshaw, C. E. & Pollard, D. D. (1995). An experimentally verified criterion for propagation across unbounded frictional interfaces in brittle, linear elastic materials. *International Journal of Rock Mechanics and Mining Sciences & Geomechanics Abstracts*, 32(3), 237-249.
- Rummel, F. (1987) Fracture mechanics approach to hydraulic fracturing stress measurements. In [editor names, initials first, then surnames] (Eds.) *Fracture mechanics of rock*, pp. 217-239. London: Academic Press.
- Sack, R. A. (1946) Extension of Griffith's theory of rupture to three dimensions. *Proceedings of The Physical Society*, 58(6), 729-736.

- Sarmadivaleh, M. (2012). Experimental and numerical study of interaction of a pre-existing natural interface and an induced hydraulic fracture. *Perth, WA: Curtin University*.
- Sarmadivaleh, M. & Rasouli, V. (2014). Test design and sample preparation procedure for experimental investigation of hydraulic fracturing interaction modes. *Rock Mechanics and Rock Engineering*, 48(1), 93-105.
- Sarmadivaleh, M. & Rasouli, V. (2015). Test design and sample preparation procedure for experimental investigation of hydraulic fracturing interaction modes. *Rock Mechanics and Rock Engineering*, 48(1), 93-105.
- Schmitt, D. R. & Zoback, M. D. (1989). Laboratory tests of the effects of pore pressure on tensile failure. *ISRM: International Society for Rock Mechanics*.
- Serway, R. A. & Jewett, J. W. (2013) Physics for scientists and engineers with modern physics. [location]: *Cengage Learning*.
- Seth, A. K. (2016) The science of selfhood. Retrieved from <https://neurobanter.com/>
- Stegent, N. A., Ingram, S. R. & Callard, J. G. (2011). Hydraulic fracture stimulation design considerations and production analysis. *SPE: Society of Petroleum Engineers*.
- Tavarez, F. A. & Plesha, M. E. (2007). Discrete element method for modelling solid and particulate materials. *International Journal for Numerical Methods in Engineering*, 70(4), 379-404.
- Technology, E. (2016). Epoxy Adhesive Application Guide. Retrieved from [http://www.epotek.com/site/files/brochures/pdfs/adhesive\\_application\\_guide.pdf](http://www.epotek.com/site/files/brochures/pdfs/adhesive_application_guide.pdf)
- U.S. Census Bureau, I. D. B. (2015). World population: 1950-2050. In. <http://www.census.gov/population/international/data/idb/worldpopgraph.php>
- Warpinski, N. R. & Teufel, L. W. (1987). Influence of geologic discontinuities on hydraulic fracture propagation (includes associated papers 17011 and 17074 ). *Journal of Petroleum Technology*, 39(02), 209-220.
- Wu, H., Golovin, E., Shulkin, Y., Chudnovsky, A., Dudley, J. W. & Wong, G. K. (2008). Observations of hydraulic fracture initiation and propagation in a brittle polymer. *ARMA: American Rock Mechanics Association*.
- Zhang, X., Jeffrey, R. G., Bungler, A. P. & Thiercelin, M. (2010). Initiation and growth of a hydraulic fracture from a borehole under toughness- or viscosity-dominated conditions. 2010/1/1/. *ARMA: American Rock Mechanics Association*.
- Zhao, Z. (1995). Determination of far-field stresses by hydraulic fracturing in Lac Du Bonnet Granite and Indiana Limestone. *Madison: University of Wisconsin*.
- Zhao, Z., Kim, H. & Haimson, B. (1996). Hydraulic fracturing initiation in granite. *ARMA: American Rock Mechanics Association*.

Zhou, J., Chen, M., Jin, Y. & Zhang, G.-q. (2008). Analysis of fracture propagation behavior and fracture geometry using a tri-axial fracturing system in naturally fractured reservoirs. *International Journal of Rock Mechanics and Mining Sciences*, 45(7), 1143-1152.

Zoback, M., Rummel, F., Jung, R. & Raleigh, C. (1977). Laboratory hydraulic fracturing experiments in intact and pre-fractured rock. *International Journal of Rock Mechanics and Mining Sciences & Geomechanics Abstracts*. Elsevier.

*Every reasonable effort has been made to acknowledge the owners of copyright material. I would be pleased to hear from any copyright owner who has been omitted or incorrectly acknowledged.*

# Copyright Permissions

07/03/2017

RightsLink Printable License

## ELSEVIER LICENSE TERMS AND CONDITIONS

Mar 07, 2017

This Agreement between Hassan Fatahi ("You") and Elsevier ("Elsevier") consists of your license details and the terms and conditions provided by Elsevier and Copyright Clearance Center.

License Number	4063580845266
License date	Mar 07, 2017
Licensed Content Publisher	Elsevier
Licensed Content Publication	Journal of Natural Gas Science and Engineering
Licensed Content Title	Numerical and experimental investigation of the interaction of natural and propagated hydraulic fracture
Licensed Content Author	Hassan Fatahi,Md Mofazzal Hossain,Mohammad Sarmadivaleh
Licensed Content Date	January 2017
Licensed Content Volume	37
Licensed Content Issue	n/a
Licensed Content Pages	16
Start Page	409
End Page	424
Type of Use	reuse in a thesis/dissertation
Portion	full article
Format	both print and electronic
Are you the author of this Elsevier article?	Yes
Will you be translating?	No
Order reference number	
Title of your thesis/dissertation	Simulation of Hydraulic Fracture Propagation Interacted with Natural Fractures
Expected completion date	Nov 2016
Estimated size (number of pages)	190
Elsevier VAT number	GB 494 6272 12
Requestor Location	Hassan Fatahi 7/5 North Street  Midland, WA 6056 Australia Attn: Hassan Fatahi
Total	0.00 AUD

**ELSEVIER LICENSE  
TERMS AND CONDITIONS**

Oct 25, 2016

This Agreement between Hassan Fatahi ("You") and Elsevier ("Elsevier") consists of your license details and the terms and conditions provided by Elsevier and Copyright Clearance Center.

License Number	3975940622876
License date	Oct 25, 2016
Licensed Content Publisher	Elsevier
Licensed Content Publication	Journal of Natural Gas Science and Engineering
Licensed Content Title	Numerical simulation for the determination of hydraulic fracture initiation and breakdown pressure using distinct element method
Licensed Content Author	Hassan Fatahi,Md Mofazzal Hossain,Seyed Hassan Fallahzadeh,Masood Mostofi
Licensed Content Date	July 2016
Licensed Content Volume Number	33
Licensed Content Issue Number	n/a
Licensed Content Pages	14
Start Page	1219
End Page	1232
Type of Use	reuse in a thesis/dissertation
Intended publisher of new work	other
Portion	full article
Format	both print and electronic
Are you the author of this Elsevier article?	Yes
Will you be translating?	No
Order reference number	
Title of your thesis/dissertation	Simulation of Hydraulic Fracture Propagation Interacted with Natural Fractures
Expected completion date	Nov 2016
Estimated size (number of pages)	190
Elsevier VAT number	GB 494 6272 12
Requestor Location	Hassan Fatahi 7/5 North Street  Midland, WA 6056 Australia Attn: Hassan Fatahi
Total	0.00 AUD

**RightsLink®**[Home](#)[Account Info](#)[Help](#)

**Title:** Fluid flow through porous media using distinct element based numerical method

**Author:** Hassan Fatahi

**Publication:** Journal of Petroleum Exploration and Production Technology

**Publisher:** Springer

**Date:** Jan 1, 2015

Copyright © 2015, The Author(s)

Logged in as:  
Hassan Fatahi

[LOGOUT](#)

### Permissions Request

This is an open access article distributed under the terms of the Creative Commons Attribution License, which permits unrestricted use, distribution, and reproduction in any medium, provided the original work is properly cited.

Springer and BioMed Central offer a reprint service for those who require professionally produced copies of articles published under Creative Commons Attribution (CC BY) licenses. To obtain a quotation, please email [reprints@springeropen.com](mailto:reprints@springeropen.com) with the article details, quantity(ies) and delivery destination. Minimum order 25 copies.

**SOCIETY OF PETROLEUM ENGINEERS LICENSE  
TERMS AND CONDITIONS**

Oct 25, 2016

This Agreement between Hassan Fatahi ("You") and Society of Petroleum Engineers ("Society of Petroleum Engineers") consists of your license details and the terms and conditions provided by Society of Petroleum Engineers and Copyright Clearance Center.

License Number	3975940115005
License date	Oct 25, 2016
Licensed Content Publisher	Society of Petroleum Engineers
Licensed Content Publication	SPE Proceedings
Licensed Content Title	Simulation of Shale Mechanical Properties in PFC2d and Calibration of Them Against Lab Results for Tensile, Uni-Axial and Confined Compression Tests
Licensed Content Author	Hassan Fatahi, Curtin University et al
Licensed Content Date	2014
Type of Use	Thesis/Dissertation
Requestor type	author of the original work
SPE member	yes
SPE member number	4092727
Format	print and electronic
Portion	full article
Will you be translating?	no
Distribution	999999
Order reference number	
Title of your thesis / dissertation	Simulation of Hydraulic Fracture Propagation Interacted with Natural Fractures
Expected completion date	Nov 2016
Estimated size (number of pages)	190
Requestor Location	Hassan Fatahi 7/5 North Street  Midland, WA 6056 Australia Attn: Hassan Fatahi
Billing Type	Invoice
Billing Address	Hassan Fatahi 7/5 North Street  Midland, Australia 6056 Attn: Hassan Fatahi
Total	0.00 AUD